Technische Universität München
TUM School of Natural Sciences

# Klinische Anwendungen spektraler Detektoren in der Computertomographie

Johannes Leopold Hammel

Vollständiger Abdruck der von der TUM School of Natural Sciences der Technischen Universität München zur Erlangung des akademischen Grades eines

Doktors der Naturwissenschaften (Dr. rer. nat.)

genehmigten Dissertation.

| | |
|---|---|
| Vorsitz: | Prof. Dr. Martin Zacharias |
| Prüfer der Dissertation: | 1. Prof. Dr. Franz Pfeiffer |
| | 2. Prof. Dr. Jan Jakob Wilkens |

Die Dissertation wurde am 25.07.2024 bei der Technischen Universität München eingereicht und durch die TUM School of Natural Sciences am 05.11.2024 angenommen.

# Abstract

Detector technology is a key factor for the efficient use of Computed Tomography (CT) in daily diagnostic routines. For example in cardiac and musculoskeletal imaging applications. The current development of energy-responsive CT detector systems enables new diagnostic possibilities. This thesis focuses on the development and evaluation of novel diagnostic applications for energy-resolving detectors in CT. First, the physical principles of X-ray interaction with matter are introduced and building on this the basic concepts of clinical Dual Energy CT (DECT) are described. Two clinical applications follow, describing spectral dynamic myocardial CT perfusion and Scout-based Dual-Energy X-ray Absorptiometry (SDEXA), which is a novel technique opportunistically measuring the Bone Mineral Density (BMD) in every patient based on an extended overview scan.

Dynamic myocardial perfusion on a CT device with spectral capabilities was investigated in a phantom study and a porcine study. Contrast Agent (CA) sensitivity in low-perfused tissue and material quantification tasks are challenging using conventional CT detectors. The main advantages of spectral detection are the increased Signal-to-Noise Ratio (SNR) in iodine density measurements and the resulting improved fitting of the acquired Time Attenuation Curve (TAC) in the myocardium. Improved detection of the under-perfused myocardium using iodine density maps was demonstrated in the phantom study, independently of the underlying perfusion fit model. Also, the possibility of dose reduction was demonstrated in both studies. Based on the presented results, the clinical translation of spectral dynamic myocardial perfusion CT seems feasible and promising.

The SDEXA technique was introduced in 2019 and evaluated in the second results chapter of this thesis regarding the most important aspects for the introduction into the clinical routine. Measurements taken on the European Spine Phantom (ESP) showed improved quantification accuracy compared to the reference standard Dual Energy X-ray Absorptiometry (DEXA) in the lower spine. Compared to volumetric acquisition of BMD, the projection-based SDEXA technique showed a high correlation in a patient cohort. The first steps towards a fully automated pipeline for SDEXA indicate encouraging results. Using a Convolutional Neural Network (CNN) based approach for vertebrae segmentation the areal Bone Mineral Density (aBMD) in the lower spine can be analyzed in every patient opportunistically. An additional analysis of microstructural parameters was performed in an ex-vivo study on a laboratory Photon Counting CT (PCCT) setup, being a promising approach for high-resolution applications in clinical PCCT.

The advantages of spectral detection in CT demonstrated for myocardial perfusion and osteoporosis applications presented in this thesis have the potential to significantly improve the diagnostic value of CT for a wide range of applications.

# Zusammenfassung

Ein Schlüsselfaktor für das breite Andwendungsspektrum der Computertomografie (CT) in der täglichen diagnostischen Routine ist die Detektortechnologie. Beispielsweise bei kardialen und muskuloskelettalen Bildgebungsanwendungen. Die aktuelle Entwicklung von spektralen CT-Detektorsystemen ermöglicht neue diagnostische Möglichkeiten. Diese Arbeit konzentriert sich auf die Entwicklung und Bewertung neuartiger diagnostischer Anwendungen für spektrale Detektoren in der CT. Im ersten Kapitel werden physikalische Prinzipien der Wechselwirkung von Röntgenstrahlen mit Materie beschrieben. Darauf aufbauend werden die Grundkonzepte der Dual Energy CT (DECT) dargelegt.

Es folgen zwei Kapitel über die spektrale dynamische myokardiale CT Perfusion und über die Übersichtsscan-basierten Dual-Energy-Röntgen-Absorptiometrie (SDEXA). Dabei handelt es sich um ein neuartiges Verfahren zur opportunistischen Messung der Knochendichte bei jedem Patienten auf der Grundlage eines erweiterten Übersichtsscans. Die dynamische Myokardperfusion mittels spektraler CT-Bildgebung wurde in einer Phantomstudie und einer Schweinestudie untersucht. Kontrastmittelsensitivität in schwach durchblutetem Gewebe und Materialquantifizierung sind mit herkömmlichen CT-Detektoren nur schwer realisierbar. Die Hauptvorteile der spektralen Detektion sind das verbesserte Signal-Rausch-Verhältnis bei der Messung der Joddichte im Myokard und der daraus resultierende genauere Fit der Zeitschwächungskurven. In der Phantomstudie wurde eine verbesserte Feststellung des schwach perfundierten Myokards nachgewiesen, unabhängig vom zugrundeliegenden Perfusions-Fit-Modell. Auch die Möglichkeit einer Dosisreduktion wurde in beiden Studien nachgewiesen. Basierend auf den vorgestellten Ergebnissen scheint die klinische Umsetzung der spektralen dynamischen Myokardperfusion mittels CT machbar und vielversprechend zu sein.

Die 2019 eingeführte SDEXA-Technik wurde im zweiten Ergebniskapitel hinsichtlich der wichtigsten Aspekte für den Einsatz in der klinischen Routine bewertet. Messungen am European Spine Phantom (ESP) zeigten eine verbesserte Quantifizierungsgenauigkeit an der unteren Wirbelsäule, im Vergleich zum Referenzstandard der Dual Energy X-ray Absorptiometry (DEXA). Zur volumetrischen Messung der Knochendichte zeigte die projektionsbasierte SDEXA-Technik eine hohe Korrelation in einer Patientenkohorte. Erste Schritte in Richtung einer vollautomatischen Auswertung für SDEXA zeigen vielversprechende Ergebnisse. Unter Verwendung eines Convolutional Neural Network (CNN) basierenden Ansatzes für die Wirbelsegmentierung kann die Flächenknochendichte in der unteren Wirbelsäule in jedem Patienten analysiert werden. Eine zusätzliche Analyse der mikrostrukturellen Parameter wurde in einer ex-vivo Studie mit einem experimentellen Photon Counting CT (PCCT) durchgeführt. Die Mikrostrukturanalyse ist ein vielversprechender Ansatz für hochauflösende Anwendungen in der klinischen PCCT.

Die Vorteile spektraler Detektoren in der CT, die in dieser Arbeit für die Anwendungen der Myokardperfusion und Osteoporose aufgezeigt wurden, haben das Potenzial, den diagnostischen Wert der CT für ein breites Spektrum von Anwendungen erheblich zu verbessern.

# Scientific publications

## 1 Publications as first author

**Hammel, Johannes**; Birnbacher, Lorenz; Campbell, Graeme; Coulon, Philippe; Ushakov, Lev; Pfeiffer, Franz; Makowski, Marcus R.; Kirschke, Jan; Pfeiffer, Daniela: Comparison of volumetric and areal bone mineral density in CT and scout scans using spectral detector technology. European Radiology Experimental 7 (1), **2023**

**Hammel, Johannes**; Birnbacher, Lorenz; Makowski, Marcus R.; Pfeiffer, Franz; Pfeiffer, Daniela: Absolute iodine concentration for dynamic perfusion imaging of the myocardium: improved detection of poststenotic ischaemic in a 3D-printed dynamic heart phantom. European Radiology Experimental 6 (1), **2022**

Scherer, Kai and **Hammel, Johannes**; Sellerer, Thorsten; Mechlem, Korbinian; Renger, Bernhard; Bähr, Andrea; Kupatt, Christian; Hinkel, Rabea; Herzen, Julia; Pfeiffer, Franz; Rummeny, Ernst; Pfeiffer, Daniela: Dynamic quantitative iodine myocardial perfusion imaging with dual-layer CT using a porcine model. Scientific Reports 9 (1), **2019**

## 2 Publications as co-author

Gassenhuber, Melina; Lochschmidt, Maximilian E.; **Hammel, Johannes**; Boeckh-Behrens Tobias; Ikenberg Benno; Wunderlich Silke; Liesche-Starnecker Friederike; Schlegel Jürgen; Pfeiffer Franz; Makowski Marcus R.; Zimmer Claus; Riederer Isabelle; Pfeiffer Daniela: Multimaterial decomposition in dual-energy CT for characterization of clots from acute ischemic stroke patients. European Radiology Experimental, **2024**

Lochschmidt, Maximilian E.; Gassenhuber, Melina; Riederer, Isabelle; **Hammel, Johannes**; Birnbacher, Lorenz; Busse, Madleen; Boeckh-Behrens, Tobias; Ikenberg, Benno; Wunderlich, Silke; Liesche-Starnecker, Friederike; Schlegel, Jürgen; Makowski, Marcus R.; Zimmer, Claus; Pfeiffer, Franz; Pfeiffer, Daniela: Five material tissue decomposition by dual energy computed tomography. Scientific Reports 12 (1), **2022**

Gassert, Florian T.; **Hammel, Johannes**; Hofmann, Felix C.; Neumann, Jan; von Schacky, Claudio E.; Gassert, Felix G.; Pfeiffer, Daniela; Pfeiffer, Franz; Makowski, Marcus R.; Woertler, Klaus; Gersing, Alexandra S.; Schwaiger, Benedikt J.: Detection of Bone Marrow Edema in Patients with Osteoid Osteoma Using Three-Material Decomposition with Dual-Layer Spectral CT. Diagnostics 11 (6), **2021**, 953

Roski, Ferdinand; **Hammel, Johannes**; Mei, Kai; Haller, Bernhard; Baum, Thomas; Kirschke, Jan S.; Pfeiffer, Daniela; Woertler, Klaus; Pfeiffer, Franz; Noël, Peter B.; Gersing, Alexandra S.; Schwaiger, Benedikt J.: Opportunistic osteoporosis screening: contrast-enhanced dual-layer spectral CT provides accurate measurements of vertebral bone mineral density. European Radiology 31 (5), **2020**

Roski, Ferdinand; **Hammel, Johannes**; Mei, Kai; Baum, Thomas; Kirschke, Jan S.; Laugerette, Alexis; Kopp, Felix K.; Bodden, Jannis; Pfeiffer, Daniela; Pfeiffer, Franz; Rummeny, Ernst J.; Noël, Peter B.; Gersing, Alexandra S.; Schwaiger, Benedikt J.: Bone mineral density measurements derived from dual-layer spectral CT enable opportunistic screening for osteoporosis. European Radiology 29 (11), **2019**

## 3 Peer-reviewed presentations

Opportunistic bone mineral density screening in overview scans using spectral detector technology, European Congress of Radiology, March 2023, Vienna, Austria

Bone Density and Quality Assessment using Spectral Detector Technology in Computed Tomography, IMXP Intl Symposium, August 2022, IAS Garching, Germany

Dynamic myocardial perfusion imaging using quantitative iodine density maps in a 3D printed heart phantom, European Congress of Radiology, July 2022, Vienna, Austria

# Contents

# Introduction

# 1

X-rays are part of the electromagnetic spectrum and are used in various applications. After their discovery by Wilhelm Conrad Röntgen in 1895, the translation to medical applications followed almost immediately. X-ray photons can penetrate the human body and generate contrast in the detected intensity between different materials, mainly bone and soft tissue. This revolutionary property, arising from the different attenuation mechanisms that mainly depend on the material's atomic number and electron density, is the basis for using X-rays in medical imaging.

The first medical X-ray images were generated using photographic plates with an exposure time of approximately 20 minutes [Spi95]. Later, live imaging could be performed using a fluorescent screen, requiring significantly less exposure time. The detection process could be optimized by using an intensifying screen fabricated out of amorphous gadolinium oxysulfide $Gd_2O_2S$ to convert the X-ray photons to visible light [Jen80]. The film base coated in silver halide emulsion is sensitive to visible light by a photochemical reaction of the silver halide crystals. Through this indirect conversion process with drastically increased sensitivity, the exposure time could be reduced to approximately one second and X-rays could be used for various medical applications without delivering a high radiation dose.

1972 Godfrey Hounsfield introduced the first commercially available Computed Tomography (CT) scanner. For the reconstruction of CT images, digital detection of X-rays is crucial. The first generation of CT systems used solid scintillators like sodium iodine or Xenon ionization chambers coupled to photomultiplier tubes [SSP21]. This design could provide high noise-free gain. These design choices were only applicable in translate-rotate scanners [Hou73]. A multichannel ionization chamber provided the first design, where multiple attenuation paths could be measured simultaneously. Scintillators coupled to photodiodes were pioneered by Siemens for third-generation scanners. Cesium iodide was the first choice for detector systems without photomultiplier tubes. High-speed scintillator-photodiode detectors were developed, enabling the modern fast acquisition CT systems. The readout electronics in these systems allow a parallel evaluation of all pixels and fast, continuous scan modes.

The indirect conversion from X-rays to visible light in the scintillator also results in the loss of spectral information of the X-ray photons. Nevertheless, indirect conversion processes were and are still the most common detection method in medical CT imaging. Already in 1976, only 4 years after the first CT scanner was introduced, Alvarez and Macovski [AM76] proposed the use of dual-energy CT imaging. With the assumption of two dominant attenuation mechanisms, the photoelectric effect and Compton scattering, the energy-dependent attenuation of X-rays can be determined when measured at two different X-ray energies. Since the physical model of the energy-dependent absorption is relatively simple, it is sufficient to separate the photons into two distinct energy groups. Although the theoretical basis and first studies were already published in the 1970s, the translation to clinical applications was not pursued until the last decade. The main reasons

for this were the lack of suitable detector technology and potential clinical applications. 30 years after Alvarez and Macovski's research, the first clinically available dual-energy CT scanner was introduced [Flo+06; Gra+09] in 2006, having a dual-source dual-detector design. It was mainly used in abdominal imaging of renal masses, liver lesions, urinary calculi, and other applications [Gra+09].
The main advantage of spectral CT imaging is the possibility to calculate material density maps by performing a material decomposition on energy-dependent measurement data. To use a physically correct model of the energy-dependent Beer-Lambert law, where spectral effects can be incorporated into the reconstruction process, detector-based spectral X-ray imaging is inevitable. First introduced for computed radiography in 1990 [SH90; Erg+90], a suitable CT detector design followed in 2011, invented by Altman et al. [Alt+11]. The Dual Layer CT (DLCT) setup showed improved Signal-to-Noise Ratio (SNR) and Contrast-to-Noise Ratio (CNR) compared to conventional CT images [Doe+17; Ehn+18]. In DLCT systems, energy-dependent information is acquired within every scan.

This thesis will focus on the evaluation of dual-energy and spectral CT applications in cardiac perfusion and osteoporosis imaging on a prototype DLCT system installed at the Klinikum rechts der Isar, Technische Universität München in 2016.
In the first part, a Three-dimensional (3D) printed cardiac phantom and porcine model were used to investigate spectral dynamic myocardial perfusion protocols. Perfusion measurements can be an important tool for diagnosing and quantifying the functional significance of stenosis in cardiac blood vessels. Anatomical visualization of stenosis using Coronary Computed Tomography Angiography (CCTA) can lead to many patients with a false positive diagnosis of functionally significant stenosis. The current state of research shows a lack of functional diagnosis of myocardial ischemia using spectral CT protocols. The additional benefit of spectral imaging could arise from an increased contrast sensitivity compared to conventional CT. To approach this issue, a dynamic heart phantom was designed and 3D printed in the course of this thesis. Investigations could then be performed on this phantom model without dose or animal health considerations. The flow of water and Contrast Agent (CA) through the phantom could be precisely adjusted, and the occlusion of a blood vessel simulated. The harvested spectral data was processed using different hemodynamic perfusion models. Also, a porcine model was used to investigate the benefits of spectral dynamic perfusion for the assessment of functional parameters. A dose reduction technique was tested using a subset of the time-dependent perfusion data.

The second part introduces a novel method for quantifying areal Bone Mineral Density (aBMD) in the lower spine, which can be used to opportunistically diagnose osteoporosis. Also, an approach to vertebral microstructure analysis in a Photon Counting CT (PCCT) was investigated. There exists a treatment gap in the diagnosis of osteoporosis, meaning that many especially elderly women suffer from the consequences of osteoporosis, like vertebral fractures, without being diagnosed. Despite the possibility of effective treatment, patients do not receive appropriate treatment. To reduce the amount of undiagnosed patients, opportunistic screening possibilities should be introduced into the clinical workflow. Spectral CT overview scans can be used to diagnose osteoporosis analog to the reference standard Dual Energy X-ray Absorptiometry (DEXA).

The so-called Scout-based Dual-Energy X-ray Absorptiometry (SDEXA) approach was applied in this thesis. A fully automated approach for osteoporosis diagnosis on spectral overview data was implemented and compared to DEXA and volumetric Bone Mineral Density (BMD) measurements. The problem of vertebra segmentation was approached using a Convolutional Neural Network (CNN). A minimal amount of human interaction is necessary to generate a DEXA-like aBMD report in every patient by extending the overview scan on the DLCT to the lumbar spine region. This yields an automated opportunistic osteoporosis screening tool with only a minor increase in the dose delivered to the patient.

# Theoretical Background

# 2

In this chapter, the theoretical foundation for CT imaging in medical applications is presented. A special focus is put on the energy-resolving capabilities of DLCT and PCCT. The theory from the generation of X-rays, interaction with matter, image reconstruction, photon statistics, energy-resolving detection, and image artifacts is presented. The last two sections will give an example of energy-resolving CT imaging using a digital phantom and some insights into the noise properties of spectral CT.

## 2.1 Generation of X-rays

This section focuses on the generation of X-rays for use in medical CT imaging. X-rays are electromagnetic radiation with an energy range of about 100 eV to 1 MeV Figure 2.1. An X-ray tube can be used to generate X-rays. It contains an electron emitter (cathode) and a positively charged anode. The cathode consists of a heated filament, which thermally emits electrons. To emit electrons, the filament, made of thoriated tungsten with a melting point of 3,410 °C, is heated to a temperature of 2,100 °C to overcome the binding energy of the electrons to the metal of the filament [Buz08]. The primary electrons generated from the cathode are controlled by a cylindrical electrode, the Wehnelt cylinder [Buz08].

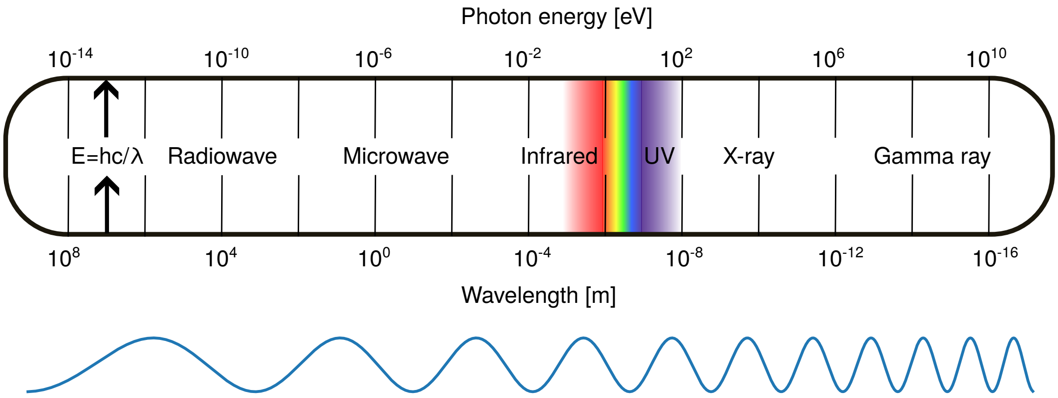

**Figure 2.1:** The electromagnetic spectrum. The energy range of electromagnetic radiation is schematically shown on a logarithmic scale in the range between 10 feV and 10 GeV. The nomenclature of electromagnetic radiation from low to high energies includes radio waves, microwaves, infrared, visible light, ultraviolet, X-rays, and gamma rays. The energy of X-rays ranges between approximately 100 eV and 1 MeV. The energy range of X-rays is further divided into soft X-rays and hard X-rays. The energy range of X-rays used in medical CT imaging is between 10 keV and 150 keV. Soft tissue and bone absorption properties in this energy range differ maximally, and therefore, optimal contrast properties are observed.

The Wehnelt cylinder is negatively charged, accelerating and focusing the electrons onto the anode. The electrons are accelerated by a high voltage, defining the peak energy of the X-ray spectrum. Double quadrupole magnets focus and deflect the electron beam onto a small focal spot on the rotating anode. An electron trap eliminates off-focal radiation, which can arise from backscatter electrons [Beh16; Sch+04]. The backscattering probability increases with the atomic number of the anode and the anode angle to the electron beam. A small focal spot is a crucial element in CT imaging, as it is a limiting factor for the system's spatial resolution. The focal spot size depends on the diagnostic application and is typically between 0.1 mm and 1.2 mm [Hud10]. X-rays are generated via the bremsstrahlung process by decelerating and deflecting the electrons in the anode material. The spectrum generated by the bremsstrahlung process is continuous and is superimposed by a characteristic line spectrum. Responsible for the characteristic line photon emittance are electrons interacting with an inner shell electron of the target material. The inner shell electron is ejected, and an electron from an outer shell fills the vacancy. This energy difference between the two shells is emitted as a photon. Thereby, the characteristic X-ray intensity is far less in sum than the bremsstrahlung intensity [Buz08]. Also, the X-ray spectrum has reduced intensities at lower photon energies, as X-rays below 30 keV are absorbed in large parts within the anode material, the beryllium exit window of the X-ray tube, and air. This effect is desirable, as low energetic photons would be fully absorbed in the patient, not contributing to the image formation by giving contrast. The X-ray spectrum can be filtered for thicker patients using a tin filter. The effect of filtration can be seen in Figure 2.11. Collimator plates after the exit window of the X-ray tube are used to collimate the X-ray beam onto the active detector array to avoid unnecessary radiation exposure to the patient.

For the penetration of patients with a diameter of up to 50 cm, X-ray energies of up to 150 keV are required [Buz08]. Further, a high flux of X-ray photons is crucial to acquire several thousand projections in a short rotation time of down to 250 ms [Raj+21]. Due to the low conversion efficiency from kinetic electron energy to bremsstrahlung X-ray energy of approximately 1% [Buz08], a high power dissipation in the form of heat has to be carried away from the X-ray anode. The dimension and weight of the X-ray tube are limited by the CT gantry design, preferring a small and lightweight X-ray tube. Rotating anodes can fulfill these requirements. These X-ray generating tubes are used in all modern CT scanners, consisting of a rotating anode, a cathode, and a vacuum tube.

A schematic of a rotating anode X-ray tube is shown in Figure 2.2.

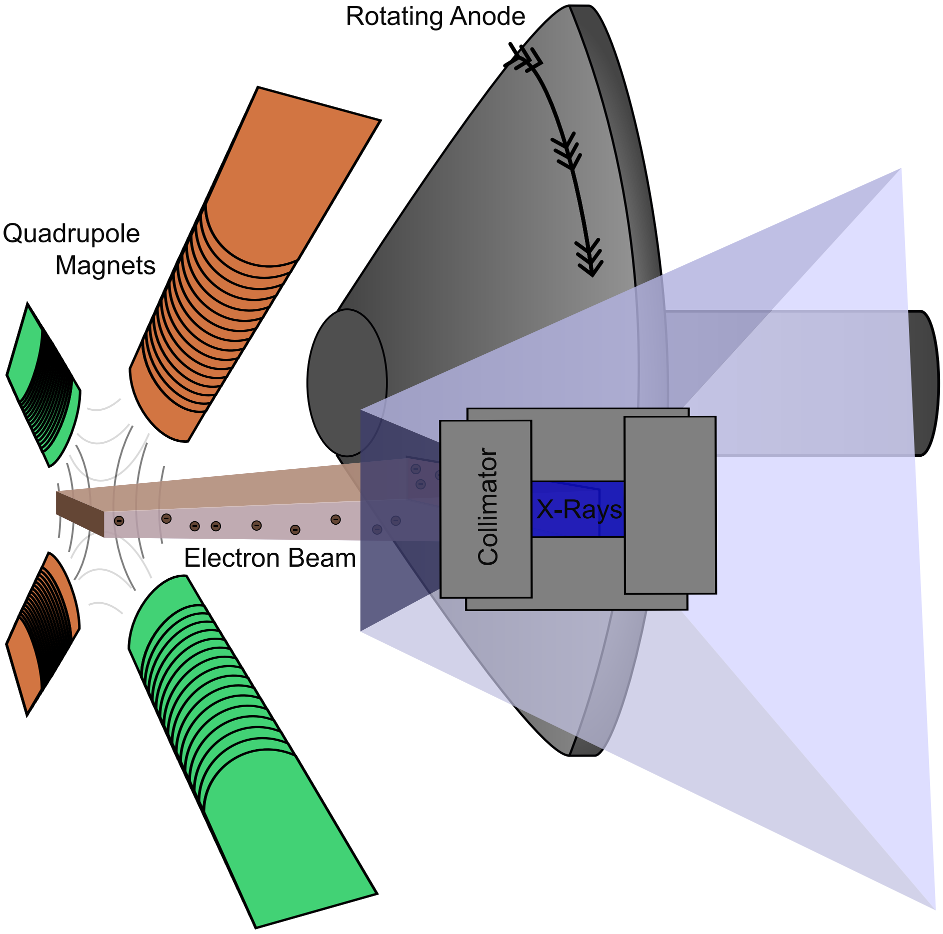

**Figure 2.2:** Schematic of a rotating anode X-ray tube. The accelerated electron beam is focused onto a drawn-out focus spot on the anode material using a quadrupole magnet setup. When exiting via the beryllium window and through the collimator plates, the effective focal spot size can be described by projecting the focal spot onto the plane of the collimator plates. The anode is rotated to evenly distribute the heat over the anode head. The cooled rotating anode design allows a high power dissipation within a small volume. With this design, the heat can be distributed over a larger area on the anode.

## 2.2 Interaction of X-rays with matter

The basis for describing the attenuating properties of matter on X-rays is the Beer-Lambert law. It states that the intensity of X-rays passing through matter is exponentially decreasing with the thickness of the material. Further, the material-specific attenuation coefficient is the proportionality factor in the exponential function. This results in the following equation for the intensity of X-rays $I(d)$ after passing through a material with thickness $d$:

$$I(d) = I_0 \cdot e^{-\mu d}, \tag{2.1}$$

where $I_0$ is the intensity of the X-ray beam before passing through the material, and $\mu$ is the attenuation coefficient of the material. The material-specific attenuation is also dependent on the energy of the X-ray beam. For inhomogeneous materials, the attenuation coefficient is a function depending on the location within the material. The number of X-ray counts can be written as:

$$I_c(d) = \int_0^{E_{\mathrm{max}}} I_0(E) \cdot e^{-\int_0^d \mu(E,s)\,\mathrm{d}s}\,\mathrm{d}E, \tag{2.2}$$

where $I_0(E)$ is the intensity of the X-ray beam before passing through the material at energy $E$, $\mu(E, s)$ is the energy-dependent attenuation coefficient at energy $E$ and location $s$ within the material, and $E_{\mathrm{max}}$ is the maximum energy of the X-ray beam. To gain a density-independent specific measure of attenuation for a material, the mass attenuation coefficient $\mu_{\mathrm{m}} = \mu/\rho$ is defined.

As conventional CT detectors are only able to measure the mean energy deposition (Section 2.5), Equation 2.1 is used to describe the attenuation of X-rays at the mean energy of the X-ray spectrum and $I_0$ is the energy deposition of the X-ray beam without a sample.

$$I_{\mathrm{e}}(0) = \int_0^{E_{\mathrm{max}}} I_0(E) \cdot E \cdot dE \tag{2.3}$$

The energy deposition with the sample follows Equation 2.2:

$$I_{\mathrm{e}}(\mathrm{d}) = \int_0^{E_{\mathrm{max}}} I_0(E) \cdot E \cdot e^{-\int_0^d \mu(E,s)\,\mathrm{d}s}\,\mathrm{d}E \tag{2.4}$$

The simplification of disregarding the energy dependency of the attenuation coefficient and spectrum is leading to beam hardening artifacts, discussed in Subsection 2.7.1.

The interaction effects of matter depend on several physical phenomena. The occurring phenomena in the energy range of medical CT imaging are the photoelectric effect, Compton scattering, and Rayleigh scattering. The photoelectric effect is the dominant attenuation mechanism at low energies, as its interaction probability is indirectly proportional to the third power of the photon energy. Inelastic scattering, also called Compton scattering is the dominant attenuation mechanism at higher energies. Its energy-dependent interaction probability is described by the Klein-Nishina formula [KN29]. Rayleigh scattering is the elastic scattering of photons at low energies. The interaction probability is negligible compared to the photoelectric effect and Compton scattering in the energy range of medical CT imaging. A logarithmic plot of the energy-dependent mass attenuation coefficient of iodine is shown on Figure 2.3, illustrating the dominant interaction mechanisms.

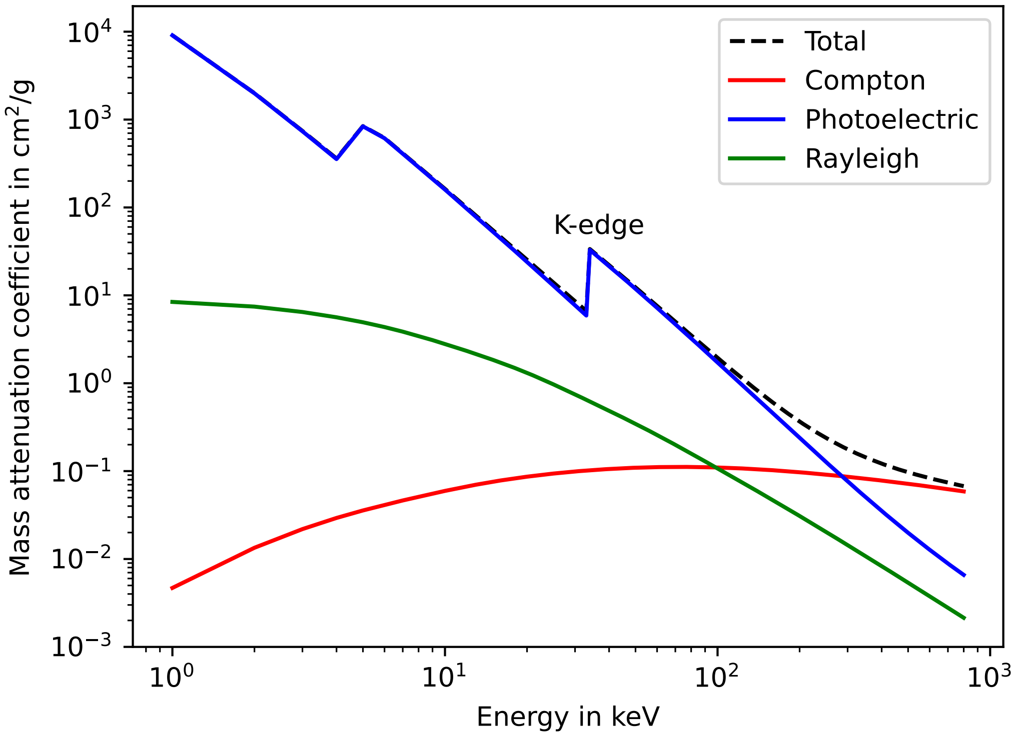

**Figure 2.3:** The mass attenuation coefficient of iodine. The mass attenuation coefficient of iodine illustrates the energy dependence of the attenuation coefficient. It is based on the respective cross-sections of Rayleigh (elastic) scattering, Compton (inelastic) scattering, and the photoelectric effect shown here for iodine (Z = 53). The K-edge is located prominently at approximately 33 keV.

The mass attenuation coefficient is the sum of the cross-sections of the occurring physical phenomena multiplied by the mass density $\rho$, the atomic number $A$, and Avogadro constant $N_\mathrm{A}$:

$$\mu = \rho \frac{N_A}{A} \sigma_\mathrm{total}. \tag{2.5}$$

The total cross-section $\sigma_\mathrm{total}$ is the sum of the photoelectric cross-section $\sigma_\mathrm{ph}$, the Compton cross-section $\sigma_\mathrm{com}$, and the Rayleigh cross-section $\sigma_\mathrm{R}$.

### 2.2.1 Photoelectric effect

In the X-ray energy range, interaction appears predominantly with electrons of the material, and interactions with nuclei can be neglected. The photoelectric effect describes a photon's interaction with an atom's electron cloud. A bound electron can be ejected into an unbound (continuum) state when the photon energy exceeds the electron's binding energy. This process is a superposition of a continuous part, and the edge jumps when the impinging photon energy is large enough to eject electrons from the next atomic shell. The vacancy is then filled with an electron from an outer shell, emitting a photon with the energy corresponding to the energy difference of the shells. The process when the emitted photon leaves the atom can be described as fluorescence radiation. Also, the emitted photon can expel another electron from one of the outer shells. This effect is known as Auger electron emission. An analytic approach to model the energy and atomic number dependence of the photoelectric absorption cross-section $\sigma_\mathrm{a}^\mathrm{ph}(E, Z)$ separably is not possible. In [Whi77], a semi-analytic approximation regarding empirical data is made. In the absence of absorption edges, the continuous part of the cross-section for the photoelectric effect can be approximated by

$$\sigma_\mathrm{ph} = C_\mathrm{ph} \frac{Z^{4-5}}{E^{2.5-3.5}}. \tag{2.6}$$

The exact values of the exponents depend on the specific element or mixture to be parameterized. $C_\mathrm{ph}$ describes an empirical constant. Since biological tissue contains mainly light elements with $Z < 20$, the absorption edges are located below the energy range of a filtered CT X-ray source spectrum, and approximation 2.6 is reasonably accurate. For heavier atoms, the separation of energy and $Z$ dependent cross-section is not possible. In such cases, tabulated values for the mass absorption coefficients are normally used in spectral X-ray imaging.

### 2.2.2 Compton scattering

The Compton effect refers to inelastic scattering. In this process, an X-ray photon collides with a quasi-free electron in the outer atomic shell, thereby creating a recoil electron. Energy and momentum conservation lead to scattered photon energy decreased by the transferred amount of energy, often expressed as an increase in wavelength,

$$\Delta\lambda = \lambda' - \lambda = \frac{h}{m_\mathrm{e}}(1 - \cos\Theta). \tag{2.7}$$

Here $\Theta$ denotes the scattering angle between the wave vector $k$ of the incoming photon and of the scattered photon $k'$. The Klein-Nishina formula gives the differential cross-section of photons scattered from a single free electron in the lowest order of quantum electrodynamics. For an incident photon of energy $E$ and scattered photon of energy $E'$, the differential cross-section is:

$$\frac{d\sigma}{d\Theta} = \frac{e^2}{8\pi m_\mathrm{e}^2} \left(\frac{E'}{E}\right)^2 \left[\frac{E'}{E} + \frac{E}{E'} - \sin^2 \Theta\right] \tag{2.8}$$

Integration over the solid angle and multiplication with $Z$, to account for all electrons of an atom with the atomic number $Z$ [KN29], delivers the relation:

$$\sigma_\mathrm{com} = Z \cdot f_\mathrm{KN}(E), \tag{2.9}$$

where $f_\mathrm{KN}$ is the energy-dependent Klein-Nishina cross-section. However, due to simplifications done by Klein and Nishina, the given relation is physically not correct, and $f_\mathrm{KN}$ also depends on the atomic number $Z$ [HJ80]. This simplification, however, leads to negligibly small deviations for low $Z$ materials in the energy range, where the Compton effect plays an important role in the overall attenuation.

The Compton scattering of X-rays is the reason why anti-scatter grids have to be placed in front of the detector. Scattered X-ray photons can lead to a strong deterioration of the image quality by introducing a blur over the whole image in projection space. The anti-scatter grid is a grid of lead strips placed directly on the detector, which only allows X-rays to pass through in a narrow-angle range coming from the source spot. The scattered X-rays are blocked by the grid and contribute to contrast formation, as they are scattered into a wide angle range.

### 2.2.3 Rayleigh scattering

Rayleigh scattering is a quasi-elastic interaction process between X-ray photons and an atom's electron cloud. The photon is scattered on the bound atomic electrons and deflected from its original path. The energy of the photon is not changed in this process. In classical electrodynamics, all electrons of the atom are considered to be in a forced oscillation with the frequency of the incoming photon during the scattering process. The differential scattering cross-section per atom for small scattering angles can be described by:

$$\frac{d\sigma}{d\Omega} = \frac{r_\mathrm{e}^2}{2} \left(1 + \cos^2 \Theta\right) Z^2, \tag{2.10}$$

where $r_\mathrm{e}$ is the classical electron radius, $\Theta$ is the scattering angle, and $Z$ is the atomic number of the atom. For large angles, scattering contributions interfere destructively. Consequently, the probability of Rayleigh scattering in the forward direction is strongly enhanced compared to other scattering angles. Therefore, Rayleigh scattering can result in undesired scatter radiation reaching the detector.

### 2.2.4 Material decomposition

Based on the physical phenomena of X-ray interaction with matter, the mass attenuation coefficient can be expressed as a sum of spectral basis functions. Figure 2.3 illustrates the energy dependency of the mass attenuation coefficient of iodine (data from National Institute of Standards and Technology (NIST) [HS04]). Generally, the low energetic regime is dominated by the photoelectric effect. Towards higher energies, scattering effects become more important. Elastic scattering is about one order of magnitude lower than the dominant effect. This observation often leads to the assumption that elastic scattering can be neglected in X-ray imaging applications. The energy-dependent mass attenuation coefficient of an arbitrary material without K-edges in the energy range of interest can be parameterized by

$$\mu(E, Z) = a_{\mathrm{ph}} f_{\mathrm{ph}}(E) + a_{\mathrm{c}} f_{\mathrm{KN}}(E), \tag{2.11}$$

with energy dependencies $f_{\mathrm{ph}}(E) = 1/E^{3.2}$ of the photoelectric effect according to [Leh+81] and $f_{\mathrm{KN}}(E) = \sigma_{\mathrm{KN}}$ the energy dependency of the Klein-Nishina cross-section for the Compton effect. The coefficients of the basis functions can be written as

$$\begin{aligned} a_{\mathrm{c}} &= \rho_{\mathrm{el}} \\ a_{\mathrm{ph}} &= C_{\mathrm{ph}} \rho_{\mathrm{el}} (Z_{\mathrm{eff}})^{3.8} \end{aligned} \tag{2.12}$$

with the effective electron density $\rho_{\mathrm{el}}$ of the material or mixture and its effective atomic number $Z_{\mathrm{eff}}$. The exponent value of $Z_{\mathrm{eff}}$ was chosen due to considerations from White et al. [Whi77]. As $f_{\mathrm{ph}}(E)$ and $f_{\mathrm{KN}}(E)$ originate from two different physical effects, they can be seen as two linearly independent vectors [AM76], spanning a 2-D vector space.

Adapting the Beer-Lambert law from equation Equation 2.2 with energy-dependent absorption coefficients $\mu(\vec{r}, E)$, the photon counts can be calculated via

$$I = \int_0^\infty I_0(E) \cdot DF(E) \cdot e^{-p(E)} dE. \tag{2.13}$$

$I_0(E)$ is the source spectrum, $DF(E)$ the detector function and $p(E)$ the projection or line-integral of a monochromatic X-ray beam:

$$p(E) = \int_0^S \mu(E, s) ds = A_{\mathrm{ph}} f_{\mathrm{ph}}(E) + A_{\mathrm{c}} f_{\mathrm{KN}}(E) \tag{2.14}$$

with

$$A_{\mathrm{ph}} = \int_0^S a_{\mathrm{ph}}(\vec{r}) ds, \quad A_{\mathrm{c}} = \int_0^S a_{\mathrm{c}}(\vec{r}) ds \tag{2.15}$$

where $A_{\mathrm{ph}}$ and $A_{\mathrm{c}}$ denote the respective contribution of photoelectric absorption and Compton scattering to the line-integral.

A DLCT detector capable of energy separation into two sufficiently independent parts can be described by the detector function:

$$DF_i(E) = D_i(E) \cdot E, \tag{2.16}$$

where $D_i$ is the absorption efficiency of sensor layers one $i = 1$ and two $i = 2$. In an ideal PCCT system, the detector function of the energy bins is a step function being one, within the energy interval of the bin and zero otherwise. A theoretical comparison between DLCT absorption efficiency and PCCT detector function is shown in Figure 2.12

and Figure 2.12. By combining Equation 2.13 and Equation 2.16, the resulting equation system can be solved numerically in order to obtain the line-integrals $A_{\mathrm{ph}}$ and $A_{\mathrm{c}}$. This data is free of beam hardening effects, as energy dependencies are included.
By performing a Filtered Back Projection (FBP) on the CT data set of line-integrals $A_{\mathrm{ph}}$ and $A_{\mathrm{c}}$, Equation 2.15 can be reversed and 3D data for the spatial distribution of photoelectric effect $a_{\mathrm{ph}}(\vec{r})$ and Compton effect $a_{\mathrm{c}}(\vec{r})$ coefficients can be reconstructed. The basis material decomposition in projection space into water and bone is equivalent to the spectral basis component decomposition. It is a simple matrix multiplication.

$$\begin{pmatrix} A_{\mathrm{water}} \\ A_{\mathrm{bone}} \end{pmatrix} = \begin{pmatrix} (\frac{\mu}{\rho})_{\mathrm{water}}(50) & (\frac{\mu}{\rho})_{\mathrm{bone}}(50) \\ (\frac{\mu}{\rho})_{\mathrm{water}}(100) & (\frac{\mu}{\rho})_{\mathrm{bone}}(100) \end{pmatrix}^{-1} \cdot \begin{pmatrix} f_{\mathrm{ph}}(50) & f_{\mathrm{KN}}(50) \\ f_{\mathrm{ph}}(100) & f_{\mathrm{KN}}(100) \end{pmatrix} \cdot \begin{pmatrix} A_{\mathrm{ph}} \\ A_{\mathrm{c}} \end{pmatrix} \tag{2.17}$$

where $(\frac{\mu}{\rho})$ defines the mass attenuation coefficient and $A_{\mathrm{water}}$, $A_{\mathrm{bone}}$ the line integral over the water and bone mass densities. The line integral can be modeled as:

$$p(E) = \int_0^S \mu(E,s)ds = A_{\mathrm{water}}(\frac{\mu}{\rho})_{\mathrm{water}}(E) + A_{\mathrm{bone}}(\frac{\mu}{\rho})_{\mathrm{bone}}(E) \tag{2.18}$$

By using an unbiased estimator, the polychromatic forward model with corresponding detector function, the X-ray spectrum and detector counts (Equation 2.13), the spectral line integrals $A_{\mathrm{water}}$ and $A_{\mathrm{bone}}$ can be estimated. FBP or more sophisticated reconstruction techniques can recover the mass densities $\rho_{\mathrm{water}}$ and $\rho_{\mathrm{bone}}$ from spectral line integrals.

Image-based decomposition can be performed without the exact knowledge of the X-ray spectrum and detector function, as it happens after the reconstruction step without using the energy-dependent Beer-Lambert law. The two sinograms from energy-dependent measurements are reconstructed using Equation 2.1 with two measured flatfield images $I_0(E_1)$ and $I_0(E_2)$ and two measured projection images $I(d)_{\mathrm{E}_1}$ and $I(d)_{\mathrm{E}_2}$. The resulting reconstructions suffer from spectral artifacts, as no energy dependence was considered. A calibration phantom with a known attenuation coefficient is used to calculate the mean energies $E_1$ and $E_2$ of the two X-ray spectra. The mean energies can be plugged into the energy-dependent function of Equation 2.11. The left side of the equation reflects the measured voxel data. By solving a linear equation system having two measurements and two unknowns in every voxel, the spectral basis functions $a_{\mathrm{ph}}$ and $a_{\mathrm{c}}$ can be calculated. The resulting basis functions can be used to calculate material density maps or monoenergetic images. Nevertheless, the resulting basis functions will be biased due to the spectral artifacts in the reconstruction.

## 2.3 Image reconstruction

The goal of medical CT imaging is to reconstruct a 3D distribution of attenuation coefficients of the patient. The contrast in the attenuation coefficient can then be used to differentiate between different tissues with varying densities. The measured data represents the line integral or projection of the attenuation coefficient along the X-ray beam.

$$p_\theta(r) = \int_{-\infty}^{\infty}\int_{-\infty}^{\infty} \mu(x,y)\delta(x\cos(\theta) + y\sin(\theta) - r)\mathrm{d}x\mathrm{d}y \tag{2.19}$$

where $p_\theta(r)$ is the measured intensity at angle $\theta$ and position $s$ of the detector array, $\mu(x, y)$ is the attenuation. The function $p_\theta(r)$ is also called the sinogram, giving the projection of the attenuation coefficient under all angles $\theta$. A flat field measurement is necessary to calculate the projection or line integral from the intensity measured at the detector. The flat field measurement is the X-ray intensity at the detector without placing a sample in the beam. It measures $I_0$ in Equation 2.1 for every detector pixel. By dividing the measured intensity by the flat field measurement, the projection $p_\theta(r)$ can be calculated. In this simplified example, the detector array is assumed to be a 1D line of pixels, and the distribution of attenuation coefficients is assumed to be 2D. The beam geometry is assumed to be a parallel beam geometry. The mathematical formulation of the measurement process, creating projection images of the attenuation coefficient distribution, is called the Radon transform. To gain the distribution of attenuation coefficients from the measured data $I(\theta, \phi)$, the Radon transform has to be inverted. The most widely used algorithm for this is the FBP, although recently iterative and Artificial Intelligence (AI) driven algorithms have gained popularity. The FBP algorithm is based on the Fourier slice theorem. Colloquially, the Fourier slice theorem states that the Two-dimensional (2D) frequency space of the attenuation coefficient's Fourier transform can be populated by the One-dimensional (1D) Fourier transform of the measured projection data. In more detail, the Fourier slice theorem states that the 1D Fourier transform of the Radon transform of a function $f(x, y)$ under the angle $\theta$ is equal to the 2D Fourier transform of the function $f(x, y)$ evaluated at the line $\phi = x\cos(\theta) + y\sin(\theta)$. The Fourier slice theorem can be expressed as follows:

$$\mathcal{F}_{1D}\left\{\mathcal{R}_\theta\left\{f(x, y)\right\}\right\} = \mathcal{F}_{2D}\left\{f(x, y)\right\}\Big|_{\phi = x\cos(\theta) + y\sin(\theta)} \tag{2.20}$$

where $\mathcal{F}$ is the Fourier transform and $\mathcal{R}$ is the Radon transform. The measurement process retrieves the projection $p_\theta(r)$ in radial sampling under the angle $\theta$. However, it is not trivial to reconstruct the attenuation coefficient distribution from the Fourier-transformed projection data, as the 2D inverse Fourier transform on Cartesian coordinates would not work on radially sampled data. The FBP algorithm solves this problem by filtering the polar sampled measured data with a high pass frequency filter. This so-called ramp or Ram-Lak filter arises from the Jacobian determinant when switching from cartesian to polar coordinates. Mathematically expressed, the FBP is now the inverse process to go from the experimentally determined projections $p(\theta, r)$ to the object function $f(x, y)$ with the use of the Fourier slice theorem. The object function can be expressed as an inverse Fourier transform:

$$\begin{aligned} f(x, y) &= \iint_{-\infty}^{+\infty} F(u, v) e^{2\pi i(ux+vy)} \mathrm{d}u\mathrm{d}v && (2.21)\\ &= \iint_{-\infty}^{+\infty} F(u = r\cos\theta, v = -r\sin\theta) e^{2\pi i(ux+vy)} \mathrm{d}u\mathrm{d}v && (2.22)\\ &= \int_0^{2\pi} \int_{-\infty}^{+\infty} P_\theta(\omega) e^{2\pi i\omega(x\cos\theta - y\sin\theta)} |\omega| \mathrm{d}\omega\mathrm{d}\theta && (2.23) \end{aligned}$$

where $\mathrm{d}u\mathrm{d}v = |r|\mathrm{d}\omega\mathrm{d}\theta$ is the Jacobian determinant and $P_\theta(\omega)$ is the 1D Fourier transform of the projection data under the angle $\theta$. Using the symmetry of the object Fourier transform with respect to the radial frequency $F(r,\theta) = F(-r,\theta+\pi)$, one can simplify Equation 2.21 to

$$f(x,y) = \int_0^{\pi} \int_{-\infty}^{+\infty} P_\theta(\omega)|\omega| e^{2\pi i\omega(x\cos\theta - y\sin\theta)} \mathrm{d}\omega \mathrm{d}\theta. \tag{2.24}$$

Figure 2.4 schematically illustrates the steps of the FBP algorithm. The measured projection data undergoes Fourier transformation along the radial direction, followed by filtering the projection data using the Ram-Lak filter. The filtered Fourier transform is then inverse Fourier transformed, resulting in a filtered sinogram, which is then back-projected onto the reconstruction grid. The back-projection is repeated for all projection angles and summed up, resulting in an image of the attenuation coefficient distribution.

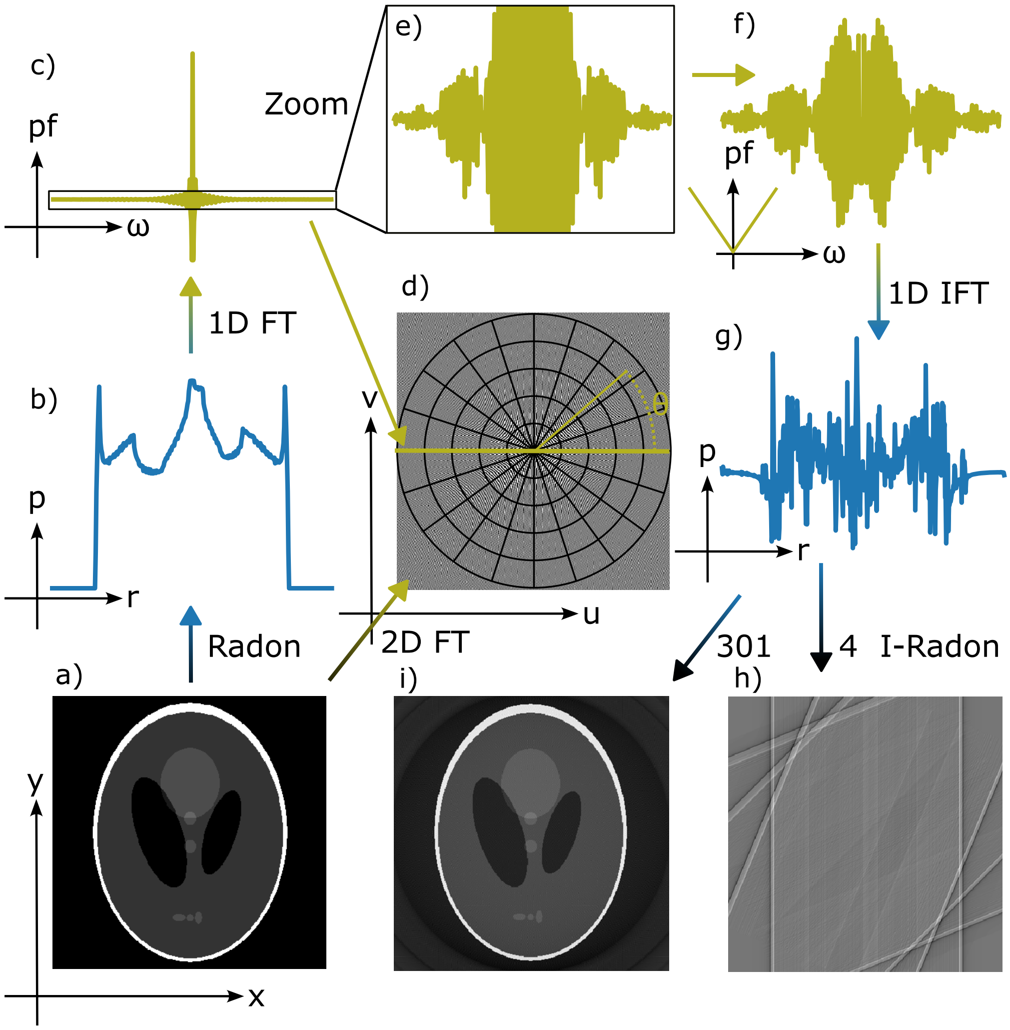

**Figure 2.4:** The working principle of FBP. **a** shows a Shepp-Logan phantom, which is a 2D distribution of attenuation coefficients. In this simplified example, a parallel beam geometry is assumed. By measuring the intensity of the X-ray beam after passing through the sample, plus the information on the flat field intensity in every pixel of the 1D detector, the line integral **b** can be calculated. It is plotted for a projection angle $\theta = 0$ degree. In **c** the 1D Fourier transform $\mathcal{F}_{1D}\left\{p_0(r)\right\} = P_0(\omega)$ is visualized. The Fourier slice theorem states that $P_0(\omega)$ is equal to the 2D Fourier transform of the phantom evaluated at the line $\theta = 0$, which is shown in **d**. The peak at frequency zero in **c** is shown in a zoomed plot in **e** and is filtered out by the Ram-Lak filter, leading to **f**. The 1D inverse Fourier transform of **f** is shown in **g**. This filtered sinogram is back-projected onto the reconstruction grid for 4 and 301 projection angles in **h** and **i**, respectively. The back projection is repeated for all projection angles and summed up.

The Ram-Lak filter is zero for low frequencies and increases linearly to one for high frequencies. When having projection data without noise contribution, the FBP algorithm using the Ram-Lak filter would perfectly reconstruct the attenuation coefficient distribution. However, measured projection data is superimposed by noise generated by detector artifacts and photon shot noise arising from the quantized nature of light. The major part of this noise is high-frequency noise. The Ram-Lak filter amplifies the noise, resulting in a noisy reconstruction. Modulated filters can be applied to the projection data to reduce the noise. The choice of the filter depends on the noise requirements set for the final reconstruction. Generally speaking, smooth filters dampen the noise at high frequencies and lead to a smeared-out reconstruction. Sharp filters, which amplify the high-frequency noise, can preserve the spatial resolution of the reconstruction. The choice of the filter is a trade-off between spatial resolution and image noise. A comparison of different filters is shown in Figure 2.5. The Cosine, Hamming, Hann, or Shepp-Logan filter, as can be seen, in Figure 2.5, have a roll-off towards higher frequencies, enabling a reduction of noise at the cost of spatial resolution. The filter function can be expressed as:

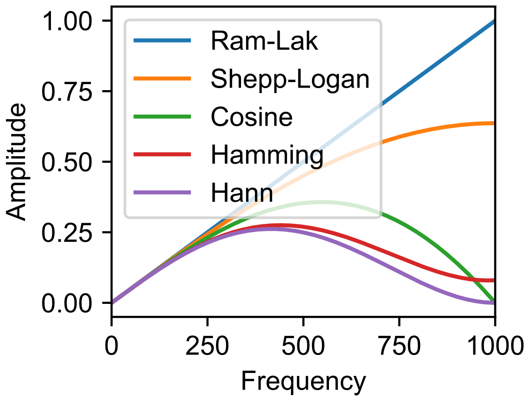

**Figure 2.5:** Various filter for the FBP algorithm.

$$f(r) = |r| \cdot b(r), \tag{2.25}$$

where the factor $b(r)$ differs according to the following filter functions:

$$b(r) = \begin{cases} 1 & \text{Ram-Lak filter,} \\ \operatorname{sinc}(\omega) & \text{Shepp-Logan filter,} \\ \cos \pi\omega & \text{Cosine filter,} \\ \alpha + (1-\alpha)\cos 2\pi\omega & \text{Hann } (\alpha = 0.5) \text{ and Hamming } (\alpha = 0.54) \text{ filter.} \end{cases} \tag{2.26}$$

The SNR of a Region Of Interest (ROI) can be calculated as follows:

$$\mathrm{SNR} = \frac{\mu}{\sigma} \tag{2.27}$$

where $\mu$ is the mean value of the ROI and $\sigma$ is the standard deviation of the ROI. The standard deviation of the ROI is mainly influenced by the noise in the projection data and the filter function. To decrease the noise in the projection data, the number of photons detected per projection time interval has to be increased. This can be achieved by increasing the X-ray tube current or the exposure time, which increases the dose to the patient and may increase the gantry rotation time when the tube's power is limited. In the low dose regime, the detector's readout noise contribution is dominant Section 2.5. At high tube power, the photon shot noise contribution is dominant. The photon shot noise-induced standard deviation is given by the square root of the number of photons detected, meaning that the SNR increases with the square root of the number of photons detected.

To increase spatial resolution in the reconstruction, the detector pixel size has to be decreased. This leads to a decrease in the number of photons detected per pixel and, therefore, a decrease in the SNR. The spatial resolution of the reconstruction is also influenced by the reconstruction filter and the X-ray tube's focal spot size. Further, the Nyquist sampling theorem must be fulfilled to reconstruct the attenuation coefficient distribution without sampling artifacts. The Nyquist sampling theorem states that the sampling frequency has to be at least twice the highest frequency present in the signal. In the case of CT imaging, the highest frequency present in the signal is the spatial frequency of the attenuation coefficient distribution, given by the spatial resolution of the reconstruction, which is again the detector pixel size divided by the system's magnification. The following equation gives the minimum number of projections required to fulfill the Nyquist sampling theorem:

$$N_{\text{proj}} \geq \frac{\pi}{2} \cdot N_{\text{pix}} \tag{2.28}$$

where $N_{\text{proj}}$ is the number of projections and $N_{\text{pix}}$ is the number of detector pixels. The number of projections is also limited by the gantry rotation time in interplay with the required temporal resolution. Modern PCCT systems are reported to achieve an in-plane spatial resolution of 125 $\mu$m [Raj+21]. Conventional reconstruction algorithms are reaching their limits, as the dose to the patient can not be arbitrarily high. Iterative reconstruction algorithms are a promising approach to overcome the limitations of conventional reconstruction algorithms. The iterative reconstruction algorithm is based on the maximum likelihood estimation. Maximum likelihood estimation is a statistical method to estimate the parameters of a model. The model can be adapted to task-specific requirements, including prior knowledge of the object.

## 2.4 Photon statistics

The quantum theory describes photons as the smallest unit of light. In contrast to the classical description of light, quantum theory describes light as a stream of photons. The number of photons in a light beam arriving at a detector is not constant but varies from one measurement to the next. This is called photon statistics or shot noise. The Poisson distribution can describe the photon statistics of a light beam. The Poisson distribution is a discrete probability distribution that expresses the probability of a given number of events occurring in a fixed time interval. Only a positive integer number of events can occur during the time interval. Some examples of Poisson distributed events are the number of events detected by a Geiger counter, the number of raindrops falling in a certain area and time interval, or the number of photons arriving at a detector. The Poisson distribution is defined as follows:

$$P(n) = \frac{\overline{n}^n e^{-\overline{n}}}{n!}, \tag{2.29}$$

where $n$ is the number of events, and $\overline{n}$ is the average number of events in the given time interval. The average number of events is directly proportional to the intensity of the light beam. The fluctuations in the number of photons arriving result from the quantized nature of light. Having a low-intensity light or X-ray beam in low-dose measurements results in low SNR originating from the standard deviation of the Poisson distribution being equal to the square root of the number of events. When discussing photon statistics using a photon counting detector, two physical phenomena must be distinguished. The first is the intrinsic photon statistics of the incoming beam; the second is the statistical nature of the photodetection process [Fox06]. Here, we will first discuss the intrinsic photon statistics of an X-ray beam in our example. The following example illustrates the discrete nature of light. If we have an X-ray source with a photon flux of $\Phi = 10^5$ photons per time interval $\Delta s$, the average number of photons arriving at the detector is $10^5$. Imagining an ideal detector with a 1 Megapixel sensor $N_{pix}$, we can expect that each pixel will receive an average number of photons of $\overline{n} = 0.1$ per time interval. In reality, pixels can only receive a positive integer number of photons. Most of the pixels will have a photon count of 0, some 1, and occasionally pixels will receive 2 or more. It is impossible to predict which pixels will receive photons and in what quantity. The average number of photons per pixel is 0.1. These fluctuations in short time intervals are called shot noise and can be described by Photon statistics. In this simplified example, we assumed that the X-ray source emits coherent and monochromatic photons with a constant rate per time interval. In a classical picture, the electric field wave can be described by

$$E(x,t) = E_0 \sin(kx - \omega t + \phi), \tag{2.30}$$

where $E_0$ is the amplitude of the wave, $k$ is the wave number, $x$ is the position, $\omega$ is the angular frequency, $\phi$ is the phase, and $t$ is the time. The intensity of the wave is proportional to the square of the amplitude if the phase is time-independent. Looking at $N$ detector pixels after a time interval $\Delta t$, $n < N$ pixels will receive one photon, and if the average number of photons per pixel is small enough, $(N - n)$ pixels will receive zero photons. The probability $P(n)$ for detecting a single event in $n$ detector pixels is given by the binomial distribution:

$$P(n) = \binom{N}{n} p^n (1-p)^{N-n}, \tag{2.31}$$

where $p = \overline{n}/N$ is the probability of a single event in a single pixel. Substituting this into Equation 2.31 gives

$$P(n) = \frac{N!}{n!(N-n)!} \left(\frac{\overline{n}}{N}\right)^n \left(1 - \frac{\overline{n}}{N}\right)^{N-n} \tag{2.32}$$

This can be rearranged into

$$P(n) = \frac{1}{n!} \left(\frac{N!}{(N-n)!N^n}\right) \overline{n}^n \left(1 - \frac{\overline{n}}{N}\right)^{N-n} \tag{2.33}$$

When looking at a large number of pixels, we can take the limit $N \to \infty$ using the Stirling approximation

$$\lim_{N\to\infty} \frac{N!}{(N-n)!N^n} = 1 \tag{2.34}$$

For $N \to \infty$, the series expansion of the exponential function $e^{-\overline{n}}$ can be used to approximate

$$\left(1 - \frac{\overline{n}}{N}\right)^{N-n} = 1 - (N-n)\frac{\overline{n}}{N} + \frac{(N-n)(N-n-1)}{2!}\frac{\overline{n}^2}{N^2} + \cdots = 1 - \overline{n} + \frac{\overline{n}^2}{2!} + \cdots = e^{-\overline{n}} \tag{2.35}$$

via the binomial theorem. Plugin in these limits into Equation 2.32 gives

$$\lim_{N\to\infty} P(n) = \frac{1}{n!}\overline{n}^n e^{-\overline{n}} \tag{2.36}$$

In conclusion, the probability of detecting $n$ photons in $N$ pixels is given by the Poisson distribution

$$P(n) = \frac{\overline{n}^n e^{-\overline{n}}}{n!} \text{ for } n = 0, 1, 2, \ldots \tag{2.37}$$

Poisson distributions are characterized by a single parameter $\overline{n}$, which is the average number of events occurring in a given time interval. The standard deviation of the Poisson distribution is given by the square root of the average number of events $\sigma = \sqrt{\overline{n}}$. The SNR is defined as the ratio of the average number of events to the standard deviation $\mathrm{SNR} = \overline{n}/\sigma = \sqrt{\overline{n}}$. This means that the SNR increases with the square root of the average number of events. In our example, a SNR of 10 would require an average number of events of 100. With increasing photon flux or dose, the SNR increases, and the fluctuations in the number of photons per pixel become relatively smaller.

The ideal detector of our previous example has a certain detection efficiency $\eta$, which is determined by a quantum efficiency $\epsilon$, which represents the probability of a photon being absorbed in the detector. The interaction probability is equivalent to the probability of a photon not being transmitted. The quantum efficiency is therefore given as

$$\epsilon = 1 - e^{-\mu d} \tag{2.38}$$

where $d$ is the thickness of the detector material, and $\mu$ is the linear attenuation coefficient. The probability distribution of the registered photons is again Poissonian with

$$P(n)_d = \frac{(\overline{n} \cdot \epsilon)^n e^{-\overline{n}\cdot\epsilon}}{n!}, \tag{2.39}$$

as the transmission probability follows a Bernoulli distribution, which acts on a Poisson process. That the transmission process follows a Bernoulli distribution can be shown as equivalent to the argumentation of the binomial distribution of photons. The proof of this can be found in Fessler [Fes00]. A visual demonstration of this is shown in Figure 2.6. It is assumed that the measurement over an integration time $T \gg \Delta t$ will increase the average number of photons per pixel to $\frac{T \cdot \Phi}{N_{\mathrm{pix}}} = \overline{n} = 100$. Quantum efficiencies from 4.5 to 82% are considered. The binomial process acts on the Poisson process, with repetitions going from 1 to 1000.

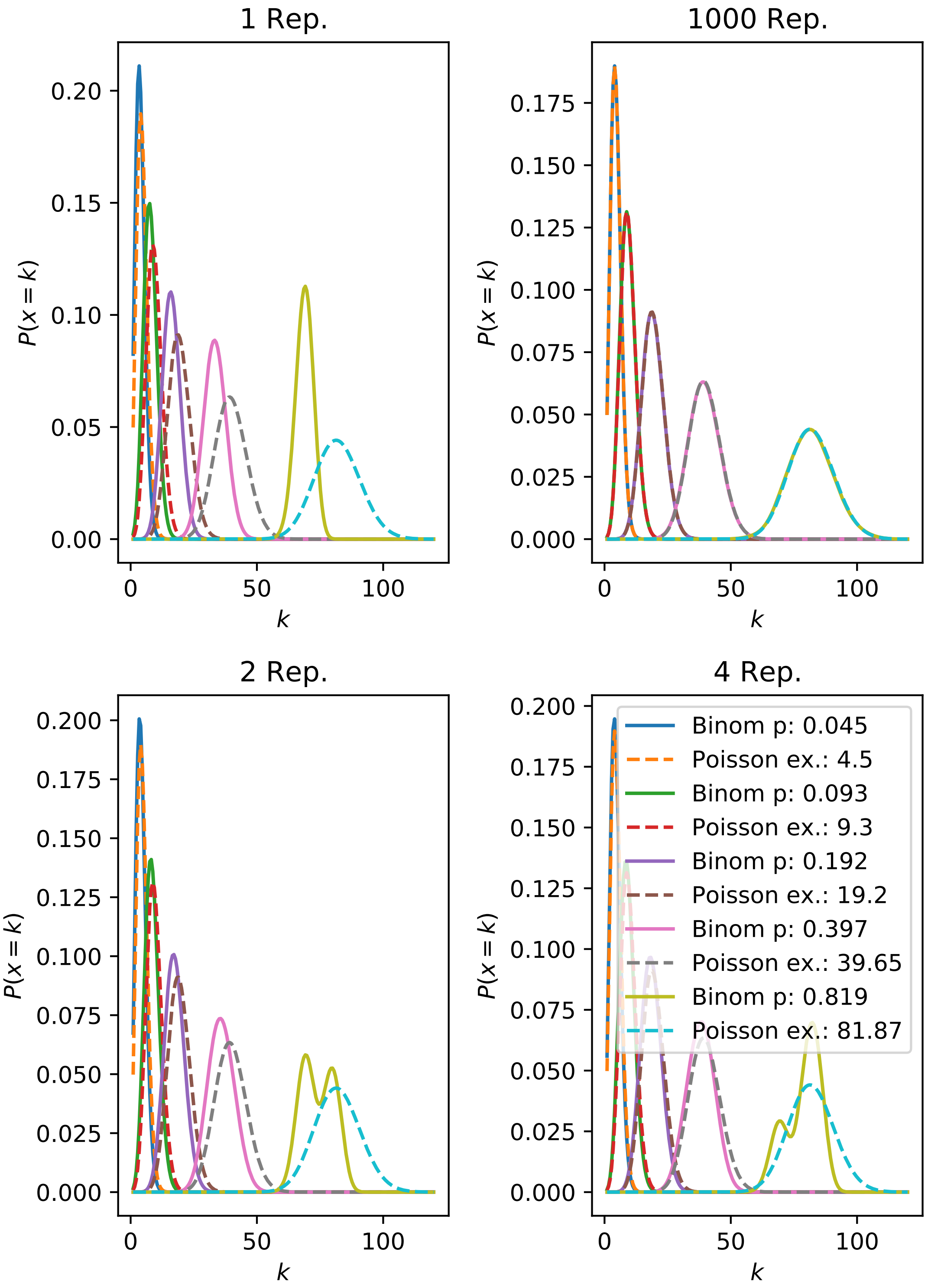

**Figure 2.6:** Caption can be found on the next page.

**Figure 2.6:** Probability mass functions: A binomial distribution on a Poisson distributed process for 1, 2, 4, and 1000 repetitions. Binomial distributions are plotted dotted, and Poisson distributions are plotted solid. The binomial probabilities range from 4.5 to 82 %. It can be observed that the binomial distribution converges to the Poisson distribution with an increasing number of repetitions. The Poisson distribution is therefore a good approximation for the binomial distribution for many photons being measured in a certain integration time. If the overall expected number of photons is low due to low quantum efficiency, the binomial distribution shows only small deviations from the Poisson distribution, even for view repetitions.

For a high number of X-ray quanta, the sterling equation can be used to approximate the Poisson distribution by a Gaussian [Buz08]:

$$P(n) = \frac{1}{\sqrt{2\pi\overline{n}}} \exp\left(-\frac{(\overline{n}-n)^2}{2\overline{n}}\right) \tag{2.40}$$

where $\overline{n}$ is the expectation value of the Poisson distribution, which equals the variance $\overline{n} = \sigma^2$. Equation 2.40 is a consequence of the central limit theorem.

Using integrating detectors like described in Section 2.5 leads to a shift in the noise distribution, which can not be considered Poissonian or Gaussian after the scintillator conversion and several correction steps like beam-hardening and dark current correction. To be able to apply a maximum likelihood estimator, the line integrals values can be scaled or shifted (noise equivalent counts scaling/shifting) [NMD01] so that the first and second moments of the noise distribution are equal to the Poisson distribution.

## 2.5 Integrating detectors in medical CT

Energy integrating detectors are most widely used in medical CT systems. They consist of a photodiode coupled to a scintillator. Incoming X-rays are absorbed in the scintillator material, which emits visible light. A photodiode converts the visible light into an electric current, which is converted into a voltage signal. The voltage signal is then amplified, digitized, and the digitized signal is stored in a memory buffer, which is read out by a Analog to Digital Converter (ADC) and stored in a computer memory. The ADC converts the analog voltage signal into a digital signal.

The visible light emitted by the scintillator is proportional to the number and energy of the incoming X-rays. Higher energy X-rays generate more visible light than lower energy X-rays, meaning that the visible light emitted is a measure of the energy deposition of the incoming X-rays. As the system is limited in its temporal sampling rate, several X-ray photons can be absorbed in the scintillator material during one sampling interval, giving rise to the term energy integrating detector. After this process, no information on the number of photons or their energies is retrievable. The acquired signal, which is directly proportional to the energy deposited in the scintillator, is used to calculate the line integral of the attenuation coefficient. As the information about the energies of the X-ray photons is not available, the line integral is calculated using the energy-independent Beer-Lambert law, making the projection data prone to spectral artifacts like beam hardening [BC76], which, if uncorrected, leads to cupping artifacts in the reconstructed image. Another problem of energy integrating detectors is the acquisition of a dark current signal, due to the readout electronics and the scintillator material itself. The dark current signal is a signal generated by the detector without any incoming X-rays. The mean value of the dark current can be calibrated and subtracted from the measured signal [Wis+02].

## 2.6 Energy-resolving medical CT

The basis of generating X-ray measurements with energy-dependent information in medical CT is either the usage of energy-resolving detectors or the change of the X-ray spectrum itself. Energy-resolving clinical CT systems are mainly using four different approaches, to get spectral information on the attenuation coefficient: dual layer detectors, photon counting detectors, dual source systems, and rapid kVp switching. The first two approaches are based on the usage of energy-resolving detectors, while the latter two approaches are based on the change of the X-ray spectrum. All four approaches are schematically shown in Figure 2.7. Measurements at two different energies can be performed using DLCT, dual source systems, and rapid kVp switching. PCCT systems are theoretically capable of measuring the energy in more than two increments, but modern clinical PCCT systems are limited to two energy bins because of several factors, including data transfer rates and lacking applications.

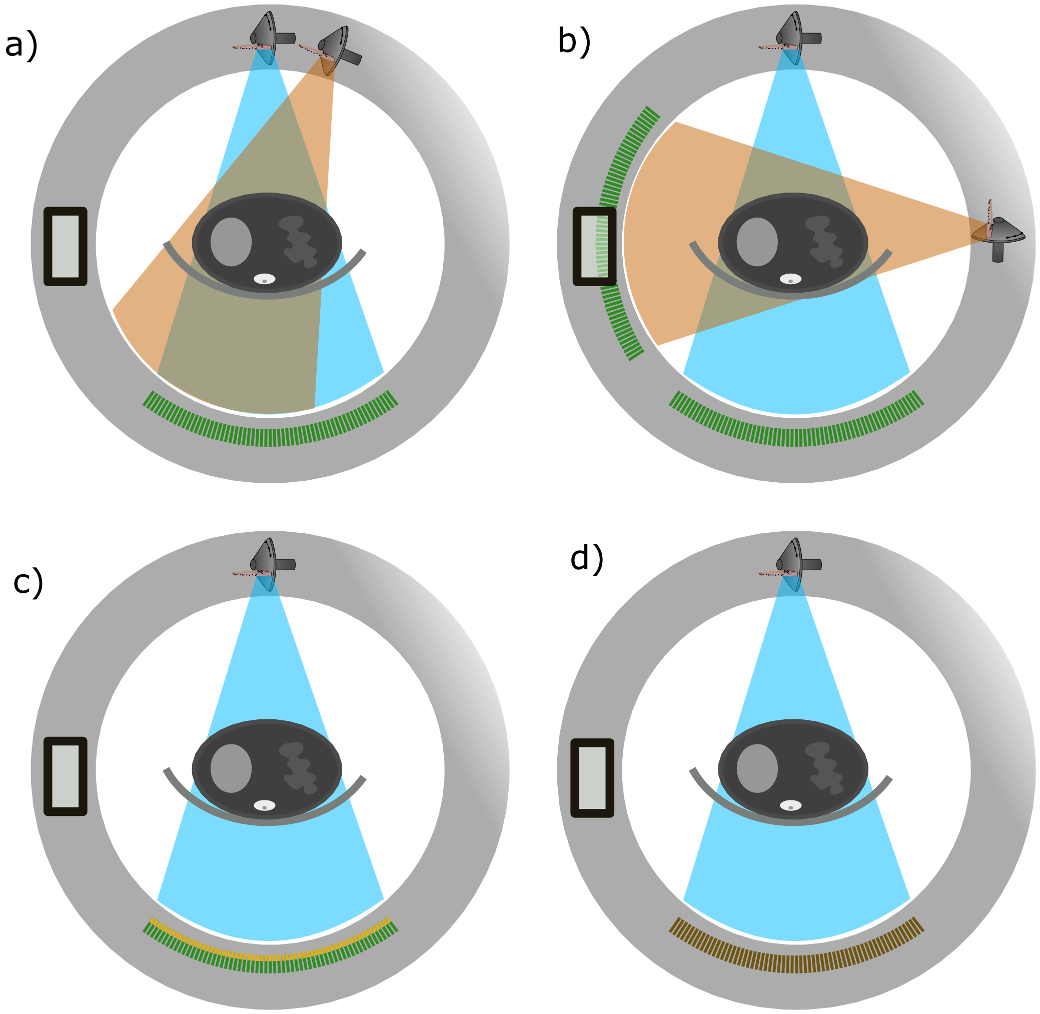

**Figure 2.7:** Technical realization of Dual Energy CT (DECT) and PCCT. The rapid kVp switching approach shown in **a** is switching the tube voltage between two different values from projection to projection. The dual-source approach shown in **b** is using two X-ray tubes with different acceleration voltages, tube currents, and beam filters. The X-ray sources are placed at an angle of 90 ° to each other within the gantry. Two conventional integrating detectors are placed on the opposite side of the X-ray sources. The DLCT approach drawn in **c** uses a dual scintillator layer detection design to assign incoming X-rays to low and high energies. The PCCT approach depicted in **d** is operated with a single X-ray source and a photon-counting detector. The photon-counting detector is capable of assigning incoming X-rays to different energy bins. Ideally, the energy response function of the detector is rectangular. In practice, this is not the case. Details are discussed in Section 2.8.

The following sections will discuss the technical realization of the detector-based approaches, as the results of this thesis are mainly based on DLCT and PCCT measurements. Theoretically, it is possible to apply the results of this thesis, generated from a clinical DLCT, to clinical PCCT systems.

### 2.6.1 Dual layer detectors

As previously mentioned, clinical DLCT is based on a system with one X-ray source operated at a constant acceleration voltage of 120 kVp in a standard setting. The energy differentiation can be achieved by an energy-responsive detector with a double-layer structure of scintillator materials [Alt+11]. A one-millimeter thick Tin Selenide (ZnSe) layer is used as a low energy filter, and a two-millimeter thick Gadolinium Oxysulfide (GOS) layer located behind the ZnSe layer absorbs all photons after the ZnSe layer [She+13]. The side-looking scintillator-coupled photodiodes measure an integrated signal of the lower energy photons in the ZnSe layer and the higher energy photons in the GOS layer. A schematic of the detector is shown in Figure 2.8.

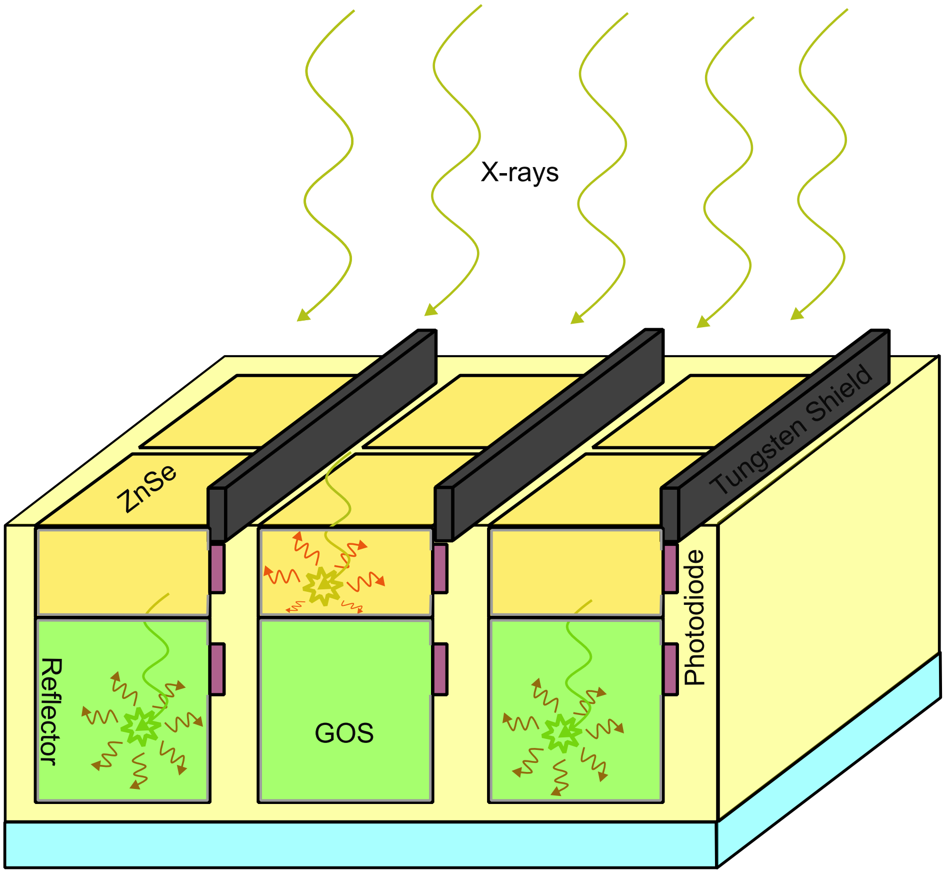

**Figure 2.8:** A schematic overview of a DLCT detector. Low energetic incoming X-rays are absorbed in the first ZnSe scintillator layer (yellow boxes) and a side-looking, edge-on, silicon photodiode coupled to the layer (purple slits) converts the visible light from the scintillator plate to an electrical signal. The photodiodes are thin enough to maintain the same detector pitch and geometrical efficiency as a conventional CT detector [She+13]. The scintillator borders have a visible light reflector to channel the light output to the photodiode. X-ray photons can pass the reflector and reach the second GOS scintillator plate. The high Z material absorbs the remaining X-rays and converts them to visible light. A tungsten shield (black boxes) protects the photodiodes from radiation. Figure is inspired by [She+13].

The energy response function of the detector is shown in Figure 2.17 a. Dedicated algorithms can be applied to generate energy-dependent sinograms (see Section 2.8). The energy response function of the detector and the tube spectrum must be known to perform the projection-based material decomposition. The energy response function of the detector can be measured using a monochromatic X-ray source like a synchrotron.

## 2.7 Image artifacts

The image quality of a reconstructed image is determined by the SNR, the spatial resolution, and the presence of image artifacts. Image artifacts are deviations of the reconstructed image from the original object. Image artifacts can be caused by the measurement process, the reconstruction algorithm, or the object itself.

### 2.7.1 Spectral artifacts

With the scope of this thesis in mind, spectral artifacts are of special interest. Spectral artifacts are caused by the energy dependence of the attenuation coefficient. The energy dependence of the attenuation coefficient is caused by the energy dependence of the photoelectric effect and the Compton effect Section 2.2. When passing through matter, X-rays are attenuated, which can be described using Equation 2.2. As the photoelectric effect is the dominant interaction mechanism at low energies, the attenuation coefficient increases with decreasing energy. Conventionally generated X-rays have a continuous spectrum with a characteristic line spectrum superimposed (Section 2.1). Low energetic photons are predominantly attenuated within the first few centimeters of matter, depending on the material. After the first few centimeters, the X-ray spectrum is hardened, meaning that a major part of the low energetic photons are absorbed, and the spectrum with its mean energy is shifted to higher energies. This is called beam hardening and is visualized in Figure 2.9.

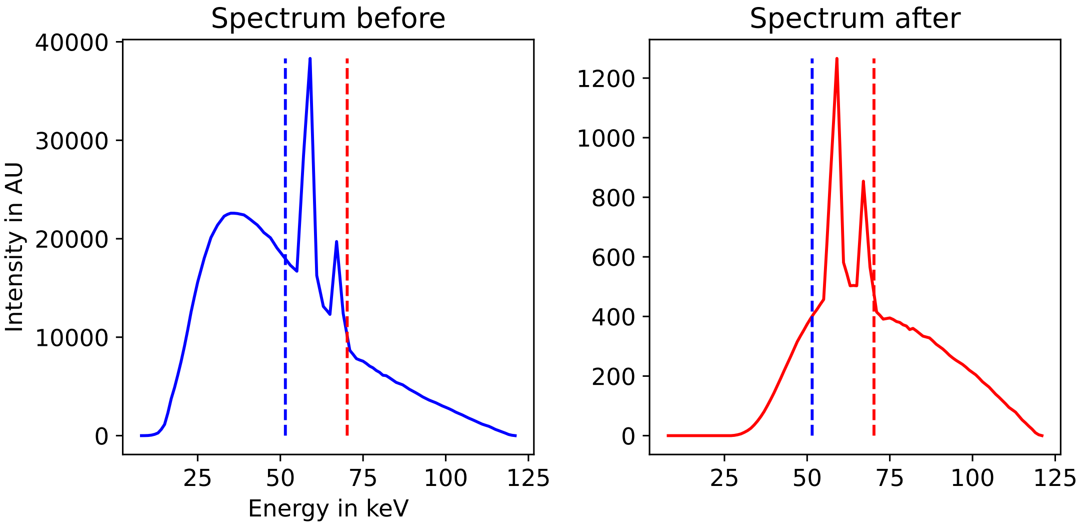

**Figure 2.9:** The change of the X-ray spectrum with beam-hardening. The spectrum of a conventional X-ray tube and its mean energy is shown in blue. After passing through matter, the spectrum is hardened, meaning that the mean energy of the spectrum is shifted to higher energies (red). The bigger part of the low energetic photons is absorbed, while the high energetic photons are less attenuated.

The attenuation of a hardened X-ray spectrum is lower than the attenuation of the original spectrum, as the higher energies get less absorbed in the very same material. This leads to a nonlinear energy dependence of the energy-averaged attenuation coefficient. Cupping artifacts can be observed in the reconstructed image. Using projection-based material decomposition Subsection 2.2.4 can avoid spectral artifacts like cupping. This is visualized in Figure 2.10.

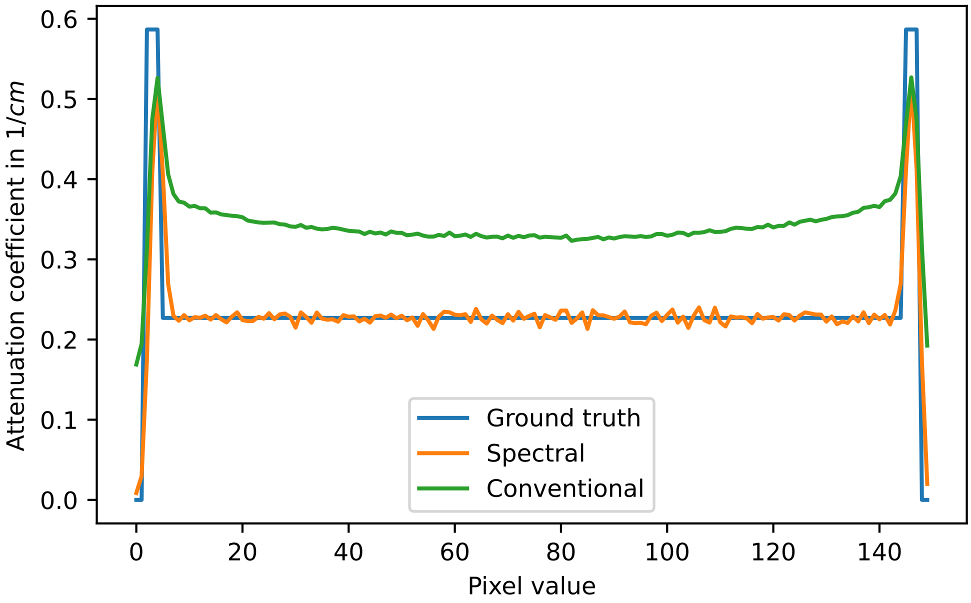

**Figure 2.10:** Cupping artifact in conventional and spectral reconstruction. A line plot through the center of a water phantom in a cylindrical container is shown. A constant attenuation coefficient is assumed (blue line). The cupping artifact is visible in the conventional reconstruction (green line), giving a high attenuation at the edges of the phantom and a decreased attenuation at the center. The artifact looks like the curved surface formed in a cylinder (or cup) by a liquid (meniscus) due to adhesion. The spectral reconstruction (orange line) is unaffected by the cupping artifact, as the energy dependence of the attenuation coefficient is considered in the projection-based material decomposition. A virtual monoenergetic reconstruction at 50 keV is shown.

Strong beam hardening artifacts can be observed, especially between two strongly absorbing objects along the beam direction, like the shoulder joints. The absorption coefficient between these structures can be drastically reduced. Further, beam hardening artifacts arising from prostheses can be a major problem in clinical CT imaging. Due to a strong absorption within the metal alloys used for prostheses, the X-ray spectrum is hardened, leading to major beam hardening artifacts. Spectral reconstruction algorithms can result in a significant reduction of streak artifacts produced by beam-hardening [Wel+17].

### 2.7.2 Other artifacts

Image artifacts can be classified into two categories: deterministic and stochastic artifacts. Examples of deterministic artifacts are beam-hardening Subsection 2.7.1, ring, and motion artifacts. Stochastic artifacts are noise (Section 2.4) and aliasing artifacts (Section 2.3). Ring artifacts are caused by a non-uniform detector response. For example, when a detector pixel is corrupted, showing a lower or no response, a ring with a lower intensity is visible in the reconstructed image at the radial position of the detector pixel. Ring artifacts can most effectively be reduced by properly calibrating the detector or post-processing in projection space by interpolating the corrupted detector pixel with neighboring pixels. Motion artifacts arise from patient movement between the acquisition of projections during a gantry rotation. In the case of cardiac imaging, this motion can not be avoided. To reduce motion artifacts, the gantry rotation time can be reduced to acquire the projections within the diastolic or even systolic phase of the heart [Dew+20]. This technique requires Electrocardiogram (ECG)-gated scans. The post-processing correction of motion artifacts includes image registration and motion correction, which can be challenging due to unknown motion patterns.

Stochastic artifacts mainly arise from the usage of low dose CT (noise) or undersampling (aliasing) to reduce the radiation dose to the patient. Mainly, sophisticated reconstruction algorithms are applied to reduce the effects of stochastic artifacts. Model-based iterative reconstruction algorithms have great potential in reducing the radiation dose in modern CT scans when compared with the traditional FBP algorithms [Liu14]. Modern reconstruction algorithms correcting for sparse sampled CT projections mainly depend on AI-based methods for the correction of undersampling artifacts [Rie+23; Dor+23; SPX22].

## 2.8 Simple simulation of projection based material decomposition

The X-ray spectrum of a conventional X-ray tube is a continuous spectrum with a characteristic line spectrum superimposed. It is characterized by the anode material, the tube voltage and current, and the filter. The heating voltage is additionally quantifying the intensity of the emitted spectrum. To change the mean energy of the spectrum, the tube voltage can be modified, leading to a shift of the maximum X-ray energy. Additionally, a filter material can be introduced into the beam to reduce the low energy intensities. This is a result of the energy dependence of the attenuation coefficient. An example material to filter out low-energy photons is tin. Tin has an atomic number of 50 and, therefore, a high attenuation at low energies. This is due to the photoelectric effect, which is the dominant interaction mechanism at low energies. The energy-dependent attenuation coefficient of tin is shown in Figure 2.11. The energy dependence of the attenuation coefficient can be used to generate two X-ray spectra with almost no overlap in energies. This setting with two spectra with almost no overlap in energies can be used to perform energy-dependent X-ray measurements. It can be applied in sequential scanning or on a dual-source setup. Another possibility to generate spectrally separated measurements is the usage of a dual-layer detector. The first scintillator layer acts as a filter for low-energy photons, while the second layer ideally absorbs all photons after the filter layer. Both scintillator layers are coupled to a photodiode. A detailed description can be found in Subsection 2.6.1. Using that setup, the energy of the incoming photons can be separated. Ideally, the detector response function can then be expressed using the energy-dependent Beer-Lambert law,

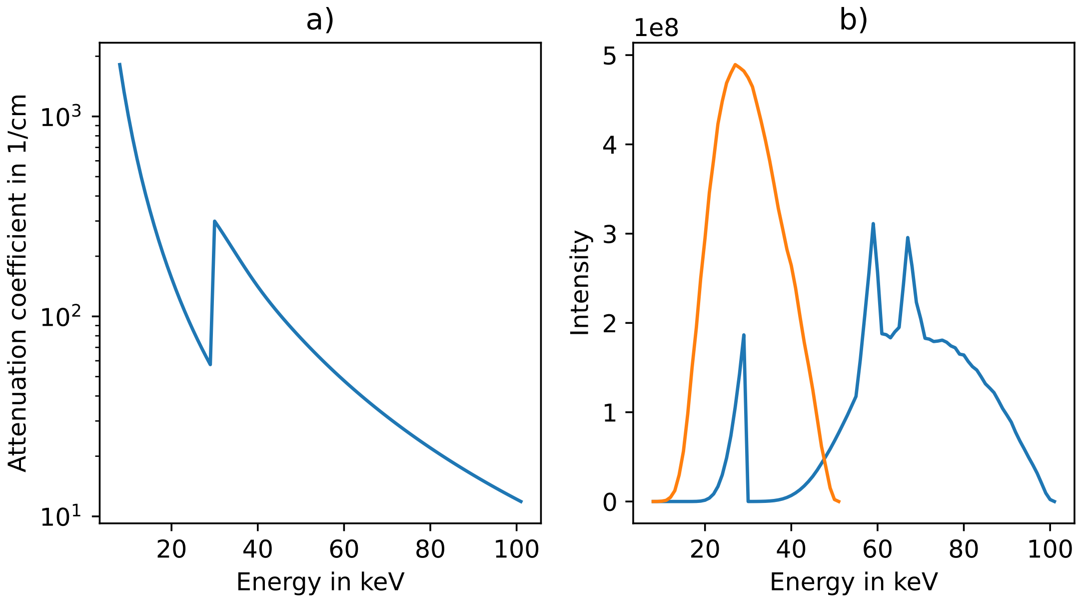

**Figure 2.11:** The effect of tin filtration. In panel **a**, the attenuation coefficient of tin as a function of energy is plotted on a logarithmic scale. The attenuation coefficient is given in $\mathrm{cm}^{-1}$. The attenuation coefficient at the low energies of the X-ray spectrum is two orders of magnitude higher than at the high energies. A drastic increase in absorption can be observed at the K-edge of tin at 29.2 keV. Apart from the K-edge, the absorption is exponentially decreasing with increasing energy. In panel **b**, the intensity in numbers of photons of two X-ray spectra are plotted. The blue spectrum with an acceleration voltage of 100 keV is filtered with a 0.4 mm thick tin filter and has five times increased heating voltage of the cathode to account for the lower photon output of the tin filter. The orange spectrum with an acceleration voltage of 50 keV is not filtered. The mean energies of high and low energy spectra are 67 keV and 30 keV, respectively. The spectral overlap is only around 5.1% of the total number of photons.

$$D(E)_{\mathrm{r}} = e^{-\mu(E)\cdot d_{\mathrm{FL}}}, \tag{2.41}$$

where $D(E)_{\mathrm{r}}$ is the detector response function for the rear layer detecting all remaining photons after the filter layer with thickness $d_{\mathrm{FL}}$ and absorption coefficient $\mu(E)$. The detector response function for the front layer is then given by

$$D(E)_{\mathrm{f}} = 1 - D(E)_{\mathrm{r}} = 1 - e^{-\mu(E)\cdot d_{\mathrm{FL}}} \tag{2.42}$$

being the scintillator attenuation in the front layer. An example detector response function is shown in Figure 2.17 a. The front layer is assumed to be 0.8 mm thick ZnSe, and the rear layer is assumed to be 2.0 mm thick $Gd_2O_2S$ GOS [She+13]. ZnSe, with its low atomic number, is a good candidate for a low-energy filter, while GOS has a higher atomic number absorbing also high energy X-rays. With the ideal detector response function, the spectral separation of a 120 kVp tungsten can be as good as approximately 40% spectral overlap. Thin reflector layers, typically consisting of a mixture of high-reflectance materials like titanium dioxide (TiO2), and separate adjacent pixels in the detector array. Optical crosstalk between pixels is reduced by the reflector layer. Using a reflector layer, cross-talk correction makes only about 11% Modulation Transfer Function (MTF) increase [CSB04; BG94]. Cross-talk in the photodiodes from traveling electron-hole pairs is in the order of 4% [JJH09]. Further, the edge-on photodiode design between the detector columns of the DLCT prevents cross-talk in detection-arc dimension [She+13]. Using reflector layers, cross-talk correction, and state-of-the-art photodiodes, the spectral response of the detector is assumed to be close to the ideal behavior shown in Figure 2.17 a.

The ideal detector response function of a Photon Counting Detector (PCD) is described by a step function, forming rectangular bins between thresholds. The theoretical spectral overlap is 0%, as the detector response function is zero for all energies outside the bin and one for all energies inside the bin.
"Physical effects such as electronic noise, incomplete charge collection, energy loss due to K-escape, or other sources contribute to a degradation of the energy resolution of the detector. As a consequence, two adjacent energy bins are not sharply separated by the energy threshold at their common boundary. [...] Effects contributing to the degradation of the energy resolution lead to an overlap of the bin-sensitivity functions" [Sch+08].
This is visualized in Figure 2.12. A simple simulation was consulted to investigate the effect of the energy response function on image quality in material decomposed images. A digital Shepp-logan phantom was generated with different densities of water, bone, and iodine. The inside region of the phantom was set to water with 1.0 g/ml mass density. The outside region (skull) is composed of Hydroxyapatite with a density of 1.0 g/ml. A small mixed region with bone and water and an iodine water mix was added to the phantom. Additionally, there is an air region inside the phantom. The phantom is 256 × 256 pixels in size. The mass density maps of the phantom are shown in panels a to c in Figure 2.13. A virtual monoenergetic image at 70 keV is shown in panel d in Figure 2.13 in Hounsfield Units (HU).

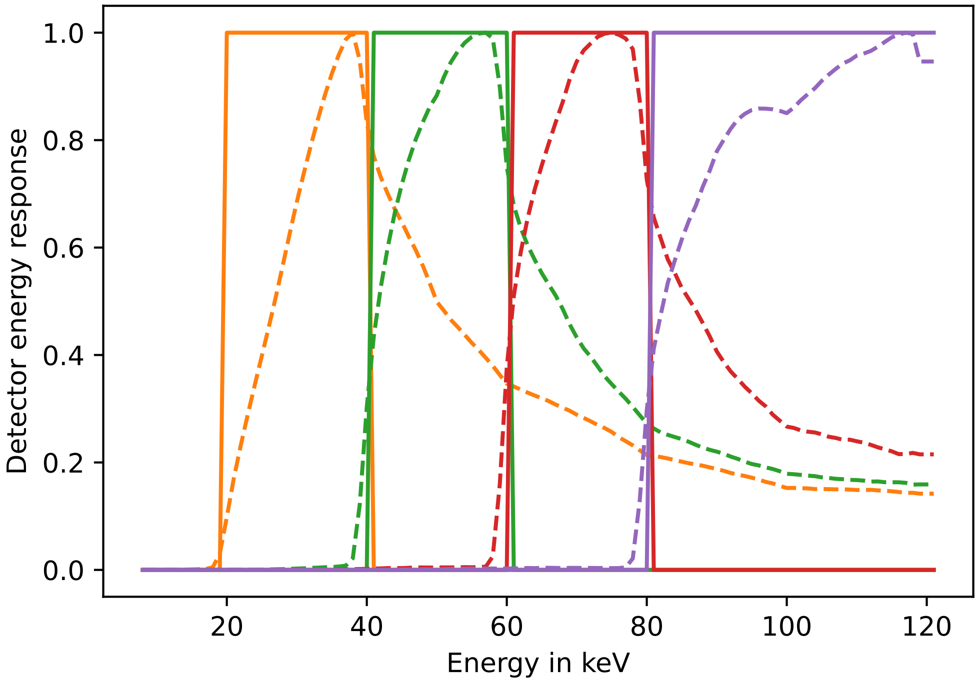

**Figure 2.12:** The energy response function of a PCD. The energy response function is plotted up to 120 keV. The solid lines are the theoretical energy response functions for bins 1 to 4 described by a step function. The dashed lines are the energy response functions simulated with a 500 $\mu$m thick GaAs sensor with 75 $\mu$m pixel pitch with an equidistant threshold spacing from 20 to 80 keV and a threshold width of 20 keV plus a 40 keV broad high energy bin from 80 to 120 keV.

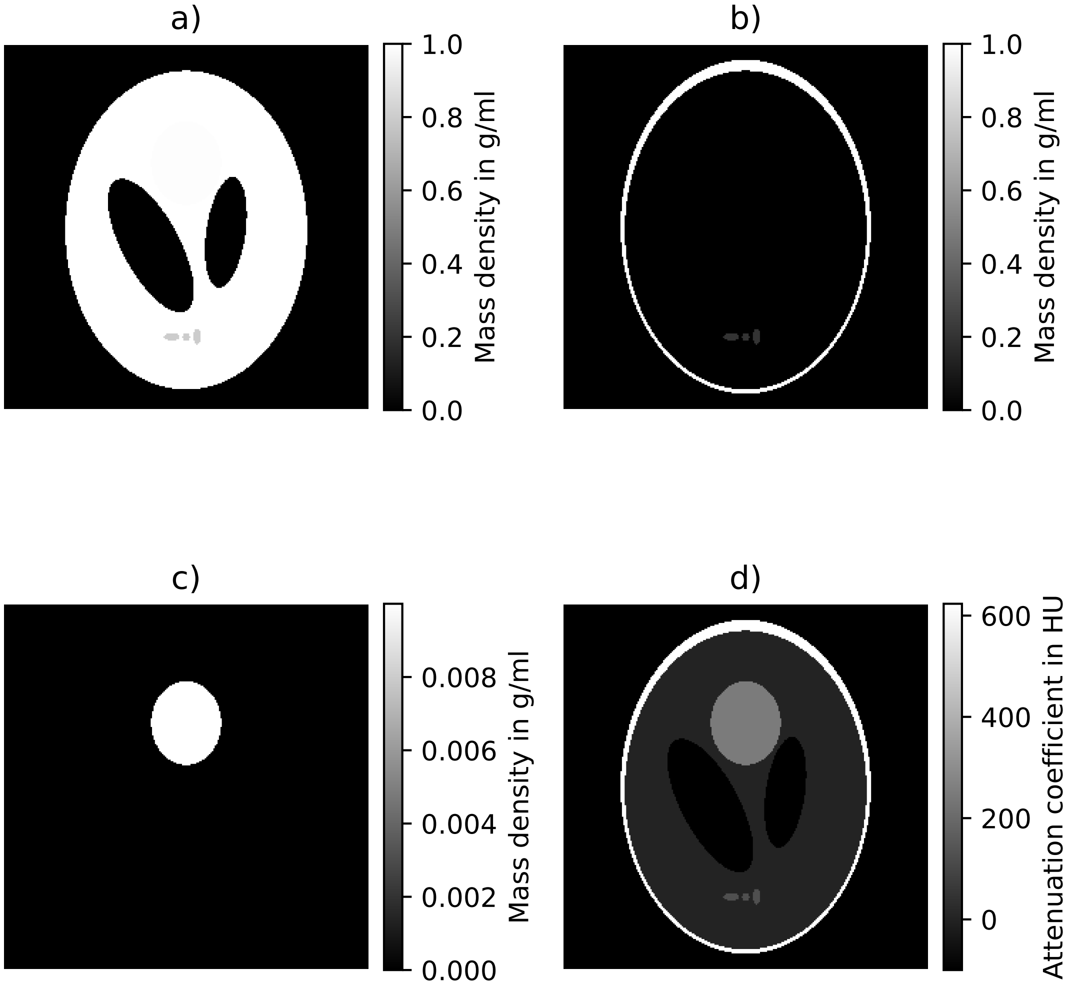

**Figure 2.13:** The digital Shepp-logan phantom used for the simulation. The phantom is composed of water, bone, iodine, and air. The inside region is water with a 1.0 g/ml mass density. The outside region (skull) is composed of Hydroxyapatite with a density of 1.0 g/ml. A small mixed region with bone and water and an iodine water mix was added to the phantom. Additionally, there is an air region inside the phantom. The phantom is 256 × 256 pixels in size. The mass density maps of the phantom are shown in panels **a** to **c** in g/ml. A virtual monoenergetic image at 70 keV is shown in panel **d** in HU. The image was generated using the Beer-Lambert law with the mass density maps and the attenuation coefficients of water, bone, and iodine.

The mass density images were forward projected onto a 256-pixel wide detector array with a pixel pitch of 1.0 mm in parallel beam geometry, generating 1000 projections for all three material areal densities. In the next steps, measurements were simulated for a 120 kVp tungsten spectrum for the DLCT and PCCT setup. Noise was added to virtual intensity measurements. Several noise components have to be considered. For the case of normal clinical exposures, the X-ray CT measurements are often modeled as the sum of a Poisson distribution representing photon-counting statistics [EF99] and an independent Gaussian distribution representing additive electronic noise [Sny+95]. Gaussian noise is modeled as a zero-mean Gaussian random variable with a standard deviation $\sigma_{\mathrm{Gauss}} = 5 \cdot 10^{-5} \cdot I_0$, being 5 permille of the flat field intensity. The Poisson noise is modeled as a Poisson random variable with a mean $\mu_{\mathrm{Poisson}} = I_{\mathrm{x}}$, being the intensity after attenuation, at every pixel. The additive noise of electric components is modeled as a zero-mean Gaussian random variable because a dark current calibration can be performed prior to the measurement. The dark current calibration is performed by measuring the detector response function without any X-ray exposure, and the mean value is subtracted from the measurement. PCCT measurements are also simulated with additive electronic noise to compare the two methods only depending on the energy response function. Electronic noise can be efficiently reduced or excluded in PCCT measurements by setting the lowest threshold to a value above the electronic noise. This is impossible in DLCT measurements, as a photon integrating approach is used with the double-layer scintillator. Further, the difference in DLCT and PCCT simulation is the energy weighting of the measurements in the DLCT case. The energy weighting is performed by weighting the X-ray counts in the scintillator layers with their corresponding energy. “Once an X-ray quantum is absorbed in the detector, the conversion process is characterized by a mean energy-dependent gain, $g(E)$ $[\cdots]$, which records a signal strength proportional to the energy imparted to the detector, $g(E) = GE$, i.e., $G$ is the conversion factor from X-ray energy to signal” [Whi+06]. The conversion factor $G$ is assumed to be 1.0 divided by the mean spectrum energy for the DLCT simulation. No energy weighting is performed for the PCCT simulation $g(E) = 1$. The simulated noisy layer and bin measurements were then used to perform a material decomposition in projection space using the Beer-Lambert law and a maximum likelihood estimator [AM76]. The material decomposition was performed for the DLCT and PCCT setup. As a flatfield image, the mean intensity value over the whole detector array was used in every pixel. Even though the measured intensities are not purely Poisson distributed but a mixture of Poisson and Gaussian noise, the maximum likelihood estimator is used in this case, as it is used in literature for spectral measurements [EF02]. There have been attempts to use a penalized weighted least square estimator for Poisson-Gaussian mixed noise [Din+18]. This approach exceeds the complexity of this simple simulation. After generating the material decomposed areal density images for water and bone, a simple filtered back projection was performed to reconstruct the images. A Ram-Lak filter was used for the reconstruction. The bone density images obtained from DLCT and PCCT with 2 and 4 bins are shown in Figure 2.14.

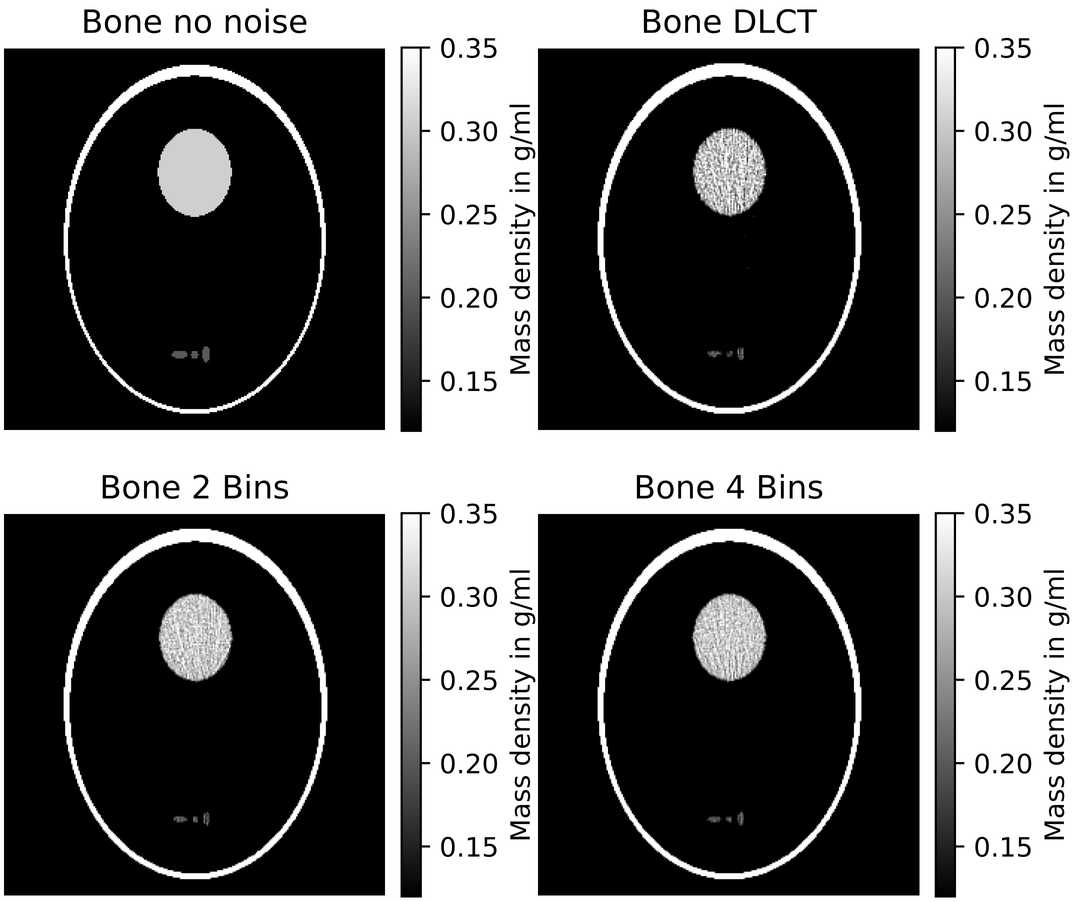

**Figure 2.14:** The bone density images obtained from DLCT and PCCT with 2 and 4 bins. The bone density images are shown in g/ml.

Quantitative values for the bone and water density images are compared in homogeneous regions for DLCT and PCCT with 2 and 4 bins. The results for bone and water densities are shown in Table 2.1 and Table 2.2. The ground truth values are compared to density values obtained from a projection-based two-material decomposition plus filtered back projection. Homogeneous ROI were selected on iodine water mix, water only, bone water mix and bone only regions. The deviations in all modalities to the ground truth values are also shown in the tables.

The mean deviations of bone densities obtained from DLCT and PCCT with 2 and 4 bins are 3.6%, 2.2% and 3.0% respectively. The mean deviations of water densities are 4.8%, 3.8% and 2.8% respectively. These values are obtained with identical noise approximations in the DLCT and PCCT simulations. In a more realistic scenario, the Gaussian noise component in the PCCT simulation could be smaller or even negligible, as by setting the lowest energy threshold effectively, the electronic noise can be avoided [Len+19].

|  | IW [mg/ml] | IW [%] | W | W | BW | BW | B | B |
|---|---|---|---|---|---|---|---|---|
| Gr. T. | 306 | 0.0 | 0 | 0.0 | 200 | 0.0 | 1000 | 0.0 |
| DLCT | 358 | 5.2 | 9 | 0.9 | 244 | 4.4 | 961 | -3.9 |
| PCCT 2 | 311 | 0.5 | 33 | 3.3 | 226 | 2.6 | 974 | -2.6 |
| PCCT 4 | 348 | 4.2 | 4 | 0.4 | 191 | -0.9 | 937 | -6.3 |

**Table 2.1:** Bone densities obtained from DLCT and PCCT with 2 and 4 bins. The bone density values are shown in mg/ml. The ground truth values are compared to density values obtained from a projection-based two-material decomposition. The deviations from the ground truth value are given in percentage. Homogeneous regions were selected in iodine water (IW) mix, water (W) only, bone water (BW) mix and bone (B) only ROI.

|  | IW [mg/ml] | IW [%] | W | W | BW | BW | B | B |
|---|---|---|---|---|---|---|---|---|
| Gr. T. | 742 | 0.0 | 1000 | 0.0 | 800 | 0.0 | 0 | 0.0 |
| DLCT | 660 | -8.2 | 989 | -1.1 | 725 | -7.5 | -24 | -2.4 |
| PCCT 2 | 744 | 0.2 | 941 | -5.9 | 757 | -4.3 | -49 | -4.9 |
| PCCT 4 | 672 | -7.0 | 991 | -0.9 | 816 | 1.6 | 15 | 1.5 |

**Table 2.2:** Water densities obtained from DLCT and PCCT with 2 and 4 bins equivalent like in Table 2.1

The noise properties in the mentioned homogeneous ROI are investigated using scatterplots of the bone and water densities. The scatterplots are shown in Figure 2.15. The anticorrelated noise in material decomposed images is introduced by the material decomposition algorithm and is not existent in the reconstructed layer and bin measurements [AM76; BZS15]. The deviations of the bone and water densities in the homogeneous ROI from the ground truth values are shown in Figure 2.16 to highlight the performance of the material decomposition algorithm on different detector-based energy separation approaches. The Pearson product-moment correlation coefficient r is -0.992, -0.991, -0.999, and -0.972 in iodine water mix, water only, bone water mix , and bone only ROI respectively. It is equal for all modalities DLCT and PCCT with 2 and 4 bins. The $r$ values are close to -1, which

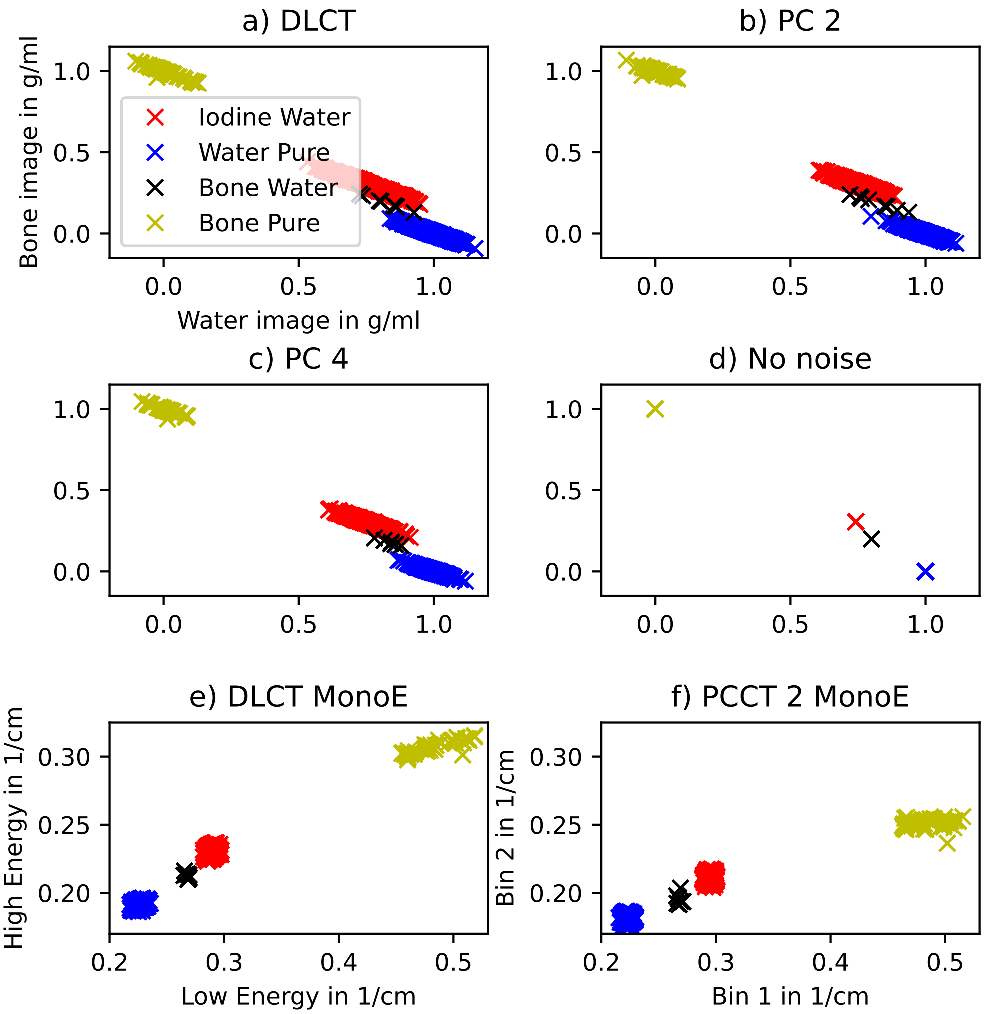

**Figure 2.15:** Scatterplots of the bone and water densities obtained from DLCT and PCCT with 2 and 4 bins in **a**, **b** and **c**. The ground truth values are shown in panel **d**. Panel **e** and **f** show the reconstructed Virtual monoenergetic image (MonoE) images from DLCT and PCCT with 2 bins. An anticorrelated noise behavior is visible in all material decomposed images. It is not existent in the reconstructed layer and bin measurements.

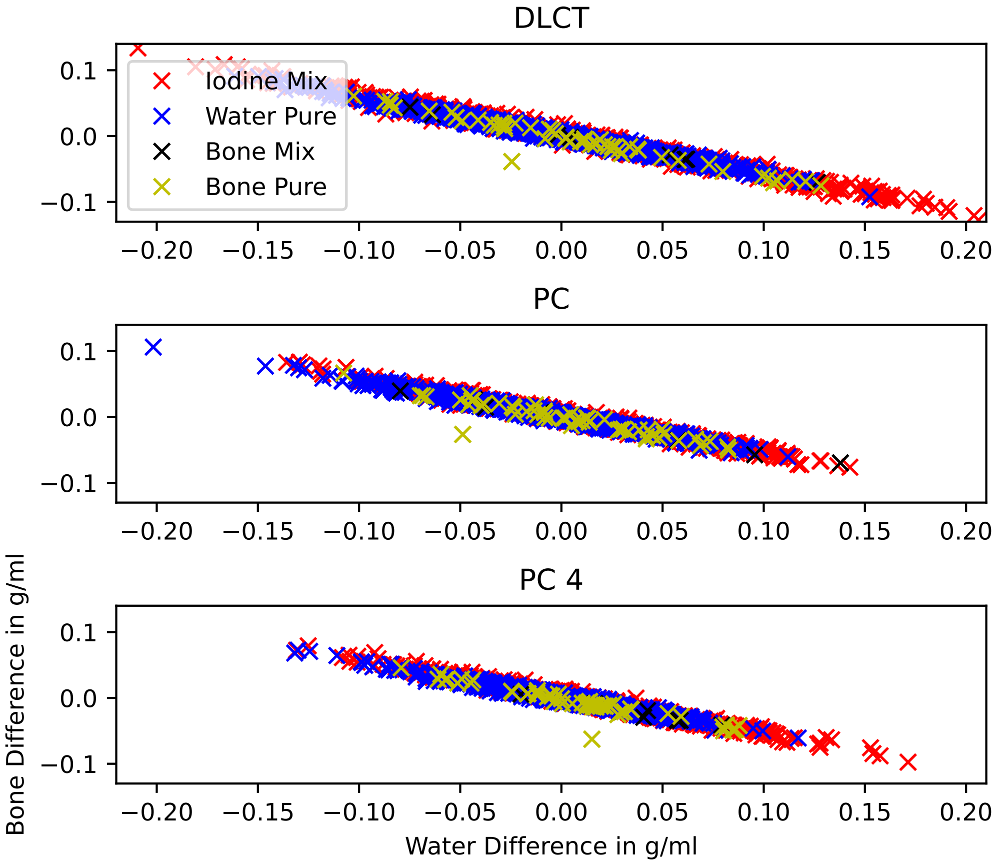

**Figure 2.16:** Scatterplots of the difference in bone and water density images obtained from DLCT and PCCT with 2 and 4 bins to noise-free images. The x and y axes are scaled equally to highlight the differences in accuracy and precision of the material decomposition algorithm. The biggest deviations can be found in the DLCT approach. The deviations in the PCCT with 2 and 4 bins are smaller compared to the DLCT approach. The differences between 2 and 4 bins are only marginal.

indicates a strong negative correlation between the bone and water densities. The $p$-value associated with the chosen alternative hypothesis is smaller than 0.0001 in all cases.
The theoretical background of anticorrelated noise in material decomposed images is discussed in [RZP07; Jam00]. It can be shown that the covariance matrix of the material decomposed images is given by

$$\mathcal{V}_{\mathrm{A}} = \mathcal{J}^{-1} \begin{pmatrix} \sigma_1^2 & 0 \\ 0 & \sigma_2^2 \end{pmatrix} (\mathcal{J}^{-1})^T = \mathcal{J}^{-1}\mathcal{P}(\mathcal{J}^{-1})^T, \tag{2.43}$$

where $\mathcal{J}_{i,j} = \partial C_i / \partial A_j$ is the Jacobian matrix of the projection-based spectral forward model in Equation 2.13 and $\sigma_1^2$ and $\sigma_2^2$ are the variances of the layer or bin measurements. The covariances (off diagonals of $\mathcal{P}$) of layer and bin measurements are zero, as they are independent. As all entries of $\mathcal{J}$ are nonzero, the off diagonals of $\mathcal{V}_{\mathrm{A}}$ are nonzero, showing a correlation in the material decomposed projections. Some calculation [RZP07; KKK88] lead to

$$cov(A_1, A_2) < 0, \tag{2.44}$$

indicating the anticorrelated noise in the material decomposed projections.

## 2.9 The Cramér-Rao lower bound for the estimator variance

The number of photon counts in an PCD bin is a random variable following a Poisson distribution. The amount of energy deposited in a scintillator layer of a DLCT is also a random variable following a Gaussian distribution [GB94; Swa73]. The counts or energy deposited in a bin or layer are statistically independent of each other [SB89]. This chapter will focus on the DLCT case. The PCD case can be treated analogously. To determine $A_1$ and $A_2$ from a DLCT measurement, the probability

$$P(M, A_1, A_2) = \prod_{j=1}^{2} \frac{1}{(2\pi\sigma_j^2)^{1/2}} e^{-\frac{(m_j-\mu_j)^2}{2\sigma_j^2}} dm_j \tag{2.45}$$

has to be maximized. $M = (m_1, m_2)$ is the measured signal in the two scintillator layers, $\mu_j$ is the mean energy deposition in the $j$-th layer, and $\sigma_j^2$ is the variance of the energy deposition in the $j$-th layer. Quantities $\mu_j$ and $\sigma_j^2$ are functions of $A_1$ and $A_2$, the X-ray spectrum, and the detector response function, given in Equation 2.49. Equivalent to the probability maximization, the negative log-likelihood function of the probability density function $P(X, A_1, A_2)$ can be minimized. It is a sum of the negative log-likelihood functions within the two layers [RH09]:

$$\mathcal{L} = \sum_{j=1}^{2} \left[ \frac{1}{2} \ln \sigma_j^2 + \frac{(m_j - \mu_j)^2}{2\sigma_j^2} \right] + \ln(2\pi) \tag{2.46}$$

A measure of the amount of information contained in this experiment is given by the Fisher information matrix [Kay]. It is the expectation value of the negative Hessian of the log-likelihood function with respect to $A_1$ and $A_2$:

$$\mathcal{F}_{i,j}(A_1, A_2) = E\left[ -\frac{\partial^2 \mathcal{L}}{\partial A_i \partial A_j} \right]. \tag{2.47}$$

The Fisher information matrix can be calculated using the log-likelihood function from the spectral forward model Equation 2.13 [AM76; RH09]. The Fisher information matrix is given by [Kay; Cow98]

$$\mathcal{F}_{\alpha,\beta} = \sum_{j=1}^{2} \frac{1}{\sigma_j^2} \left( \frac{\partial \mu_j}{\partial A_\alpha} \right) \left( \frac{\partial \mu_j}{\partial A_\beta} \right) + \frac{1}{2} \sum_{j=1}^{2} \frac{1}{\sigma_j^4} \left( \frac{\partial \sigma_j^2}{\partial A_\alpha} \right) \left( \frac{\partial \sigma_j^2}{\partial A_\beta} \right). \tag{2.48}$$

It is worth mentioning that the terms with a second derivative disappear in the calculation of the matrix elements as a result of taking the expectation value. The inverse of the Fisher information matrix is called the Cramér-Rao information matrix. It is a lower bound for the variance of any unbiased estimator [Kay] and gives the lower limit for the variance that is propagated from the measurements into the estimates related to the Fisher information matrix. It can be used to determine the minimum variance of a maximum likelihood estimator for the spectral basis coefficients $A_1$ and $A_2$.

According to Equation 2.13 and the assumptions of Section 2.8, the mean energy deposition $\mu$ in the scintillator layers in dependence of the ZnSe front layer thickness $d_{\text{ZnSe}}$ is given by

$$\mu_{\text{Front}}(d_{\text{ZnSe}}) = C \int_0^\infty E \Phi(E) \left( 1 - e^{-d_{\text{ZnSe}} \mu_{\text{ZnSe}}(E)} \right) e^{-\sum_{\alpha=1}^{2} f_\alpha(E) A_\alpha} dE, \tag{2.49}$$

and

$$\mu_{\text{Rear}}(d_{\text{ZnSe}}) = C \int_0^\infty E \Phi(E) e^{-d_{\text{ZnSe}} \mu_{\text{ZnSe}}(E)} e^{-\sum_{\alpha=1}^{2} f_\alpha(E) A_\alpha} dE, \tag{2.50}$$

where $C$ is a constant representing the solid angle of the detector and the product of the anode current and the exposure time, $E$ is the energy of the incoming photon, $\Phi(E)$ is the X-ray spectrums' intensity, and $A_\alpha$ is the spectral basis coefficient line integral. The Cramer-Rao Lower Bound (CRLB) for the variance of an unbiased estimator is given by

$$\sigma_{A_i}^2 \geq \mathcal{F}_{i,i}^{-1} \tag{2.51}$$

where $\sigma_{A_i}^2$ is the variance of the estimated spectral basis coefficient's line integral for $A_i$ and $\left(\mathcal{F}^{-1}\right)_{i,i}$ is the diagonal element of the inverse of the Fisher information matrix [RH09]. For $\alpha = \beta$ this gives us

$$\mathcal{F}_{\alpha,\alpha} = \sum_{j=1}^{2} \frac{1}{\sigma_j^2} \left( \frac{\partial \mu_j}{\partial A_\alpha} \right)^2 + \frac{1}{2} \sum_{j=1}^{2} \frac{1}{\sigma_j^4} \left( \frac{\partial \sigma_j^2}{\partial A_\alpha} \right)^2. \tag{2.52}$$

The variance of the mean energy deposit in the $j$-th layer is given by [GB94; Swa73]

$$\sigma_{\text{Front}}^2(d_{\text{ZnSe}}) = C \int_0^\infty E^2 \Phi(E) \left( 1 - e^{-d_{\text{ZnSe}} \mu_{\text{ZnSe}}(E)} \right) e^{-\sum_{\alpha=1}^{2} f_\alpha(E) A_\alpha} dE, \tag{2.53}$$

and

$$\sigma_{\text{Rear}}^2(d_{\text{ZnSe}}) = C \int_0^\infty E^2 \Phi(E) e^{-d_{\text{ZnSe}} \mu_{\text{ZnSe}}(E)} e^{-\sum_{\alpha=1}^{2} f_\alpha(E) A_\alpha} dE. \tag{2.54}$$

The derivatives of the mean energy deposit and the variance of the mean energy deposit in relation to the spectral basis coefficients are given by

$$\begin{aligned}
\frac{\partial\mu_{Front}(d_{\text{ZnSe}})}{\partial A_\alpha} &= C\int_0^\infty E(-f_\alpha(E))\Phi(E)\left(1-e^{-d_{\text{ZnSe}}\mu_{\text{ZnSe}}(E)}\right)e^{-\sum_{\alpha=1}^2 f_\alpha(E)A_\alpha}dE\\
\frac{\partial\mu_{Rear}(d_{ZnSe})}{\partial A_\alpha} &= C\int_0^\infty E(-f_\alpha(E))\Phi(E)e^{-d_{\text{ZnSe}}\mu_{\text{ZnSe}}(E)}e^{-\sum_{\alpha=1}^2 f_\alpha(E)A_\alpha}dE\\
\frac{\partial\sigma^2_{\text{Front}}(d_{\text{ZnSe}})}{\partial A_\alpha} &= C\int_0^\infty E^2(-f_\alpha(E))\Phi(E)\left(1-e^{-d_{\text{ZnSe}}\mu_{\text{ZnSe}}(E)}\right)e^{-\sum_{\alpha=1}^2 f_\alpha(E)A_\alpha}dE\\
\frac{\partial\sigma^2_{\text{Rear}}(d_{\text{ZnSe}})}{\partial A_\alpha} &= C\int_0^\infty E^2(-f_\alpha(E))\Phi(E)e^{-d_{\text{ZnSe}}\mu_{\text{ZnSe}}(E)}e^{-\sum_{\alpha=1}^2 f_\alpha(E)A_\alpha}dE.
\end{aligned}$$

The effect of the front layer thickness can be visualized using an example with a 120 kVp tungsten spectrum filtered with a 3.5 mm thick Aluminum filter and a maximum photon flux of $2\cdot 10^{11}$ photons. The detector response function is assumed to be ideal for a ZnSe detector like given in Equation 2.42. The calcium-integrated density along the X-ray path is assumed to be 0.775 g/cm$^2$, and the water-integrated density is assumed to be 10 g/cm$^2$. The solid angle current time product is assumed $C = \Omega I_A T = 10^{-6}\cdot 0.2$ mAs. The optimal front layer thickness $d_{\text{ZnSe}} \approx 0.8$ mm is calculated by the CRLB for the variance of the spectral basis coefficients (see Figure 2.17).

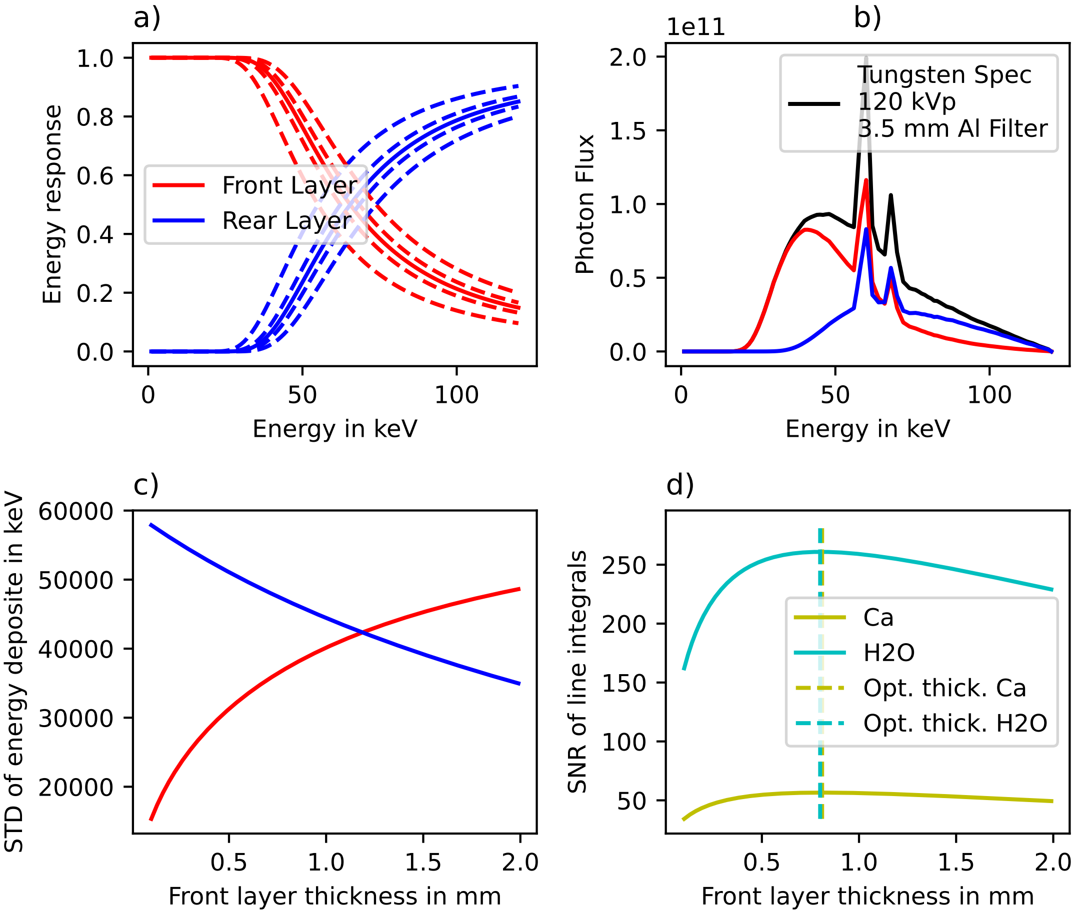

**Figure 2.17:** An example for the CRLB in DLCT with calcium-integrated density along the X-ray path being 0.775 g/cm$^2$ and the water-integrated density being 10 g/cm$^2$. Panel **a** shows the energy response function of an ideal Dual Layer (DL) detector for varying front layer thicknesses around 0.8 mm ZnSe. The rear layer is assumed to be 2.0 mm thick $Gd_2O_2S$ (GOS) [She+13]. The solid red and blue lines are the detector response functions for the front and rear layers, respectively. The dashed black lines are the detector response functions using different front layer thicknesses of 0.5, 0.7, 0.8, 0.9, and 1.1 mm. Panel **b** is the corresponding photon flux from a 120 kVp tungsten spectrum filtered with a 3.5 mm thick Aluminum filter. It also visualizes how many photons are detected in the front and rear layers. Panel **c** shows the Standard Deviation (STD) of energy deposited in the front and rear layer for varying front layer thicknesses ranging from 0.1 to 2.0 mm ZnSe. In panel **d**, the SNR of the spectral basis coefficients $A_{\mathrm{Ca}}$ and $A_{\mathrm{H_2O}}$ using the estimation from the CRLB is plotted in dependence of the front layer thickness. The optimal front layer thickness (Opt. thick.) is defined as the front layer thickness, where the SNR is maximal. The optimal front layer thickness is 0.81 and 0.80 mm ZnSe for Calcium and water, respectively.

"The similar behavior of the SNR in the two basis images as a function of $d_{\mathrm{ZnSe}}$ can be explained by the fact that the strongest dependence of the noise [...] results from the determinant of the Fischer information matrix, which affects noise in both basis images in the same way" [RH09].

To estimate the optimal front layer thickness in a clinical DLCT, the CRLB for varying integrated material densities has to be considered. Not only the acquisition angle is crucial, but also patient geometries and the X-ray spectrum. As the front layer thickness is a fixed quantity in a DLCT setup, the optimal front layer thickness should be chosen for the most common patient geometries.

# Cardiac perfusion

# 3

This chapter focuses on spectral dynamic myocardial perfusion imaging. First, the underlying physiological background and existing imaging methods are explained. The gamma variate fitting routine is introduced and compared to a tracer kinetic model. A dynamic heart phantom is presented, which was used to validate the spectral dynamic myocardial perfusion protocol of the DLCT system. The results presented in Section 3.3 about the dynamic heart phantom are published in “Absolute iodine concentration for dynamic perfusion imaging of the myocardium: improved detection of poststenotic ischaemic in a 3D-printed dynamic heart phantom“ [Ham+22]. Furthermore, the gamma variate fitting routine is used in Section 3.4 to quantify iodine density maps in a porcine model, which is based on results published in “Dynamic Quantitative Iodine Myocardial Perfusion Imaging with Dual-Layer CT using a Porcine Model“ [Sch+19].

Some paragraphs and figures can appear similar or identical to the publications of the author. Compared to the original publication, the text has been slightly modified to achieve a better integration into this doctoral thesis.

The last section describes the browser-based IntelliSpace Discovery perfusion plugin for a simple integration of a perfusion analysis into the clinical workflow.

## 3.1 Spectral dynamic myocardial CT perfusion

### 3.1.1 Myocardial ischemia and cardiac imaging

Heart failure is a global health burden and is one of the leading causes of death worldwide. In 2015, approximately 15.9 million myocardial infarctions occurred worldwide [Moz+15]. Ischemic heart disease is the most common cause of death (7.249 million deaths worldwide in 2008), accounting for 12.7% of the total global mortality [FAF13]. Myocardial ischemia is also responsible for angina, unstable angina, cardiac arrhythmias, heart failure and is caused by conditions such as Coronary Artery Disease (CAD) or hypertrophic cardiomyopathy [Dew+20]. Along with major advances in cardiovascular science and medicine, a steady decline in deaths from cardiovascular disease has been observed in relation to scientific advances [NB12; LT05]. Cardiac imaging plays a central role in preventing, diagnosing, and treating myocardial ischemia. The aim is to obtain both anatomical and functional information about myocardial blood flow non-invasively. Anatomical visualization of CAD can be provided by CCTA, which has a high diagnostic accuracy for CAD detection in patients with low or moderate pretest probability. However, in patients with positive findings and higher pretest probability, it lacks specificity [Hub+13]. As a result, the number of invasive coronary angiography and revascularization procedures is considered to be higher than necessary [Bit+16; Joe+17]. In 2019, the European Society of Cardiology renewed its key recommendations for basic testing, diagnostics, and risk assessment. CCTA is recommended as the initial test for diagnosing CAD in symptomatic patients in whom obstructive CAD cannot be excluded by clinical assessment alone.

Functional imaging for myocardial ischemia is recommended when CCTA has shown

CAD of uncertain functional significance or is of no diagnostic value [Knu+20]. There are two X-ray-based methods for functional testing: invasive coronary angiography, optionally in combination with fractional flow reserve measurement and cardiac dynamic perfusion with CT. In stable CAD, focusing on medical therapy and lifestyle changes is key, and the ISCHEMIA trial [Mar+20] supports this by showing that invasive coronary angiography may not be helpful. On the other hand, invasive angiography remains an important option for treating unstable CAD by allowing doctors to perform immediate revascularization. A variety of non-invasive cardiac imaging modalities differ in the degree to which they provide anatomical, functional and information beneficial for therapy in assessing myocardial perfusion and coronary microcirculation. Common to all imaging modalities is the need for a tracer or contrast agent. In the case of myocardial ischemia, less or delayed contrast is measured. The conventional method for diagnosing functionally relevant myocardial ischemia is Single-Photon Emission Computed Tomography (SPECT). It has been used for decades and is widely available in clinical practice [Dew+20]. However, rest/stress SPECT imaging suffers from low temporal and spatial resolution [Dew+20; Ago+16]. Together with Positron Emission Tomography (PET), these techniques are the reference standard for quantitative myocardial perfusion imaging. Although SPECT and especially PET suffer from low spatial resolution, they provide high functional information on quantitative myocardial perfusion. Ultrasound is used for bedside diagnosis of cardiac ischemia, whereas Cardiac Magnetic Resonance (CMR) is reserved for more complex patients [Dew+20]. Two CT perfusion approaches are defined in the literature. Static Computed Tomography Perfusion (CTP), which allows the calculation of several qualitative, semi-quantitative parameters by using only a single shot during peak myocardial contrast enhancement. Whereas dynamic CTP acquires a “CT-movie” at several time points. For a comprehensive, more detailed overview of myocardial perfusion imaging methods, refer to the consensus statement on “clinical quantitative cardiac imaging for the assessment of myocardial ischemia” [Dew+20]. While perfusion CMR is a well-established technique for the detection of myocardial ischemia without radiation exposure for patients, CTP offers several advantages compared to CMR. First, a CMR examination of the myocardium takes 45 to 60 minutes, whereas CT of the heart, including calcium scoring, CCTA, and dynamic CTP analysis can be performed within 10 minutes. Especially in an emergency setting, this is of special importance. Short scan time in CT also helps to avoid movement artifacts. In static CTP, optimal contrast between healthy, underperfused, and infarcted myocardial tissue is achieved and then visualizes hypoattenuation of the myocardium. To ensure correct timing, a test bolus has to be tracked and the enrichment within the aorta determined [Vli+12]. The major advantage of static CTP is that myocardial blood flow can be rapidly assessed and the underlying radiation dose is comparatively low. Using rest/stress protocols, especially in combination with CCTA, a good assessment of suspected CAD has been reported [Yan+15; Ko+12]. However, static CTP only provides a semi-qualitative analysis while also being highly susceptible to temporal perfusion artifacts and thereby heavily reliant on the correct timing.

### 3.1.2 Dynamic myocardial CT perfusion

The main advantage of CT is the high spatial resolution, which offers the possibility of anatomical diagnosis like coronary stenosis. In combination with a dynamic CTP acquisition, it can offer a combined assessment of stenosis and functional parameters [Nou+22; Var+15]. Considering the relatively small thickness of the myocardium, high resolution has a high potential to improve the detection of even small regions of subendocardial ischemia. Multiple studies showed evidence that myocardial perfusion imaging can significantly increase the accuracy of assessing flow limiting CAD or areas of prior infarction [Bla+09; Hul+12; Geo+09]. In dynamic CTP, a set of subsequent CT scans within a 20 to 40 seconds timeframe quantifies the myocardial perfusion using iodine CA. Imaging the complete first pass of contrast agent through the heart is necessary [Car+16]. The temporal sampling frequency is dependent on the CT scanner‘s rotation time. Furthermore, a fast rotation time is crucial to acquire images without motion artifacts. Current CT systems can scan patients without motion artifacts when the heart rate does not exceed 90 Beats Per Minute (BMP) [Nou+22]. Myocardial ischemia is diagnosed if one measures less or delayed contrast agent over time in the Time Attenuation Curve (TAC).

Non-spectral CT scanners allow for quantitative analysis of hemodynamics by utilizing Tracer Kinetic Modeling (TKM) (see Subsection 3.2.2). The underlying HU-based assessment is susceptible to beam-hardening effects induced by the iodine contrast agent [Buc+16]. Further physiological models must be considered that relate HU to the actual blood or iodine flow [Bin+14]. Myocardial CT perfusion suffers from relatively high patient dose, low SNR, high CA volume and is thus not used frequently [Dew+20]. Combining dynamic myocardial CTP with spectral CT techniques would allow addressing some of those current limitations. Successful beam hardening correction has already been addressed in Stenner et al. [Ste+10] and Levi et al. [Lev+19]. Dual source DECT provides high temporal resolution but increases cross scatter and reduces the SNR [Pat+20]. However, there is still potential to increase the SNR, reduce dose, or improve quantitative iodine determination. Even more, PCCT with the potential for high spatial, temporal, and spectral resolution could allow for both quantitative iodine concentration values for myocardial perfusion and high spatial resolution for visualization of coronary arteries.

Huber et al. [Hub+13] showed that evaluating dynamic CTP stress perfusion images of the myocardium provides high diagnostic accuracy compared with invasive coronary angiography and fractional flow reserve measurement. DECT showed a higher reproducibility of dynamic myocardial perfusion measurements in comparison to a HU-based evaluation [So+12]. Further, Sánchez-Gracián et al. [Sán+16] demonstrated that iodine quantification in myocardial perfusion stress DECT benefits the differentiation of healthy and ischemic or necrotic myocardium. Fahmi et al. [Fah+16] reported on quantitative myocardial perfusion images and thereby demonstrated a superior assessment of myocardial infarcts compared to a conventional measurement. Sellerer et al. [Sel+18] showed an improved Root Mean Square Deviation (RMSD) of observed iodine concentrations (with respect to true values) for different measurement configurations using a modern clinical DLCT system.

Spectral or dual-energy CT with iodine density maps offers higher CNR and signal enhancement regarding contrast agent sensitivity for cardiac dynamic perfusion imaging [Sch+19], thereby opening up new perspectives for a reduction of radiation dose and volume of injected contrast agent. Especially in regions with low contrast accumulation like the myocardium, improved quantification of the iodine density down to 0.5 mg/ml plays a crucial role [Ehn+18; Sel+18].

The detector coverage of most DECT systems in spectral mode is not sufficient to cover the whole myocardium during perfusion measurements within one shot, making it inapplicable for patient perfusion measurements at the time of today. Nevertheless, systems are available with a high detector coverage of up to 16 cm that can run in sequential dual-energy mode, acquiring spectral information in two consecutive heartbeats. The image-based material decomposition in sequential mode is prone to movement artifacts, which leads to biases in the iodine density images. Also, because of the electrocardiographic triggering in dual-energy mode, there would be a halving of the number of available time points for the dynamic CTP. For more information on myocardial CTP, we refer to "Society of cardiovascular computed tomography expert consensus document" by Patel et al. [Pat+20].

## 3.2 Models for perfusion quantification

There exist various tracer kinetic models for dynamic myocardial CTP and also CMR perfusion [Pel+16]. For example, different compartments like a 2-compartment model can be applied to model fluid exchange between vessels and Extravascular Extracellular Space (EES). However, models are prone to systematic errors and must be validated, e.g. the Arterial Input Function (AIF) can deviate strongly due to collateral myocardial blood flow [Pel+16]. In contrast to that, the Gamma Variate Fit (GVF) model exists. It simply describes the function to fit the TAC. In the content of this thesis, it was applied to absolute iodine densities and HU. In the following chapters, perfusion data of the cardiac phantom introduced in Section 3.3, were used.

### 3.2.1 Gamma variate fitting using absolute iodine densities

The idea of gamma variate fitting to a dynamic perfusion curve was first proposed in 1959 [Eva59; Tho+64] as a graphical representation that bears a remarkable resemblance to indicator-dilution curves without recirculation. It can be derived from a simple convective dispersion model of blood flow [HL84] and is mostly used in dynamic Magnetic Resonance Imaging (MRI) [Ben+97]. The basic form of the function takes four parameters $A$, $t_0$, $\alpha$ and $\beta$ and has the following form:

$$y(t) = \left\{ \begin{array}{ll} A \cdot (t - t_0)^{\alpha} \cdot e^{\frac{-(t-t_0)}{\beta}}, & \text{if } t > t_0. \\ 0, & \text{if } t \leq t_0. \end{array} \right\} \tag{3.1}$$

Before curve fitting, the measured signal-time curve must be converted to a CA concentration curve, which can be more challenging in MRI perfusion imaging. Spectral CT allows the direct measurement of CA concentration curves in mg/ml iodine density, leading to quantitative parameters derived from a GVF. CA Maximum Perfusion (MP) is thereby defined as the maximal uptake of CA in tissue and can be measured in mg/ml/s.

Additionally, there are several other parameters used for quantitative perfusion imaging, namely the Time To Peak (TTP), Peak Enhancement (PE), and the total iodinated Blood Volume (BV). TTP indicates the point in time when maximal peak enhancement is reached in seconds, PE the maximal increase in iodine density in mg/ml, and iodinated BV is related to uptake/storing/flush out behavior within the respective structures as the time integral over the GVF. Additional information like AIF for a baseline time course of the CA can be implemented.

Although the GVF is the appropriate choice to model TAC curves very correctly, the fit parameters can have interdependent influences. For example, altering the parameters $\alpha$ and $\beta$ not only affects the rise and fall times of the function but also changes the location and magnitude of the function maximum [Mad92]. This mathematical undesired property can lead to an unstable fitting process. To visually compare the influence of fit parameters on the function, see Figure 3.1. The covariance of the fitting parameters can be estimated,

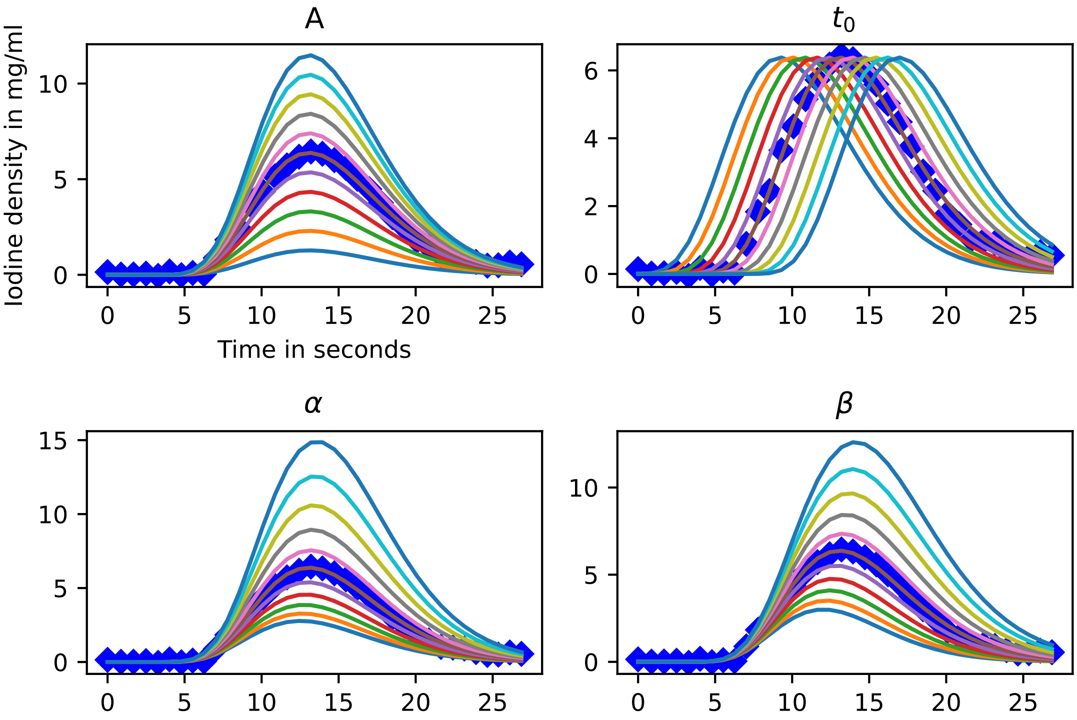

**Figure 3.1:** The influence of fit parameters on the gamma variate function. The parameters $A$, $t_0$, $\alpha$ and $\beta$ are altered by a percentage variation of 80, 150, 5 and 10% from the middle line, respectively. The blue diamonds are measurement results from the phantom model introduced in Section 3.3. Except from $t_0$, all function parameters alter the maximum value of the fit. All x labels show the time in seconds.

leading to the matrix $\overleftrightarrow{p_{\text{cov}}}$ for $A$, $t_0$, $\alpha$ and $\beta$.

$$\overleftrightarrow{p_{\text{cov}}} = \begin{bmatrix} 0. & 0. & 0. & 0. \\ 0. & 0.68 & -0.9 & 0.11 \\ 0. & -0.9 & 1.22 & -0.15 \\ 0. & 0.11 & -0.15 & 0.02 \end{bmatrix}. \tag{3.2}$$

The diagonals provide the variance of the parameter estimate. To compute one standard deviation error on the parameters

$$\overrightarrow{p_{\text{err}}} = \sqrt{diag(\overleftrightarrow{p_{\text{cov}}})} \tag{3.3}$$

can be used. Noise contributions to the TAC alter the fit parameters, but especially the errors on the parameters $\overrightarrow{p_{\text{err}}}$. This can be observed in Figure 3.2. The maximum deviation from the mean value within all fit parameters calculates to 414, 65, 36, and 19% for $A$, $t_0$, $\alpha$ and $\beta$. These deviations appear extremely high, especially under the premise of only minor noise in TAC. What is actually of relevance is the deviation of physical parameters introduced from these largly varying fit parameters. Despite the highly varying

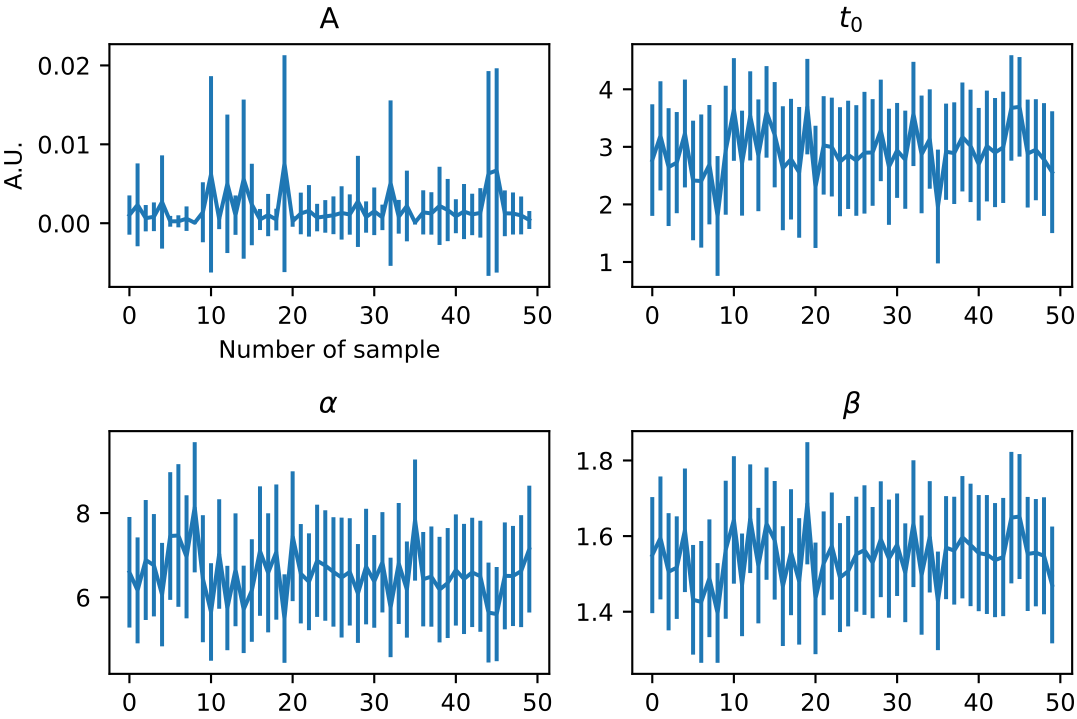

**Figure 3.2:** The evolution of fit parameters with 50 times Gaussian noise of 0.1 mg/ml added to a TAC measured from a phantom model (see Section 3.3). All 50 samples with Gaussian noise using a Standard Deviation (SD) of 0.1 mg/ml are plotted on the x-axis. The y-axis displays the value of the fit parameters and corresponding error estimations in Arbitrary Units (AU).

fit parameters and errors in those, the trend of the fitted curve looks very similar in all samples. The resulting deviation of physical parameters estimated from the fit stays below 10% for all parameters with $A$, $t_0$, $\alpha$ and $\beta$ being 9.9, 2.3, 1.7 and 2.7% (see Figure 3.5). The impact of image noise in TAC on the estimation of dynamic or functional parameters appears to be in an acceptable range. As outlined in Equation 3.2, the covariance between the fit parameters is not zero. Especially, $t_0$ and $\alpha$ show a highly anticorrelated behavior. This can be further visualized by plotting $t_0$ and $\alpha$ in a scatter plot with 50 noise simulated TAC, all with a SD of 0.1 mg/ml in Figure 3.3. The consequence of this mathematical property of the GVF can be an unstable fitting result, leading to strongly varying fit parameters. This can be visualized using the loss function of the fit (Figure 3.4).

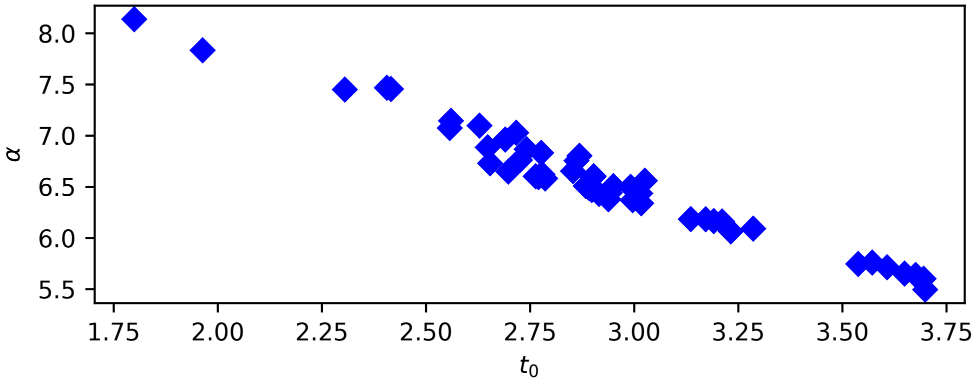

**Figure 3.3:** The fit parameters $t_0$ and $\alpha$ showing anticorrelated behaviour, for TAC with gaussian noise of SD 0.1 mg/ml.

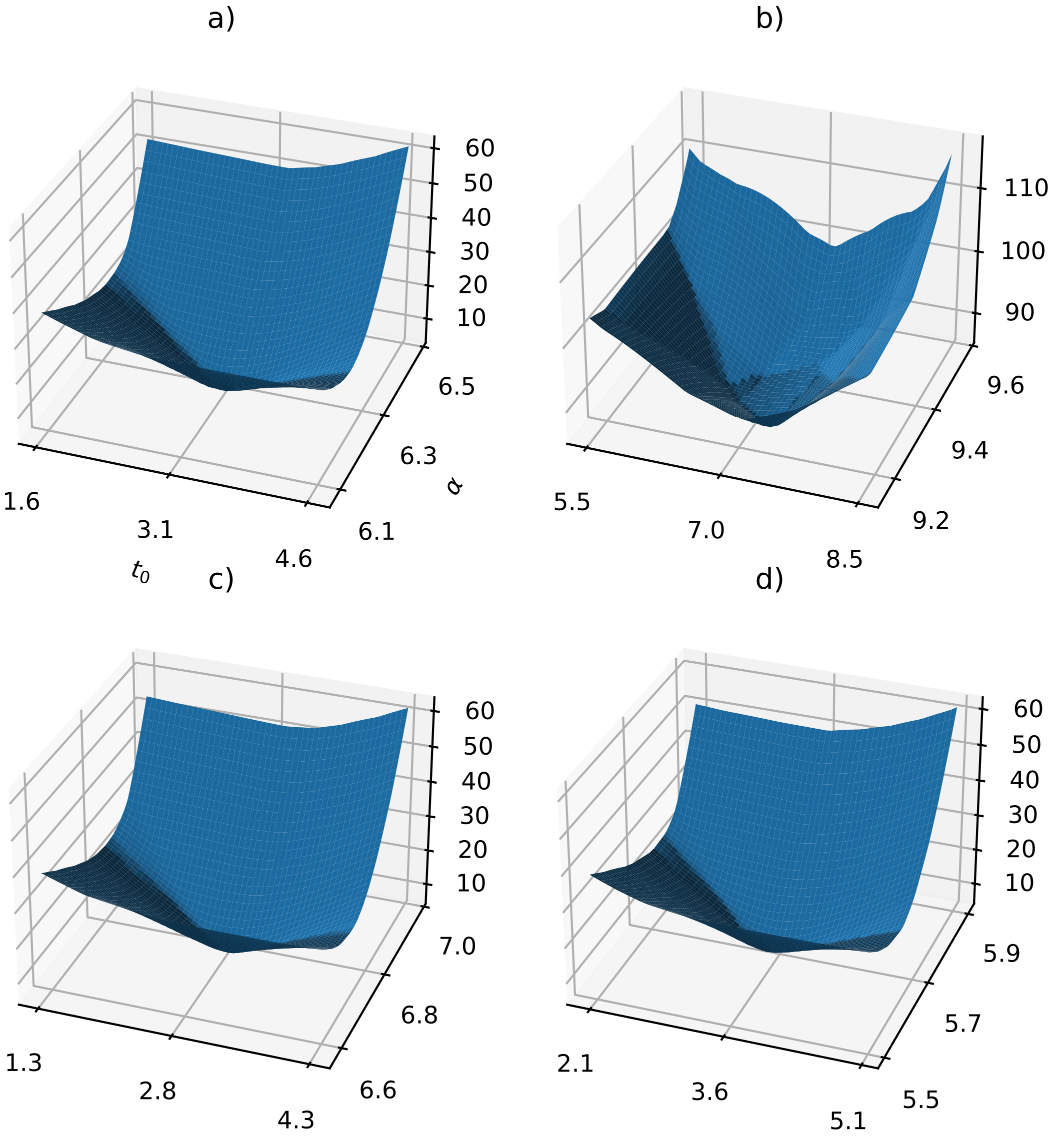

**Figure 3.4:** A plot of the loss function in dependence of varying parameters $t_0$ and $\alpha$ using four curves with varying Gaussian noise contribution. In subfigure **a**, the original loss function without any Gaussian noise added is plotted. In **b**, Gaussian noise with a high SD of 3.0 mg/ml is added. A flattened plateau with a minimum loss can be observed. Minimum noise with SD of 0.1 mg/ml is added in **c** and **d**. It can be observed that the minima shift drastically, although only small noise contributions were introduced.

The minimum loss values in Figure 3.4 **a**, **b**, **c** and **d** account for 3.8, 87, 5.3 and 5.3 mg/ml. As already discussed, these major variations in fit parameters have a minor influence on determining the physical parameters derived from the fitting curve. This can be visualized in the evolution of physical parameters under Gaussian noise in Figure 3.5.

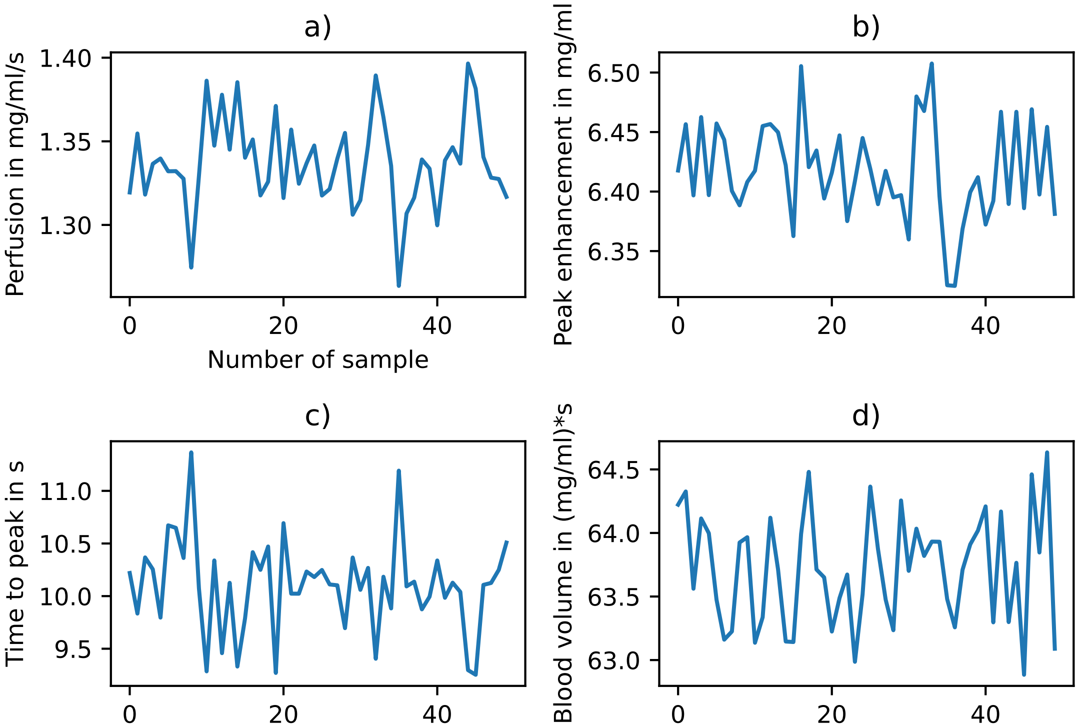

**Figure 3.5:** The evolution of physical parameters MP, PE, TTP and the total iodinated BV in **a** to **d** with Gaussian noise of SD 0.1 mg/ml applied 50 times to the original TAC.

A simplified fitting routine for the GVF model was derived by Madsen et al. [Mad92] and validated with Monte Carlo simulated perfusion curves from 20 glioma patients [CN04]. The simplified fitting routine was tested on phantom data from Section 3.3 and compared to the original fitting routine. Without the estimation of physical parameters, the fitting routine for two fit parameters was found to be approximately three times faster than the original fitting routine. The number of function calls for numerical Jacobian approximation was reduced from 50 to 6 times. The deviations of the physical parameters MP, PE, TTP and the total iodinated BV calculated from the fit results were found to be 10, 0, 1 and 17%, respectively. The Root Mean Square Error (RMSE) of the fit from the original TAC was found to be 0.77 mg/ml being 12% of the PE using the simplified fit routine. An increased fit accuracy was achieved using the full GVF model with a RMSE of 0.14 mg/ml or 2.2% of the PE. It can be concluded that the use of the simplified GVF fitting routine is an appropriate choice, especially if the perfusion data has a high resolution with a big number of TAC needed to be fit or a fast generation of perfusion maps is crucial for the clinical application.

### 3.2.2 Tracer kinetic modeling

The principle of TKM is the fitting of TAC measured in tissue, which is assumed to be proportional to the injected dose. Each individual voxel comprises the flooding, deflooding, and potentially the recirculation of CA schematically shown in Figure 3.6. Additionally, the TAC of the AIF is sampled as a measure of the injected CA dose and, therefore, the inflow into the so-called compartment. The time-dependent measured CA concentration in tissue $c_{\mathrm{t}}(t)$ is then modeled via the equation

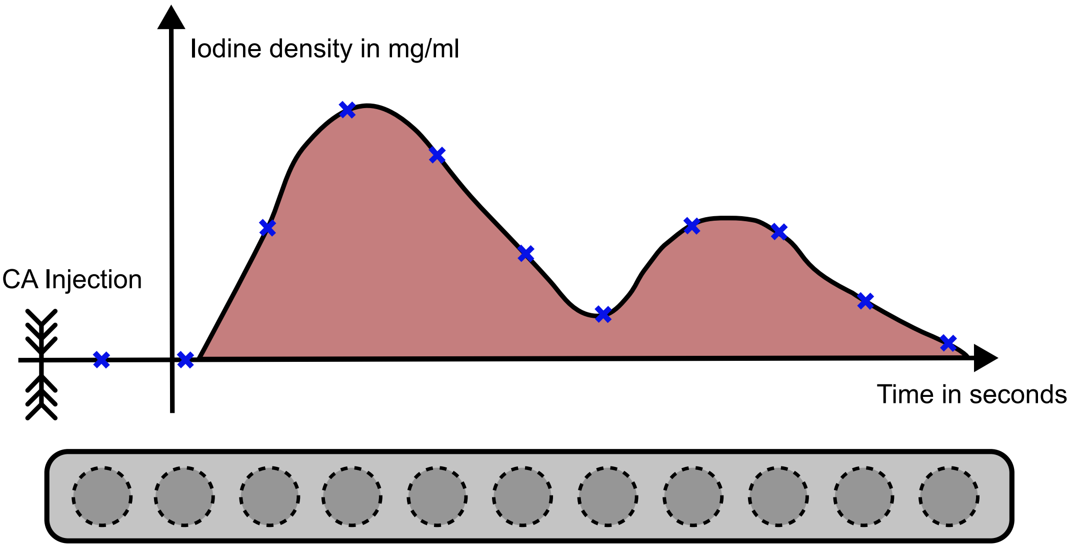

**Figure 3.6:** Schematic of a dynamic perfusion measurement in CT imaging. After the injection of CA the temporal progression of CA flooding, deflooding, and recirculation is sampled. For this, an ECG triggered axial scan of the ROI is performed. The gray circles at the bottom of the schematic and the blue crosses on the TAC visualize the scanning timepoints of the dynamic perfusion protocol.

$$c_{\mathrm{t}}(t) = F_{\mathrm{P}} \cdot R(t) * c_{\mathrm{a}}(t) \tag{3.4}$$

where $F_{\mathrm{P}}$, $R(t)$ and $c_{\mathrm{a}}(t)$ are the plasma flow constant, tissue characteristic residue function, and the measured supplied concentration (AIF), respectively. A schematic of a two-compartment model with the exchange of CA between EES and intravascular space can be seen in Figure 3.7. Detailed information about TKM can be found in “Tracer-kinetic modeling of dynamic contrast-enhanced MRI and CT: A primer” [IS13]. The most simple and very generic model to represent the tissue characteristic residue function $R(t)$ is an exponential function decaying with time

$$R(t) = \exp(-\lambda \cdot t), \tag{3.5}$$

derived from the differential equation for blood flow

$$v\frac{dc_{\mathrm{t}}(t)}{dt} = Fc_{\mathrm{a}}(t) - Fc_{\mathrm{t}}(t), \tag{3.6}$$

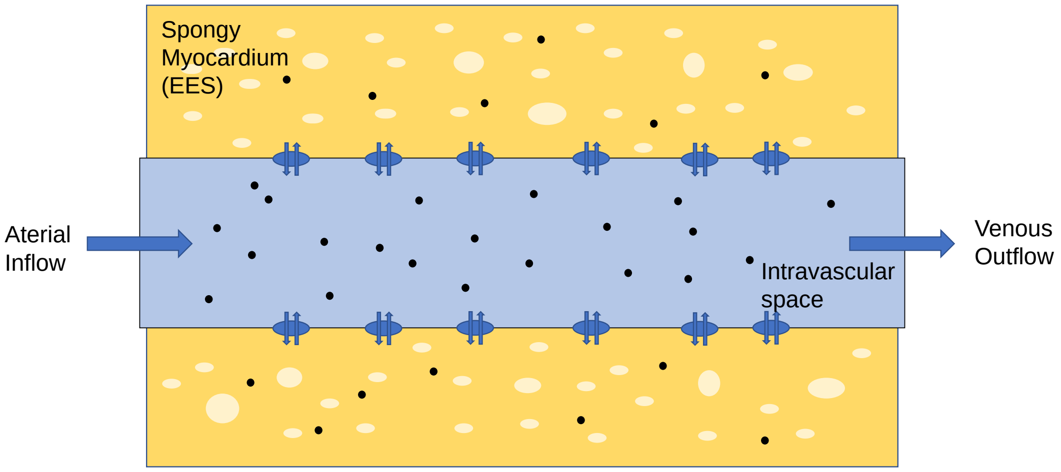

**Figure 3.7:** The sketch shows the perfusion flow within the intravascular space and the permeability-surface exchange to EES. Black dots show the distribution of contrast agent molecules. Important perfusion parameters can be tuned using this model. The proportion of plasma volume and EES, as well as the permeability, plays an important role.

with $F$ denoting the flow that transports the contrast agent into and out of the compartment with volume $v$. An example of a AIF and the impact of the fit parameter $\lambda$ and resulting Mean Transit Time (MTT), being the inverse of $\lambda$ [IS13] can be seen in Figure 3.8. The AIF values are taken from the dynamic heart phantom described in Section 3.3. No exchange between EES and tissue is modeled. The uptake of CA is simply directly proportional to the contrast concentration at inflow, and the deflooding is modeled by the contrast concentration within the tissue using the same flow transport constant. This simplified model of the blood flow is suitable in situations where exchange to EES is precluded or negligible within the time interval of flooding and deflooding of the tissue. A third option would be a fast exchange, where the total volume $v$ would be the union of EES and tissue volume. Three physical parameters can be derived for the one-compartment model: the flow $F$, volume $v$, and the corresponding MTT. The simple model assumptions lead to only two free fitting parameters, making the model-fitting process very stable and fast. The utilization of more complex models with up to four parameters can lead to more accurate fits of TAC with the downside of potential overfitting and determination of parameters, which can not be reliably measured within the precision of the experiment [IS13]. The variation of fit parameters under the addition of noise for a simple one-compartment model can be seen in Figure 3.9. The loss function of the fit is visualized, giving an idea about the fit stability around the minimal point.

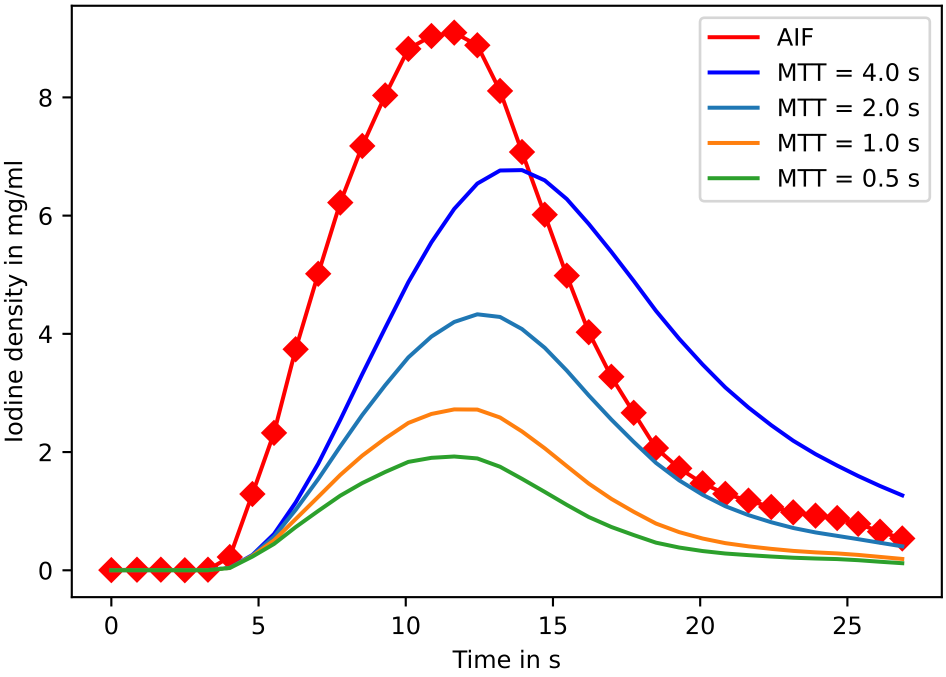

**Figure 3.8:** The AIF is shown as a red line with red diamonds. Different $\lambda$ values are plotted using a constant $F_{\mathrm{P}}$ value. A peak shift in the y and x direction can be observed. Also, the deflooding is delayed with decreasing $\lambda$ values, leading to an increase in MTT values. $\lambda$ values of 0.25, 0.5, 1.0, and 2.0 respectively MTT of 4.0, 2.0, 1.0, and 0.5 seconds are plotted.

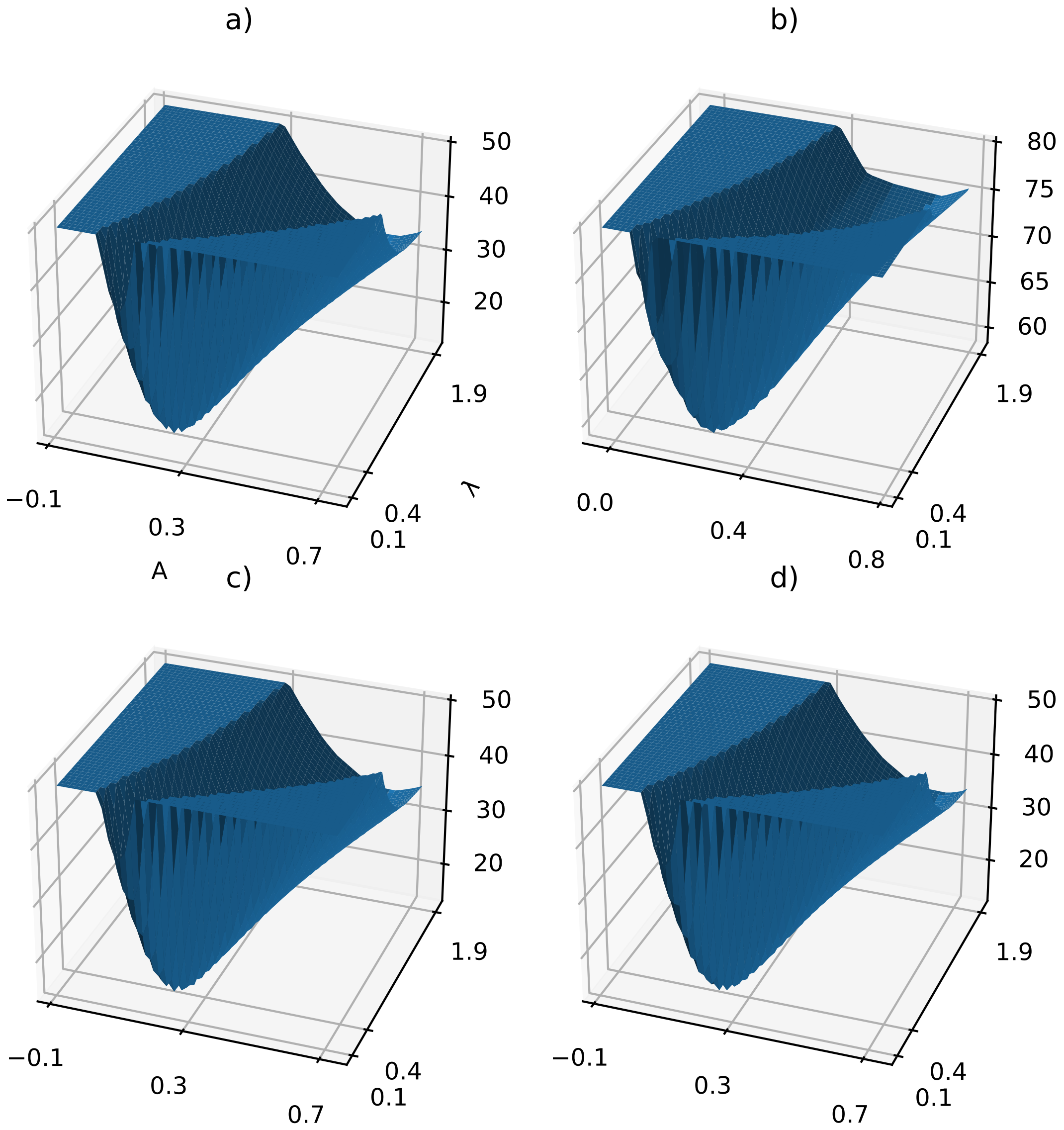

**Figure 3.9:** A plot of the loss function in dependence of varying parameters $F$ and $\lambda$ using four curves with varying Gaussian noise contribution. The loss values are clipped at 50 or 80 mg/ml to visualize the minimum. In subfigure **a**, the original loss function without any Gaussian noise added is plotted. In **b**, Gaussian noise with a high SD of 2.0 mg/ml is added. Minimum noise with SD of 0.1 mg/ml is added in **c** and **d**. With the addition of Gaussian noise, the minima do shift only by a small fraction. Further, the shape of the loss function is very similar from **a** to **d**, only with a slightly shifted minimum value.

The equivalent plot for the GVF model is shown in Figure 3.4. Like in Figure 3.2, Gaussian noise with a SD of 0.1 mg/ml was applied 50 times and the maximum deviation from the mean value calculates to 6.04, 6.98 % for $F$ and $\lambda$. In comparison to the high percentage deviations in fit parameters previously observed in the GVF model, the parameter deviations in one compartment model are negligibly small. The correlation between both fit parameters is positive, with a Pearson correlation coefficient of 0.921. As a visual comparison between the TKM and GVF model, the fit of the TAC of a single voxel is plotted in Figure 3.10. Both models perform very well, with a RMSD of 0.17 and 0.37 mg/ml for GVF and TKM, respectively. This accounts for 2.6 and 5.7 % of the peak enhancement value of 6.4 mg/ml. The GVF model is slightly better in fitting the peak enhancement and the tail of the TAC. The accuracy of the perfusion maps, especially the TTP, and MTT will be evaluated in Section 3.3.

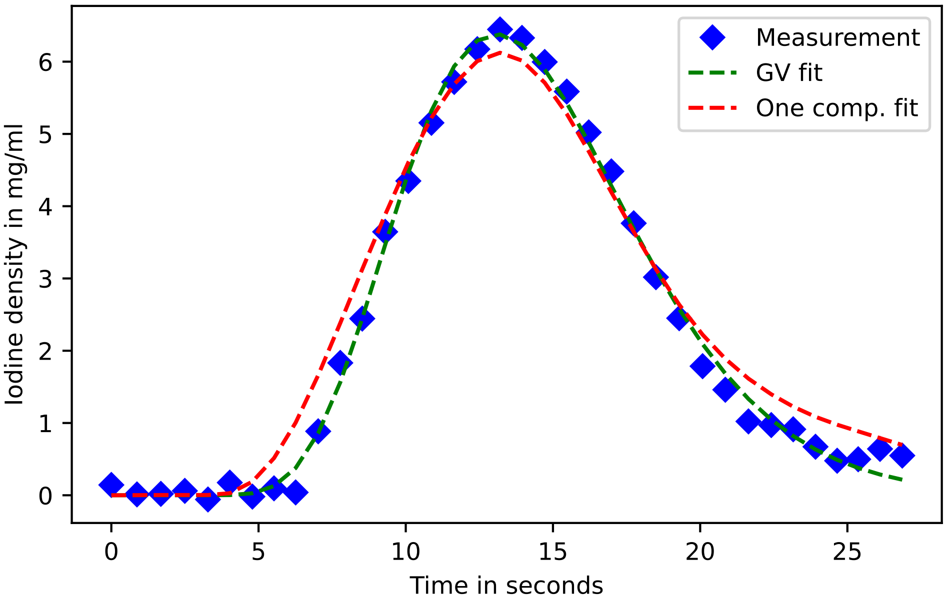

**Figure 3.10:** Perfomance TKM and GVF model for the fitting of a TAC in a single voxel. The blue diamonds are the measurement results from the phantom model in Section 3.3. The GVF is plotted in green and the TKM result in red. The RMSD are very small in comparison to the peak enhancement value of approximately 6.4 mg/ml being 0.17 and 0.37 mg/ml for GVF and TKM.

## 3.3 Dynamic perfusion in a 3D-printed heart phantom

Large parts of this section were published in Hammel et al. ”Absolute iodine concentration for dynamic perfusion imaging of the myocardium: improved detection of poststenotic ischaemic in a 3D-printed dynamic heart phantom” [Ham+22].
In this proof of principle study, we use spectral data acquired by a dual-energy CT system for cardiac dynamic perfusion, examining a dynamic 3D-printed heart phantom with simulated stenosis to utilize the increased CNR of dual-energy CT for the assessment of functional parameters.

**Background**: To investigate the detection capabilities of myocardial perfusion defects of dual-energy computed tomography technology using time-resolved iodine-based maps for functional assessment of coronary stenosis in a dynamic heart phantom.
**Methods**: An anatomical heart model was designed using a 3D printing technique. The lumen of the right coronary artery was reduced to 25% of the original areal cross-section. Scans were acquired with a 64-slice dual-layer CT equipment using a perfusion protocol with 36 time points. For distinguishing hemodynamically affected from unaffected myocardial regions, conventional and spectral MTT parameter maps were compared. A dose reduction technique was simulated by using a subset of time points of the TAC.
**Results**: The tracer kinetic modeling showed decreased errors on fit parameters from conventional to spectral TAC (42% reduction for A and 40% for $\lambda$). Three characteristic regions (highly, moderately, and not affected by the simulated stenosis) can be distinguished in all spectral perfusion maps. The best distinction was observed on MTT maps. An Area Under the Curve (AUC) value of 1.00 for the voxel-wise differentiation of hemodynamically affected tissue was achieved, versus a 0.89 AUC for conventional MTT maps. By temporal under-sampling, a dose reduction of approximately 78% from 19 to 4.3 mSv was achieved with a 0.96 AUC for spectral data.
**Conclusion**: Dual-energy CT can provide time-resolved iodine density data, which enables the calculation of absolute quantitative perfusion maps with decreased fitting errors, improving the accuracy for poststenotic myocardial ischemic detection in a 3D-printed heart phantom.

### 3.3.1 Methods

#### Phantom design

The heart model was used to simulate the flow circulation in a human heart. The study topic could, in principle, be investigated in a small sponge-filled cavity with two inflows and an outflow. In this simpler form, the model would be better controllable. Nevertheless, a heart model was used to get closer to a clinically relevant situation, where further parameters, like the AIF or cavity volume, correspond more precisely to real dynamic perfusion measurements in cardiac imaging. To model the circulation dynamics within the ventricles and the heart muscle, significant simplifications were made regarding the human circulatory system. Since in our designed study, only hemodynamic processes of the heart were tested, all processes before the blood inflow through the superior and inferior vena cava and after the blood outflow from the aortic arch were neglected. The blood inflow into the cardiac system was simulated by an inflow of water with variable flow velocity. The sink was modeled by two tubes exiting the left ventricle and the myocardium. The pulmonary circulation was simulated by two tubes with appropriate flow resistance. Furthermore, a sponge-like 3D-printed structure was located in the left ventricle's heart muscle to mimic the contrast medium perfusion in the myocardium. A schematic view of the flow through the 3D-printed heart phantom is visualized in Figure 3.11.

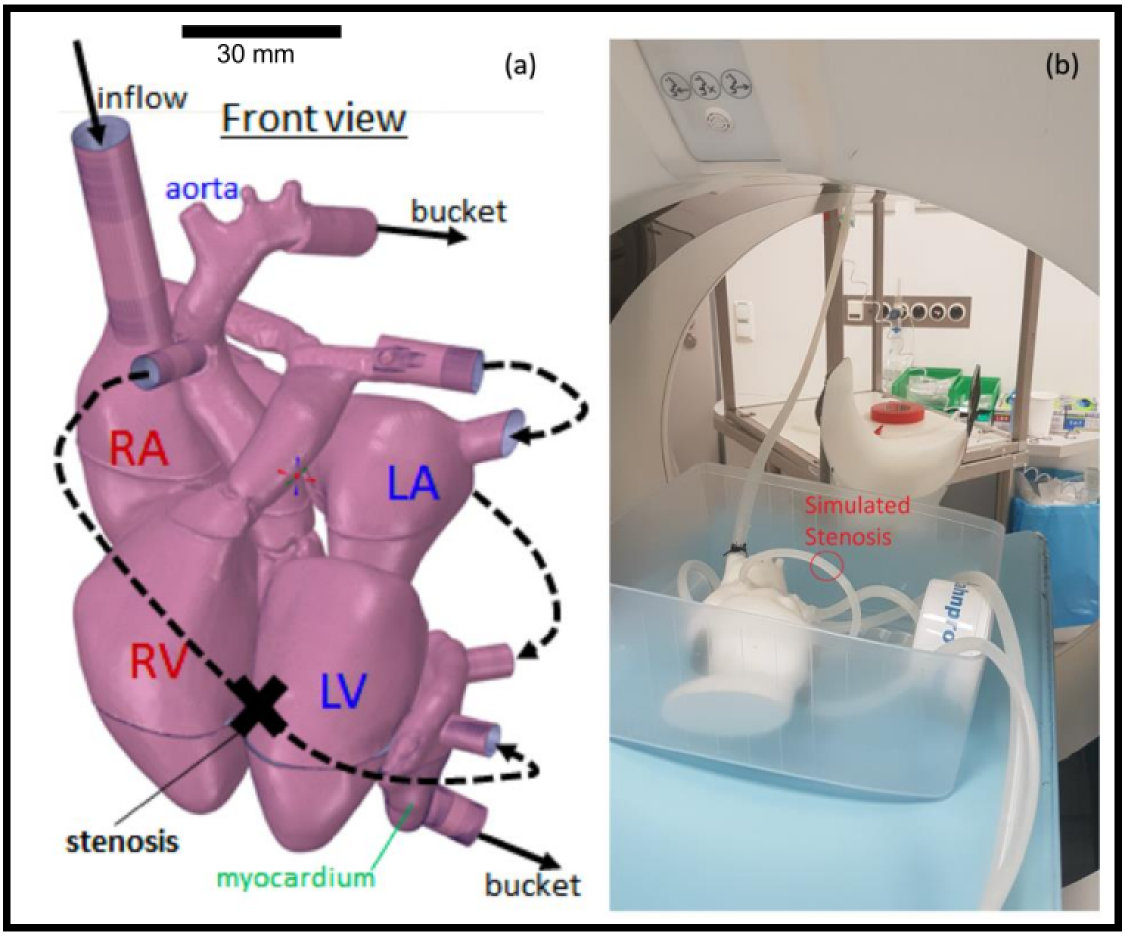

**Figure 3.11: a** Inflow, outflow (bucket) and connecting arrows indicate the location of the connecting tubes. Right Atrium (RA), Right Ventricle (RV), Left Atrium (LA) and Left Ventricle (LV). **b** A picture of the heart model within the gantry of the spectral CT system. During the performance of the dynamic scan, the container is filled with water.

Perfusion of water and contrast agent mixture is only possible in the material-free part of this structure (active myocardial area), which is in the following also called myocardium-like tissue. A photographic view and a volume-rendered picture of the phantom anatomy and the "myocardium-like" tissue are shown in Figure 3.12. In this 3D model, no exchange between compartments is considered, and only a reduction of flow velocity through myocardium-like tissue is simulated, which can be motivated by a negligible permeability-surface exchange in comparison to the blood flow within the vessels [Eck+18].

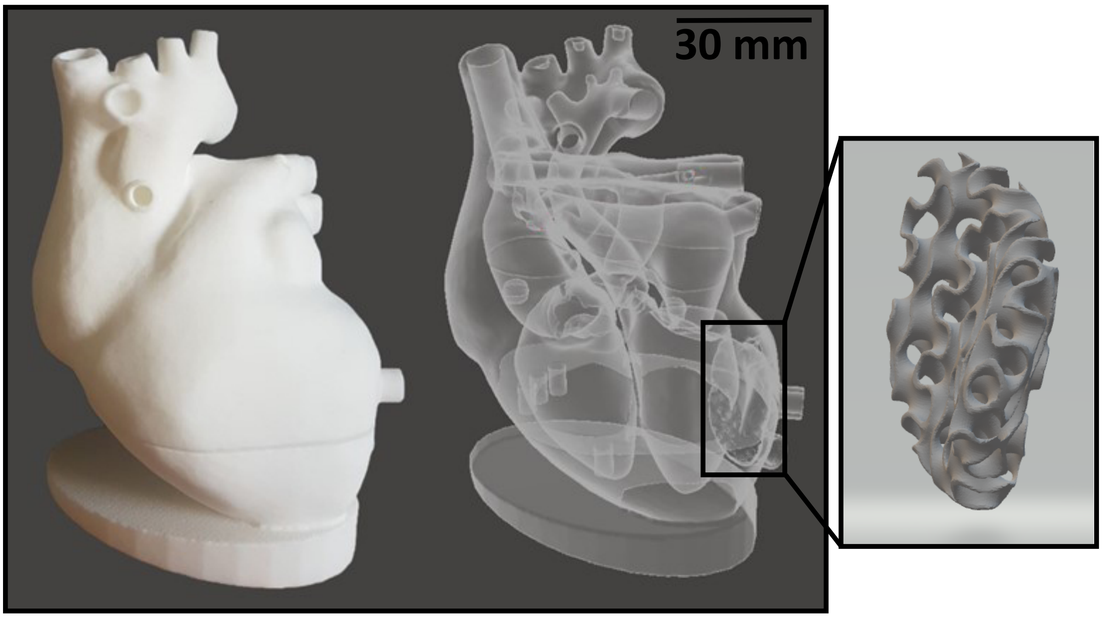

**Figure 3.12:** 3D-printed model is shown as photography (left) and 3D rendering (right). The phantom inflow is situated at the top left, simulating the blood influx from the end-piece of the superior vena cava into the right atrium. Water streams through the opened tricuspid valve into the right ventricle, from where the pulmonary circle is fed. The pulmonary resistance is simulated using a tube connection from the pulmonary arteries to the pulmonary veins. Passing the left atrium, left ventricle, and aortic valve, the contrast bolus splits into three outflows. The beginning of the aorta represents the blood flow of the body circuit. Two smaller outflows at the beginning of the aorta act as the right coronary artery and the left anterior descending artery. The reduced flow of the myocardium is simulated by a sponge-like 3D printed structure (black box). An additional connection from the myocardium acts as a sink. Figure reproduced from [Ham+22].

For the construction of the phantom geometry, a patient CCTA scan from a 64-slice single-source dual-layer CT scanner (IQon, Philips Healthcare, Best, The Netherlands) was used [1]. The specifications of this device can be found in Section 5. The CCTA protocol was acquired in helical acquisition mode centered around the left ventricle. An acceleration voltage of 120 kVp and a current time product of 40 mAs was applied. A soft convolution kernel (type B) with a pixel spacing of 0.8 mm and a slice thickness of 0.9 mm was used for reconstruction. From this scan, a true-to-scale model of the heart chambers and blood vessels was obtained using segmentation software. The segmentation has been simplified by excluding small blood vessels and complicated structures in order to enable a robust 3D model. The extensive simplifications made to the phantom make it very generic to any patient's anatomy. Right and left ventricle wall thickness was approximately equivalent, considering that wall thickness and structure do not affect noise values, as the absorption of the 3D-printed materials plays a minor role in total absorption (compared to the absorption from the water bath). A laser sintering polyamide powder (PA2200, EOS GmbH, Munich, Germany) was used for fabrication in a commercial 3D printer (Formiga P110, EOS GmbH, Munich, Germany). The additive technology allows all components to be printed without support structures. PA2200 has absorption properties similar to those of human tissues and is water-resistant [Mue+17]. In this study, it acts as a container (ventricles-like) and flow-limiting structure (myocardium-like). The ".stl" files can be made available by requesting them from the author of this thesis. Considering the strongly simplified blood supply into the myocardium-like tissue, a region supplied by left anterior descending and right coronary arteries was simulated. These vessels are modeled using two connection tubes from the aorta directly supplying the myocardial tissue. The lumen of the right coronary artery was then reduced to 25% of the original areal cross-section. This value was determined empirically by checking the effect of a blockage on contrast agent distribution into the myocardium. The comparison of blocked (right coronary artery) and opened (left anterior descending artery) supply tubes was made within one perfusion scan, and the perfusion analysis was then performed on the axial view, which intercepts the plane of the two myocardial inflow tubes. The simplified geometry of the phantom with only two supplying tubes is inherently more efficient in the middle region of the simulated myocardium, which is closer to the coronaries than the external regions. No pulsatile flow was utilized.

### Experimental setup and protocol settings

A standard myocardial perfusion imaging protocol with a fixed tube voltage of 120 kVp and an exposure of 100 mAs per time point was used on a 64-slice single source dual-layer CT scanner with a detector coverage of 4 cm and a rotation time of 0.27 seconds (IQon, Philips Healthcare, Best, The Netherlands). To get an accurate sampling of the contrast agent flooding, 36 time points over 26.9 seconds were imaged, resulting in a total dose-length product of 1.296 mGy×cm and a CT Dose Index volume (CTDIvol) of

---

[1] A scan of a patient was used. The extensive simplifications made to the phantom make it very generic to any patient's anatomy and make it impossible to conclude the patient's identity. The CCTA was only important for the true-to-scale model.

326 mGy (36 time points × 9 mGy per scan). With a thorax conversion factor of 0.015 mSv/(mGy×cm), this accumulates to an effective dose of approximately 19 mSv. An axial perfusion protocol with electrocardiographic triggering at 40% of the heart rhythm was used. To simulate realistic acquisition time points, the electrocardiographic device was connected to a colleague standing in the control room, who had a heart rate of approximately 70 BMP. As only a part of the myocardial tissue was simulated in this simplified model, "full coverage" of the region of interest was achievable without shuttle mode. The heart phantom inside a water bath, mimicking adequate human absorption, was placed in the dual-layer CT unit and connected to the water tap via a plastic hose. A dual syringe injection system (Stellant, MEDRAD, Inc., Indianola, PA, USA) was connected to the superior vena cava by a cannula. The perfusion measurement was started a few seconds after the contrast medium injection (1.0 ml/s CA for 10 seconds with an iodine concentration of 400 mg/ml followed by Natrium Chloride (NaCl) solution). Flow parameters were adapted to produce resolvable TAC with a full-width half maximum of approximately 10 seconds and maximum values of around 8 mg/ml or 250 HU in the AIF. Spectral raw data were reconstructed using a standard soft tissue filter kernel (type B) with an axial slice thickness of 1.0 mm, a 1.0-mm slice interval, and a pixel spacing of 0.49 pixel/mm (generated with IntelliSpace Portal 11.0, Philips Healthcare, Best, The Netherlands). A soft reconstruction kernel (type B) was used for both the conventional HU and the spectral iodine density images. The experiment was performed four times to work out the correct flux of contrast agent and water corresponding to time-attenuation curves expected in patients. Unfortunately, due to variable frame conditions like the water supply to the phantom, no inter-experimental comparison was investigated within the scope of this study.

### Postprocessing software

A trace-kinetic modeling software tool [Eck+18] was adapted for postprocessing voxel-wise TAC using a 1-compartment model for the description of dynamic contrast-enhanced images [IS13]. There are two main reasons for using tuneable postprocessing. The clinical perfusion software available at the site cannot handle spectral datasets. Also, the simplified heart model poses challenges to the clinical software, which is optimized for real heart perfusion measurements. The Python software could be adapted to these circumstances. The extracted model parameters were used to calculate quantitatively evaluable results like blood flow, blood volume, and MTT maps. The AIF was measured within the "right ventricle." Bolus-based perfusion methods typically obtain the AIF from an easily visible anatomical region, such as the left ventricle. In this case, the myocardium-like tissue, supplied from the right coronary artery and left anterior descending artery, was simulated. The myocardium-like tissue insert was situated in the left ventricle wall. No myocardial tissue was simulated within the right ventricle, making it a stable region for determining the AIF. TACs were modeled using the formula:

$$\mathrm{TAC} = A \cdot convolution(\mathrm{AIF}, e^{-\lambda \cdot T}) \tag{3.7}$$

where $T$ corresponds to all measured time points. The bound-constrained minimization method L-BFGS-B [Zhu+97; Byr+95; Vir+20] algorithm from the Python library SciPy was used for the fitting of the TAC. A minimum example of the implemented code is provided in the supplementary materials Section 5. To calculate the errors associated with the fitting parameters, the formula:

$$\Delta x^i = \sqrt{f_{\text{tol}} \cdot (H^{-1})_{ii}} \tag{3.8}$$

was used, where $\Delta x^i$ determines the error of the fit parameter $i$ ($A$ and $\lambda$ from the one compartment model), $f_{\text{tol}}$ is the upper bound where the minimization routine stops iterating, and $H^{-1}$ is the inverse Hessian matrix.

#### Classification accuracy analysis

AUC at the Receiver Operating Characteristic (ROC) analysis was computed for binary classification of voxel values into ischemic and nonischemic. This was done for two regions within the myocardium-like tissue to quantify the ability to differentiate different degrees of hypoperfusion. AUC values were calculated using the Python open-source software library scikit-learn 1.0 [Ped+11]. The ROC curves were generated by a simple threshold classifier (if the MTT was over the threshold, then the voxel was hypoperfused). No probabilities were assigned to individual voxels. A bootstrapping analysis was applied to the receiver operating characteristic curves to investigate the confidence intervals for the different AUC values (bounds percentile of 5% to 95% and number of bootstraps 1,000).

#### Dose reduction

Phantom measurements were performed using a high dose equal to 9 mGy CTDIvol for every time point. To reduce the dose, several scenarios are conceivable. By reducing the tube current, the exposure per rotation can be decreased. This will lead to a decrease in the SNR in the reconstructed images. Iterative reconstruction techniques may be able to compensate for that. Within the scope of this investigation, the 1-compartment contrast kinetic modeling was tested on reduced sampling points using spectral dynamic perfusion data. Only 8 of 36 time points were utilized to calculate perfusion parameters. The sampling rate was artificially decreased from approximately 0.8 to 3.0 seconds for all TAC, including the AIF. By following this very simple approach, a dose reduction of approximately 78% from 19 mSv to 4.3 mSv can be achieved.

### 3.3.2 Results

#### Fit accuracy of postprocessing

The SNR in a homogenous region inside the “right ventricle” at a maximally enhanced time point increased from 7.40 to 112.02 from conventional HU to iodine density maps. Using a distinct point within the active area of the stenotic region, a decreased error on fit parameters from conventional to spectral TAC (42% reduction for $A$ and 40% for $\lambda$) can be shown. The fit behavior for one specific voxel within an ischemic region is visualized in Figure 3.13.

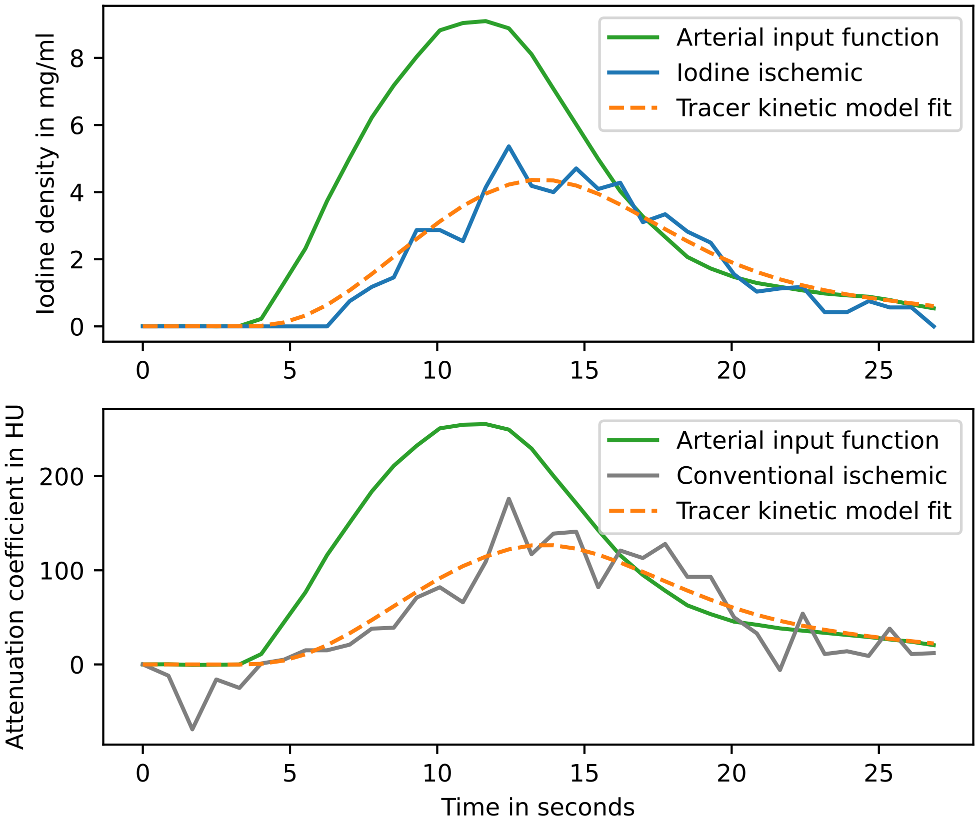

**Figure 3.13:** Tracer kinetic fit behavior of spectral (top) and conventional (bottom) perfusion data in highly affected myocardial tissue. The SNR of TAC is calculated by dividing the maximum value of the tracer kinetic fit function by the standard deviation of the error of the fit. Decreased fit parameter errors at this voxel can be calculated for the spectral perfusion measurement compared to the conventional TAC fit (42% reduction for A and 40% for $\lambda$). Figure reproduced from [Ham+22].

### Iodine-based perfusion maps

The absolute, quantitative iodine TAC used to calculate blood flow, volume fraction, and mean transit time parameter maps are depicted in Figure 3.14. Three characteristic regions in all maps can be defined as corresponding to regions of interest which are high, moderately, and unaffected by the simulated stenosis. The best distinction of those regions can be seen on MTT maps. The upper part of the displayed window was strongly affected by the introduced stenosis. MTT over 2.2 seconds were observed in the spectral data. An unaffected region was located in the apical part of the myocardium. Here, the supplying artery (tube) was not blocked during the experimental setup. MTT below 2.0 seconds were measured in this area for spectral data. The very ending of the apical region of the phantom myocardium-like tissue could be classified as moderately affected. The mean value and standard deviation for the highly affected region in MTT maps calculated from conventional and spectral data were $3.08 \pm 0.44$ and $2.73 \pm 0.13$ seconds, respectively.
Additionally, perfusion maps were calculated using the GVF model. Peak enhancement, perfusion, blood volume, and TTP can be derived from the GVF model. The results are shown in Figure 3.15. The GVF model qualitatively shows a very similar behavior as the 1-compartment model.

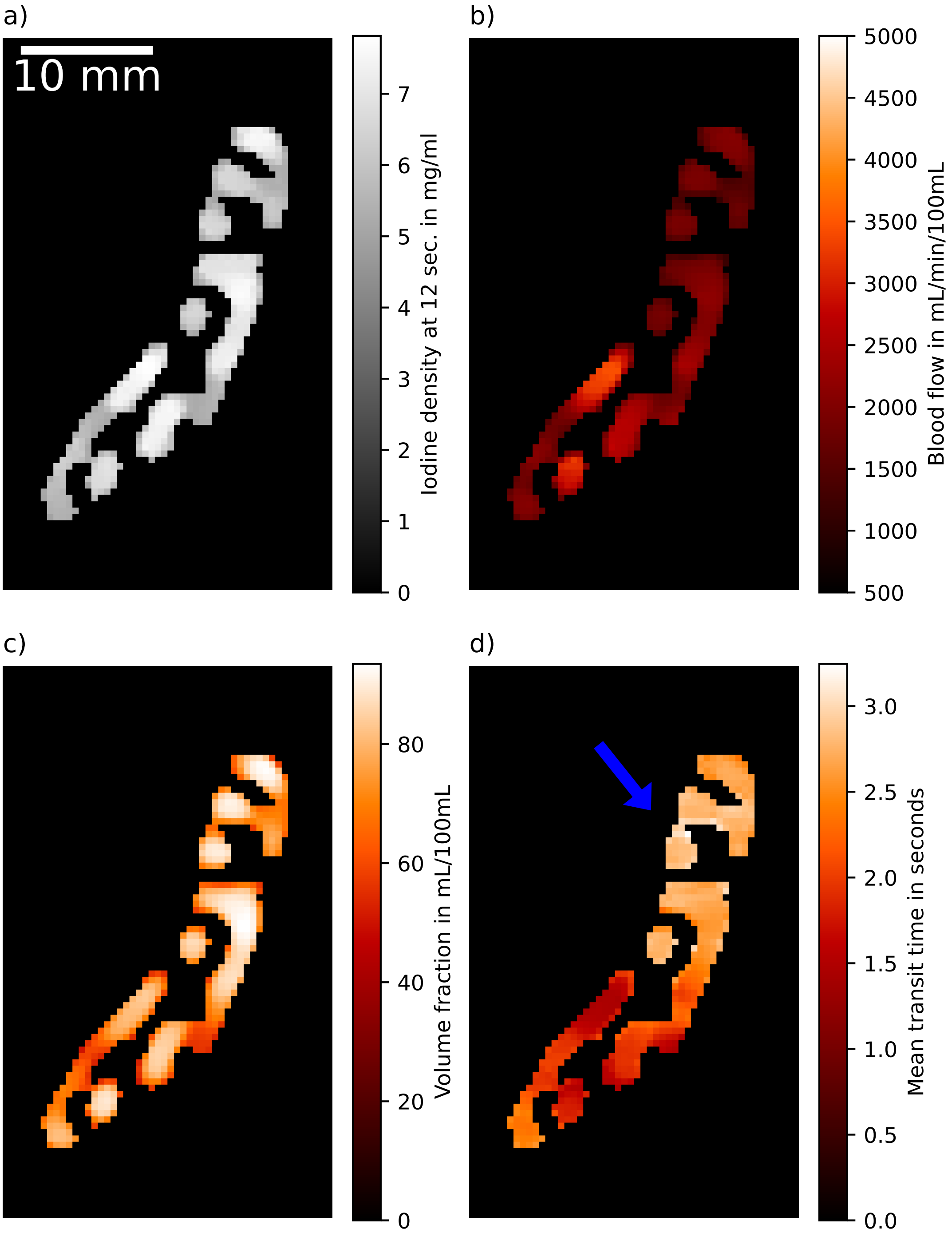

**Figure 3.14:** Absolute and quantitative iodine-based analysis of myocardial dynamics derived from 1-compartment fitting of iodine density-to-time attenuation curves in the active myocardium-like tissue area. The phantom's spongy myocardium-like tissue in axial view is imaged. **a** Iodine density image at 12 seconds of the perfusion protocol in grayscale to distinguish it from perfusion maps. **b** Image with blood flow normalized to the tissue volume (ml/min/100 ml). **c** Image showing the volume fraction representing the compartment volume relative to the total volume of the region of interest (e.g., ml/100 ml). **d** Mean transit time map. Image parts, which appear bright red in **d** are classified as hemodynamically affected myocardium-like tissue (blue arrow). Figure reproduced from [Ham+22].

An averaged line profile of the MTT map plotted through the myocardium-like tissue from top to bottom is presented in Figure 3.17. The line profile was calculated from the MTT map in Figure 3.14 **d** using the average over all MTT values along the x-axis, where MTT values were not zero. The line profile goes along the y-axis of Figure 3.14 **d**, plotting the averaged values. All voxel values in the active myocardium-like area along one row were averaged to get a reduced noise line profile. High variations in the conventional MTT line plot could be observed. The differentiation between the varying affected myocardium-like tissues was strongly affected by a high noise contribution in the conventional measurement. Iodine-based MTT maps showed a comparably small noise contribution (as previously reported, approximately 40% error reduction in fit parameters) with a step-like function through the differently affected tissue and continuous gradient between the plateaus, allowing to introduce thresholds of 2.5 and 2.0 seconds for the differentiation between highly and moderately affected tissue (orange dashed line) and unaffected and moderately affected regions (green dashed line) in spectral data, respectively. The thresholds were determined empirically from spectral MTT maps, particularly for this phantom design, and cannot be adapted to human myocardial perfusion. The absolute values of spectral MTT decreased as well in the unaffected as in the ischemic area compared to conventionally calculated MTT maps, resulting from variable AIF. This is a general problem of tracer kinetic modeling using the arterial input function as a fit reference. The AIF must be selected manually by drawing a ROI within the supplying vessel. In our experiment, this ROI was the same for iodine data as well as conventional data. The selection still leads to minor variations in the TAC. This can be visualized (Figure 3.16) by plotting the normalized AIF of iodine and HU data. Also, in Figure 3.16 the normalized TAC of an ischemic voxel and their corresponding fits are plotted. The fit behavior looks very similar, but the fit parameters and therefore the derived physical parameters like MTT deviate because the initial AIF differ. In the current example, a MTT value of 2.89 and 3.17 seconds was calculated for the iodine and conventional fit respectively.

The comparison of the line profiles of the GVF model and one-compartment model are shown in Figure 3.18. A very similar trend can be observed in both models on a qualitative level. Two y-axis scales are used to display the different values of the GVF model and one-compartment model.

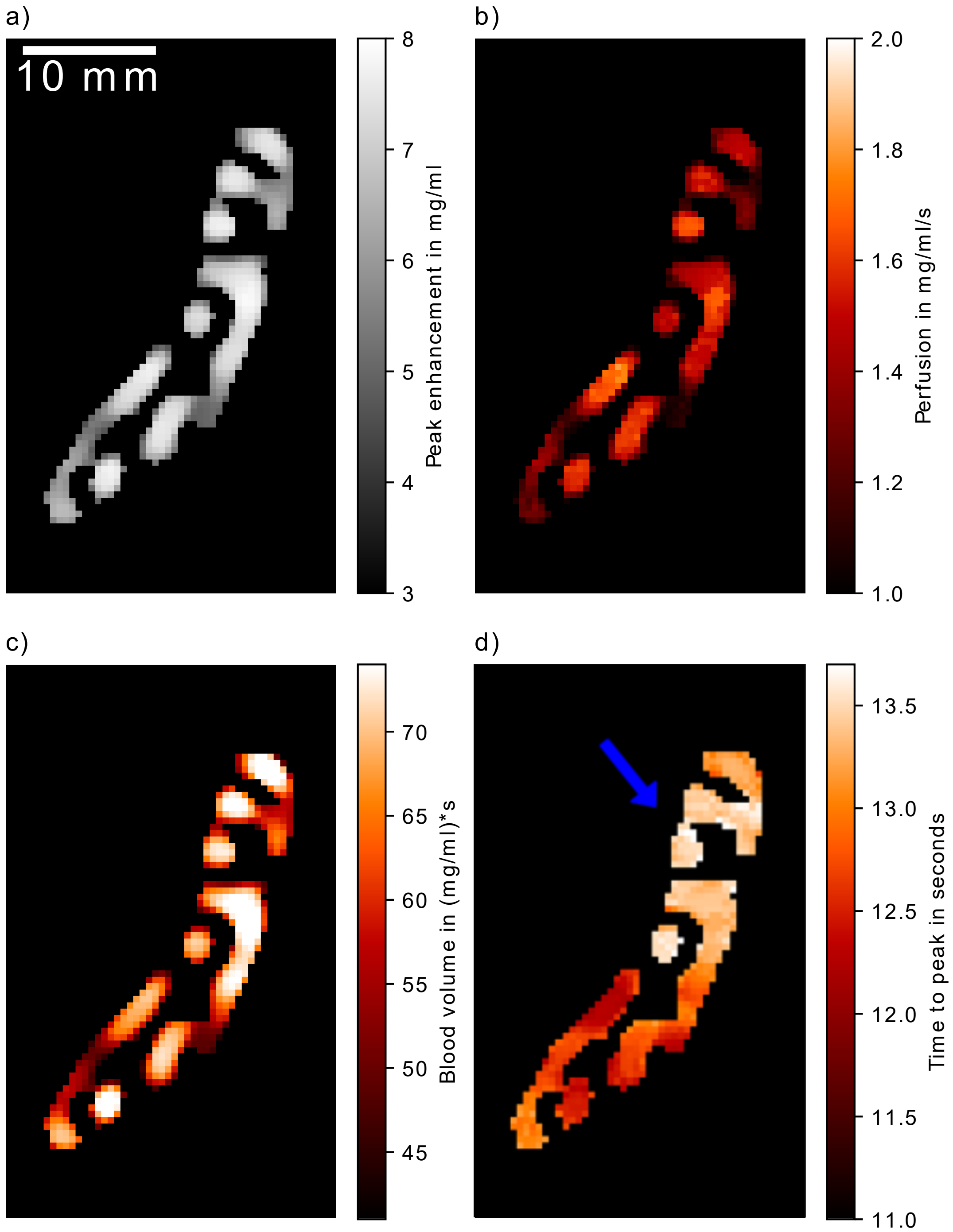

**Figure 3.15:** Absolute and quantitative iodine-based analysis of myocardial dynamics derived from GVF model on iodine density TAC in the active myocardium-like tissue area. The phantom's spongy myocardium-like tissue in axial view is imaged. **a** The peak enhancement indicates the maximal increase in iodine density derived from the curve fit. **b** The perfusion relates to the highest temporally gradient in influx of iodine. It is calculated using the derivative of the curve fit shown in Figure 3.10. **c** The iodine volume depicted here is related to uptake/storing/flush out behaviour within the respective structures. It is calculated using the integral of the GVF curve shown in Figure 3.10. **d** The time to peak indicates the point in time when maximal peak enhancement is reached. Image parts, which appear bright red in **d** are classified as hemodynamically affected myocardium-like tissue (blue arrow).

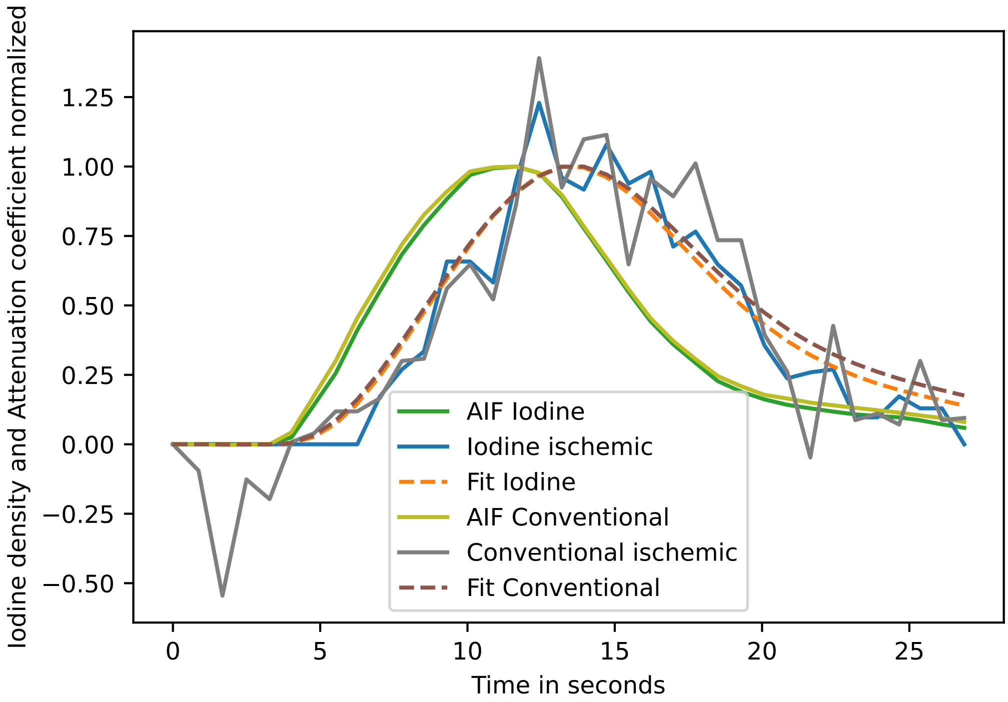

**Figure 3.16:** Normalized AIF from iodine and HU data and corresponding TAC fits of ischemic voxels are shown. Please consider, that all curves are normalized to have a maximum value of 1.00.

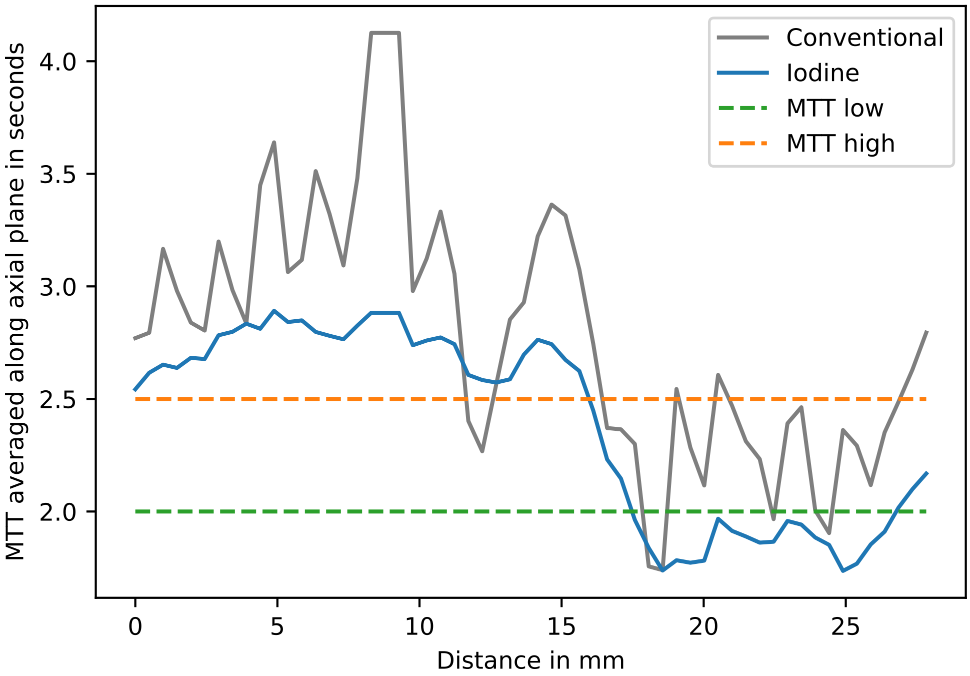

**Figure 3.17:** MTT line profile from top to bottom of the myocardium in axial view (in reference to Figure 3.14). Voxel values from iodine and conventional measurements are averaged along one row (left to right) in axial view to reduce variance. The x-axis displays the distance starting at zero for the top row of the myocardium-like tissue. Highly affected, unaffected, and moderately affected myocardium-like tissue from left to right. Thresholds are plotted at 2.5 and 2.0 seconds for the differentiation between highly and moderately affected tissue (orange-dashed line) and unaffected and moderately affected regions (green dashed line), respectively. Figure reproduced from [Ham+22].

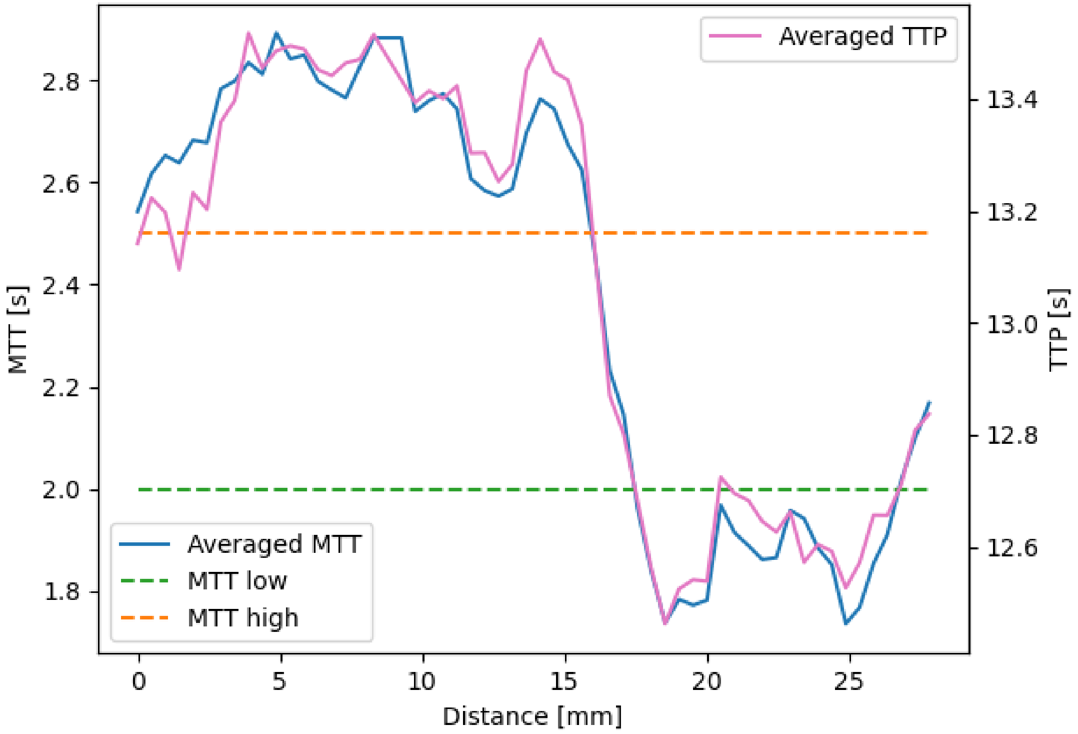

**Figure 3.18:** TTP line profile of GVF (in reference to Figure 3.15) in comparison to MTT from the one-compartment alike in Figure 3.17. For a detailed description of the line profile, see Figure 3.17. Two y-axes are used to display the MTT and TTP, respectively. Thresholds are plotted at 2.5 and 2.0 seconds (MTT) or rather 13.2 and 12.7 seconds (TTP) for the differentiation between highly and moderately affected tissue (orange-dashed line) and unaffected and moderately affected regions (green dashed line), respectively

### Classification accuracy analysis

ROC curves are displayed in Figure 3.19. The ground truth values for ischemic versus nonischemic voxels are selected based on the distance of the voxels to the supplying stenotic and non-stenotic coronary artery, respectively. Voxels above the middle line (y-axis) of Figure 3.14 are labeled as affected tissue. For the AUC analysis, the highly and moderately affected region were combined and compared with the unaffected region. The AUC analysis was only performed on one z-slice, which intercepts both supplying tubes. The ROC curves illustrate the classification accuracy based on the MTT maps from conventionally acquired perfusion maps versus MTT maps from iodine perfusion measurements. The perfect AUC value of 1.00 demonstrates the continuously decreasing MTT value from ischemic to nonischemic regions in spectral perfusion measurements. Due to lower fit accuracies and higher fluctuations (refer to the "Fit accuracy of postprocessing" section) in conventional measurements, the voxel-wise classification accuracy was reduced to an AUC value of 0.89. A bootstrapping analysis led to the following results for AUC values and 95% confidence intervals:

- classification with conventional MTT maps: 0.893 [0.868 to 0.917];
- classification with spectral MTT maps: 1.000 [1.000 to 1.000];
- classification with spectral reduced dose MTT maps: 0.961 [0.946 to 0.975].

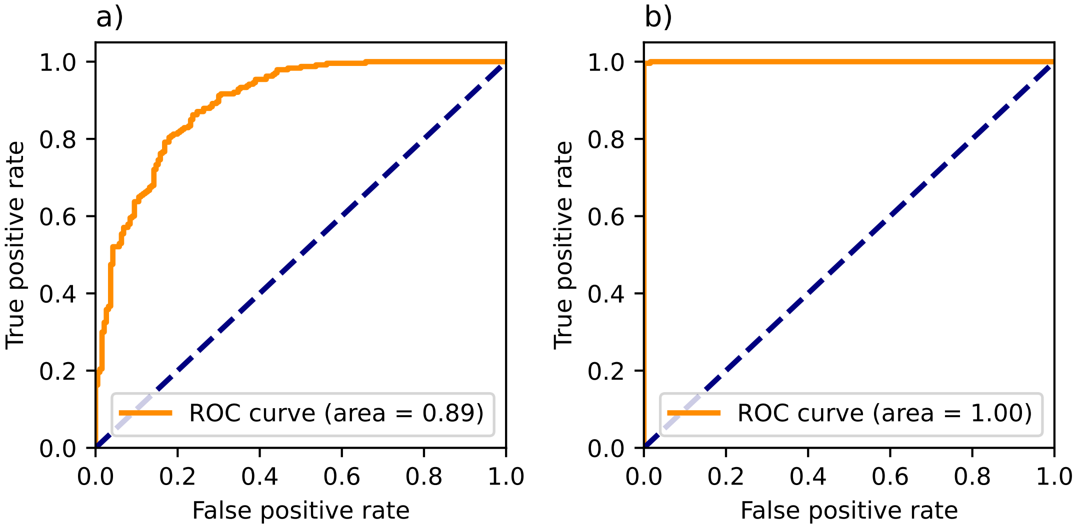

**Figure 3.19:** ROC analysis for conventionally (**a**) and spectrally (**b**) derived MTT values. The ground truth classification of voxels to ischemic and nonischemic regions is based on the distance of the voxels from the blocked and non-stenotic supplying arteries, respectively. The AUC value of 1.00 from the spectrally derived MTT ischemia classification was achieved due to the continuous MTT decrease from ischemic to nonischemic regions. The blue dashed line signifies random distribution. Figure reproduced from [Ham+22].

### Dose reduction

Classification accuracy for the differentiation of ischemic from nonischemic regions was tested on MTT maps calculated from normal dose and reduced dose spectral TAC. The AUC value decreases to 0.96 (Figure 3.20 d), because of the reduced fit accuracy from the contrast kinetic 1-compartment model on 8 time points (63% smaller error in parameter $A$ from normal sampling; $\lambda$ with no difference in fit error). Relative deviation in averaged blood flow values calculated from reduced sampling TAC was 9.3%. When comparing MTT maps visually (Figure 3.20 a, b) increased inhomogeneities within the different regions could be observed. Not every voxel could be classified correctly based on threshold values; however, the visual impression still allowed to determine the site of the ischemic region (Figure 3.20 b, top part).

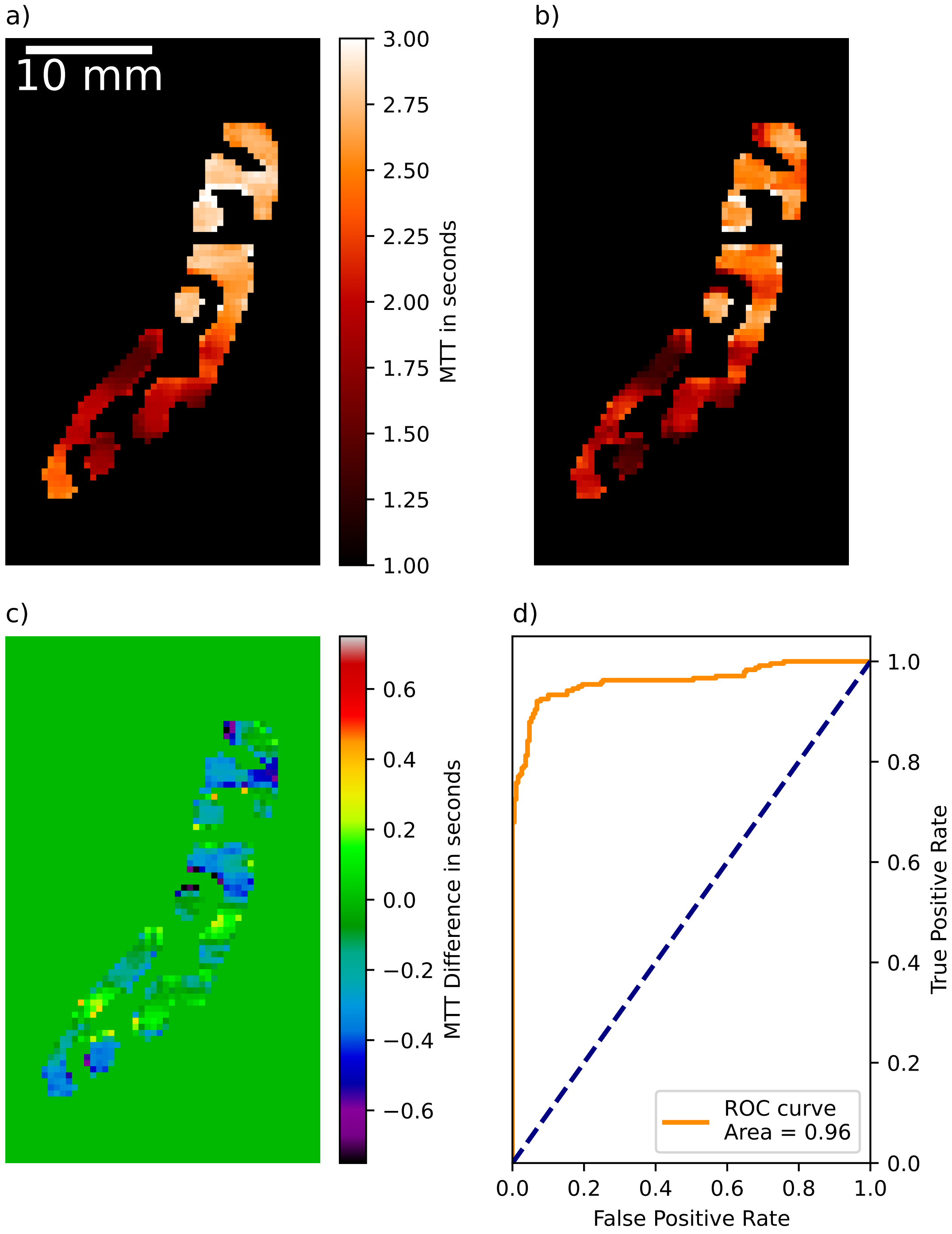

**Figure 3.20: a** Comparison of normal dose iodine derived MTT map with **b** simulated reduced dose dynamic perfusion acquisition. **c** differential image of normal and reduced dose measurements. **d** Receiver operating characteristic analysis for classification characterization of stenotic regions using the reduced dose data. Deviations within the MTT map of the ischemic and nonischemic regions increase when applying the contrast agent kinetic model to the reduced number of time points. Nevertheless, a differentiation is achievable using the reduced dose with an AUC of 0.96. Figure reproduced from [Ham+22].

### 3.3.3 Discussion

Validation measurements for dynamic processes using CT require the use of special phantom models. To demonstrate the detectability of stenoses with dual-energy CT scanners, the determination of hemodynamic parameters by dual-energy CT dynamic myocardial perfusion imaging was performed. An anatomical heart model was designed and produced using 3D-printing techniques. The dynamic heart phantom could be flooded with water and contrast medium. The flow through the heart chambers and into the myocardium was imitated. An increased SNR from conventional to spectral perfusion data (from 7.40 to 112.02) lead to a fitting process with smaller errors on fitting parameters and derived perfusion parameters using a 1-compartment model. Because the material decomposition is based on the photoelectric effect and Compton effect-based images, the anticorrelated noise can be modeled and removed from the image [Mec+17; PG17]. The material decomposition provides a low-noise image with a relatively high signal. As discussed in Section 3.4, iodine density maps show the highest signal enhancement and CNR within several spectral parameter maps. Also, this inherently reflects the contrast agent flooding and washout behavior and generates a comprehensive baseline at 0 mg/ml. Our spectral perfusion data showed a step-like function through the differently affected tissue, while the noise contribution in conventionally derived data forbids this voxel-wise analysis, indicated by high fluctuations in the line profile. For conventional perfusion data, Gaussian smoothing in plane or an increased slice thickness [Nou+22] for averaging in z direction must be applied. The smoothing operation will decrease the spatial resolution in all contrast kinetic fit-derived maps. MTT and TTP maps derived from a one-compartment model and GVF model show very similar trends on a different scale. The GVF model has four fit parameters, requires more computational time, and the fit parameters are more prone to noise than the one-compartment model. Contrariwise, the one-compartment model has only two fit parameters but relies on the determination of the AIF which can lead to variations in physical parameters. The GVF model does not take into account a AIF as a fit reference. Further, the variation of fit parameters with noise does not affect the physical parameters remarkably. Considering iodine densities for the measurement of TAC, the GVF can fit the progression of the contrast agent more accurately, as it does not rely on the AIF as a fit reference. By using the iodine density as input to the GVF model, the derived physical parameters are quantitative values with the units mg/ml, mg/ml/s, (mg/ml)×s and seconds for peak enhancement, perfusion, blood volume and mean transit time, respectively. Quantitative values make sense for the comparison of different patients and scanner types. Nevertheless, they will be affected by the amount of CA injected and the flow rate. To maintain the comparability of the perfusion parameters, the same amount of CA per kg and flow rate must be used. Using the parameter maps derived from GVF within the patient to discriminate between ischemic and nonischemic regions can also make sense without a standardized protocol. Non-qualitative values derived from HU measurements using the GVF model can also lead to worse discrimination between ischemic and nonischemic regions.

The reason for the reduced flow at the very end of the apical region of the phantom's myocardium is due to the hemodynamic design of the myocardium-like tissue, having only two supplying tubes. The moderately affected outer region was therefore not considered in the data analysis. A dose reduction of approximately 78% from 19 mSv to 4.3 mSv was achieved by reduced sampling of time points. Visual differentiation between ischemic and nonischemic regions was still possible. By reducing the current time product and using iterative reconstruction techniques to keep the SNR at a constant level, we expect to be able to reduce the radiation dose to less than 2.0 mSv, being well below all reported dose values for dynamic CT myocardial perfusion studies as reported by Varga-Szemes et al. [Var+15] from 9.4 to 18.8 mSv. In this study, we used a dual-layer CT system. A drawback of this technology is the detector coverage of only 4 cm, which decreases the field of view in the z-direction, limiting the assessment of the full myocardium within one shot. However, one can expect that spectral CT technologies improve rapidly towards larger detector coverage to image the whole myocardium without additional table movement. Other spectral acquisition technology like fast emerging photon-counting CT is also conceivable. This technology can acquire images at very high spatial resolution without electronic noise and with improved tissue contrast [Flo+20]. Simultaneous material decomposition of two or three contrast agents may develop the possibility of simultaneous acquisition within the time period of flooding, saturation, and late enhancement. This approach could be used to decrease the dose or increase the sampling rate without having to increase the number of CT acquisitions. There are some other publications regarding the use of phantom models in cardiac imaging. Boltz et al. [Bol+10] constructed an anthropomorphic beating heart phantom to analyze cardiac CCTA protocols. The phantom was anatomically and functionally designed to be very close to a real-world situation. For example, the beating and corresponding electrocardiographic signals can be modeled to investigate motion artifacts and perform stent imaging. Also, the chambers can be flooded with a mixture of water and contrast agent. Nevertheless, this phantom design was selected to investigate anatomically relevant information. Dynamic perfusion within the myocardium (e.g., TAC) cannot be simulated using this approach. On the other hand, Chiribiri et al. [Chi+13] built a perfusion phantom that simulates myocardial first-pass magnetic resonance perfusion. This approach could easily be adapted to CT perfusion by using iodinated contrast agents instead of gadolinium-based contrast agents. The phantom establishes a very controlled and reproducible environment for modeling dynamic perfusion. In comparison to our approach, it is not able to reproduce the correct anatomically relevant structures of a human heart. Beam hardening artifacts from highly absorbing contrasted heart chambers would not be represented by using the approach by Chiribiri et al. [Mec+17]. Also, the phantom design chosen in this approach is static and cannot simulate movement artifacts from the heart. Heart movement is a source of potential bias in real patient measurements. It can be superimposed by breathing. The static 3D-printed structure neglects these issues. An elastic image registration-based method to improve the characterization of CT-based estimates of myocardial perfusion can be applied to reduce these artifacts [Iso+11]. The phantom design with two connection tubes directly supplying the myocardium-like tissue allows better flow control in our model since the 3D-printed parts are static and no luminal control/stenosis would be possible. The lumen of the right coronary artery was then reduced to 25% of the original areal cross-section via clamping. This resulted in a degree of uncertainty being a limitation, which should be addressed in future work. Integrating pulsatile flow and pressure-dependent elastic vessels in our experiments can increase the accuracy and the performance of the quantitative perfusion analysis towards more realistic data. For our proof-of-principle experiments to assess if stenosis and the consequent reduced myocardial perfusion can be analyzed, we think that this single degree of perfusion is sufficient. The assessment of in vivo patient data is crucial for further investigations towards spectral dynamic myocardial perfusion imaging. A recent study [Nou+22] investigated dynamic myocardial perfusion CT in nine centers around the world, finding an incremental diagnostic value compared to CCTA as a standalone modality. Especially, a higher specificity (72% for CCTA, 89% for CCTA plus perfusion imaging) offers the opportunity to reduce unnecessary cardiac interventions after anatomical assessment alone. Spectral acquisition may be the key technology to overcome the limitation of low CNR in CT [Ste+10]. Fahmi et al. [Fah+16] showed increased inhomogeneities (dark band on the myocardium) in conventional 120-kVp pig images resulting from beam hardening artifacts from highly absorbing ventricles. These artifacts could be avoided by using 70-keV virtual monoenergetic images, leading to a more reliable assessment of nonischemic defects. A full CT analysis of the heart including calcium scoring using CCTA and dynamic myocardial perfusion could be performed within 10 minutes. This workflow may provide a comprehensive, one-stop, noninvasive and superior method for the evaluation of CAD and myocardial perfusion.

## 3.4 Dynamic perfusion using a porcine model

Most of the following section has already been published in Scherer and Hammel et al. "Dynamic Quantitative Iodine Myocardial Perfusion Imaging with Dual-Layer CT using a Porcine Model" [Sch+19] and adapted for the scope of this thesis. It focuses on the dynamic perfusion analysis of a porcine model using the GVF model and the maximal slope method. The results are compared to a semi-static two-shot approach.

### 3.4.1 Abstract

When using CCTA, the functional hemodynamics within the myocardium remain uncertain. In this study, myocardial CT perfusion imaging using an iodine contrast agent strongly improved the assessment of myocardial disorders. However, a retrieval of such dynamics using Hounsfield units from conventional CT poses concerns with respect to beam-hardening effects and low CNR. DECT offers approaches to overcome aforementioned limitations. Quantitative peak enhancement, perfusion, time to peak, and iodine volume measurements inside the myocardium were determined, resulting in 0.92 mg/ml, 0.085 mg/ml/s, 17.12 seconds, and 29.89 mg/(ml × s), respectively. We report on the first extensive quantitative and iodine-based analysis of myocardial dynamics in a healthy porcine model using a DLCT. We further elucidate the potential of reducing the radiation dose from 135 to 18 mGy and the contrast agent volume from 60 to 30 ml by presenting a two-shot acquisition approach and measuring iodine concentrations in the myocardium in-vivo down to 1 mg/ml, respectively. We believe that dynamic quantitative iodine perfusion imaging may be a highly sensitive tool for the precise functional assessment and monitoring of early myocardial ischemia.

### 3.4.2 Introduction

In this study, we report on the very first extensive quantitative and iodine-based analysis of myocardial dynamics in a healthy porcine model in rest, using a DLCT. We include the presentation of iodine perfusion, time to peak, peak enhancement, and volume maps. In the first step, we show, in congruence with previous studies, that low-energy virtual MonoE-keV images and iodine density maps are superior in comparison to conventional images in the depiction of temporal opacification of the myocardium concerning relative signal enhancement and CNR. Afterward, the temporal uptake of iodine is modeled using a GVF and corresponding dynamics deduced from the model in a pixel-wise manner. Further, we elucidate the possibility and performance of quantitatively assessing the myocardial peak enhancement map using a semi-static two-shot approach. Based on the accuracy and consistency of determining low iodine densities with modern spectral systems, we suggest that dynamic quantitative iodine perfusion imaging may be a highly sensitive tool for the precise functional assessment and monitoring of early myocardial ischemia if a valid database for stress and/or rest can be established.

## 3.4.3 Material and methods

### Ethics statement

Animal care and all experimental procedures were performed in strict accordance with the German and National Institutes of Health animal legislation guidelines and were approved by the Bavarian Animal Care and Use Committee (AZ $55.2. - 1 - 54 - 2532 - 62 - 13$).

### Acquisition of CT myocardial perfusion

CT images of the healthy pig (31.75 cm mean diameter, 76 kg) were acquired with a 64-slice single source DLCT IQon scanner with a detector coverage of 4 cm and a rotation time of 0.27 seconds (Philips Healthcare, The Netherlands). The specifications of this device can be found in Section 5. The spatial resolution is 2.47 pixels per mm, resulting in a pixel size of $(0.40 \times 0.40)\text{mm}^2$. The ECG-triggered temporal resolution aggregates to 1.08 scans per second, or a full acquisition of the specified range every 0.92 seconds. The firmware version of the scanner was 4.1.0.0. The perfusion scan was conducted in stationary mode with 120 kVp and a mean tube current of 100 mAs. Scans were reconstructed with a soft kernel (Philips type B) and a slice thickness of 3 mm. Within 26 seconds, 36 scans were recorded so that the full first pass of the contrast bolus was imaged. Hereby, the scans were ECG-triggered and adjusted to the cardiac cycle with an increment of zero. Each scan was conducted with a CTDIvol of 9 mGy, resulting in a CTDIvol of 135 mGy and 18 mGy for the extensive analysis of myocardial dynamics (15 scan points) and the two-shot approach, respectively. The perfusion scan was conducted using 40 ml of contrast agent (Ultravist 300, Bayer, Bayer AG, Leverkusen, Germany, iodine content 300 mg/ml) at a flow rate of 4 ml/s. The contrast agent was injected into the ear vein via an 18-gauge catheter using a dual syringe injection system (Stellant, MEDRAD, Inc., Indianola, PA, USA).

### Contrast-to-Noise and relative signal enhancement

Conventional, MonoE and iodine density reconstructions alongside their standard deviations (within respective ROI of $50\ \text{mm}^2$) were directly obtained from the Philips IntelliSpace Portal. The Relative Increase in Signal (RIS) (Figure 3.21 c) and temporal CNR (Figure 3.21 b) during contrast uptake were calculated as

$$\text{RIS} = \frac{S_{t=23.3\text{s}} - S_{t=0.0\text{s}}}{S_{t=0.0\text{s}}} \tag{3.9}$$

and

$$\text{CNR} = \frac{S_{t=23.3\text{s}} - S_{t=0.0\text{s}}}{\sqrt{\sigma_{t=23.3s} + \sigma_{t=0.0\text{s}}}} \tag{3.10}$$

respectively. Here, $S_{t=23.3\text{s}}$ and $S_{t=0.0\text{s}}$ correspond to the different signals within each of the image channels at maximal/saturated and minimal iodine concentration within the myocardium, respectively.

### Retrieval of myocardial dynamics

A certain slice within the thorax was determined for further processing and 15 data points in time, with minor structural movement were selected from the iodine density images. In order to model the first pass of contrast bolus through the heart, arteries and myocardium, GVF were used, as proposed in the literature for both MRI and CT [Mad92; MdBK08]:

$$I(t) = A(t - t_0)^{\alpha} \exp^{\frac{-(t-t_0)}{\beta}} \tag{3.11}$$

whereas $I(t)$ is the time dependent iodine density and $A$, $t_0$, $\alpha$, $\beta$ are fit parameters. Thereby, the data was fitted in a two-step sequence: in a first fit, all 15 data points were used, and a preliminary peak time was determined. In a second fit, data exceeding the initial peak by more than 12 seconds, i.e. accounting to the second pass of contrast agent was correspondingly neglected. Afterward, quantitative iodine perfusion, peak enhancement, time to peak, and iodine volume (in imitation of the conventional blood volume) were calculated based on the maximal slope method [MG03]:

$$\text{Perfusion} = \frac{d}{dt}[I(t)]_{\text{max}} \tag{3.12}$$

$$\text{Peak Enhancement} = I_{\text{max}} - I_{\text{min}} \tag{3.13}$$

$$\text{Time to Peak} = t(I_{\text{max}}) - t(I_{\text{min}}) \tag{3.14}$$

$$\text{Volume} = \int_0^{50\text{s}} I(t)\, dt \tag{3.15}$$

Finally, the aforementioned maps were filtered with a median filter with a 3 × 3 kernel to reduce noise arising from the pixel-wise assessment. Note that data were not normalized or scaled with respect to arterial input functions, hemocrit-scale, Cerebral Blood Volume (CBV) factor, or other physiological models for multiple reasons: firstly, within this animal study, corresponding values and models are not available. Secondly, we wanted to provide absolute and quantitative, i.e. unscaled values to the readers, which are independent of assumptions made in underlying physiological models. Correspondingly, the iodine volume map presented here does not represent iodine volumes in the sense of milliliters, but rather gives a quantitative measure of the area under the curve of the temporal iodine density in the unit of (mg/ml)×s. The latter is thereby related to the tissue's overall blood intake capacity, its storing as well as the flush-out behavior.

A detailed description of the Graphical Processing Unit (GPU)-implemented GVF routine can be found in Section 3.5. With the IntelliSpace Discovery (ISD) platform, it is possible to fit and view the perfusion maps in a browser-based environment. Furthermore, the perfusion data from the Picture Archiving and Communication System (PACS) system can be transferred to the ISD platform easily, and the integrated workstation can be used to perform the perfusion analysis.

## 3.4.4 Results

A healthy pig (31.75 cm in mean diameter, 78 kg) was scanned using a DLCT system (IQon, Philips Healthcare, Best, The Netherlands) with a detector coverage of 4 cm and a peak voltage of 120 kVp. An overall volume of iodine contrast agent of 40 ml (Ultravist 300, Bayer, Bayer AG, Leverkusen, Germany) was injected into the ear vein, which corresponds to a concentration of 154 mg/kg body weight. Within this animal study, scans were immediately acquired after injection to track the bolus and enable hemodynamic analysis throughout the whole thorax. ECG-triggered dynamic axial scans were adjusted to the cardiac cycle with an increment of zero, with the scanning area covering the mid-part of the left ventricular myocardium. A total of 36 consecutive scans were acquired. Finally, no automatic motion-correction algorithm for the heart was used as the entire heart volume was imaged only fragmentary. Therefore, data points with extensive motion in the heart or other thorax structures were manually abandoned, resulting in a non-equidistant sampling of the curve with 15 scan points. Figure 3.21-a shows the corresponding HU for conventional and mono-energetic reconstruction as well as the iodine density of the porcine myocardium at the initial stage and high contrast agent enrichment, i.e. 23.3 seconds after the contrast agent injection. In congruence with previous dual-energy studies on other indications, the temporal relative signal increase during iodine uptake with respect to image noise is highest in the case of the low mono-energetic channels as well as the iodine density map itself [Lou+18; Kau+16]. This is also well reflected in the temporal CNR (Figure 3.21 b) and relative signal enhancement (Figure 3.21 c), where the virtual MonoE-40 keV and iodine density images outperform the conventional HU image by far.

Since the temporal opacification of the myocardium is quantitatively and most sensitively depicted (as an iodine density offset arising from soft tissue is nearly absent) within the iodine density map, this channel was used for further iodine-dynamics analysis. Figure 3.22-a displays a transversal porcine thorax slice for different scan times after the initial injection of contrast agent. Notice a subsequent bolus pass/enrichment of iodine within the right and left heart ventricle as well as myocardium for the exemplary scan times of 7.5, 10.9, and 23.3 seconds, respectively. In the first step, imaging data of

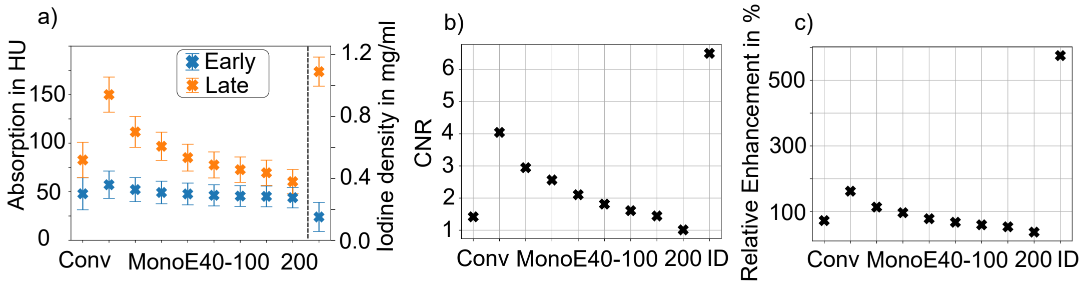

**Figure 3.21:** **a** Conventional and mono-energetic Hounsfield units and iodine density of the early (blue points) and late myocardium (orange). The early stage is measured at second zero without iodine enhancement. The late myocardial stage is depicted at second 23.3 with maximal contrast agent enrichment. Error bars correspond to the standard deviation within a ROI of 50 $mm^2$ of the respective image channels. **b** Temporal CNR and **c** relative signal enhancement of the myocardium during contrast uptake derived from **a**, demonstrating a superior depiction of the myocardial opacification within the iodine density imaging channel. Figure reproduced from [Sch+19].

15 scan points was temporally modeled in a pixel-wise manner using gamma variate fit functions, as proposed in literature [Mad92; Kra+96]. Using a two-step fitting routine, only the first pass of the contrast agent was considered so that artifacts arising from recirculation were excluded. Figure 3.22-b displays data points and the corresponding fit for an exemplary pixel in various ROI showing a high degree of correlation of model and measurements (as quantified by the coefficient of determination $R^2$ being close to 1), even in case of a non-equidistant temporal sampling. The corresponding transversal thorax slices obtained from the model (Figure 3.22 c) are of smoother appearance than the original data, contingent on the fact that outliers and noise are damped via the fitting routine. This, however, is an essential premise for the meaningful retrieval of perfusion and peak enhancement map. Please note distinctive discrepancies between the model and measured data for late scan times arising from a correction of recirculation, as indicated by low iodine density areas, among others, in the right ventricle.

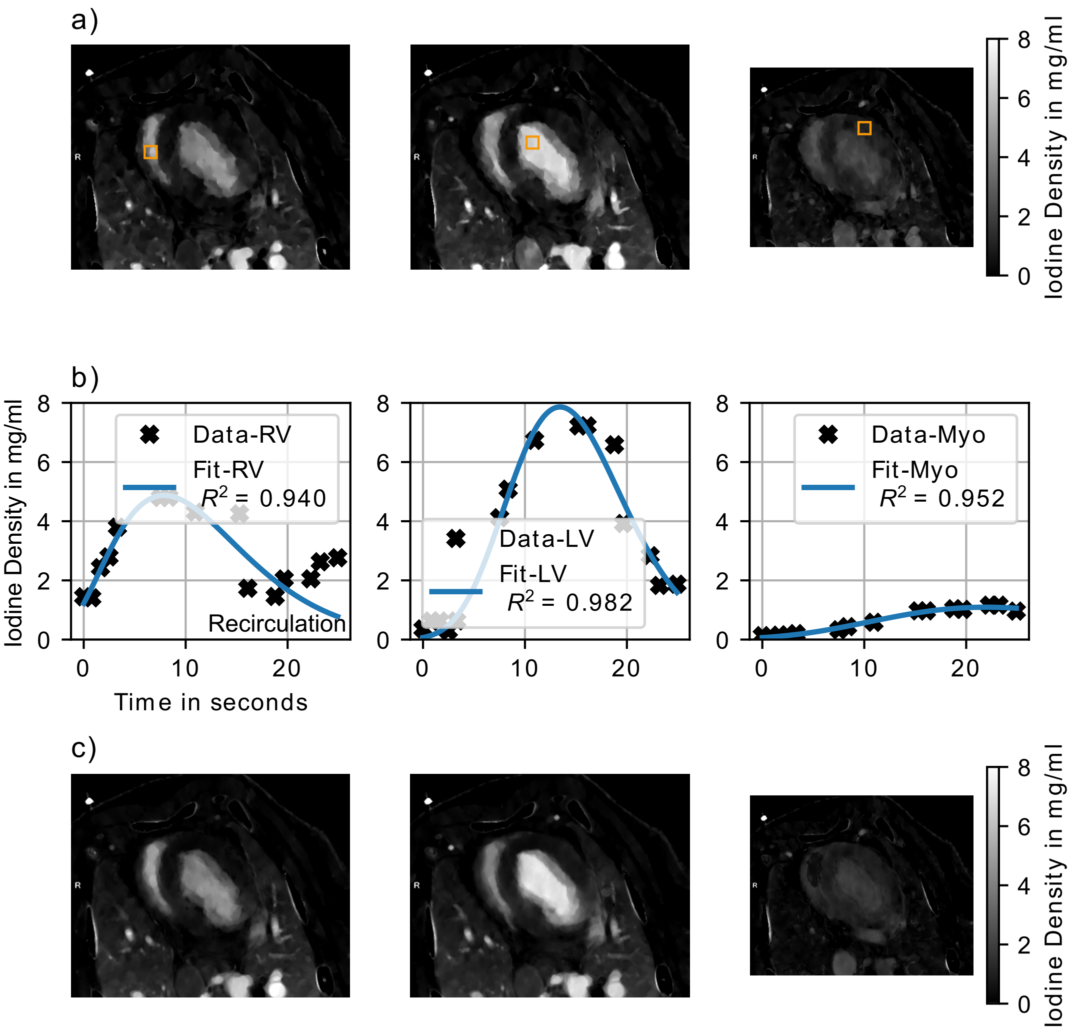

**Figure 3.22:** **a** Measured transversal quantitative iodine density slices of the porcine thorax showing a subsequent opacification within the RV and LV as well as the Myocaridum (Myo). **b** Iodine density values vs. scan time as obtained from the dynamic dual-energy perfusion CT for an exemplary pixel for various ROI as indicated by yellow boxes in **a**, which were selected by an experienced radiologist. A high accordance of data and fit was obtained using a gamma variate fit model. Note that only the first pass of contrast agent was considered, and blood recirculation was correspondingly neglected for the fit. **c** Transversal quantitative iodine density slices of the porcine thorax obtained from the model agree with the measured data, as shown in **a**. Note that distinctive discrepancies in late scan times arise from the neglect of recirculation. Figure reproduced from [Sch+19].

In the next step, the fitted data was used to derive the absolute, quantitative iodine peak enhancement, perfusion, time to peak, and volume maps as depicted in Figure 3.23, using the maximal slope method [MG03]. A peak enhancement value (Figure 3.23 a), which is given as the maximal absolute increase in iodine density within the measured time frame, of 0.92 mg/ml (11.86 % of the value found in the descending aorta) was determined within the myocardium. The corresponding perfusion value (Figure 3.23 b), i.e. the maximal slope of the temporal iodine density curve, was determined to be 0.085 mg/ml/s. This value amounts to only 6.7 % of the value found within the descending aorta, contingent on a limited influx of contrast agent through the coronary arteries in combination with a slow uptake/diffusion within the dense muscular tissue. Interestingly, similar values were found in the ventral region of the lungs. As expected for a healthy animal, the time to peak map (Figure 3.23 c) indicates simultaneous and consistent perfusion throughout the entire myocardium, approximately 4 to 5 seconds after the bolus passes through the descending aorta. Only a small ventral region with a delayed maximal opacification was found. However, as depicted in the very right line plot in Figure 3.22-b, the iodine density itself only yields minimal changes within the timeframe of 16 to 24 seconds. Finally, the overall volume of iodine perfusing the porcine thorax was calculated by integrating the temporal iodine density curves. As the myocardial enrichment remains high for late scan times and a flush out of iodine from the muscle is relatively slow in comparison to vascular and ventricular heart structures, the fitted curves were integrated within a timeframe of 50 seconds (so that the iodine density drops below a threshold value of 0.25 mg). Here, a value of 29.89 (mg/ml)×s was calculated within the myocardium, which accounts for 29.43 % of the volume dwelling in the aorta. An overview of all perfusion parameters for various exemplary locations in the thorax is given in Table 3.1.

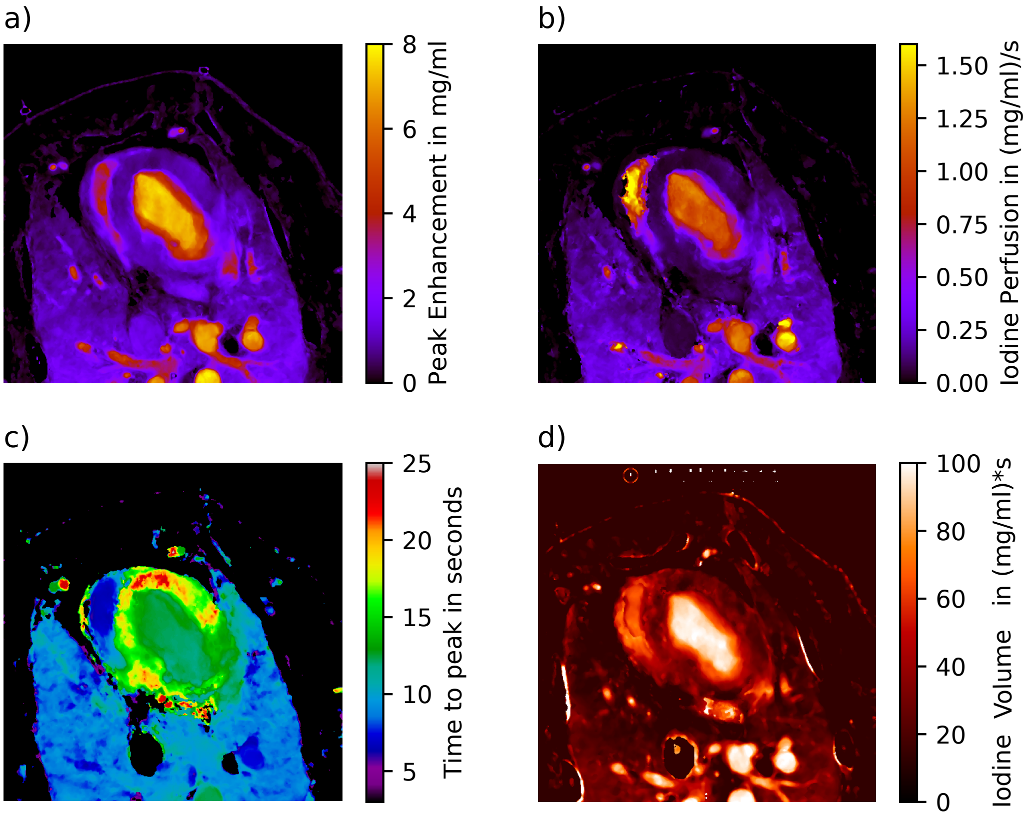

**Figure 3.23:** Absolute and quantitative iodine-based analysis of myocardial dynamics: **a** peak enhancement, **b** perfusion, **c** time to peak and **d** volume maps of the porcine thorax, derived from the gamma variate fit model using the slope method. The peak enhancement indicates the maximal increase in iodine density, the perfusion relates to the highest temporal gradient in the influx of iodine, and the time to peak indicates the point in time when maximal peak enhancement is reached. The iodine volume is related to uptake/storing/flush out behavior within the respective structures. Note that areas where the gamma variate fit failed (for instance in the cava inferior) or areas, where the iodine density remained below 0.55 mg/ml during the scan, are color-coded black. Figure reproduced from [Sch+19].

**Table 3.1:** Quantitative iodine-based peak enhancement, perfusion, time to peak and iodine volume of the myocardium compared to the heart, lungs, and arteries.

| | **Peak Enhancement** [mg/ml] | **Iodine Perfusion** [mg/ml/s] | **Time to Peak** [s] | **Iodine Volume** [(mg/ml)*s] |
|---|---|---|---|---|
| Myocardium | 0.92 | 0.085 | 17.12 | 29.89 |
| Left Ventricle | 7.52 | 1.269 | 12.39 | 96.77 |
| Right Ventricle | 3.77 | 1.561 | 6.72 | 62.73 |
| Descending aorta | 7.76 | 1.232 | 12.26 | 98.19 |
| Ventral Lung | 1.01 | 0.19 | 8.66 | 17.26 |
| Pulmonary artery | 6.92 | 1.25 | 9.83 | 95.93 |

The simultaneous analysis of all perfusion parameters allows for a specific diagnosis of myocardial disorders: a reduced peak enhancement with a normal time-to-peak value indicates scarred/fibrotic myocardium, limiting the absolute capacity of the myocardium, while in the presence of a delayed peak value, an ischemic disorder is considered [FJR15]. Further, the perfusion pattern, which is related to the temporal change of blood flow in both volume and velocity, is thereby a good indicator of a blocked or limited supply of blood through the coronary arteries. Therefore, quantitative CT perfusion of the myocardium assessed by absolute iodine concentration measurements over time has the potential to significantly increase the performance of CT for the detection of myocardial ischemia in patients with ischemic heart disease. The blood volume (or, in this case, the iodine volume map) gives additional information on the overall blood intake capacity, its storing as well as the flush-out behavior.

A major drawback of a precise flow dynamics analysis is the necessity of a sufficient temporal sampling of the iodine density curve. This implies acquisitions before and during iodine contrast enrichment until myocardial saturation is reached, which poses concerns with respect to radiation dose. For an initial assessment of the myocardial blood flow (for instance in case of a screening modality or when myocardial ischemia is uncertain), we propose to derive the quantitative, iodine peak enhancement map from a semi-static two-shot approach in stress and/or rest without the need of modeling/fitting the data. For this, two scans are obtained in the myocardial saturation phase (in this case at 23.3 and 24.9 seconds). To obtain a homogeneous pattern within the myocardium, the corresponding two iodine densities are averaged and smoothed by a minor Gaussian blur (to mimic the fitting routine). Finally, to directly calculate the peak enhancement, an offset value from literature or a control measurement is subtracted. Note that in a conventional HU-based assessment an arterial curve must be obtained in order to normalize data, which however is obsolete in the case of quantitative, absolute iodine density values. Figure 3.24 a,b compare the ground truth peak enhancement map of the fully sampled scan with the one obtained by the two-shot acquisition method, respectively. The peak enhancement values within the ventricles and arteries are underestimated by far. However, in the case of the saturated myocardium, the two-shot approach yields very similar values to the model. The relative error within the peak enhancement (Figure 3.24 c) accounts for values in the range of 5 to 15% and is considerably homogeneous within the overall myocardium.

Note that the remaining dynamics parameters as derived by the maximum slope method remain not assessed, as here the precise onset as well as saturation of iodine throughout the myocardium must be tracked in time.

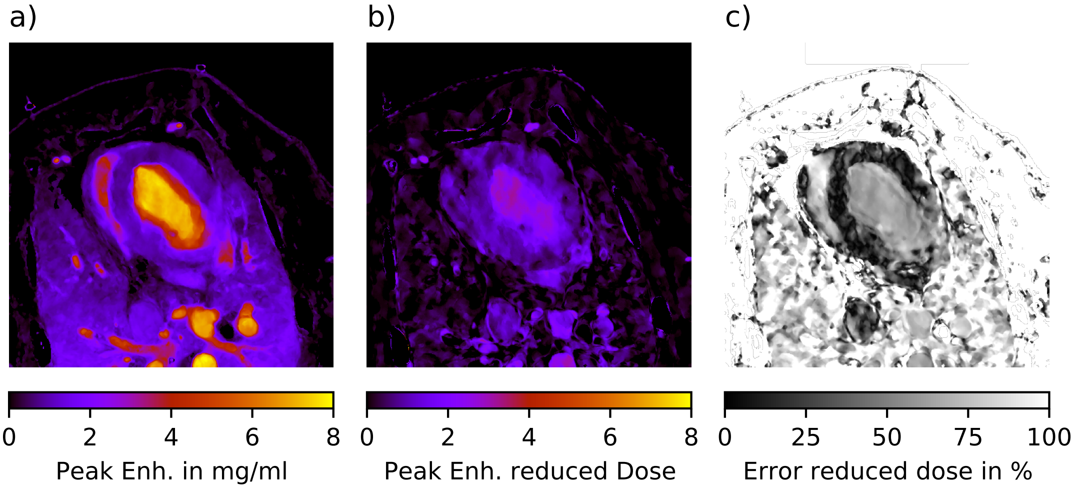

**Figure 3.24: a** Quantitative iodine-based peak enhancement of the porcine thorax as derived from the dynamics analysis based on 15 scans. **b** Quantitative iodine-based density peak enhancement of the porcine thorax as derived from a semi-static two-shot approach during myocardial contrast saturation. Notice that arterial and ventricular structures are strongly underestimated in comparison to **a**. **c** Relative error in the determination of the peak enhancement of **b** in comparison to the ground truth **a**. Within the myocardium, the deviation is quite homogeneously patterned and accounts for values in the range of 5 to 15%. Figure reproduced from [Sch+19].

### 3.4.5 Discussion

Within this study, we showed that by using a state-of-the-art dual-energy perfusion CT imaging technique, it is possible to deduce absolute iodine-based flow dynamics of the heart, arteries, and myocardium in a pig model. This allows for an assessment of the functional properties of the latter quantitatively. Thereby, major advantages arise in comparison to conventional HU-based diagnosis: firstly, the increase in image contrast during perfusion is most pronounced in the iodine density map, helping with a better visual assessment of the myocardium and potential ischemic or infarcted regions. This allows for a more rigid fit of the imaging data, as well as the potential to reduce the amount of contrast agent and radiation dose. Secondly, the image values examined by the radiologist are not affected by beam hardening artifacts and hence are independent of factors such as patient size and variations between different CT platforms, facilitating a value-based assessment. Finally, the obtained image data is quantitative, which renders an acquisition and consequent normalization with an arterial curve unnecessary, provided that the concentration of contrast agent with respect to patient characteristics is reliably controlled. Given the establishment of an extensive clinical database comparing iodine-based dynamical indicators for various myocardial dysfunctions, in both stress and rest, we believe that DECT may allow for a fast, rigid, highly sensitive, and specific assessment of heart diseases.

However, an essential requirement for the establishment of such a database and using data without normalization is that the quantitative iodine densities present in the human myocardium can be measured precisely and in a reproducible manner. In the presented animal study, a volume of 40 ml of Ultravist 300 (Ultravist 300, Bayer, Bayer AG, Leverkusen, Germany) was injected and an offset-adjusted iodine density of 0.92 mg/ml found within the myocardium. Note that the corresponding iodine in-vivo concentration of 154 mg/kg body weight, is well below volumes typically applied in clinical routine. In a study comparing various dual-energy scanners Sellerer et al. demonstrated, by using an abdominal phantom and mimicking various patient sizes, that even low iodine concentrations below 1 mg/ml (dependent on underlying dual-energy technique and patient size) can be reliably measured with a relative error around 10% only [Sel+18]. Older studies reported similar values, i.e. a constant absolute error of 0.1 mg/ml in case of iodine concentrations below 1 mg/ml [Li+13]. Given a relative increase of iodine density within the healthy myocardium of 575% (0.16 mg/ml to 1.08 mg/ml) during contrast uptake within our study, the accuracy of modern systems can be considered sufficiently high.

We further demonstrated that a semi-static two-shot approach yields a deviation of 5 to 15% in the iodine peak enhancement value in comparison to one derived from the full scan. Ensuing from previous studies showing that ischemic and infarcted regions of the myocardium exhibit a 23% and 47% decreased mean iodine density, we believe that the quantitative semi-static approach may not be highly specific, however may be a good first indicator for myocardial malfunction (e.g. in case of a reduced peak enhancement or delayed time to peak value) in an initial assessment [Sán+16]. Further, previous studies on quantitative iodine perfusion implied the usage of 60 ml of Ultravist 370 (approximate iodine concentration of 317 mg/kg-bodyweight) resulting in an iodine density of 2.56 mg/ml within the healthy myocardium [Sán+16]. As we found a value of approximately 1 mg/ml in the myocardium (iodine concentration of 154 mg/kg-bodyweight) which can be reliably measured with modern DECT systems and allows for meaningful modeling of the data, we believe that a reduction of applied iodine volume/concentration by a factor of 2 is possible.

Finally, in this animal study, 15 scan points were used for the analysis, in order to model early enrichment of arteries and ventricles, accounting for a CTDIvol of 15 × 9 mGy equalling 135 mGy. In a clinical setting when only the myocardium is of interest, early scan times after the injection can be neglected and an equidistant sampling of myocardial perfusion slope and saturation with 8 to 12 points is generally sufficient. Correspondingly a CTDIvol of 72 to 108 mGy can be expected, being well below a critically considered value of 250 mGy.

The purpose of this experiment is considered a proof of principle investigation. As the DECT technique offers several advantages regarding quantitative image results using iodine contrast agent, the main point of our manuscript focuses on an initial investigation of quantitative perfusion measurements. The added value of this study is to show the advantage of quantitative iodine density maps in comparison to conventional CT images. In terms of the improved CNR and the relative signal enhancement using contrast agent density maps in DECT perfusion imaging, our results are relevant to several clinical perfusion use cases with animals or even humans. Indeed, the improvement of clinical diagnosis should be considered in further statistically meaningful studies with the benefit of various patient groups and myocardial disorders in rest and stress conditions. This will permit the establishment of a valid database of quantitative iodine-based hemodynamic parameters. Hereby it will be of essential importance to clarify which of the quantitative hemodynamic indicators are of major diagnostic importance. Further, within this study a dual-layer IQon Scanner (Philips Healthcare, The Netherlands) was used, providing a detector coverage of 4 cm only. A spatially limited examination of the heart (especially the myocardium) however bears the risk of overlooking locally confined flow defects.

## 3.5 IntelliSpace Discovery perfusion plugin

The browser-based ISD platform enables the generation of plugins and provides a simple data transfer from the PACS and an integrated dicom viewer to display the plugin results. The ISD platform is a research platform and not a clinical product. Several plugins were integrated into the ISD platform in recent years. A detailed description of the plugin development and usage can be found in the TUM Wiki: "IS Discovery: Using Spectral Plugins":

`https://wiki.tum.de/display/CTRM/IS+Discovery%3A+Using+Spectral+Plugins`

Different models for perfusion quantification are defined in Section 3.2. Having a different amount of free parameters, the models vary strongly in the execution time for the model fit. The GVF model with 4 free parameters is very slow, and one voxel can be fitted in approximately 1.3 seconds. In comparison, the MP model with 2 free parameters like the one-compartment model used performs the fit in approximately 0.01 seconds. To fit a dynamic dataset of 512 × 512 × 100 voxels, a sequential voxel-wise fitting approach is impractical and would take several hours even for the simple 2-parameter models. The

matrix size of 512 × 512 will presumably give way to bigger sizes like 1024 through increased resolution in modern PCCT systems. Therefore, a parallel fitting approach needs to be implemented using GPU powered parallel fitting of TAC. The Multi-Thread-Optimization library was used to implement a parallel fitting approach. By running the fitting on a workstation connected to the internal clinical network, the ISD platform can be used to fit the dynamic perfusion datasets. The most recent version of the fitting package can be found here:
`https://gitlab.lrz.de/e17/ctperfusion/-/tree/VSR?ref_type=heads`
The perfusion map computation routine can be described by the fitting of a 4D input dataset. The GVF model is used in this example and must be performed per each voxel. There are two ways to formulate the GVF function, a regular and simplified model [Mad92; CN04]. The regular form involves fitting 4 parameters, while the simplified form uses parameter estimations and reformulation to decrease the number of free parameters to one. It is possible to fit both function forms. The simplified form is less computationally expensive. However, first results show a decrease in fit accuracy compared to the regular GVF function (see Subsection 3.2.1). This can be partially explained by instabilities in the parameter estimation routines due to the noise. The perfusion map computation process can be divided into three phases: pre-processing, fitting, and the actual perfusion map calculations. The pre-processing step consists of two parts. The first part aims to identify valid voxels, as voxels outside the investigated area of interest do not need to be processed. The second part estimates initial fit parameters for each voxel out of observed data points. Some of those parameters may stay fixed during the fitting process, depending on how many parameters are fitted for. Note, that the regular GVF fitting does not use these estimates and has default fixed initialization values. The next step is the actual fitting routine. Here a Multi Thread Optimization (MOT) library is used named OpenCL, which is specifically designed for solving many small-scale problems. MOT suits the task of GVF very well. As an optimization algorithm, the Levenberg Marquardt (LM) optimizer is used with numerical derivatives and boundary constraints. LM does not support constraints, but constraints can be imposed as high penalties in the objective function. LM tries to minimize the least square error in order to get the best GVF parameters. GPU memory is the biggest constraint on how many fits can be processed in parallel. To avoid out-of-memory errors, a batching mechanism is implemented. One of the crucial points in the fitting process is the linear search for the $t_0$ parameter. It is necessary because the GVF is of non-converging nature when $t_0$ is off (± 3 to 4 time units) from the solution. This can happen due to the discontinuities and undefined values. The linear search for $t_0$ tackles this problem by initializing the $t_0$ parameters to several specific time points. After each initialization, fitting is performed in quick mode, where the optimizer is limited to 5 iterations only. All parameters are stored in an array during the linear search. Parameters are updated when a specific $t_0$ initialization yields a better fit performance (smaller least square error). At the end of the $t_0$ search, a full fit is performed, where the optimizer has a higher optimization step count limit. One big disadvantage of the $t_0$ linear search is the increased execution time. The perfusion map computation is the last step of the pipeline. It starts by taking the fit parameters and resampling the GVF function from $t_0$. Resampled data points are transferred to the GPU kernels to calculate the perfusion maps. Each GPU kernel operates on one voxel and outputs several perfusion map values

and statistics. The final results are reshaped into the original volume dimensions. This step also supports batching to avoid out-of-memory errors. Future projects should focus on the integration of the current routine to Docker. The involved MOT library has a complex structure. This complexity forces us to divide the routine into three steps, as it is not fully customizable. That comes with the big disadvantage of moving Central Processing Unit (CPU) data to GPU multiple times. The linear search algorithm for $t_0$ involves fitting multiple times under different initializations. The CPU GPU data transfer burden is more crucial in this case. MOT uses numerical derivatives by default. Numerical derivative calculation involves executing the objective function 2 times and approximating the derivative. Analytical derivatives can speed up this process. Unfortunately, the initial attempts to integrate GVF function derivatives into the MOT pipeline were not successful to this point.

When using the ISD platform for dynamic perfusion analysis, it is self-evident that an automated image registration step is needed. The first results using the Fast Elastic Image Registration (FEIR) algorithm [Kab+09; Kab+10] on porcine data showed promising results. The FEIR algorithm can be used to register the conventional HU-based dynamic perfusion datasets. The deformable vector fields can then be applied to spectral datasets like the iodine density maps.

# Osteoporosis Imaging

# 4

This chapter focuses on the opportunistic diagnosis of osteoporosis using spectral detector technology. The results of SDEXA are published in “Comparison of volumetric and areal bone mineral density in CT and scout scans using spectral detector technology“ [Ham+23] (see page vii). Compared to the original publication, the text has been slightly modified to achieve a better integration into this doctoral thesis.

## 4.1 Diagnostics for osteoporosis: the treatment gap

With an aging population worldwide, osteoporosis and resulting fragility fractures become a socio-economic burden, resulting in an increasing need for early diagnosis and treatment [Cly+20]. Twenty-two million women and 5.5 million men were estimated to have osteoporosis [Her+13] in the European Union, but only a minority of patients receive treatment [GL15; McC+21]. This phenomenon is called the treatment gap for osteoporosis. In the United States, after an osteoporotic fracture, only 9% of the patients underwent consecutive osteoporosis testing [Cly+20]. The WHO reference standard for diagnosing osteoporosis is the DEXA technique applied to the femur neck or lumbar spine [AZ18]. The aBMD is determined by spectrally separated measurements using a K-edge filter and varying acceleration voltages. The marginal diagnostic rate may be a result of reduced sites with DEXA availability and therefore limited screening possibilities [Mil16]. To overcome this treatment gap along with the huge socioeconomic burden of fractures in older people, universal access to such facilities should be supported [Com20]. Other available X-ray based techniques are the 3D Quantitative Computed Tomography (QCT) Volumetric Trabecular Bone Mineral Density (vBMD) assessment on conventional CT scanners using a reference phantom. Promising results for the diagnosis with significantly increased osteoporosis detection rates from 17.1 % to 46.4 % for DEXA and QCT, respectively [Li+13] were shown. With the introduction of spectral CT systems, a retrospective, opportunistic, phantom-less quantification of vBMD was made possible by using virtual monoenergetic images for the material decomposition into bone and soft tissue maps [Ros+19; Mei+17; Lau+20; Lau+19; Koc+21]. The niche technology High Resolution peripheral Quantitative Computed Tomography (HR-pQCT) allows the assessment of complementary quality parameters for bone morphology or simulating loading conditions via finite element analysis [Whi+20]. Further methods for the assessment of bone health not relying on X-rays are quantitative ultrasound [GC02] and magnetic resonance imaging [Pha+06] e.g., for quantification of trabecular structures.

In Section 4.2 and Section 4.3 spectral CT scout scans (also called overview or topogram) from a detector-based dual-energy system are used to determine aBMD maps. A projection-based material decomposition is applied to opportunistically determine aBMD values in patients undergoing a CT examination, which is also known as SDEXA [Lau+19; Lau+20]. In principle, DEXA and SDEXA could use almost the same processing. DEXA needs spectral information, which is generated by filtration, while scout scans from a dual-energy

CT system can use a spectral detector to fulfill this task. Both methods then need the calculation of the aBMD and segmentation.

## 4.2 DEXA and SDEXA using the European spine phantom

### 4.2.1 Background

The European Spine Phantom (ESP) is a reference phantom for DEXA and QCT measurements [Kal+95; Kal92; Gen+94]. It is used for quality assurance and stability checks of these systems. The semi-anthropomorphic phantom is equipped with three different vertebral inserts L1 to L3, resembling aBMD values from 0.5 to 1.5 g/cm$^2$ in steps of 0.5 g/cm$^2$. These aBMD values represent the range of osteoporotic to normal bone. The inserts are made of a mixture of calcium Hydroxyapatite (HA) and water-equivalent resin, resembling the attenuation coefficient of soft tissue. The trabecular bone structures contain a HA density of 50, 100, and 200 mg/cm$^3$ for L1 to L3, respectively. The cortical structures are made of HA with a density of 800 mg/cm$^3$. The standard dimension is 260 × 180 × 110 mm in width, depth, and height, respectively. Additional adipose tissue rings can be placed around the phantom to simulate different body sizes. The manufacturing process has an accuracy of 3% within the specified values. A photograph of the ESP is shown in Figure 4.1. The phantom is available from the manufacturer QRM GmbH, Moehrendorf, Germany.

### 4.2.2 Methods

The ESP was scanned on a dual-layer spectral CT system (IQon, Philips Healthcare, Best, The Netherlands) with a tube voltage of 120 kVp and different Dose Length Product (DLP) values ranging from 0.9 to 17.2 mGy×cm in 11 steps (0.9, 1.7, 2.6, 4.3, 6.0, 7.3, 8.6, 10.7, 12.9, 15, 17.2 mGy×cm). The specifications of this device can be found in Section 5. Two scan settings with and without adipose tissue extension rings were used. The ESP was placed in the center of the field of view, and the raw data of the scout view was used to determine the aBMD values from L1 to L3 and the corresponding standard deviations. A scan without the phantom was performed to determine the background signal to correct the absorption from the scanner table. 2D masks of the vertebral bodies were generated using the high-dose measurements and applied to the low-dose measurements. Anterior-Posterior (AP) and lateral scans were performed in all dose settings. aBMD values were determined with and without background correction. To extract the aBMD values from the detector raw data, a tool from the manufacturer (Philips Healthcare, Best, The Netherlands) was used to generate photo and Compton images. Using the photo and Compton images, monoenergetic line integrals $P_{\mathrm{L}}$ and $P_{\mathrm{H}}$ at 50 and 200 keV are calculated for water:

$$P_{\mathrm{L}} = \mu_{\rho,\mathrm{water,photo}}(50) \cdot \rho_{\mathrm{water}} \cdot P_{\mathrm{photo}} + \mu_{\rho,\mathrm{water,compton}}(50) \cdot \rho_{\mathrm{water}} \cdot P_{\mathrm{compton}} \tag{4.1}$$

$$P_{\mathrm{H}} = \mu_{\rho,\mathrm{water,photo}}(200) \cdot \rho_{water} \cdot P_{photo} + \mu_{\rho,\mathrm{water,compton}}(200) \cdot \rho_{water} \cdot P_{compton} \tag{4.2}$$

$\mu_{\rho,\mathrm{water,photo}}(50, 200)$ and $\mu_{\rho,\mathrm{water,compton}}(50, 200)$ are the photoelectric and Compton attenuation coefficients of water at 50 and 200 keV, respectively. $P_{\mathrm{photo}}$ and $P_{\mathrm{compton}}$

**Figure 4.1:** A photograph of the ESP.

are the photoelectric and Compton data extracted from the detector. Monoenergetic line integrals $P_{\mathrm{L,ST}}$ and $P_{\mathrm{H,ST}}$ are also calculated for soft tissue. The aBMD values are calculated from the line integrals using the following formula:

$$\mathrm{aBMD} = \frac{-R_{\mathrm{ST}} \cdot P_{\mathrm{H}} + P_{\mathrm{L}}}{\mu_{\rho,\mathrm{bone}}(50) - \mu_{\rho,\mathrm{bone}}(200) \cdot R_{\mathrm{ST}}}, \tag{4.3}$$

where $\mu_{\rho,\mathrm{bone}}(50)$ and $\mu_{\rho,\mathrm{bone}}(200)$ are the mass attenuation coefficients of bone at 50 and 200 keV, respectively. $R_{\mathrm{ST}}$ is the soft tissue correction factor. It is applied to correct the different compositions of the phantom's adipose tissue rings [CNA05]. The so-called soft tissue correction factor can be calculated from the high and low energy measurements directly by using the following formula:

$$R_{\mathrm{ST}} = \frac{P_{\mathrm{L,ST}}}{P_{\mathrm{H,ST}}} \tag{4.4}$$

$P_{\mathrm{L,ST}}$ and $P_{\mathrm{H,ST}}$ are mean values measured in a ROI within pure soft tissue. In patients, the soft tissue correction factor accounts for the different composition of the adipose tissue. Another possibility to account for this is to use literature values for the soft tissue correction factor. The aBMD values were compared to the reference values provided by the manufacturer and DEXA measurements. The DEXA measurements were performed on a GE Lunar Prodigy (General Electric, Fairfield, USA) with a DLP of approximately 1.7 mGy×cm and an acceleration voltage of 76 kVp. The aBMD values were determined using the manufacturer's software. Lateral and AP values were measured using the same scan settings for no adipose tissue ring and the small ring.

### 4.2.3 Results

Figure 4.2 shows a variety of aBMD measurements of the ESP using the IQon spectral CT system without background correction. All measurements performed with a DLP of 6.0 mGy×cm or higher show at least decent image quality. The image quality in AP measurements with ring and lateral measurements with and without ring at a dose of 0.9 mGy×cm are not sufficient to determine the aBMD values. To achieve reasonable image quality, 6.0 or even 8.6 mGy×cm need to be applied in lateral view images with adipose tissue extension rings. With a dose of 6.0 mGy×cm, the image quality is still noisy, but sufficient to determine the mean aBMD values in the vertebral bodies. In lower dose measurements, the material decomposition algorithm fails in a large part of the pixels, leading to biased aBMD values. In Figure 4.3 DEXA images of the ESP are shown. No proper image data is available from the GE Lunar Prodigy, therefore the images from the aBMD report are used.

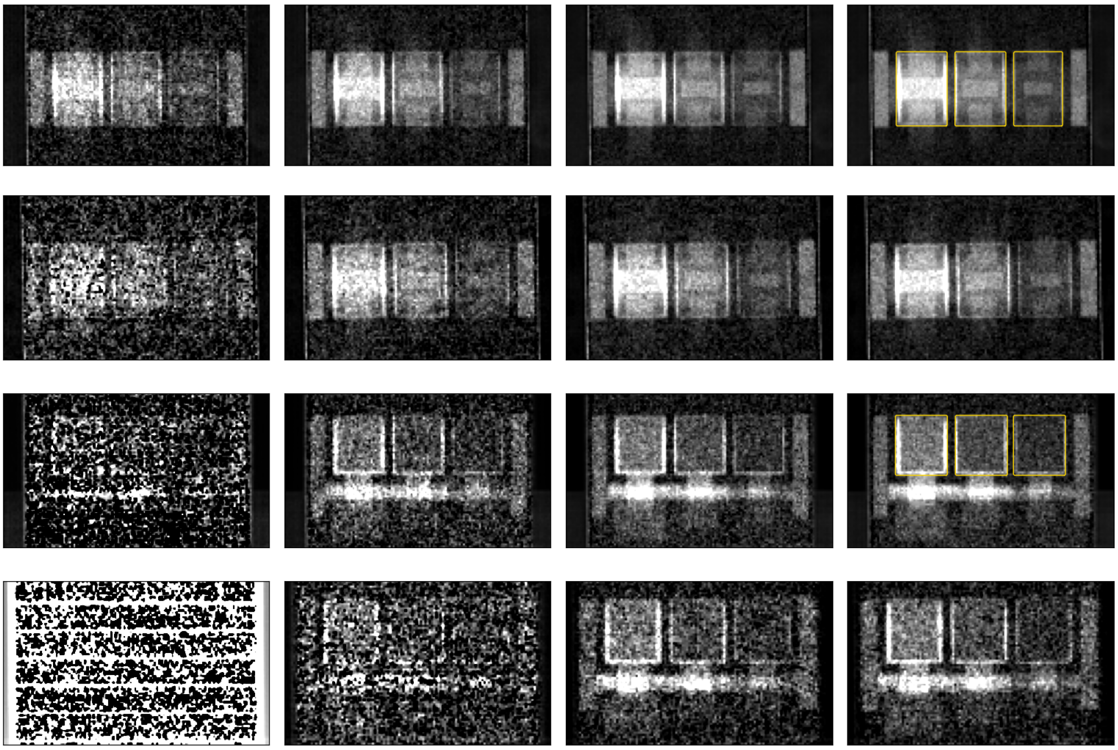

**Figure 4.2:** AP and lateral aBMD measurements of the ESP using the IQon spectral CT system. Dose values of 0.9, 2.6, 6.0, and 8.6 mGy×cm are shown from left to right. The first two rows show the aBMD values without and with adipose tissue ring in AP projection. The third and fourth rows show the corresponding images in lateral projection. All images are windowed to the same scale, ranging from 0.0 to 2.0 g/cm$^2$. Especially in the lateral projection, the aBMD values are very noisy or even not interpretable using the low dose measurements. The applied masks to calculate the aBMD values are plotted as golden lines in the high dose AP and lateral projections.

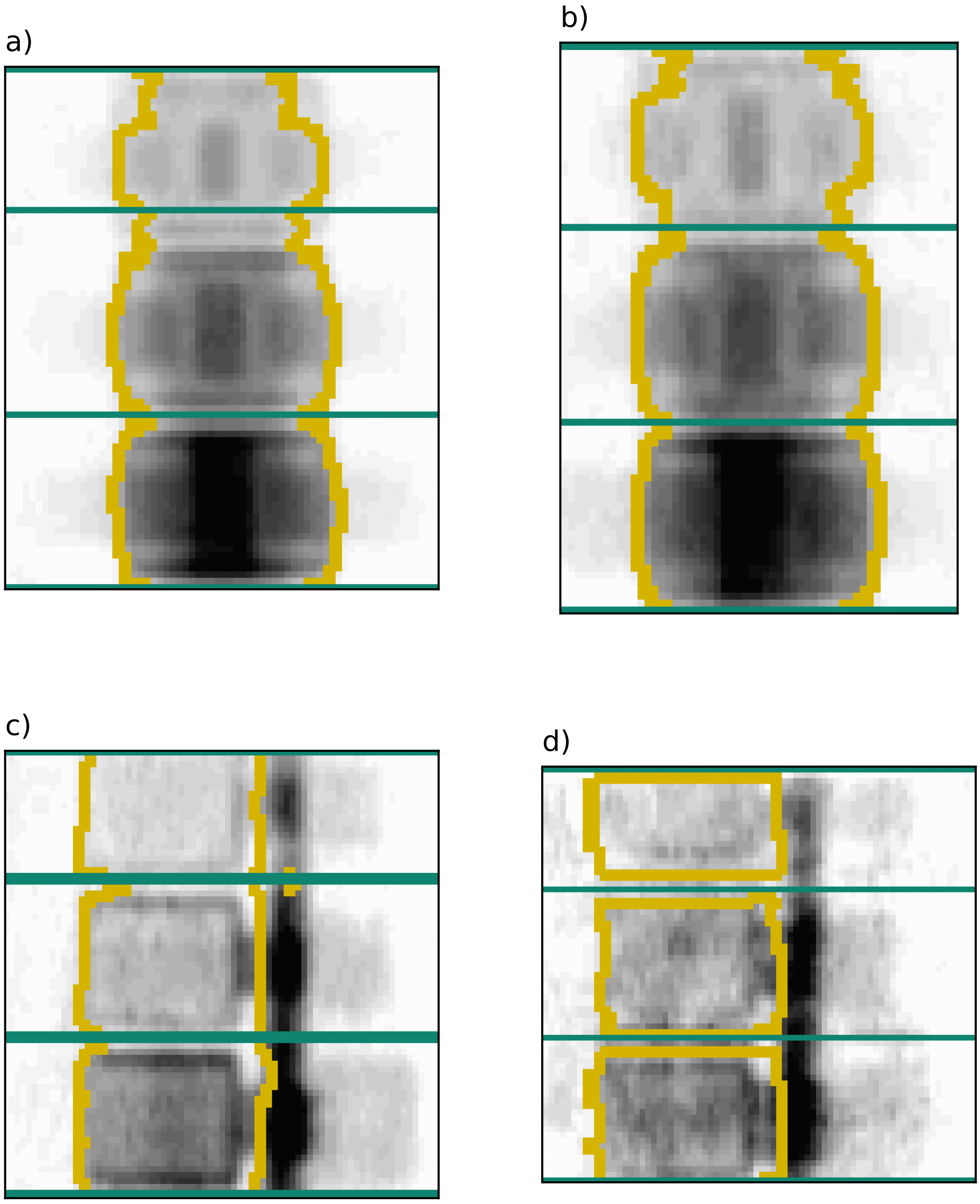

**Figure 4.3:** AP and lateral aBMD measurements of the ESP using the GE Lunar Prodigy. **a** and **b** show images taken in AP projection, **c** and **d** show images taken in lateral projection. **a** and **c** are taken without adipose tissue ring, **b** and **d** are taken with adipose tissue ring. The applied masks to calculate the aBMD values are plotted as golden lines. The green lines are the separating lines between the different vertebral bodies. It is only possible to extract the aBMD report and no measurement data from the GE Lunar Prodigy. The images included in the report are used for this figure, and no colorbars can be displayed. Further, it should be mentioned, that the images visualize intensity values and not aBMD maps.

It is evident, that the automatically generated masks differ from manually generated masks in Figure 4.2. The masks generated by the manufacturer in AP projection are too small and do not cover the whole vertebral body. In lateral projection, the masks are too large and include parts of the cortical bone structure. The values for AP measurements with extension ring are plotted in Figure 4.4. The aBMD values measured from scout projection images of the IQon and GE Lunar Prodigy are plotted against the reference values provided by the manufacturer.

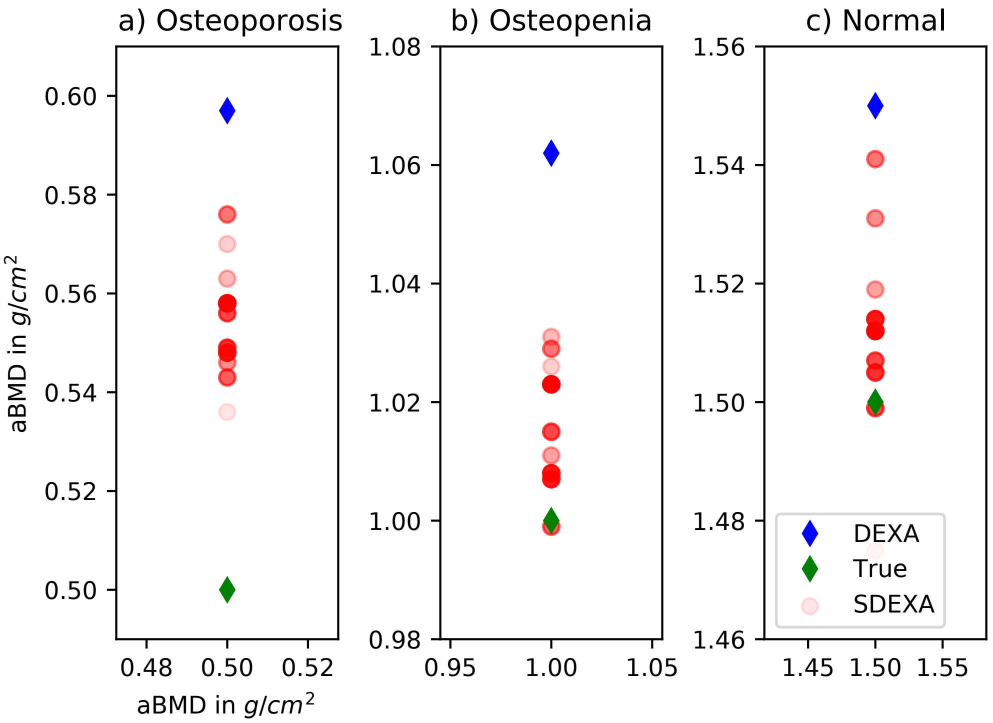

**Figure 4.4:** aBMD values for vertebral bodies L1 to L3 measured in AP projection with extension ring using the IQon scout images, the GE Lunar Prodigy and the reference values provided by the manufacturer. All dose levels measured using the SDEXA method are plotted in red, with the more translucent dots representing the lower dose measurements on a scale. In the osteoporitic aBMD vertebral body L1, the SDEXA and DEXA method overestimate the aBMD at matched dose by 11.6 % and 19.4 %, respectively. L2 and L3 are overestimated by 2.3, 6.2, and 0.8, 3.3 % for the SDEXA and DEXA methods, respectively.

Laterally measured aBMD values without extension ring are plotted in Figure 4.5. As the quality of the lowest dose measurements is not sufficient, the aBMD values are not plotted. The plots of the setting with extension ring in lateral projection and without ring in AP projection are not plotted, but all values can be examined in table Table 4.1. The corresponding deviations in percentage are presented in Table 4.2. DEXA values and deviations are given in Table 4.3. Background correction is not listed, as the deviations are negligible. In AP scans, the maximum deviation at the lowest dose of 0.9 mGy×cm is without an extension ring at L1 3.8 %. The mean deviation at the lowest dose level in all settings is 1.9 %. In lateral scans, no background correction is applied, as the table is present in the field of view.

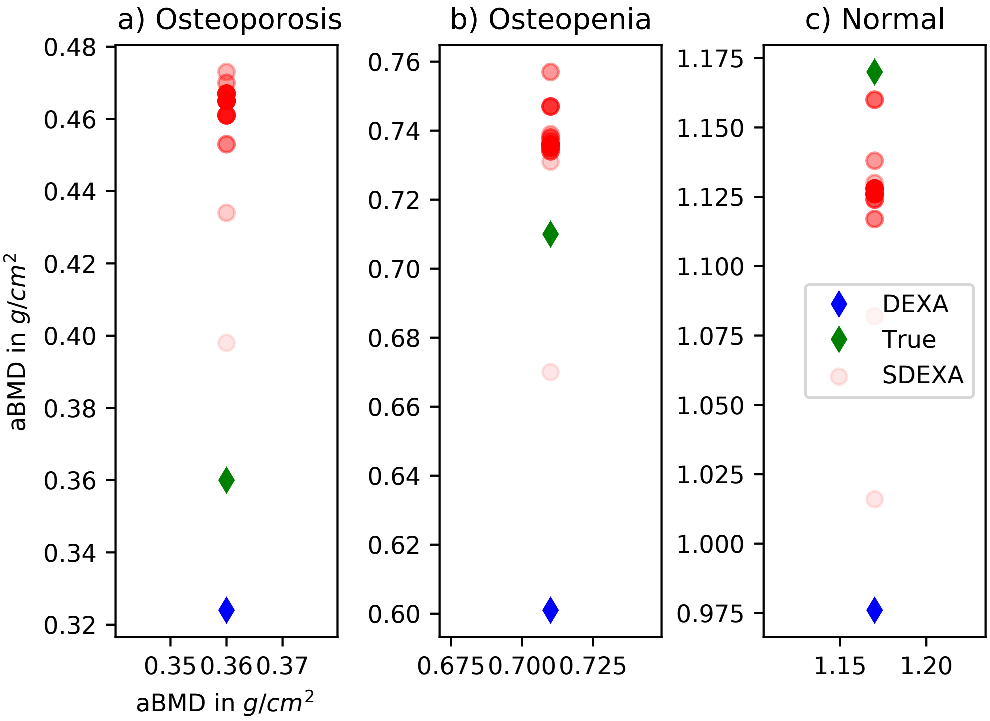

**Figure 4.5:** Equivalent to Figure 4.4 but for lateral measurements without extension ring. In the osteoporitic aBMD vertebral body L1, the SDEXA and DEXA method deviate from the specified aBMD by 29.2 % and -10.0 %, respectively. L2 and L3 are deviating by 3.6, -15.6 and -3.6, -16.6 % for the SDEXA and DEXA method, respectively.

| | S1 | S2 | S3 | S4 | S5 | S6 | S7 | S8 | S9 | S10 | S11 |
|---|---|---|---|---|---|---|---|---|---|---|---|
| CTDIvol [mGy] | 0.02 | 0.04 | 0.06 | 0.11 | 0.15 | 0.18 | 0.21 | 0.26 | 0.31 | 0.37 | 0.42 |
| DLP [mGy*cm] | 0.90 | 1.7 | 2.6 | 4.3 | 6.0 | 7.3 | 8.6 | 10.7 | 12.9 | 15.0 | 17.2 |
| L1 AP nR | 0.56 | 0.59 | 0.55 | 0.56 | 0.57 | 0.55 | 0.56 | 0.55 | 0.56 | 0.56 | 0.57 |
| L1 SD AP nR | 0.30 | 0.25 | 0.20 | 0.19 | 0.19 | 0.18 | 0.18 | 0.17 | 0.18 | 0.17 | 0.17 |
| L2 AP nR | 0.97 | 0.97 | 0.98 | 0.97 | 0.98 | 0.97 | 0.98 | 0.96 | 0.96 | 0.97 | 0.97 |
| L2 SD AP nR | 0.41 | 0.36 | 0.34 | 0.32 | 0.30 | 0.30 | 0.30 | 0.30 | 0.30 | 0.30 | 0.30 |
| L3 AP nR | 1.46 | 1.48 | 1.50 | 1.50 | 1.50 | 1.50 | 1.51 | 1.49 | 1.50 | 1.49 | 1.51 |
| L3 SD AP nR | 0.57 | 0.54 | 0.53 | 0.51 | 0.51 | 0.50 | 0.50 | 0.49 | 0.50 | 0.50 | 0.49 |
| L1 AP sR | 0.54 | 0.57 | 0.56 | 0.56 | 0.55 | 0.58 | 0.54 | 0.56 | 0.55 | 0.55 | 0.56 |
| L1 SD AP sR | 0.53 | 0.34 | 0.28 | 0.23 | 0.21 | 0.20 | 0.20 | 0.20 | 0.18 | 0.18 | 0.18 |
| L2 AP sR | 0.90 | 1.03 | 1.03 | 1.01 | 1.01 | 1.03 | 1.00 | 1.02 | 1.01 | 1.01 | 1.02 |
| L2 SD AP sR | 0.68 | 0.44 | 0.40 | 0.35 | 0.33 | 0.33 | 0.33 | 0.33 | 0.31 | 0.31 | 0.31 |
| L3 AP sR | 1.15 | 1.48 | 1.50 | 1.52 | 1.53 | 1.54 | 1.50 | 1.51 | 1.50 | 1.51 | 1.51 |
| L3 SD AP sR | 1.03 | 0.62 | 0.57 | 0.56 | 0.53 | 0.54 | 0.53 | 0.52 | 0.53 | 0.52 | 0.52 |
| L1 LAT nR | 0.02 | 0.40 | 0.43 | 0.47 | 0.47 | 0.45 | 0.47 | 0.46 | 0.46 | 0.47 | 0.46 |
| L1 SD LAT nR | 1.48 | 0.44 | 0.36 | 0.30 | 0.28 | 0.27 | 0.27 | 0.24 | 0.24 | 0.24 | 0.23 |
| L2 LAT nR | 0.26 | 0.67 | 0.73 | 0.74 | 0.76 | 0.74 | 0.74 | 0.73 | 0.75 | 0.74 | 0.74 |
| L2 SD LAT nR | 1.55 | 0.52 | 0.52 | 0.44 | 0.40 | 0.40 | 0.40 | 0.37 | 0.38 | 0.35 | 0.38 |
| L3 LAT nR | 0.31 | 1.02 | 1.08 | 1.13 | 1.14 | 1.12 | 1.16 | 1.12 | 1.13 | 1.13 | 1.13 |
| L3 SD LAT nR | 2.30 | 0.74 | 0.59 | 0.54 | 0.52 | 0.51 | 0.53 | 0.49 | 0.47 | 0.48 | 0.48 |
| L1 LAT sR | 0.25 | -0.04 | 0.37 | 0.43 | 0.46 | 0.48 | 0.43 | 0.48 | 0.46 | 0.47 | 0.48 |
| L1 SD LAT sR | 8.39 | 2.72 | 0.76 | 0.46 | 0.38 | 0.36 | 0.32 | 0.32 | 0.32 | 0.29 | 0.26 |
| L2 LAT sR | -0.37 | 0.01 | 0.52 | 0.72 | 0.70 | 0.72 | 0.71 | 0.75 | 0.74 | 0.75 | 0.72 |
| L2 SD LAT sR | 9.22 | 3.41 | 1.09 | 0.56 | 0.49 | 0.46 | 0.46 | 0.44 | 0.42 | 0.40 | 0.38 |
| L3 LAT sR | 1.48 | -0.60 | 0.90 | 1.07 | 1.14 | 1.11 | 1.14 | 1.14 | 1.12 | 1.14 | 1.14 |
| L3 SD LAT sR | 8.93 | 4.88 | 1.37 | 0.68 | 0.62 | 0.53 | 0.56 | 0.55 | 0.52 | 0.51 | 0.51 |

**Table 4.1:** aBMD values at different dose levels (Scan 1 to Scan 11)in different settings in g/cm$^2$. The mean and SD are calculated in AP and lateral (LAT) views with small ring (sR) and no ring (nR). The aBMD values provided by the manufacturer are 0.5, 1.0, and 1.5 g/cm$^2$ in AP view and 0.36, 0.71, and 1.17 g/cm$^2$ in lateral view. The SD values are calculated as the standard deviation of the pixels included in the mask. Negative values, especially in the lateral view, are due to the fact, that low dose measurements do not provide enough statistics to perform a material decomposition accurately. This is also visible in Figure 4.2. Figure 4.4 and Figure 4.5 plot the aBMD values L1 to L3 of AP sR and LAT nR, respectively.

|  | S1 | S2 | S3 | S4 | S5 | S6 | S7 | S8 | S9 | S10 | S11 |
|---|---|---|---|---|---|---|---|---|---|---|---|
| CTDIvol [mGy] | 0.02 | 0.04 | 0.06 | 0.10 | 0.15 | 0.18 | 0.21 | 0.26 | 0.31 | 0.37 | 0.42 |
| DLP [mGy*cm] | 0.90 | 1.70 | 2.60 | 4.30 | 6.00 | 7.30 | 8.60 | 10.70 | 12.90 | 15.00 | 17.20 |
| L1 AP nR | 12 | 18 | 10 | 12 | 14 | 11 | 12 | 11 | 11 | 12 | 14 |
| L2 AP nR | -3 | -3 | -2 | -3 | -2 | -3 | -2 | -4 | -4 | -3 | -3 |
| L3 AP nR | -3 | -1 | 0 | 0 | 0 | 0 | 1 | -1 | 0 | 0 | 0 |
| L1 AP sR | 7 | 14 | 13 | 12 | 9 | 15 | 9 | 11 | 10 | 10 | 12 |
| L2 AP sR | -10 | 3 | 3 | 1 | 1 | 3 | 0 | 2 | 1 | 1 | 2 |
| L3 AP sR | -23 | -2 | 0 | 1 | 2 | 3 | 0 | 0 | 0 | 1 | 1 |
| L1 LAT nR | -94 | 11 | 21 | 31 | 31 | 26 | 30 | 28 | 28 | 30 | 29 |
| L2 LAT nR | -64 | -6 | 3 | 4 | 7 | 4 | 4 | 3 | 5 | 4 | 4 |
| L3 LAT nR | -74 | -13 | -8 | -3 | -3 | -5 | -1 | -4 | -4 | -4 | -4 |
| L1 LAT sR | -31 | -112 | 4 | 18 | 27 | 34 | 20 | 34 | 28 | 31 | 32 |
| L2 LAT sR | -152 | -99 | -27 | 1 | -1 | 2 | 1 | 6 | 4 | 6 | 2 |
| L3 LAT sR | 27 | -151 | -23 | -8 | -2 | -5 | -3 | -3 | -4 | -3 | -2 |

**Table 4.2:** The SDEXA deviations from specified aBMD in %.

|  | aBMD | Deviation |
|---|---|---|
| L1 AP nR | 0.61 | 23 |
| L2 AP nR | 1.07 | 7 |
| L3 AP nR | 1.57 | 5 |
| L1 AP sR | 0.60 | 19 |
| L2 AP sR | 1.06 | 6 |
| L3 AP sR | 1.55 | 3 |
| L1 LAT nR | 0.32 | -10 |
| L2 LAT nR | 0.60 | -15 |
| L3 LAT nR | 0.98 | -17 |
| L1 LAT sR | 0.40 | 10 |
| L2 LAT sR | 0.68 | -5 |
| L3 LAT sR | 0.90 | -23 |

**Table 4.3:** The aBMD values from DEXA in g/cm$^2$ and the deviation from the specified aBMD in %.

### 4.2.4 Discussion

The results show that the SDEXA approach can quantify the aBMD in the ESP phantom more accurately than the applied DEXA measurements. A disadvantage of the DEXA measurements is the automated segmentation of the ESP phantom, which cannot segment the phantom correctly. This is especially visible in the lateral view, where the segmentation of the phantom exceeds the vertebral geometry. Using the SDEXA approach, the segmentation is performed manually on the high-dose image, allowing for more accurate segmentation of the phantom. When looking at the comparable dose levels of 1.7 mGy×cm corresponding to 40 $\mu$Gy in SDEXA and 37 $\mu$Gy in DEXA, the SDEXA approach is more accurate than the DEXA measurements in all settings except for L1 to L3 determination in lateral view with a small ring. Here, the low dose level of 1.7 mGy×cm is insufficient to provide a sufficient amount of photons being detected in the dual layer detector, which is used in the SDEXA approach. At higher dose levels, the SDEXA approach can provide more accurate results and is superior to the DEXA measurements for osteopenic and normal bone densities. For the osteoporotic vertebral body L1, a constant overestimation of approximately 30% is visible for the SDEXA approach with the small and no ring setting. In the analysis applied for SDEXA the cortical bone structures are included in the segmentation. In projection space, the cortical structures give rise to high aBMD values. This is especially important for the L1 vertebral body measurement, as the cortical bone structures with 800 mg/ml HA density deviates most from the trabecular area with 50 mg/ml. In conclusion, a dose adaptation for SDEXA should be applied when measuring patients in different settings. In AP view, the applied DLP of 1.7 mGy×cm can be sufficient to correctly determine the aBMD. Only when dealing with very adipose patients, a higher dose level might be necessary. In lateral view, a higher dose level of 4.3 mGy×cm should be applied, especially when dealing with adipose patients. For highly adipose patients, even higher dose levels might be necessary. To avoid too high dose levels, AP measurements should be considered for highly obese patients. Also, the following CT examination should be considered when determining the dose level for SDEXA measurements. Preferably, the SDEXA dose should not exceed 10% of the following CT examination.

## 4.3 Comparison of volumetric and areal bone mineral density

Most parts of this section are published in [Ham+23] (see page vii).
**Background**: To determine whether denoised aBMD measurements from scout scans in spectral detector CT correlate with volumetric trabecular BMD for opportunistic osteoporosis screening.
**Methods**: A 64-slice single-source dual-layer spectral CT scanner was used to acquire scout scan data of 228 lumbar vertebral bodies within 57 patients. Scout scans in AP view were performed with a dose of 0.06 mSv and spectrally decomposed into aBMD values. A spectral dictionary denoising algorithm was applied to increase the SNR. vBMD was determined via material decomposition. A 3D convolutional network for image segmentation and labeling was applied for automated vBMD quantification. Projected maps were used to compare the classification accuracy of AP and lateral scout scans.

**Results**: The denoising algorithm led to the minimization of anticorrelated noise in spectral maps and an SNR increase from 5.23 to 13.4 ($p$-value $< 0.002$). Correlation analysis between vBMD and measured AP aBMD, projected AP, and lateral aBMD showed a Pearson correlation coefficient of 0.68, 0.81, and 0.90, respectively. The sensitivity and specificity for the osteoporosis classification task were higher in lateral projection images than in AP crystallizing in an increased AUC value of 0.99 versus 0.90.

**Conclusion**: Denoised material-specific aBMD maps show a positive correlation to vBMD enabling spectral scout scans as an opportunistic predictor for osteoporotic patients. This could be applied routinely as a screening tool in patients undergoing a CT examination.

### 4.3.1 Objectives

Our study explores an approach to automated BMD testing for radiology departments. First, we show how to calculate aBMD data and present a denoising algorithm improving the SNR of aBMD results. Denoising is applied, as scout acquisitions are conducted with a very low dose, and additionally, material decomposition introduces anti-correlated noise onto the aBMD material maps. As a standard of reference, spectrally determined vBMD values from the subsequent CT measurements are used, allowing the generation of projected aBMD masks from CT data to obtain a matched comparison between vBMD and aBMD. In clinical routine, a direct comparison of vBMD/QCT and SDEXA is hardly possible on a detailed level since CT systems and DEXA systems require different patient positioning. With our approach using the same CT system, where we compare SDEXA with vBMD, we know the beam geometry and position. This allows us to match vBMD with SDEXA in a more precise way. In comparison to Laugerette et al. [Lau+19; Lau+20], where phantom measurements and fracture differentiation on scout measurements were analyzed, we investigated the correlation between measured aBMD and vBMD. Further, we generate projected aBMD images in AP and lateral views from the spectral CT data and compare the osteoporosis classification accuracy for both views. The aim of this study was to reveal that SDEXA measurements are suited as osteoporosis markers, likewise volumetric BMD, and to assess the correlation between these BMD measurement methods.

### 4.3.2 Methods

#### Study design and patient selection

In this retrospective study, 57 patients aged 17 to 80 with an average of 43 years and a gender distribution of 23 female and 34 male subjects were included. From the initial population, two subjects were excluded because of the overlay of intravenous or oral contrast agents on scout images in the lumbar spine region. This causes severe overestimation of aBMD values. Further, 10 patients with low-quality AP scout scans were excluded from the analysis, as no dose adaptation was used for larger patients. All examinations were performed between March and September 2021, as the automated segmentation tool anduin [Löf+20b] was maintained and offline after that period. Further statistical verification with an increased patient population is in the pipeline.

### Protocol settings

A standard CT abdomen protocol with a fixed tube voltage of 120 kVp and an exposure of from 20 to 122 mAs per rotation (1.80 to 10.5 mGy CTDIvol) was used on a 64-slice single source dual-layer CT scanner with a detector coverage of 4 cm and a rotation time of 0.33 seconds (IQon, Philips Healthcare, Best, The Netherlands). The specifications of this device can be found in Section 5. Scout scans were acquired with a peak tube voltage of 120 kVp and a tube current of 30 mA. The CTDIvol and dose length product (estimated dose converted from 2D to 3D) are approximately 0.06 mGy and 3.5 mGy×cm ($<$ 0.06 mSv, k=0.015 for abdomen and pelvis) in scout measurements and on average 7.2 mGy and 400 mGy×cm ($\approx$ 6.0 mSv, k=0.015 for abdomen and pelvis) in abdomen CT protocols. Spectral raw data were reconstructed using a standard soft tissue filter kernel (type B) with an axial slice thickness of 0.9 mm. The isotropic pixel spacing in the x-y-plane ranged from 0.56 to 0.97 mm physical distance between the center of each pixel (generated with IntelliSpace Portal 11.0, Philips Healthcare, Best, The Netherlands).

### Denoising in material selective images

Anticorrelation noise appears on material decomposed images with structural correlation [KKK88; Mec+17]. An algorithm by Mechlem et al. was adapted to reduce noise amplification in spectral material maps [Mec+17]. The anticorrelated noise contribution can be minimized by a weighted addition of spectral maps generating a reference image at a certain energy where anticorrelated noise maximally cancels out. We refer to this as the minimum noise image. Dictionary denoising separates image features from noise by using a sparse representation by natural image patches. These so-called dictionary atoms are linearly combined to fit the original noisy image. Dictionary denoising on the minimum noise image was applied to identify structures and edges. Denoised basis material images were calculated by applying a local linear transformation to the processed minimum noise image.

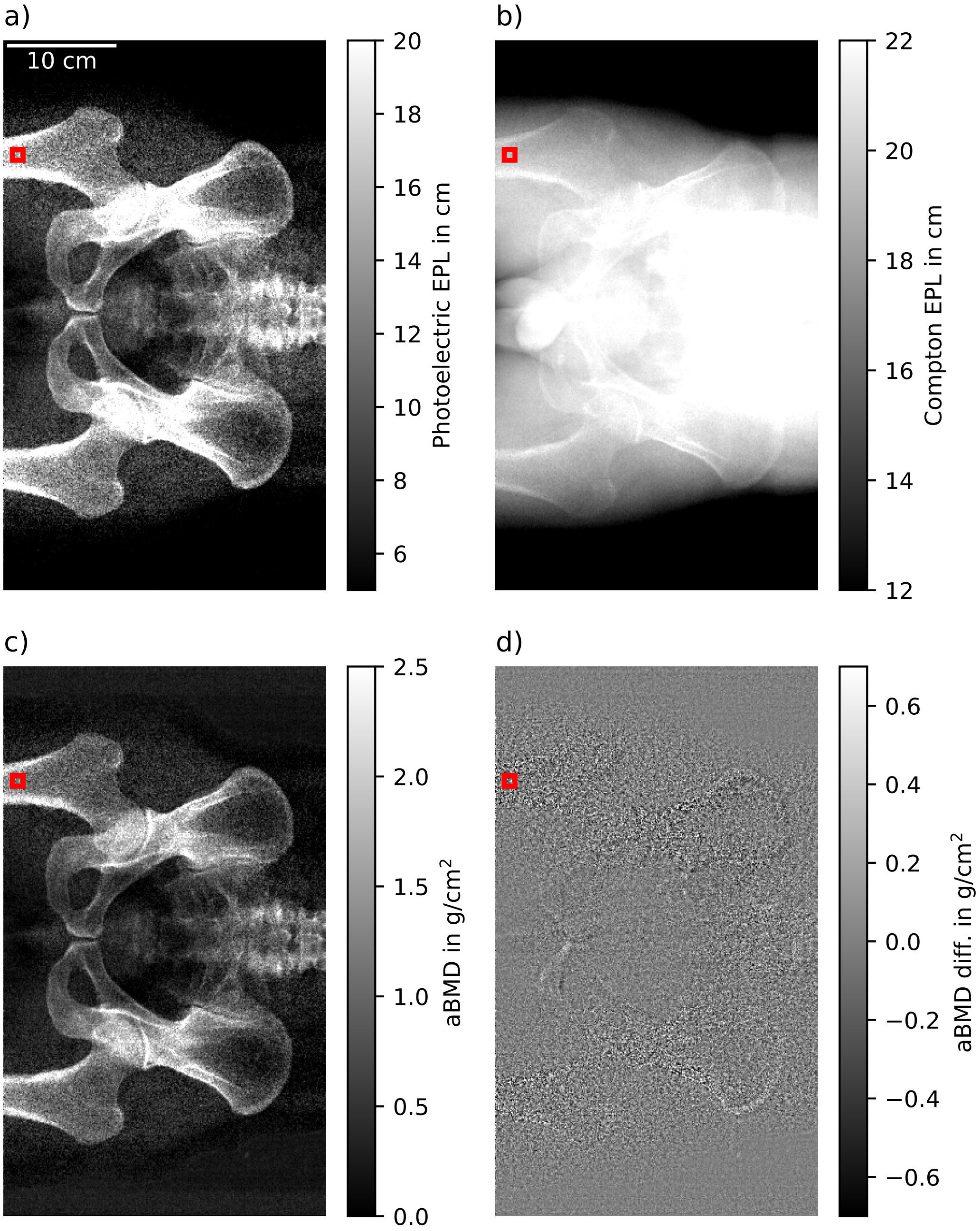

**Figure 4.6:** Overview of spectral maps. The photoelectric **a** and Compton **b** water Equivalent Path Length (EPL) images are combined to generate an aBMD map **c** in every patient. The aBMD maps can be generated from raw photoelectric and Compton images or by using the denoised EPL data. Subfigure **d** shows the difference image of the aBMD map generated from raw and denoised spectral maps. An increased difference can be observed in bone regions like the hip or femur. Figure adapted from [Ham+23].

### Bone mineral density calculation

Figure 4.7 gives a schematic overview of how measured and projected results were calculated. To generate aBMD (Figure 4.7 f and Figure 4.6 c) maps from spectral scout scans, a raw data extraction tool from the CT machine manufacturer was provided. Using the raw data files from the scanner, water EPL, photoelectric and Compton images (Figure 4.6 a and b) and resultant virtual monoenergetic projection values can be determined (refer to electronic supplementary material in [Lau+19]). No soft tissue correction factor was applied, as it resulted in an aBMD offset for patients with oral and intravenous contrast agents in the ROI selected for soft tissue correction. 2D masks corresponding to aBMD images for the quantification of vertebra-specific aBMD values are generated automatically. For this, the freely available bonescreen anduin research tool [Löf+20b] was used to generate a labeled CT segmentation (Figure 4.7 c yellow mask) of all vertebral bodies within the scout-associated CT measurement. The labeled vertebral bodies can be distinguished in trabecular and cortical voxels. The trabecular mask is used as an input to the forward projection algorithm, which creates projected scout scans from CT images (Figure 4.7 e) [All+19]. The forward projection algorithm is implemented using the appropriate CT geometry parameters and a banana-shaped detector focused on the focal spot of the X-ray tube. A fan angle of 52.5 degrees covers 512 detector columns. In z-direction, a scanning approach is simulated, where the patient is moved through a collimated beam with a coverage of four detector pixels in z-direction. By adjusting the projection angle to 0 or 90 degrees, AP and lateral scout images can be projected. Volumetric BMD (Figure 4.7 c) images as well as 3D spine masks (Figure 4.7 c yellow mask) can serve as input for the projection algorithm. By projecting the vBMD maps, artificially generated aBMD maps in lateral and AP views were generated for every patient. Correlation and classification analysis was performed on those projected aBMD maps, as well as measured aBMD maps from spectral scout images. To obtain a trabecular-based 2D mask for aBMD quantification on scout measurements (Figure 4.7 f yellow mask), projected aBMD maps (Figure 4.7 e) together with an image registration step were used. The open-source software SimpleITK [Yan+18; Low+13] served as an affine and translatory registration library. An aBMD value for lumbar vertebral bodies L1 to L4 was obtained in all patients. The volume of interest to calculate a spectral vBMD was automatically segmented using the trabecular CT masks obtained from the bonescreen anduin research tool (Figure 4.7 c yellow mask). vBMD maps were generated by a material decomposition from virtual monoenergetic images (Figure 4.7 a and b) into hydroxyapatite and water maps (Figure 4.7 c and d) via the solution of the following linear equation system:

$$\begin{pmatrix} \mu_{50} \\ \mu_{200} \end{pmatrix} = A \cdot \begin{pmatrix} \rho_{\text{water}} \\ \rho_{\text{bone}} \end{pmatrix} = \begin{pmatrix} \left(\frac{\mu}{\rho}\right)_{\text{water}}(50) & \left(\frac{\mu}{\rho}\right)_{\text{bone}}(50) \\ \left(\frac{\mu}{\rho}\right)_{\text{water}}(200) & \left(\frac{\mu}{\rho}\right)_{\text{bone}}(200) \end{pmatrix} \cdot \begin{pmatrix} \rho_{\text{water}} \\ \rho_{\text{bone}} \end{pmatrix}, \quad (4.5)$$

where $\mu_{50/200}$ are the attenuation coefficients at monoenergetic images 50 and 200 keV, $(\mu/\rho)_{\text{water/bone}}(50/200)$ are the mass attenuation coefficients of water and bone at 50 and 200 keV, and $\rho_{\text{water/bone}}$ are the hydroxyapatite and water maps. Three different approaches for measuring the patient-specific aBMD value were compared to the spectrally assessed trabecular vBMD (Figure 4.9):

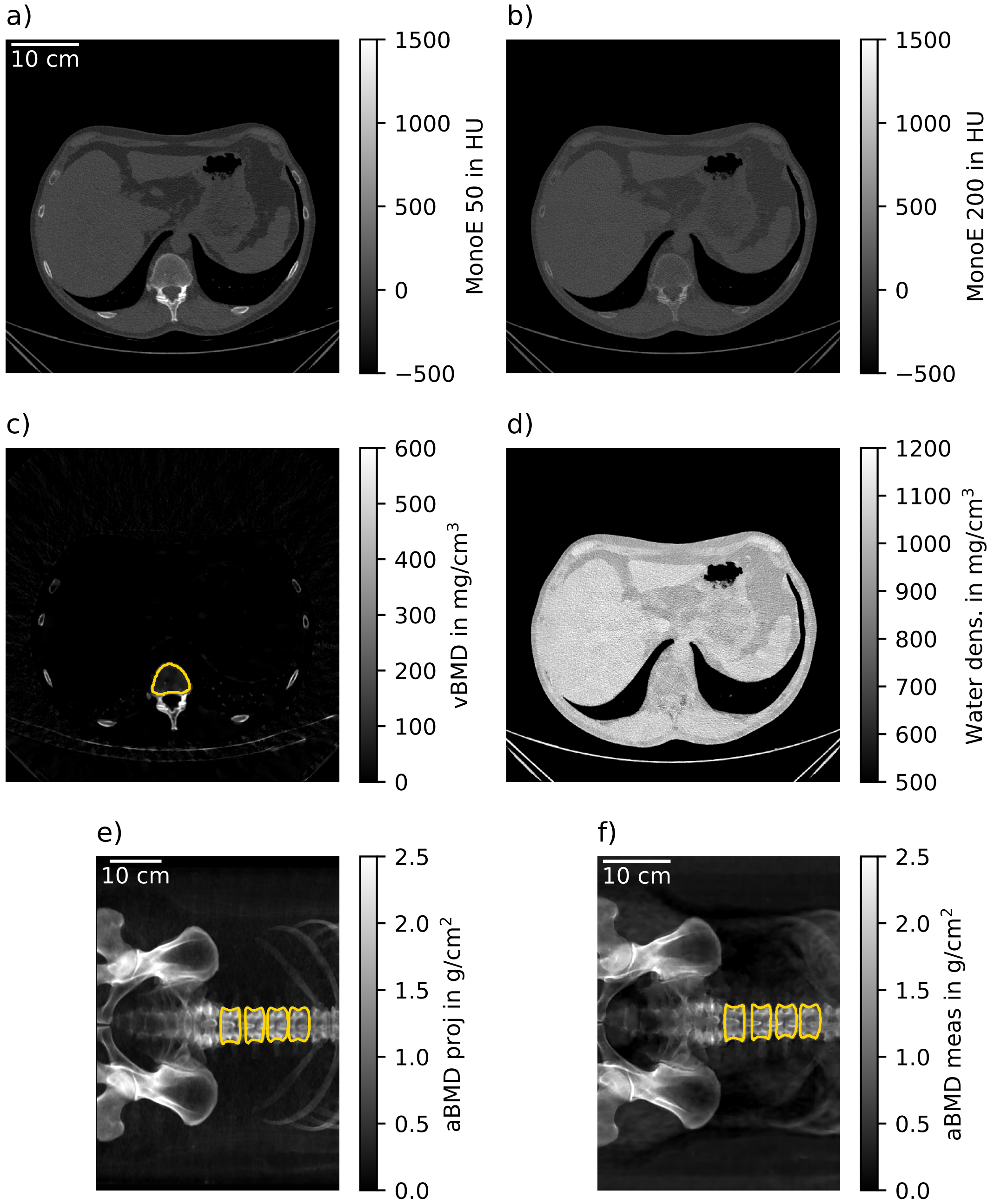

**Figure 4.7:** Schematic of BMD quantification in 3D and 2D data. Subfigures **a** and **b** visualize the monoenergetic images at 50 and 200 keV at the same windowing in a certain slice. By solving the linear equation system given in Equation 4.5 in every voxel, vBMD **c** and water maps **d** are calculated. The yellow mask in subfigure **c** visualizes the trabecular bone mask generated with the anduin tool. Subfigure **e** shows the AP projected aBMD map and projected borders of the trabecular mask. Subfigure **f** is the aBMD map calculated directly from the spectral scout measurement, overlaid with the borders of the projected and registered trabecular mask. Figure adapted from [Ham+23].

- SDEXA using denoised spectral scout measurements along with material decomposition into bone (aBMD) and water images (Figure 4.9 a),
- AP projected aBMD from vBMD maps equivalent to measured aBMD (Figure 4.9 b),
- Lateral aBMD projections preventing the overlay of trabecular structures with the spinal process (Figure 4.9 c and e).

#### Statistical analysis

The open-source scientific computing library for Python, SciPy [Vir+20] was used to calculate a linear least-squares regression to correlate the 3D with 2D BMD measurements. The slope, intercept, Pearson correlation coefficient, and $p$-value for a hypothesis test whose null hypothesis is that the slope is zero were obtained. Further, the standard error of the estimated slope was assessed, and a 95% confidence interval on slope and intercept was calculated by using a two-sided inverse student's $t$-distribution. In addition, a two-sided T-test for the null hypothesis that two independent samples have identical mean values was used. To compare the classification accuracy of aBMD measurements, a ROC for a binary classification task was consulted [Ped+11]. The AUC was calculated by a general function for integration using the trapezoidal rule.

### 4.3.3 Results

#### Denoising in material selective images

The SNR in a homogenous soft tissue ROI without bone contribution could be significantly increased for photoelectric images (p-value $< 0.002$) from a mean value of 5.23 to 13.4. No significant increase could be observed in the equivalent ROI in Compton images (p-value $> 0.05$). The noise reduction algorithm shows qualitatively superior performance in regions with bone contribution (Figure 4.6 d), which is more problematic to quantify, as homogenous bone regions are hard to obtain in scout images. In an ROI of a patient's femur (Figure 4.6 red squares), an SNR increase from 6.16 to 28.7 was determined in photoelectric EPL images and 3.93 to 18.7 in aBMD images. A line plot through the red square region was assessed in Figure 4.8-a. The two peaks, especially visible in the photoelectric EPL line, illustrate the cortical bone, whilst the dip in between corresponds to the cancellous bone. The dashed, and solid lines show the line profile along the denoised and raw datasets in photoelectric and Compton EPL images. The solid blue line visualizes the profile along the weighted addition or minimum noise image, which is similar to the conventional result from an integrating detector. It is important that the weighted addition of raw spectral images and denoised datasets are alike. This is shown by the equal course of the solid and dotted blue lines. Figure 4.8-b shows a histogram obtained for pixel values from the red square ROI in Figure 4.6. illustrating the noise suppression of the denoising algorithm. The translucent histograms correspond to raw data, whilst the dense histograms show denoised data. The EPL changes for Compton and combined datasets are small, indicated by the result of no significant increase in the SNR. The standard deviation in photoelectric images differs strongly. Figure 4.8-c indicates the anticorrelation characteristic of spectral results. The Pearson correlation coefficient in the bone and soft tissue ROI equals -0.80 and -0.93. No significant anticorrelation ($p > 0.05$) was obtained in denoised spectral maps. Figure 4.8-d equivalent to Figure 4.8-a plots the profile in the aBMD map for raw and denoised data. As the contribution of photoelectric EPL maps is much larger for aBMD calculation than the Compton contribution, the noise suppression due to the spectral denoising algorithm derivatives from the photoelectric EPL behavior in Figure 4.8-a. The denoising step alters the mean per patient measured aBMD densities to a small extent only, with a maximum per patient deviation of 1.7 %.

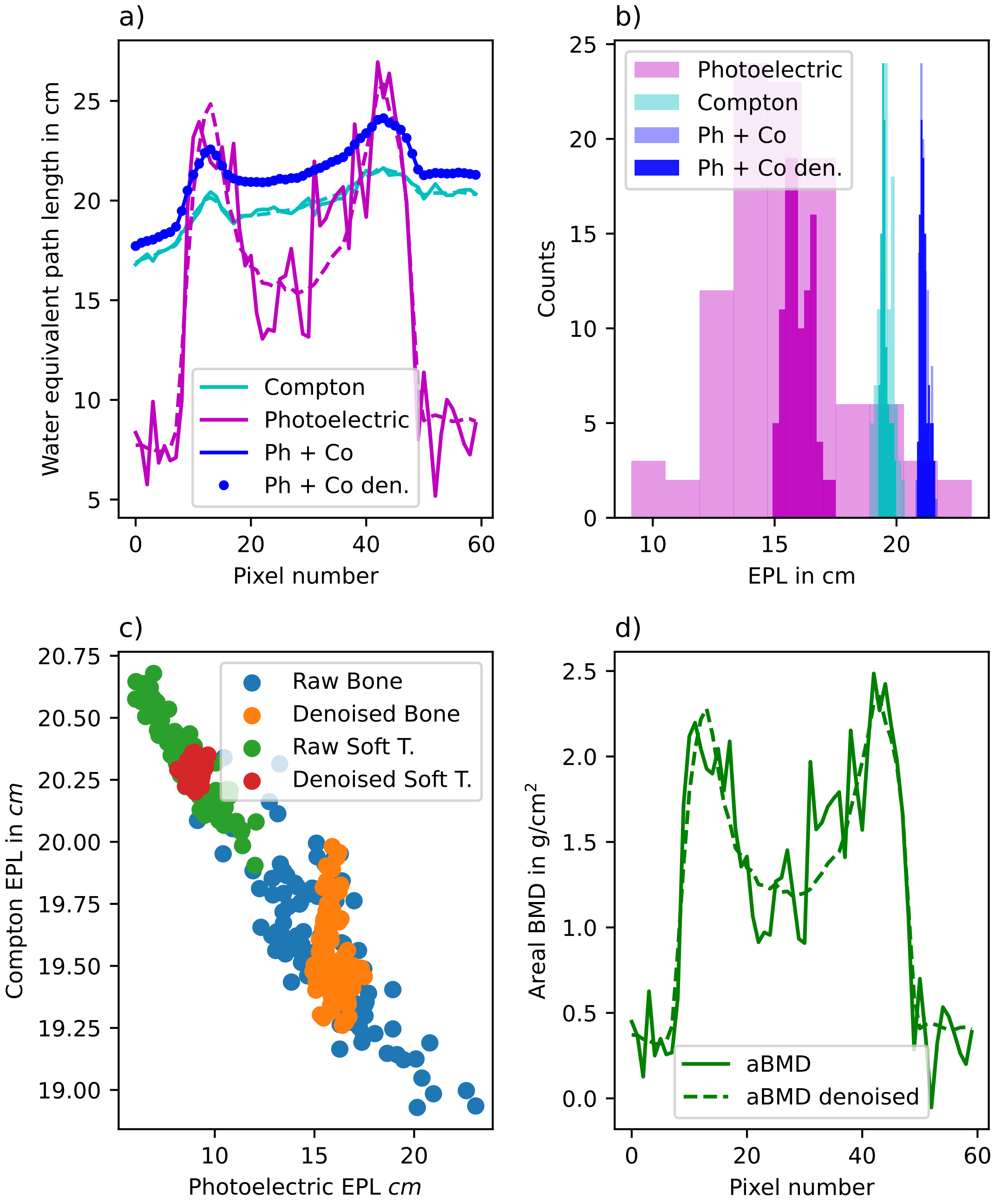

**Figure 4.8:** Behavior of anticorrelated noise and spectral denoising. Subfigure **a** visualizes the line profile through the femur bone in a representative patient. The raw data is plotted using a solid linestyle, while denoised line profiles are plotted with dashed lines or dotted in the case of weighted addition (Ph + Co). Subfigure **b** shows a histogram of photoelectric, Compton, and weighted combination for raw (translucent) and denoised (opaque) bone data in a ROI (see red square Figure 4.6). Subfigure **c** reveals a scatterplot of raw and denoised datapoints in a soft tissue and bone ROI. The anticorrelation of spectral maps and the reduction of this behavior by denoising can be demonstrated. Subfigure **d** displays the line profile equivalent like in **a** for aBMD maps generated from spectral data. Figure adapted from [Ham+23].

### Correlation analysis

The spectral trabecular vBMD served as a ground truth classification of the osteoporotic status in every patient, with a BMD $< 80$ mg/ml being classified as osteoporotic, leading to 6 female and 1 male out of 57 patients being classified as osteoporotic. This threshold was adapted from the American College of Radiology guidelines [oRad18; Sof12]. The correlation coefficient between trabecular vBMD and measured AP aBMD, projected AP aBMD and projected lateral aBMD was found to be 0.68, 0.81, and 0.90, respectively. The calculated slopes and their 95% confidence interval were $113.6 \pm 39.5$, $150.4 \pm 29.7$ and $203.0 \pm 27.2$ in 1/cm. The classification accuracy for projected data was compared on AP and lateral aBMD values (Figure 4.9 d) using the AUC value. The classification on lateral projected aBMD with the reference of spectral trabecular vBMD led to an AUC of 0.99 with a true positive rate of 94% and a false positive rate of 0% using the threshold 0.55 g/cm$^2$. The classification accuracy using projected AP values decreased to an AUC of 0.90 with a true positive rate of 94% and a corresponding false positive rate of 43% using a threshold of 0.93 g/cm$^2$. The ROC was not calculated for scout-derived AP aBMD values, as 4 of 7 osteoporotic individuals had to be excluded because of noisy scout images. Using the threshold BMD $< 120$ mg/ml as classifying osteopenic and osteoporotic patients vs. normal the statistic in scout measurements was sufficient with 19 normal and 23 osteoporotic/osteopenic patients. An AUC of 86% with a true positive rate of 95% and a corresponding false positive rate of 43% using a threshold of 1.22 g/cm$^2$ were measured. The denoising of measured data had no influence on the ROC.

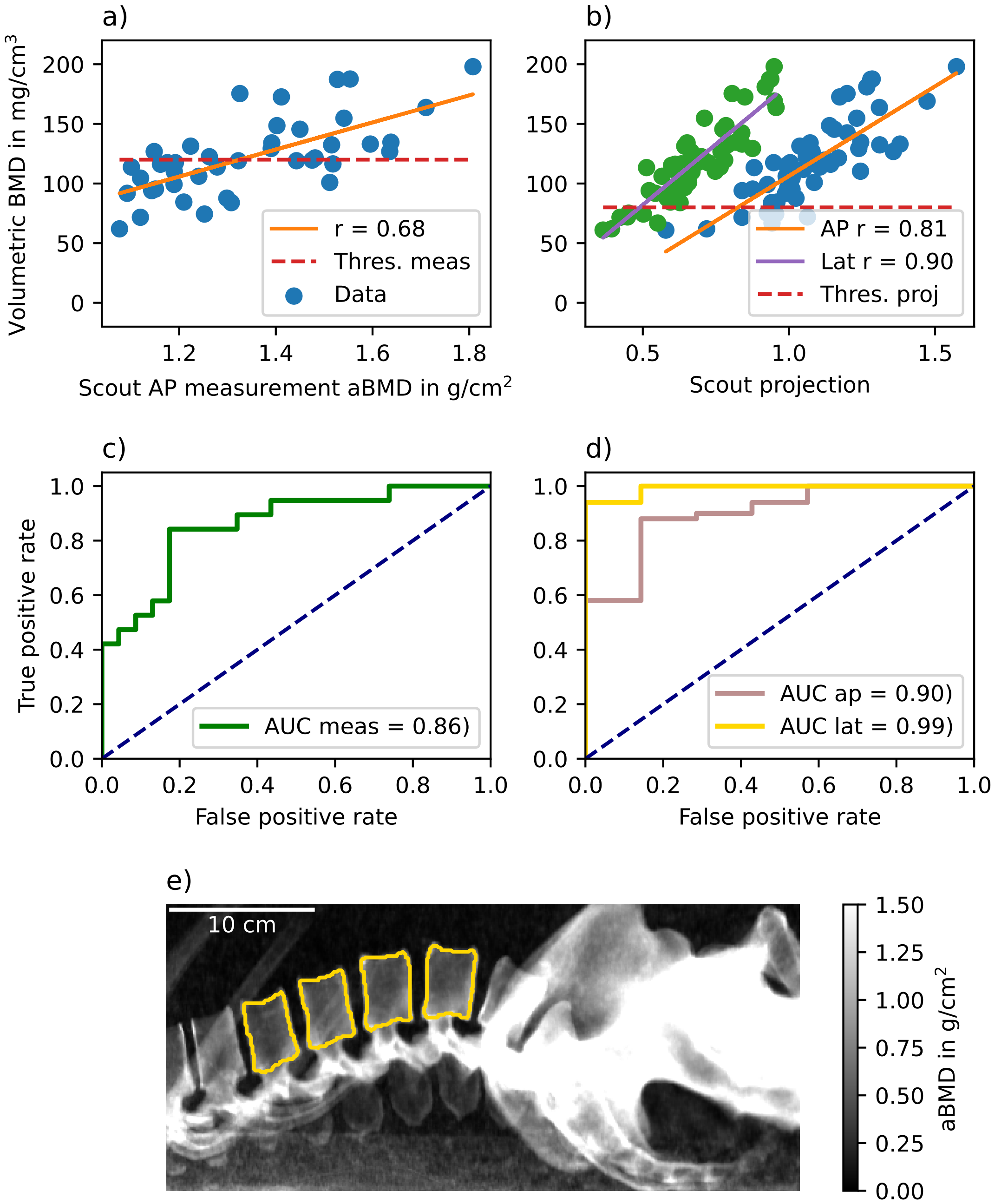

**Figure 4.9:** Correlation and classification analysis of measured and projected aBMD values with trabecular vBMD. **a** The correlation between patient-specific measured AP aBMD and vBMD values with a correlation coefficient $r$ of 0.68. **b** The correlation between AP/lateral projected aBMD values and the vBMD. At ROC analysis, the thresholds 120 and 80 mg/ml were used for measured and projected data, respectively. **c** and **d** The classification analysis on measured and projected aBMD values for correctly classifying osteoporotic patients based on the ground truth of trabecular vBMD values. Subfigure **e** displays an example of a lateral projected aBMD map. Note that one can separate between the trabecular and spinal process structures. Furthermore, an overlay of the rips is visible in lumbar vertebrae L1 and L2. Figure adapted from [Ham+23].

### 4.3.4 Discussion

DEXA is a 2D spectral technique for the assessment of aBMD and is the World Health Organization (WHO) reference standard for diagnosing osteoporosis. Several studies indicate that the volumetric assessment of BMD performs substantially better as a predictor for prevalent and consecutive vertebral fractures compared to DEXA [Löf+20a; Löf+19; Löf+21], where lateral aBMD measurements outperform AP acquisition [Yu+95]. Nevertheless, the radiation dose of a high-quality quantitative CT protocol at the spine is much higher, e.g. about 1.0, and 1.6 mSv for men and women assessed using Monte Carlo calculations, respectively [Eng17]. To avoid unnecessary exposure to patients from CT scans, spectral scout images could be used as a preliminary indicator for osteoporosis. Scout measurements are taken in every patient to select the Field Of View (FOV) for the CT protocol and to apply automated dose modulation. By extending the scout protocol to the lumbar spine region in every patient, aBMD values could be acquired as additional pre-CT information, also in CT protocols where the lumbar spine is not in the FOV. In case of low aBMD values, the CT protocol could be extended to examine the lumbar spine region to perform a follow-up diagnosis of the osteoporosis status. Further studies should focus on how well the SDEXA technique can detect consecutive fractures. For this approach, reasonable image quality must be achieved in scout measurements. Material decomposition algorithms on spectral image data lead to low SNR in material selective images [AS79]. In our work, to decrease image noise originating from anticorrelated noise, photoelectric and Compton EPL images are used as the input to a dictionary-based denoising algorithm. The denoising step showed only minor differences in per patient calculated aBMD and no differences in the ROC analysis on scout data. This is due to measuring a mean value within the vertebral body, averaging the anticorrelated noise introduced by material decomposition. We expect a beneficial effect for denoising, especially for an automated segmentation algorithm. Noise-suppressed images and raw images lead to the same values in the minimum noise image on a pixel level. This indicates that the noise reduction algorithm does not change quantitative absorption values, as it only removes the anticorrelated noise from spectral maps.

The correlation analysis shows a high degree of correlation ($r = 0.68$) between spectrally measured aBMD with trabecular vBMD. Similar studies comparing DEXA with QCT observed $r$-values of 0.61 and between 0.54 and 0.65 [Yu+95; Miy+12], suggesting a similar performance of our method to DEXA. With an AUC value of 86% for distinguishing normal from osteopenic plus osteoporotic patients, SDEXA measurements show high classification accuracy with a sensitivity of 95%, however with a mediocre specificity of 57%. Especially in the low BMD range, a point cloud with moderate correlation exists. This can be a result of overestimation of low BMD in AP views, as the spinal processes overlap and additional osteophyte formation, vertebral fracture and degenerative changes of the spine can falsify the aBMD value [Kin+98; CKL16; Gup+20]. A comparison of the classification accuracy for osteoporosis showed improved sensitivity and specificity in lateral scout projections. Especially in the low BMD range, the degree of correlation is improved noticeably for 2D and 3D BMD values. Volumetric BMD values were derived by a material decomposition into hydroxyapatite-specific BMD and water, and not the reference standard QCT. In recent studies, it was shown that spectrally derived BMD values are on par with conventional QCT measurements [Ros+19], or can be even closer to true BMD concentrations [Koc+21].

A notable limitation in our patient population is the low number of osteoporotic patients. Only three osteoporotic patients could be analyzed with measured scout data. The applied scout dose should be adapted to the patient's body mass index to impede degraded scout quality. Further, not all CT protocols feature a scout image, including the lumbar spine. An extended field of view on these scout scans leads to increased dose values. However, the additionally applied dose as given in the Subsubsection 4.3.2 with $< 0.06$ mSv is very low in comparison to CT applied dose of approximately 6.0 mSv. Especially, a comparison to the current reference standard DEXA is lacking. The reason for this is the retrospective nature of this study. Only a rare minority of patients undergoing abdominal CT examinations received a DEXA scan within a reasonable time interval. A reason for this is the absence of a DEXA device in our radiology department.

In this study, we have found a positive correlation between spectral trabecular vBMD and scout scan aBMD ($r$=0.68) as well as projected AP ($r$=0.81) and lateral aBMD ($r$=0.90). A noise reduction technique and an automated mask generation algorithm were utilized to generate joint BMD values. Using the extended scout scan protocol for opportunistic osteoporosis detection, with an additional dose of only a fraction of the CT dose, could be a first indicator for a low BMD value and may be earmarked for further investigations.

## 4.4 Automated segmentation of scout scans

In the previous sections, the SDEXA approach was introduced. The SDEXA approach requires a fully automated segmentation of the overview scan to determine the aBMD in every patient opportunistically. The following section describes the development of a CNN based segmentation algorithm for the automated segmentation of scout scans.

### 4.4.1 Segmentation algorithm

A CNN based segmentation algorithm was developed to automatically segment overview scans from the SDEXA approach. The CNN segmentation was neither used in Section 4.2 nor in Section 4.3. Manually generated segmentations were used for the ESP phantom, and 3D masks were forward projected in Section 4.3 for the perfect registration of 3D and 2D masks in volumetric and areal BMD determination. The automated segmentation of SDEXA scans is a crucial step in the fully automated aBMD report generation in the SDEXA pipeline. The CNN based segmentation algorithm was developed in Python using the PyTorch lightning framework `https://github.com/Lightning-AI/lightning`. To access the code, you can log in to the GitLab repository `https://gitlab.lrz.de/e17/scout-spine-segmentation`. You can read the README.md file in the repository for a detailed description. The input data for training, validation, and testing must be a 512 × 512 pixel Portable Network Graphics (PNG) image. The manually segmented masks are combined with denoised SDEXA photoelectric images to crop and pad the images to the correct size. The masks are saved as 512 × 512 pixel PNG images. If a semantic segmentation for vertebral bodies is desired, the masks must be normalized to the number of labels (e.g., 4 labels + background = 5) visualized in Figure 4.10. The CNN architecture

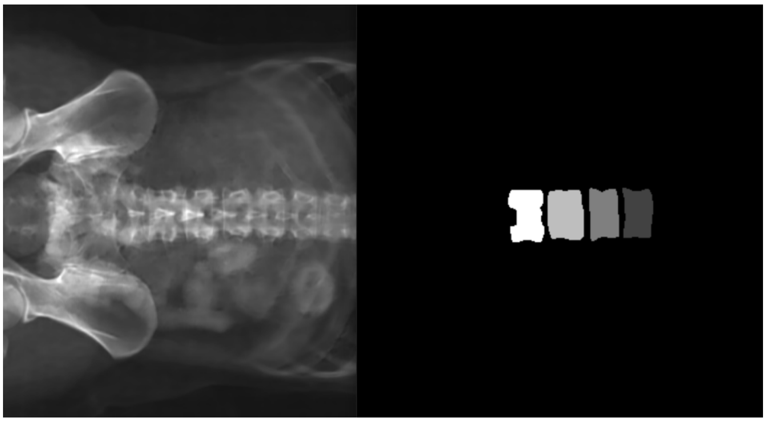

**Figure 4.10:** Denoised SDEXA scan and corresponding semantic segmentation of the vertebral bodies. The segmentation mask is normalized to 5 unique values. The background is represented by the value 0. The vertebral bodies are represented by the values 1 to 4. Both images must be 512 × 512 pixel PNG images. The segmentation mask is used, to crop and pad the SDEXA scan to the correct size. The segmentation mask is used as the ground truth for the CNN training. The CNN output is a 512 × 512 pixel PNG image with 5 unique values.

is based on a modified U-Net architecture [RFB15] with batch normalization after each layer. The U-Net is an open-source convolutional network architecture for fast and precise image segmentation. Semantic segmentation requires a pixel-wise classification of the input image. The loss function is based on the cross entropy loss in combination with a dice loss. An argmax function is used to get the final segmentation mask. The Adam optimizer is used. The PyTorch backend is used for training. A Nvidia GTX TITAN X (NVIDIA Corporate, Santa Clara, CA, USA) graphic card with 12 GB of memory using CUDA 11.2 was accessed. Tensorboard is used to visualize the training process [Aba+15]. To perform a segmentation, the trained model can be loaded using a checkpoint file.
In a second step, the results from Subsubsection 4.3.3 were compared to the results of the CNN based segmentation. The masks for the aBMD quantification in Subsubsection 4.3.3 were generated using a 3D segmentation of the trabecular spine in the CT scan. Those 3D masks were forward projected to the detector plane and registered with the SDEXA scan. On the other hand, the CNN based segmentation masks trained on 289 images were used for the aBMD quantification. First, the dice score, which is a measure of the similarity of two segmentation masks, was calculated. Further, the aBMD values were generated from the forward projected masks and CNN masks and compared to volumetric aBMD values like in Figure 4.9. Also, the ROC curves were generated for the CNN based segmentation and the forward projected 3D masks. Not all datasets from Figure 4.9 could be used, as the 3D masks were not 100% accurate for the labeling of the vertebral bodies. Mislabeled vertebral bodies would lead to meaningless dice scores. From the 44 datasets used in Subsubsection 4.3.3, five had to be excluded due to inaccurate 3D masks.

### 4.4.2 Preliminary results

The generation of ground truth data on SDEXA measurements is still ongoing at the time of writing this thesis. Therefore, a short glimpse of the results generated with 289 images is presented here. After a training of 45 epochs, a training, validation, and test loss of 0.015, 0.073, and 0.060 was achieved. The training and validation loss is shown in Figure 4.11-e. The training loss is shown in blue and the validation loss is in orange. The test loss is indicated by a red diamond. An example of the segmentation results is also shown in Figure 4.11-c. In the second step, the results from Subsubsection 4.3.3 were consulted to analyze the CNN based segmentation performance. Except for one outlier with a dice score of 34%, all other datasets had a dice score of 71% or higher.

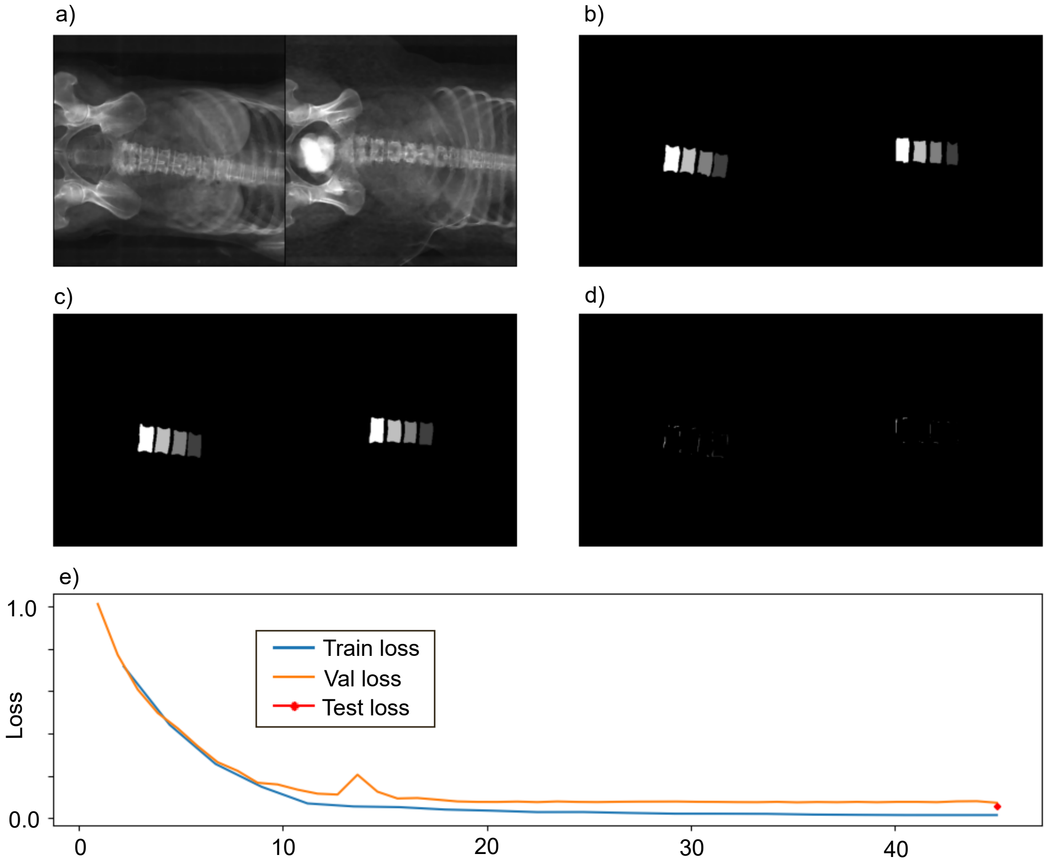

**Figure 4.11:** Two example images of a denoised SDEXA scan in panel **a** and corresponding semantic segmentation of the vertebral bodies in panel **b** (ground truth mask). The segmentation mask is normalized to 5 unique values. The background is represented by the value 0. The vertebral bodies are represented by the values 1 to 4. The predicted mask in **c** and a difference image in **d** are shown. Training, validation, and test loss are plotted in **e**. The training loss is depicted in blue, and the validation loss is in orange. The test loss is indicated by a red diamond. A rapid decrease in the training and validation loss is visible within the first 10 epochs. After 20 epochs, the training and validation loss is stabilizing on a plateau.

The mean dice score was 82% with a standard deviation of 8.6%. An example of a segmentation mask generated by the CNN and the forward projected 3D mask is shown in Figure 4.12. The outlier is shown in panel d, while the other datasets are randomly selected. Analogous to Figure 4.9 the aBMD values were compared to the volumetric BMD values in Figure 4.13. The correlation coefficient is decreased from 0.68 to 0.54 when using the CNN based segmentation masks. When excluding the outlier, the correlation coefficient is 0.57. The aBMD values are also shifted to lower values. The mean difference between the aBMD values is 0.095 g/cm$^2$. The fitted slope has a value of 92.6 ± 48.5 1/cm in a 95% confidence interval. The ROC curves are also shown in Figure 4.13. The AUC is decreased from 0.86 to 0.84 when using the CNN based segmentation masks.

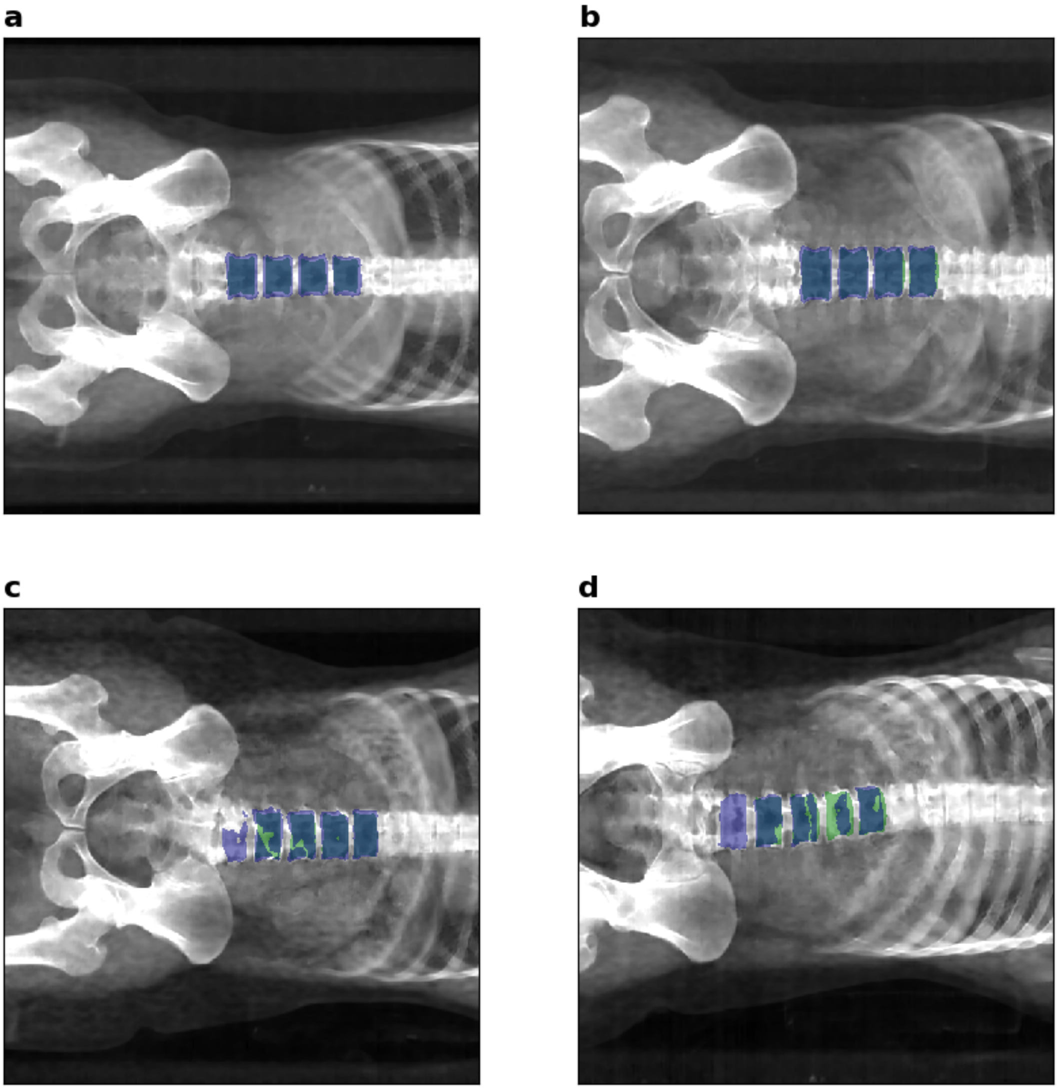

**Figure 4.12:** Four examples of segmentation masks generated by the CNN and the forward projected 3D mask. The CNN based segmentation masks are shown in blue, and the forward projected 3D masks are in green. The outlier is shown in **d**, while the other datasets are randomly selected.

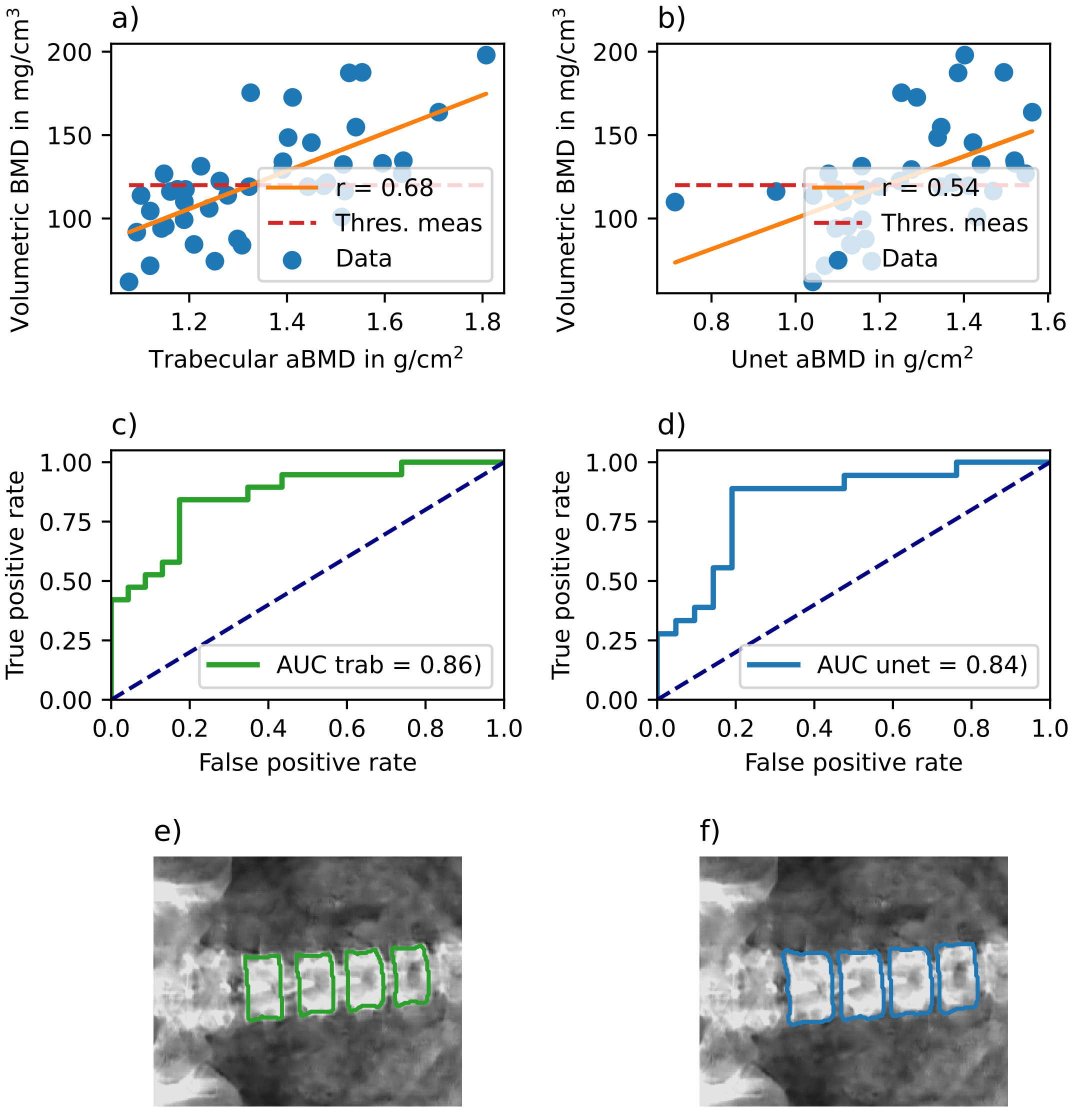

**Figure 4.13:** Correlation and classification analysis of measured and projected aBMD values with trabecular vBMD. aBMD values from forward projected masks and CNN based segmentation masks are compared. **a** The correlation between patient-specific measured AP aBMD and vBMD values with a correlation coefficient $r$ of 0.68. Subfigure **b** shows the correlation of **a** using CNN masks instead of forward projected masks. The correlation coefficient is decreased to 0.54. **c, d** ROC curves for the classification of osteoporotic patients based on the ground truth of trabecular vBMD values using forward projected masks and CNN based segmentation masks. The AUC is decreased from 0.86 to 0.84 when using the CNN based segmentation masks. **e, f** Example image of a denoised SDEXA scan with corresponding segmentation mask generated by the forward projection and the CNN. The CNN based segmentation mask is shown in blue, and the forward projected 3D mask is in green.

The CNN based segmentation masks contain a bigger ROI than the forward projected masks. This is due to the fact that the CNN based segmentation masks are trained on manually labeled data. The manual labeling of the vertebral bodies is not as accurate as the forward projection of the trabecular 3D masks. The CNN based segmentation masks contain the cortical bone of the vertebral bodies, which is not included in the forward projected masks. Further differences are visible in Figure 4.12. The CNN based segmentation masks can show incomplete segmentations of vertebral bodies and labeling of vertebral bodies, which are not L1 to L4.

### 4.4.3 Discussion

The results of the CNN based segmentation are promising. The segmentation masks generated by the CNN are comparable to the forward projected masks. The CNN based segmentation masks are not as accurate as the forward projected masks. Especially when looking at the outside regions of the vertebral bodies, the CNN based segmentation masks include a bigger ROI than the forward projected masks. This is because the CNN based segmentation masks are trained on manually labeled data. In the manual labeling of the vertebral bodies, it can be difficult to distinguish between the trabecular region and the cortical bone, particularly as these structures overlap each other in the projected scout plane. Distinguishing between the trabecular region and cortical bone is only possible in the 3D volume. The forward projected masks are generated from the 3D masks. Therefore, the forward-projected masks contain only the trabecular region of the vertebral bodies. The forward projected masks contain cortical bone, as the line integral through the trabecular region also contains the cortical bone. Depending on the patient-specific anatomy of the vertebral bodies, there will be more or less cortical bone in the forward projected masks. The CNN based segmentation masks can also contain small regions outside the vertebral bodies, particularly in pixels with partial volume effects. When comparing the aBMD values from the two segmentation approaches against the vBMD values, the correlation decrease is partially resulting from the outlier produced by a off segmentation mask of the CNN, but also from the bigger ROI of the CNN based segmentation masks. This aligns with the approach of comparing the aBMD values from the forward projected masks with the vBMD values. The correlation is expected to be maximal when the ROI of the aBMD values and the vBMD values are perfectly aligned. This is achieved by the forward projection and registration of the 3D masks done in Section 4.3. For a fully opportunistic approach, quantifying the aBMD in every scout scan, the CNN based segmentation masks have to be used, as a CT image of the corresponding ROI including L1 to L4, is not always available. With the CNN based segmentation, it is possible to generate a DEXA like aBMD map for every patient undergoing a spectral scout scan, including the vertebral bodies L1 to L4. It is expected that the accuracy of the CNN based segmentation masks can still be increased by training the CNN on more data. The CNN based segmentation masks are trained on 289 scout scans at the time of writing. Especially when dealing with patients with complicated anatomy, oral contrast agent, or metal implants, more training data is needed. Currently, approximately 500 scout scan datasets exist for labeling.

## 4.5 PCCT measurements of vertebral bodies

35 lumbar vertebral bodies harvested from 12 human cadavers originally obtained for studies [Gas+23a; Gas+23b] were measured in a preclinical PCCT setup for assessing qualitative HA and microstructure parameter analysis. The final results will compare the gained parameter with a clinical darkfield scanner setup [Fin+19; Wil+21]. To the point of writing this thesis, the evaluation is still ongoing, and the results are not yet available. The following section will give an overview of the measurement PCCT setup and the assessment of the HA and microstructure parameters.

### 4.5.1 Laboratory PCCT setup

The measurements were performed at the PCCT setup Biwakschachtel of the Technical University of Munich (TUM) in Garching, Germany. The used detector system (Flite X1, Direct Conversion AB, Danderyd, Sweden) is a PCD hybrid pixel detector with a 750 $\mu$m Cadmium Telluride (CdTe) sensor. The detector active area is 1536 × 128 pixels ($\approx$ 155 × 13 $\text{mm}^2$) with a native pixel size of 100 $\mu$m, arranged in a horizontal pattern of 12 chip modules with a chip gap of one pixel. The system has two energy thresholds per pixel and has an integrated charge-sharing correction [Sel+19]. The statically mounted X-ray tube (XWT-160-CT, X-RAY WorX GmbH, Garbsen, Germany) is a micro-focus tube with a tungsten reflection target and a 2 mm thick beryllium window. It can be operated at tube voltages of up to 160 kVp and has a maximum target power output of 300 W. Furthermore, the tube has a minimal focal spot size of 2.0 on 3.0 $\mu$m (hor. on vert.), which broadens with increasing target power to its maximum of approximately 150 on 320 $\mu$m at a power of 120 W. The beam has an opening angle of about 30 degrees and can be varied in its shape by an attached collimator [Sel+19]. The necessary calibration of system parameters needed for the material decomposition is described in [Ehn+17; Mec+18]. A material decomposition into water and HA was performed to measure the bone density in the vertebral samples.

The vertebral bodies were placed in a glass container to avoid movement during the measurement. The container was placed on a rotation stage and mounted on a linear stage. An overview of the measurement setup is shown in Figure 4.14.

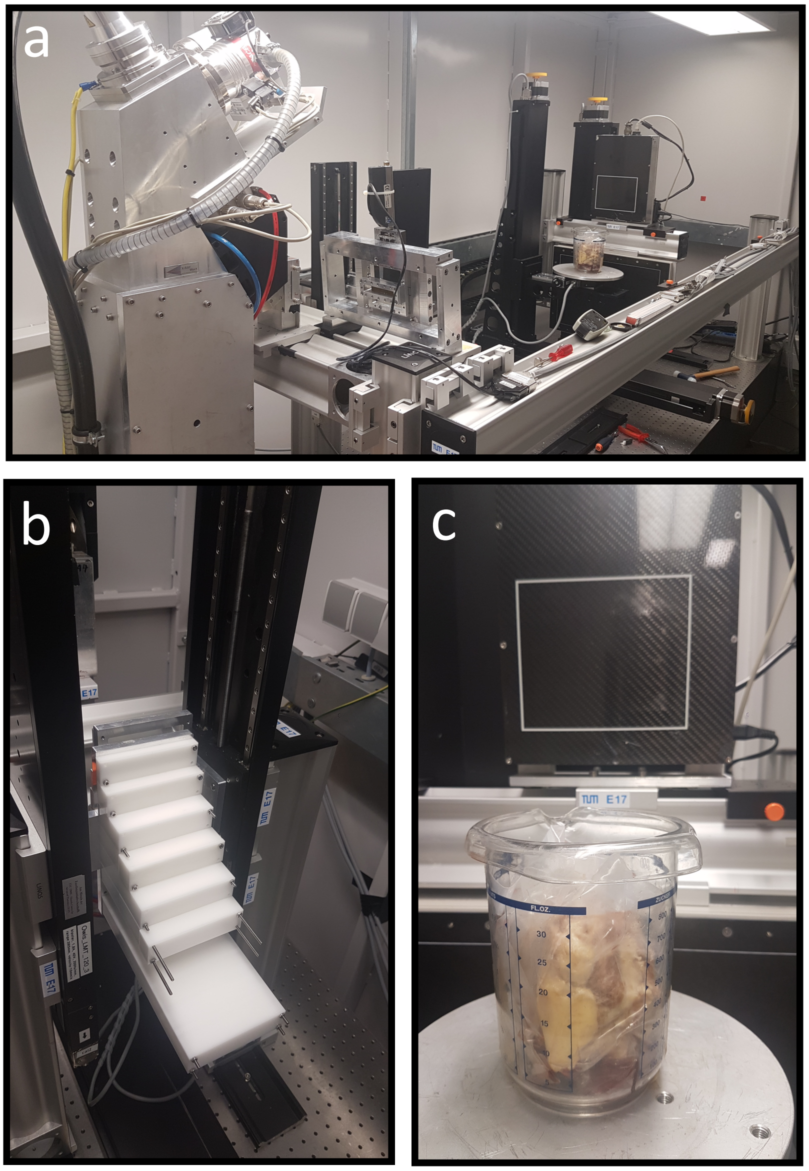

**Figure 4.14:** PCCT with vertebral bodies and calibration phantom. In **a**, the whole measurement setup is shown. From left to right, it contains the X-ray microfocus tube, linear stages to move the calibration phantom and sample on the rotation stage, and the PCD detector. **b** and **c** show a close-up of the calibration phantoms and the sample in front of the detector.

The source-to-object distance was set to 1500 mm, and the object-to-detector distance to 200 mm. The magnification factor is calculated to be 1.13, and the resulting effective pixel size is 88 $\mu$m. An isotropic resolution was used (slice thickness 88 $\mu$m). 1600 projection angles on a 360-degree rotation were applied with an integration time of 0.2 seconds per projection. For spectral measurements, several frames were taken per step, leading to a total scan time of approx. 2.5 hours for one detector coverage of approximately 1 cm. Conventional measurements (with reduced dose, only one frame per step) of the sample were taken in z-scanning mode to cover all three vertebral bodies of the sample, having a z-coverage of 12 cm. The peak acceleration voltage was set to 110 keV and an in-house developed reconstruction software (pyCT) based on Python was used for reconstruction. A cone beam reconstruction geometry was assumed, and a Hamming filter was applied during the FBP algorithm.

### 4.5.2 Microstructure parameter analysis

To investigate the microstructure parameters of the vertebral bodies, a segmentation of the trabecular bone was performed by a radiologist in training using the open-source software itk-SNAP [Yus+06]. The segmentation was performed on the conventional CT images. The resulting binary mask was then applied to the spectral images. The trabecular bone contours were segmented using the scikit-image library, namely the find_contour function of measure (version 0.17.2) [LC87]. The level along which to find contours was set to 0.31 1/cm for the conventional reconstruction and 350 mg/ml HA density for the spectral reconstruction. All other options were set to default. The marching cubes algorithm can create a set of contours around trabecular bone structures. The resulting contours were then used to calculate the microstructure parameters. To reduce computational time, the algorithm was applied on 2D axial slices in multiprocessing mode. The resulting parameters were then averaged over the whole sample. An example of the resulting contours is shown in Figure 4.15.

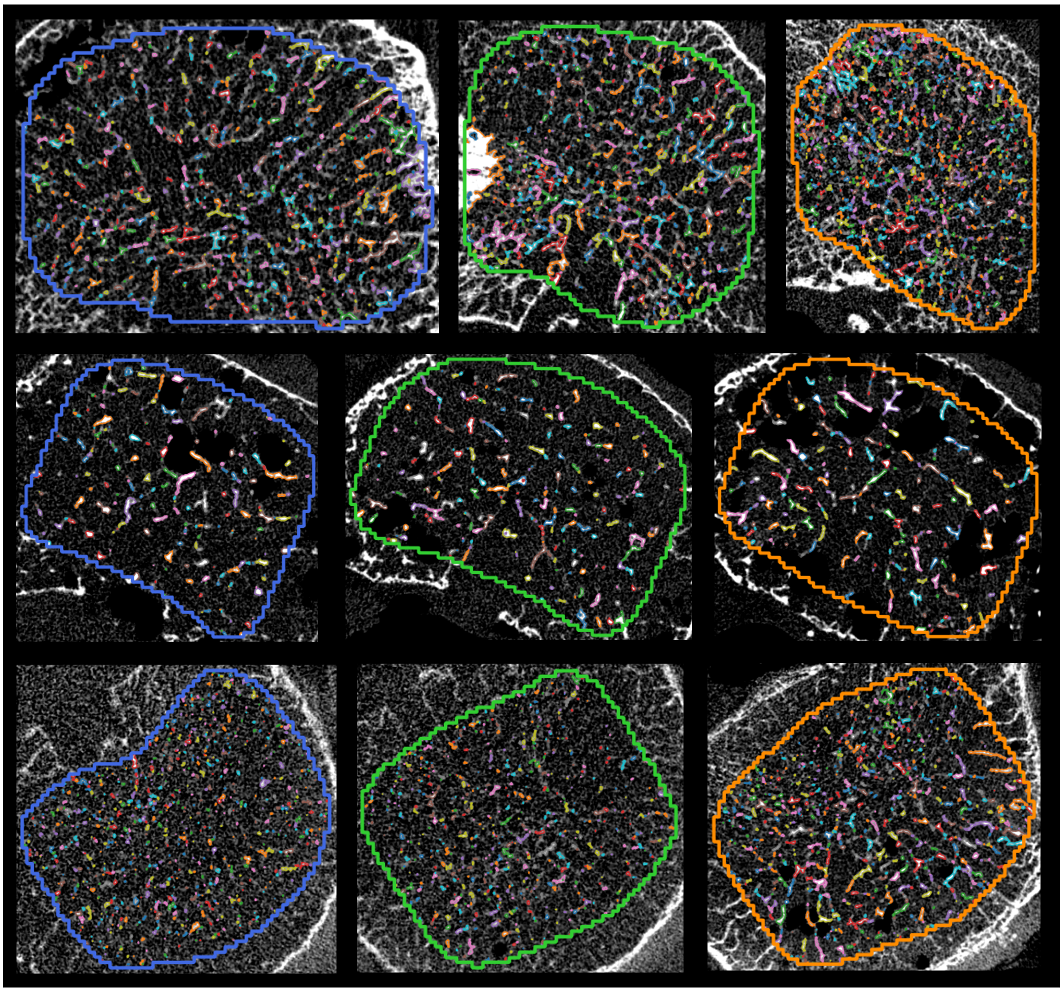

**Figure 4.15:** The visualization of vertebral contours. Three different samples with the corresponding segmentation of the vertebral bodies 1, 2, and 3 are shown in blue, green, and orange, respectively. The contours of the trabecular bone structures are shown using multiple color codes. The zoom factors are different for each sample, so the displayed image sizes are not comparable.

The following parameters were calculated from the segmented contours within the trabecular bone [Bou+10]:

- **Bone volume fraction (BV/TV)**: The ratio of the bone volume to the total volume of the sample.
- **Bone surface fraction (BS/TV)**: The ratio of the bone surface to the total volume of the sample.
- **Specific bone surface fraction (BS/BV)**: The ratio of the bone surface to the bone volume of the sample.
- **Trabecular number per pixel (Tb.N)**: The number of trabecular structures per pixel.
- **Mean trabecular thickness (Tb.Th)**: The average thickness of the trabecular structures.
- **Mean trabecular volume (Tb.V)**: The average volume of the trabecular structures.
- **Degree of anisotropy (DA)**: A measure of the orientation of the trabecular bone structures.

The Degree of Anisotropy (DA) is calculated using Mean Interception Lenght (MIL) vectors [HM84; Odg97]. Every fifth axial slice was analyzed using nine directions (uneven to not include 0 and 180 degrees). Per direction, 10 parallel lines were drawn. The lines were spaced by 20 pixels. The middle line was set to cross the center of gravity of the segmentation mask. All lines were then extended to the edge of the segmentation mask. The center of gravity was calculated using ndimage.center_of_mass from the scipy library (version 1.5.2) [Vir+20]. The algorithm then searches for points along the lines where the background changes to the foreground, i.e. where the line enters an object. These points are called phase changes. The phase changes are then used to calculate the MIL vector. The length of the MIL vector is the total length of the line segments divided by the total number of phase changes. Its direction is defined by the angle between the line and the x-axis. The nine MIL vectors are used to fit an ellipsoid within the 2D axial slice. The ellipsoid radii a and b are used to calculate the DA using the following formula:

$$\mathrm{DA} = 1 - \frac{1}{a^2} / \frac{1}{b^2} = 1 - \frac{b^2}{a^2} \tag{4.6}$$

where $a$ is the major and $b$ the minor axis of the ellipsoid ($a > b$). The DA of every fifth slice was calculated and then averaged over the whole vertebral body. DA values were calculated for the conventional and spectral reconstruction for all vertebral bodies of the samples. As the DA is measured in axial slices, it indicates the anisotropy of the trabecular bone structures in the axial plane, giving information about the orientations perpendicular to the z-axis. An example of the MIL vectors and the fitted ellipsoid is shown in Figure 4.16.

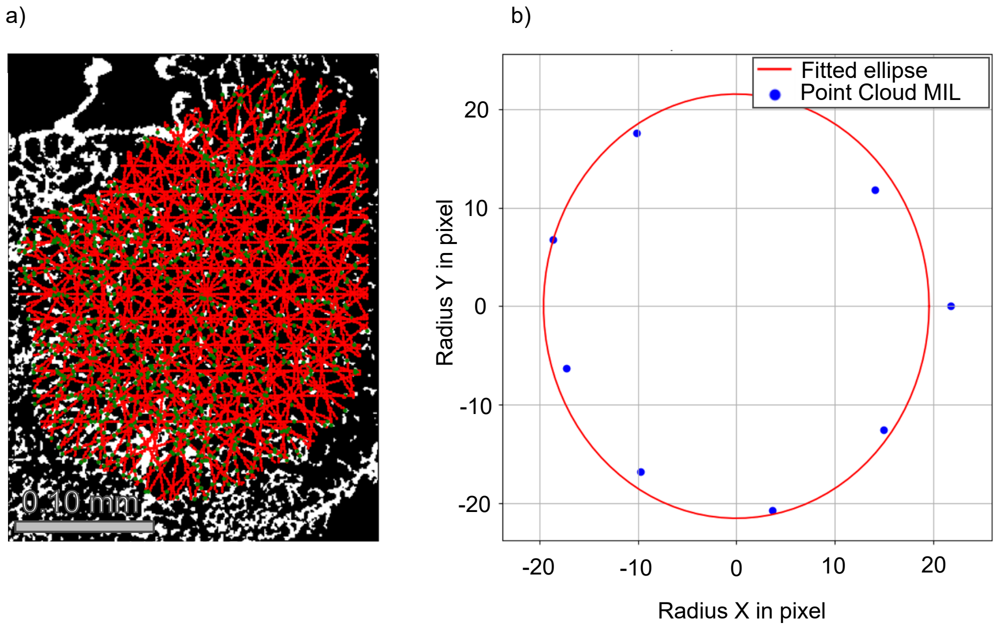

**Figure 4.16:** The visualization of the MIL vectors and the fitted ellipsoid. In **a**, the straight lines to calculate the MIL vectors of sample 245 in slice index 900 are shown in red, and the phase change points are highlighted in green. The corresponding MIL vectors are plotted in **b**. The ellipsoid in red fits the MIL vectors. The DA is calculated using the ellipsoid radii $a = 19.6$ and $b = 21.5$ pixels. The DA value is 0.17. The voxel size is 88 $\mu$m.

### 4.5.3 Comparison to clinical darkfield scanner

The final results of the PCCT measurements will be compared to the results of a clinical darkfield scanner setup [Fin+19; Wil+21]. It is expected to find a correlation between microstructure parameters and the dark field signal of the vertebral bodies. Especially, the DA is expected to correlate with the dark field signal. The dark field signal is a measure of the small-angle scattering of the sample. The small-angle scattering is caused by the trabecular bone structures. The DA is a measure of the orientation of the trabecular bone structures. Therefore, when measured from different orientations, the darkfield signal could show an anisotropy of the directions oriented perpendicular to the spine (z-axis). The DA values measured from the PCCT in conventional mode should be used for the analysis of microstructure parameters and DA analysis, as the resolution of the conventional images is approximately four times higher than the resolution of the spectral images. The spectral resolution is degraded by the binning in detector pixels, which is necessary to avoid high noise contribution in spectral maps. Spectral maps like the HA density can be used to calculate the bone density of the sample. The high resolution necessary for the microstructure parameter analysis is not needed for the bone density calculation, as mean values within the trabecular bone are calculated.

# Conclusion and Outlook

# 5

This thesis has presented new applications for cardiac perfusion and osteoporosis imaging using spectral detectors in clinical CT. Most results presented are acquired using a DLCT system operating in daily clinical routine. Spectral data can be accessed in every scan and was used to show possible improvements in diagnostic accuracy in patient cohorts, animal models, phantoms, and post-mortem human specimens.

In the first part of this thesis, Chapter 2, an introduction to the theoretical background of X-ray CT imaging from the generation of X-rays, the interaction with matter, the spectral detection, and finally the reconstruction of an image are present. A focus lies on spectral detection using a DLCT system, which is important for most results generated during this PhD project. Also, PCCT is introduced and compared to DLCT using the simulation of spectral acquisition with a digital Shepp-Logan phantom. The avoidance of spectral artifacts and the introduction of anti-correlated noise in material decomposition maps are discussed. It should be considered, that the simulation is based on a simplified model of the spectral detection mechanism and cannot represent the real behavior of the detector, but it is a good approximation for the comparison of the two spectral detection methods concerning the material decomposition and noise behavior of material maps.
Most of the presented clinical results are based on DLCT data. Some results based on PCCT data are presented in Section 4.5 investigating post-mortem human vertebral bodies in a preclinical laboratory setup. Chapter 3 focuses on the application of spectral data in dynamic myocardial perfusion imaging. This technology enables 'moving' images of the perfusion of the myocardium by acquiring a series of scans during the passage of a contrast agent bolus in ECG triggered mode. By using a DLCT system, conventional CT images, as well as spectral images like iodine density maps, can be reconstructed. The opportunity to access spectral maps like the iodine density distribution was used to assess perfusion-specific functional parameters within the phantom's myocardium. The GVF model and the TKM were compared on data from a dynamic perfusion phantom. In the approach of a GVF model, blood inflow independent, absolute perfusion parameters are calculated for every voxel, while the TKM model takes the arterial blood inflow and resulting tracer distribution into account. Within the simulated myocardium of the phantom, a perfusion defect was introduced. The perfusion-derived parameters MTT and TTP from the TKM and the GVF model, respectively, showed the best results in the detection of the perfusion defect. Both perfusion maps showed very similar behavior in locating the perfusion defect. Using a classification analysis based on a voxelwise comparison of the perfusion maps, the iodine density was found to be superior to the conventional dataset in the detection of underperfused myocardium. By using a simple dose reduction technique with a reduced number of time points, we showed the possibility of achieving a similar diagnostic accuracy in the detection of perfusion defects when accessing spectral information. This is a very promising result because the dose burden of dynamic perfusion imaging is a major concern in clinical routine. Similar findings concerning dose reduction

and also SNR increase were made in the clinical study of a porcine model. A GVF analysis was performed on iodine density maps, and quantitative perfusion maps were generated. In contrast to the phantom study, recirculation of CA within the left and right ventricle was observed and has to be considered in the fitting process of the GVF model. Within the myocardial tissue, no recirculation was observed within the protocol duration. Disregarding the recirculation, the GVF model can precisely reproduce the TAC curve of the porcine model. A dose reduction using only two time points can remodel the PE of the full fit with only small deviations of 5 to 15%. The results of the porcine model study show the potential of the spectral information in dynamic myocardial perfusion imaging. Further studies should investigate the application in a clinical setting with a patient cohort.

In the second part of this thesis, the application of the so-called overview scans for the opportunistic determination of the aBMD in all patients is presented. The opportunistic determination of the aBMD is of special importance in the diagnosis of osteoporosis due to the treatment gap. The ESP is used for a quantitative comparison between the reference standard DEXA and the CT based aBMD tool SDEXA. SDEXA was able to determine the quantitative values of the ESP more precisely than DEXA with a dose-matched protocol in most phantom settings. To validate the SDEXA approach in a clinical setting, a patient cohort of 57 patients was examined, and the aBMD was compared to volumetric BMD measurements. A denoising and segmentation step was applied to automatically determine the aBMD. The preliminary results of the automated segmentation of the lower vertebral bodies showed a good agreement with the ground truth generated by forward projection from the CT data. Results with a reduced dice score were mainly caused by incorrect assignment of vertebral body labels. The high correlation coefficient and classification accuracy indicate that the SDEXA approach is feasible for the opportunistic determination of the aBMD in a clinical setting. This chapter also includes the first results of microstructure parameter analysis in post-mortem human vertebral bodies using a preclinical, laboratory PCCT setup. The preliminary results indicate that microstructure analysis in trabecular bone is feasible using PCCT data. The high resolution, which can be achieved using the PCD detector in a laboratory setup, is not directly transferable to a clinical setting, but recent developments in PCD technology show, that high-resolution scans in a clinical setting are already possible.

The presented results in this thesis show the potential of spectral data in clinical CT imaging. Especially based on the rapid development of PCD technology for clinical applications by several vendors, the possible use cases of spectral and high-resolution data in clinical routine will increase in the future. High-resolution iodine density data of the whole myocardium acquired with high temporal resolution enabled by the dual-source CT technology could be used for the quantification of perfusion defects with a small areal spread, leading to an early detection of myocardial ischemia in patients. This non-invasive technique could act as a gatekeeper for further invasive examinations like coronary angiography. The necessary technological developments can be expected within the next 10 years. Just recently, due to major improvements in cardiac CT imaging, CCTA was recommended as basic testing for the diagnosis of CAD in European guidelines. Similar developments can be expected for dynamic myocardial perfusion. Multiple CA injection protocols with different K-edges might be a very efficient dose-saving technique for dynamic perfusion as well as multiphasic CA protocols, not only in cardiac imaging. By differentiating several CA, the time-dependent distribution of these CA can be determined by using different injection time points and only one CT examination. An example of this protocol would be the acquisition of native, arterial, and portal-venous CA distribution in cardiac imaging in only one examination. With the CA determining the portal-venous phase distribution being injected several seconds before the arterial CA. The K-edge differences of these CA may then be used in PCD technology to differentiate and quantify the distributions individually. A native image can be generated by virtual subtraction of both CA attenuation contributions. The spectral capabilities of the PCD technology and high-resolution CT acquisitions are highly likely to change the diagnostics in cardiac imaging. Stenosis in small vessels may become visible. By combining a high-resolution static cardiac CT with image-based modeling for coronary blood flow and dynamic perfusion protocols, a wide range of information focusing on the functional effect of one or multiple stenoses can be considered and used to adapt an optimized form of therapy. Also, the diagnosis of osteoporosis could drastically benefit from recent and future developments in spectral CT imaging. A one-stop-shop approach for the assessment of quantitative BMD and qualitative microstructure parameters is thinkable with the use of high resolution spectral CT. To remain with the example of a one-stop-shop for osteoporosis imaging using PCD technology, a protocol design may look like described in the following. A low-dose, spectral overview scan of the patient can be used to determine the 2D aBMD. With the utilization of automated image segmentation algorithms, the automated generation of a DEXA-like report is given to the radiologist. This approach is presented for the AP examination of aBMD in the lumbar spine within this thesis but may be extended to the hip and femur. Also, an automated evaluation of lateral aBMD values using a dual scout acquisition protocol could be beneficial, as the overlay with cortical structures in the lumbar spine can be avoided. If the patient can be diagnosed as osteopenic or osteoporose according to 2D aBMD data, a further CT protocol should be adjusted to the particular region with a reduced aBMD. Especially for osteopenic patients, this may be helpful, as the analysis of bone quality parameters may prevent a false positive diagnosis. Patients in the transition region having a slightly reduced aBMD but bone quality parameters in an adequate range may still be effectively treated by an increase of sporty activity and the adaption of a healthy lifestyle. Still challenging remains the quantitative classification of bone quality parameters and the inter-device comparability.

The first steps toward this promising potential of spectral imaging in clinical CT were conducted in this thesis. Based on the presented results, the next steps toward clinical application would be studies on patient cohorts.

# Supplementary Material

## Scanner information IQon Spectral CT

A 64-slice single-source dual-layer CT scanner (IQon, Philips Healthcare, Best, The Netherlands) was used in most parts of this thesis. The following section contains important scanner information about this device. The information presented in Table 5.1 is extracted from the Philips product specifications sheet, the technical reference guide and dicom tags.

**Figure 5.1:** Picture of the IQon in the radiology department of the Klinikum rechts der Isar.

| **Features** | **Specifications** |
|---|---|
| Generator power | 120 kW |
| kVp setting | 80, 100, 120, 140 kVp |
| mA range (step size) | 10 to 1000 (1 mA) |
| Coverage | 40 mm |
| Material | Solid-state yttrium-based scintillator; GOS |
| Dynamic range | 1000000:1 |
| Maximum rotation speed | 0.27 seconds |
| MonoEnergetic range | 40 keV to 200 keV |
| FOV with spectral results | 50 cm |
| Focus-isocenter distance | 570 mm |
| Focus-detector distance | 1040 mm |
| Maximum scannable range | 2100 mm |
| Pitch | 0.07 to 1.5 |
| Z-position accuracy | ± 0.25 mm |
| Focal spot sizes, quoted to IEC | Small: 0.6 × 0.7; Large: 1.1 × 1.2 |
| Smart focal spot | x- and z-deflection |
| Slip ring | Optical; 5.3 Gbps transfer rate |
| Data sampling rate | Up to 4800 views/revolution/element |
| Collimations | 64 × 0.625 down to 2 × 0.625 |
| Spatial resolution | High mode 16 lp/cm; Standard mode 13 lp/cm |
| Absorption range | -1024 to +3071 HU |
| Spectral reconstruction speed | 3 to 5 minutes for the majority of cases |
| Spectral image matrix | 512 × 512 |

**Table 5.1:** Specification table of the IQon extracted from the Philips product specifications sheet, the technical reference guide and dicom tags.

## Minimum example of one compartment model fit

```
import numpy as np
from scipy.optimize import minimize
import matplotlib.pyplot as plt

# sample AIF (arterial input function) using iodine density [mg/ml] map
aif = np.array([0.  , 0.01, 0.01, 0.  , 0.01, 0.22, 1.29, 2.32, 3.74, 5.02, 6.22,
      7.18, 8.03, 8.82, 9.04, 9.1 , 8.88, 8.11, 7.08, 6.02, 4.98, 4.03,
      3.27, 2.66, 2.07, 1.72, 1.47, 1.29, 1.18, 1.07, 0.98, 0.92, 0.88,
      0.79, 0.65, 0.54])

# sample voxel inside simulated myocardium [mg/ml]
myo_iod = np.array([0.  , 0.  , 0.  , 0.  , 0.  , 0.  , 0.  , 0.  , 0.  , 0.75, 1.18,
      1.46, 2.87, 2.87, 2.54, 4.14, 5.36, 4.19, 4.  , 4.71, 4.09, 4.28,
      3.11, 3.34, 2.82, 2.49, 1.55, 1.04, 1.13, 1.18, 0.42, 0.42, 0.75,
      0.56, 0.56, 0.])

# time points of dynamic perfusion measurment [s]
times = np.array([ 0.  , 0.9, 1.7, 2.5, 3.3, 4.  , 4.8, 5.5, 6.3, 7.  , 7.8,
       8.5, 9.3, 10.1, 10.9, 11.6, 12.4, 13.2, 13.9, 14.7, 15.5, 16.2,
      17.  , 17.7, 18.5, 19.3, 20.1, 20.9, 21.6, 22.4, 23.2, 23.9, 24.7,
      25.4, 26.1, 26.9])

curve = myo_iod

# convolution of aif using an exponential function with fit parameter lambda (lam)
def convolution(times, lam, aif):
    expon = np.exp(-lam * times)
    y = np.convolve(aif, expon, mode='full')
    # scaling down by a factor dt
    y = y * (times[1] - times[0])
    # first half of convolution
    half = int(len(y) / 2 + 1)
    y = y[0:half]
    return y

# Scaling factor + convolution
def modelfunction(parameters, times, aif):
    modelcurve = parameters[0] * convolution(times, parameters[1], aif)
    return modelcurve

# wrapper to minimize modelfunction
def min_wrapper(parameters, *args): # args = (curve, times, aif)
```

```
    diff = args[0] - modelfunction(parameters, args[1], args[2])
    return np.sum(diff ** 2)

def fit(curve, times, aif):
    startparameters = np.zeros(2)
    bounds = [(0, None), (0, None)]
    method = ’L-BFGS-B’
    fit_results = minimize(min_wrapper, startparameters, args=(curve, times, aif), metho
    fitparameters = fit_results.x
    fit = modelfunction(fitparameters, times, aif)
    return fitparameters, fit

fitparameters, fit = fit(curve, times, aif)

# get physical parameters
def phys_par(fitparameters):
    # fit parameters to the ’physiological’ model
    F = fitparameters[0] ∗ 6000. # Blood flow
    v = fitparameters[0] / fitparameters[1] ∗ 100 # blood volume
    mtt = 1 / fitparameters[1] # mean transit times
    return F, v, mtt

# convert the fit parameters back to physiological parameters
F, v, mtt = phys_par(fitparameters)
print("Physics␣parameters:")
print("Flow:␣", F, "Volume:␣", v, "Mean␣transit␣time:␣", mtt)

plt.figure()
plt.plot(times, aif, label=’AIF’)
plt.plot(times, curve, label=’Curve’)
plt.plot(times, fit, label="Curve␣fit")
plt.ylabel(’Iodine␣density␣[mg/ml]’)
plt.xlabel(’Time␣[s]’)
plt.legend()
plt.show(block=False)
```

# Acknowledgments

I am very grateful to all the people who have supported me in the development of my PhD project. I was very lucky to be able to work with many talented and inspiring people who have helped me to grow both as a scientist and as a person. In particular, I would like to thank . . .

. . . Franz Pfeiffer, the supervisor of my PhD project, for giving me the opportunity to work in his group and for his continuous support and guidance. He has supported me since my master's thesis in his group and successfully connected me to collaborators from industry and clinics.

. . . Daniela Pfeiffer, my advisor, for her passionate guidance, especially in the early stages of my PhD project. She has always been there for questions and discussions and has helped me to expand my medical background and understand the clinical relevance of my work. She has also been a great mentor and introduced me to several radiologists and clinicians, leading to fruitful collaborations.

. . . Thorsten Sellerer and Lorenz Birnbacher for sharing their expertise and valuable input and discussions on several topics like spectral imaging and clinical applications. They have been great colleagues and friends.

. . . Manuel Schultheiss and Clemens Schmid for helping me with IT-related and algorithmic problems. I could work and progress a lot faster on several projects with their help.

. . . Maximilian Lochschmidt and Lennard Kaster, whom I enjoyed supervising during their master's thesis. They have been a great help on my projects and worked very independently and successfully on their research topics. Thank you also for proofreading my thesis.

. . . Jakob Häusele, Kirsten Taphorn and Daniel Berthe for being great colleagues and friends in the PhD office, for many interesting coffee breaks and discussions, for proofreading my thesis and for helping me organize my PhD defense.

. . . Kai Mei, Felix Kopp, Peter Neol, Kai Scherer for their great support and introduction to the CT Research Group at the beginning of my master's and PhD projects.

. . . Alexandra Gersing, Benedikt Schwaiger, Jan Kirschke, Andreas Sauter, Florian Gassert, Rafael Adolf, Ferdinand Roski, Jon Rischewski and all other radiologists involved in clinical CT research for their valuable input and fruitful collaborations leading to several publications. Working with you and getting meaningful insights into radiology was a great pleasure.

. . . Marcus Makowski and Ernst Rummeny for enabling the clinical CT research at the radiology department of the Klinikum rechts der Isar.

. . . Veronica Bodek and Nelly de Leiris for helping me a lot with the organization of

working contracts, travel expenses, and other administrative tasks.
. . . Felix Gebser, Christiane Schmeichel, David Jany, and Bernhard Renger for keeping the IT infrastructure at MRI running. It was a great pleasure to spend time with you and get insights into physics-related topics at the radiology department.
. . . the radiological technologists for being supportive and enabling me to perform my research measurements at the CT scanner.
. . . Klaus Achterhold and Martin Dierolf for their essential help in the background, keeping the server infrastructure at E17 running and handling radiation protection tasks for the whole chair.
. . . Graeme Campbell and Philippe Coulon from Philips Healthcare for supporting our group with the SDEXA project and providing us with the necessary software and expertise.
. . . and all other members of the chair and the radiology department for making the last four years so memorable and successful.

Im Besonderen möchte ich mich bei meinen Eltern bedanken. Eure liebevolle Erziehung und bedingungslose Unterstützung haben mich mein ganzes Leben lang begleitet. Ihr habt mir den Freiraum gegeben, mich zu entfalten und meine eigenen Entscheidungen zu treffen. Dank eurer Liebe und eurer Unterstützung konnte ich meinen Weg ohne Sorgen und Ängste gehen. Ich bin unendlich dankbar für alles, was ihr für mich getan habt. Ihr seid die besten Eltern, die man sich wünschen kann.
Ich möchte mich auch bei meiner Schwester bedanken. Seit wir Kinder sind, haben wir eine tiefe und unkomplizierte Verbindung. Du warst immer für mich da, hast mir zugehört und dich für mein Leben interessiert. Das bedeutet mir sehr viel.
Danke auch an meine Freunde und Verwandte. In den Jahren meiner Promotion habt ihr mir immer ein gutes Gefühl gegeben und diese Zeit zu etwas ganz Besonderem gemacht. Ihr habt mich motiviert, an mich geglaubt und mir geholfen. Ich bin dankbar für eure Begleitung und eure Freundschaft.

Zum Schluss möchte ich meiner Frau danken. Sabsi, ich bin unendlich dankbar für deine Liebe und Unterstützung. Du hast mich bei allen meinen Entscheidungen unterstützt und bist immer für mich da. Während meiner Promotion warst du meine größte Stütze. Du gibst mir Kraft, Mut und Freude.

# Abbreviations

**MTF** Modulation Transfer Function

**AI** Artificial Intelligence

**FBP** Filtered Back Projection

**ZnSe** Tin Selenide

**GOS** Gadolinium Oxysulfide

**NIST** National Institute of Standards and Technology

**CRLB** Cramer-Rao Lower Bound

**STD** Standard Deviation

**ADC** Analog to Digital Converter

**CT** Computed Tomography

**CT** Computertomografie

**ISD** IntelliSpace Discovery

**PACS** Picture Archiving and Communication System

**GPU** Graphical Processing Unit

**MOT** Multi Thread Optimization

**LM** Levenberg Marquardt

**CPU** Central Processing Unit

**RMSE** Root Mean Square Error

**CNN** Convolutional Neural Network

**PNG** Portable Network Graphics

**FEIR** Fast Elastic Image Registration

**ROI** Region Of Interest

**TUM** Technical University of Munich

**BMD** Bone Mineral Density

**aBMD** areal Bone Mineral Density

**AP** Anterior-Posterior

**LAT** lateral

**SNR** Signal-to-Noise Ratio

**vBMD** Volumetric Trabecular Bone Mineral Density

**AUC** Area Under the Curve

**DEXA** Dual Energy X-ray Absorptiometry

**SDEXA** Scout-based Dual-Energy X-ray Absorptiometry

**SDEXA** Übersichtsscan-basierten Dual-Energy-Röntgen-Absorptiometrie

**QCT** Quantitative Computed Tomography

**HR-pQCT** High Resolution peripheral Quantitative Computed Tomography

**EPL** Equivalent Path Length

**WHO** World Health Organization

**FOV** Field Of View

**ESP** European Spine Phantom

**HA** Hydroxyapatite

**CdTe** Cadmium Telluride

**DA** Degree of Anisotropy

**MIL** Mean Interception Lenght

**TKM** Tracer Kinetic Modeling

**SPECT** Single-Photon Emission Computed Tomography

**PET** Positron Emission Tomography

**CTP** Computed Tomography Perfusion

**PCCT** Photon Counting CT

**PCD** Photon Counting Detector

**EES** Extravascular Extracellular Space

**GVF** Gamma Variate Fit

**PE** Peak Enhancement

**MP** Maximum Perfusion

**AU** Arbitrary Units

**SD** Standard Deviation

**3D** Three-dimensional

**2D** Two-dimensional

**1D** One-dimensional

**MTT** Mean Transit Time

**TAC** Time Attenuation Curve

**CAD** Coronary Artery Disease

**CCTA** Coronary Computed Tomography Angiography

**CNR** Contrast-to-Noise Ratio

**AIF** Arterial Input Function

**CTDIvol** CT Dose Index volume

**DLP** Dose Length Product

**BMP** Beats Per Minute

**CA** Contrast Agent

**NaCl** Natrium Chloride

**HU** Hounsfield Units

**ROC** Receiver Operating Characteristic

**CMR** Cardiac Magnetic Resonance

**MRI** Magnetic Resonance Imaging

**DECT** Dual Energy CT

**DLCT** Dual Layer CT

**DL** Dual Layer

**MonoE** Virtual monoenergetic image

**RMSD** Root Mean Square Deviation

**RIS** Relative Increase in Signal

**ECG** Electrocardiogram

**RV** Right Ventricle

**RA** Right Atrium

**LV** Left Ventricle

**LA** Left Atrium

**Myo** Myocaridum

**CBV** Cerebral Blood Volume

| | |
|---|---|
| **BV** | Blood Volume |
| **TTP** | Time To Peak |

# List of Figures

# List of Tables

# Bibliography

1. Abadi, M., Agarwal, A., Barham, P., Brevdo, E. & Chen, Z. TensorFlow: Large-Scale Machine Learning on Heterogeneous Systems (2015) (cit. on p. 116).
2. Agostini, D. *et al.* Performance of cardiac cadmium-zinc-telluride gamma camera imaging in coronary artery disease: a review from the cardiovascular committee of the European Association of Nuclear Medicine (EANM). *European Journal of Nuclear Medicine and Molecular Imaging* **43,** 2423–2432 (13 Dec. 2016) (cit. on p. 46).
3. Akkawi, I. & Zmerly, H. Osteoporosis: Current concepts. *Joints* **6,** 122–127 (2 June 2018) (cit. on p. 93).
4. Allaire, B. T. *et al.* Prediction of incident vertebral fracture using CT-based finite element analysis. *Osteoporosis International* **30,** 323–331 (2 Feb. 2019) (cit. on p. 107).
5. Altman, A., Shapiro, O., Levene, S. & Wainer, N. (2011) (cit. on pp. 2, 25).
6. Alvarez, R. E. & Macovski, A. Energy-selective reconstructions in X-ray computerised tomography. *Physics in Medicine and Biology* **21,** 002 (5 Sept. 1976) (cit. on pp. 1, 12, 35, 37, 41).
7. Alvarez, R. & Seppi, E. A Comparison of Noise and Dose in Conventional and Energy Selective Computed Tomography. *IEEE Transactions on Nuclear Science* **26,** 2853–2856 (2 Apr. 1979) (cit. on p. 114).
8. Behling, R. Pitfalls: Reliability and Performance of Diagnostic X-Ray Sources. *Medical Physics* **43,** 3903–3903 (6Part47 June 2016) (cit. on p. 6).
9. Benner, T., Heiland, S., Erb, G., Forsting, M. & Sartor, K. Accuracy of gamma-variate fits to concentration-time curves from dynamic susceptibility-contrast enhanced MRI: Influence of time resolution, maximal signal drop and signal-to-noise. *Magnetic Resonance Imaging* **15,** 307–317 (3 Jan. 1997) (cit. on p. 48).
10. Bindschadler, M., Modgil, D., Branch, K. R., Riviere, P. J. L. & Alessio, A. M. Comparison of blood flow models and acquisitions for quantitative myocardial perfusion estimation from dynamic CT. *Physics in Medicine and Biology* **59,** 1533–1556 (7 Apr. 2014) (cit. on p. 47).
11. Bittencourt, M. S. *et al.* Clinical Outcomes After Evaluation of Stable Chest Pain by Coronary Computed Tomographic Angiography Versus Usual Care. *Circulation: Cardiovascular Imaging* **9** (4 Apr. 2016) (cit. on p. 45).
12. Blankstein, R. *et al.* Adenosine-Induced Stress Myocardial Perfusion Imaging Using Dual-Source Cardiac Computed Tomography. *Journal of the American College of Cardiology* **54,** 1072–1084 (12 2009) (cit. on p. 47).
13. Blasse, G. & Grabmaier, B. C. *Luminescent Materials* (Springer Berlin Heidelberg, 1994) (cit. on p. 32).

14. Boltz, T. *et al.* An anthropomorphic beating heart phantom for cardiac X-ray CT imaging evaluation. *Journal of Applied Clinical Medical Physics* **11,** 191–199 (1 2010) (cit. on p. 77).
15. Bouxsein, M. L. *et al.* Guidelines for assessment of bone microstructure in rodents using micro-computed tomography. *Journal of Bone and Mineral Research* **25,** 1468–1486 (7 2010) (cit. on p. 126).
16. Brooks, R. A. & Chiro, G. D. Beam hardening in X-ray reconstructive tomography. *Physics in Medicine and Biology* **21,** 390–398 (3 1976) (cit. on p. 22).
17. Brown, K. M., Zabic, S. & Shechter, G. Impact of spectral separation in dual-energy CT with anti-correlated statistical reconstruction. *Proceedings of the 13th fully three-dimensional image reconstruction in radiology and nuclear medicine,* 491–494 (2015) (cit. on p. 37).
18. Bucher, A. M. *et al.* Quantitative evaluation of beam-hardening artefact correction in dual-energy CT myocardial perfusion imaging. *European Radiology* **26,** 3215–3222 (9 Sept. 2016) (cit. on p. 47).
19. Buzug, T. M. *Computed Tomography* (Springer Berlin Heidelberg, 2008) (cit. on pp. 5, 6, 22).
20. Byrd, R. H., Lu, P., Nocedal, J. & Zhu, C. A Limited Memory Algorithm for Bound Constrained Optimization. *SIAM Journal on Scientific Computing* **16,** 1190–1208 (5 1995) (cit. on p. 63).
21. Carmi, R., Shapiro, O. & Braunstein, D. *Resolution enhancement of X-ray CT by spatial and temporal MLEM deconvolution correction* in. **5** (IEEE, 2004), 2765–2768 (cit. on p. 32).
22. Carmi, R., Naveh, G. & Altman, A. *Material Separation with Dual-Layer CT* in. **4** (IEEE, 2005), 1876–1878 (cit. on p. 96).
23. Caruso, D. *et al.* Dynamic CT myocardial perfusion imaging. *European Journal of Radiology* **85,** 1893–1899 (10 2016) (cit. on p. 47).
24. Chan, A. & Nelson, S. *Simplified gamma-variate fitting of perfusion curves* in. **2** (IEEE, 2004), 1067–1070 (cit. on pp. 53, 91).
25. Chiribiri, A. *et al.* Perfusion phantom: An efficient and reproducible method to simulate myocardial first-pass perfusion measurements with cardiovascular magnetic resonance. *Magnetic Resonance in Medicine* **69,** 698–707 (3 2013) (cit. on p. 77).
26. Choi, M. K., Kim, S. M. & Lim, J. K. Diagnostic efficacy of Hounsfield units in spine CT for the assessment of real bone mineral density of degenerative spine: correlation study between T-scores determined by DEXA scan and Hounsfield units from CT. *Acta Neurochirurgica* **158,** 1421–1427 (7 July 2016) (cit. on p. 114).
27. Clynes, M. A. *et al.* The epidemiology of osteoporosis. *British Medical Bulletin* **133,** 105–117 (1 Apr. 2020) (cit. on p. 93).
28. Compston, J. Reducing the treatment gap in osteoporosis. *The Lancet Diabetes and Endocrinology* **8,** 7–9 (1 Jan. 2020) (cit. on p. 93).

29. Cowan, G. *Statistical Data Analysis CLARENDON PRESS • OXFORD* 1998 (cit. on p. 41).

30. Dewey, M. *et al.* Clinical quantitative cardiac imaging for the assessment of myocardial ischaemia. *Nature Reviews Cardiology* **17,** 427–450 (7 2020) (cit. on pp. 30, 45–47).

31. Ding, Q., Long, Y., Zhang, X. & Fessler, J. A. Statistical Image Reconstruction Using Mixed Poisson-Gaussian Noise Model for X-Ray CT (Jan. 2018) (cit. on p. 35).

32. Doerner, J. *et al.* Image quality evaluation of dual-layer spectral detector CT of the chest and comparison with conventional CT imaging. *European Journal of Radiology* **93,** 52–58 (Aug. 2017) (cit. on p. 2).

33. Dorosti, T. *et al.* Optimizing Convolutional Neural Networks for Chronic Obstructive Pulmonary Disease Detection in Clinical Computed Tomography Imaging (Mar. 2023) (cit. on p. 30).

34. Eck, B. L. *et al.* The role of acquisition and quantification methods in myocardial blood flow estimability for myocardial perfusion imaging CT. *Physics in Medicine and Biology* **63** (18 2018) (cit. on pp. 60, 63).

35. Ehn, S. *et al.* Basis material decomposition in spectral CT using a semi-empirical, polychromatic adaption of the Beer Lambert model. *Physics in Medicine and Biology* **62,** N1–N17 (1 Jan. 2017) (cit. on p. 122).

36. Ehn, S. *et al.* Assessment of quantification accuracy and image quality of a full-body dual-layer spectral CT system. *Journal of Applied Clinical Medical Physics* **19,** 204–217 (1 Jan. 2018) (cit. on pp. 2, 48).

37. Elbakri, I. A. & Fessler, J. A. Statistical Image Reconstruction for Polyenergetic X-Ray Computed Tomography. *IEEE TRANSACTIONS ON MEDICAL IMAGING* **21,** 89 (2 2002) (cit. on p. 35).

38. Engelke, K. Quantitative Computed Tomography—Current Status and New Developments. *Journal of Clinical Densitometry* **20,** 309–321 (3 July 2017) (cit. on p. 114).

39. Erdogan, H. & Fessler, J. Monotonic algorithms for transmission tomography. *IEEE Transactions on Medical Imaging* **18,** 801–814 (9 1999) (cit. on p. 35).

40. Ergun, D. L. *et al.* Single-exposure dual-energy computed radiography: improved detection and processing. *Radiology* **174,** 243–249 (1 Jan. 1990) (cit. on p. 2).

41. Evans, R. L. Two comments on the estimation of blood flow and central volume from dye-dilution curves. *Journal of Applied Physiology* **14,** 457–457 (3 May 1959) (cit. on p. 48).

42. Fahmi, R. *et al.* Quantitative myocardial perfusion imaging in a porcine ischemia model using a prototype spectral detector CT system. *Physics in Medicine and Biology* **61,** 2407–2431 (6 2016) (cit. on pp. 47, 78).

43. Fessler, J. Statistical image reconstruction methods for transmission tomography. *Handb Med Imaging* **2** (Jan. 2000) (cit. on p. 20).

44. Finegold, J. A., Asaria, P. & Francis, D. P. Mortality from ischaemic heart disease by country, region, and age: Statistics from World Health Organisation and United Nations. *International Journal of Cardiology* **168,** 934–945 (2 Sept. 2013) (cit. on p. 45).
45. Fingerle, A. A. *et al.* Imaging features in post-mortem x-ray dark-field chest radiographs and correlation with conventional x-ray and CT. *European radiology experimental* **3,** 25 (1 July 2019) (cit. on pp. 122, 128).
46. Flohr, T. *et al.* Photon-counting CT review. *Physica Medica* **79,** 126–136 (October 2020) (cit. on p. 77).
47. Flohr, T. G. *et al.* First performance evaluation of a dual-source CT (DSCT) system. *European Radiology* **16,** 256–268 (2 2006) (cit. on p. 2).
48. Fox, M. Quantum Optics: An Introduction. *Oxford Master Series in Pysics* (Sept. 2006) (cit. on p. 19).
49. Franco, A., Javidi, S. & Ruehm, S. G. Delayed Myocardial Enhancement in Cardiac Magnetic Resonance Imaging. *Journal of Radiology Case Reports* **9** (6 June 2015) (cit. on p. 87).
50. Gassert, F. T. *et al.* Comparing CT-Like Images Based on Ultra-Short Echo Time and Gradient Echo T1-Weighted MRI Sequences for the Assessment of Vertebral Disorders Using Histology and True CT as the Reference Standard. *Journal of Magnetic Resonance Imaging* (July 2023) (cit. on p. 122).
51. Gassert, F. T. *et al.* Dark-field X-ray imaging for the assessment of osteoporosis in human lumbar spine specimens. *Frontiers in Physiology* **14** (July 2023) (cit. on p. 122).
52. Gauntt, D. M. & Barnes, G. T. X-ray tube potential, filtration, and detector considerations in dual-energy chest radiography. *Medical Physics* **21,** 203–218 (2 1994) (cit. on pp. 40, 41).
53. Genant, H. K. *et al.* Universal standardization for dual X-ray absorptiometry: Patient and phantom cross-calibration results. *Journal of Bone and Mineral Research* **9,** 1503–1514 (10 Dec. 1994) (cit. on p. 94).
54. George, R. T. *et al.* Adenosine Stress 64- and 256-Row Detector Computed Tomography Angiography and Perfusion Imaging. *Circulation: Cardiovascular Imaging* **2,** 174–182 (3 May 2009) (cit. on p. 47).
55. Golob, A. L. & Laya, M. B. Osteoporosis: Screening, Prevention, and Management. *Medical Clinics of North America* **99,** 587–606 (3 May 2015) (cit. on p. 93).
56. Gonnelli, S. & Cepollaro, C. The use of ultrasound in the assessment of bone status. *Journal of Endocrinological Investigation* **25,** 389–397 (4 Apr. 2002) (cit. on p. 93).
57. Graser, A., Johnson, T. R., Chandarana, H. & Macari, M. Dual energy CT: Preliminary observations and potential clinical applications in the abdomen. *European Radiology* **19,** 13–23 (1 2009) (cit. on p. 2).
58. Gupta, A. *et al.* DEXA sensitivity analysis in patients with adult spinal deformity. *Spine Journal* **20,** 174–180 (2 Feb. 2020) (cit. on p. 114).

59. Hammel, J., Birnbacher, L., Makowski, M. R., Pfeiffer, F. & Pfeiffer, D. Absolute iodine concentration for dynamic perfusion imaging of the myocardium: improved detection of poststenotic ischaemic in a 3D-printed dynamic heart phantom. *European Radiology Experimental* **6** (1 Dec. 2022) (cit. on pp. 45, 59, 61, 65, 67, 71, 73, 75).

60. Hammel, J. *et al.* Comparison of volumetric and areal bone mineral density in CT and scout scans using spectral detector technology. *European Radiology Experimental* **7** (1 Dec. 2023) (cit. on pp. 93, 103, 106, 108, 111, 113).

61. Harpen, M. D. & Lecklitner, M. L. Derivation of gamma variate indicator dilution function from simple convective dispersion model of blood flow. *Medical Physics* **11,** 690–692 (5 Sept. 1984) (cit. on p. 48).

62. Harrigan, T. P. & Mann, R. W. Characterization of microstructural anisotropy in orthotropic materials using a second rank tensor. *JOURNAL OF MATERIALS SCIENCE* **19,** 761–767 (1984) (cit. on p. 126).

63. Hawkes, D. J. & Jackson, D. F. An accurate parametrisation of the x-ray attenuation coefficient. *Physics in Medicine and Biology* **25,** 1167–1171 (6 1980) (cit. on p. 11).

64. Hernlund, E. *et al.* Osteoporosis in the European Union: Medical management, epidemiology and economic burden: A report prepared in collaboration with the International Osteoporosis Foundation (IOF) and the European Federation of Pharmaceutical Industry Associations (EFPIA). *Archives of Osteoporosis* **8** (1-2 Dec. 2013) (cit. on p. 93).

65. Hounsfield, G. N. Computerized transverse axial scanning (tomography): Part 1. Description of system. *The British Journal of Radiology* **46,** 1016–1022 (552 Dec. 1973) (cit. on p. 1).

66. Hubbell, J. & Seltzer, S. *Tables of X-Ray Mass Attenuation Coefficients and Mass Energy-Absorption Coefficients (version 1.4)* 2004 (cit. on p. 12).

67. Huber, A. M. *et al.* Myocardium: Dynamic versus Single-Shot CT Perfusion Imaging. *Radiology* **269,** 378–386 (2 Nov. 2013) (cit. on pp. 45, 47).

68. Huda, W. *Review of radiologic physics* 255 (Lippincott Williams and Wilkins, 2010) (cit. on p. 6).

69. Hulten, E. A., Bittencourt, M. S., Ghoshhajra, B. & Blankstein, R. Stress CT perfusion: Coupling coronary anatomy with physiology. *Journal of Nuclear Cardiology* **19,** 588–600 (3 2012) (cit. on p. 47).

70. Ingrisch, M. & Sourbron, S. Tracer-kinetic modeling of dynamic contrast-enhanced MRI and CT: A primer. *Journal of Pharmacokinetics and Pharmacodynamics* **40,** 281–300 (3 2013) (cit. on pp. 54, 55, 63).

71. Isola, A. A. *et al.* Image registration and analysis for quantitative myocardial perfusion: Application to dynamic circular cardiac CT. *Physics in Medicine and Biology* **56,** 5925–5947 (18 2011) (cit. on p. 77).

72. James, F. Statistics. *The European Physical Journal C* **15,** 195–201 (1-4 Mar. 2000) (cit. on p. 40).

73. Jenkins, D. in, 59–76 (Springer Netherlands, 1980) (cit. on p. 1).

74. Ji, F., Juntunen, M. & Hietanen, I. Electrical crosstalk in front-illuminated photodiode array with different guard ring designs for medical CT applications. *Nuclear Instruments and Methods in Physics Research, Section A: Accelerators, Spectrometers, Detectors and Associated Equipment* **607,** 150–153 (1 Aug. 2009) (cit. on p. 32).

75. Joergensen, M. E. *et al.* Functional Testing or Coronary Computed Tomography Angiography in Patients With Stable Coronary Artery Disease. *Journal of the American College of Cardiology* **69,** 1761–1770 (14 2017) (cit. on p. 45).

76. Kabus, S., Klinder, T., von Berg, J. & Lorenz, C. in, 116–127 (2010) (cit. on p. 92).

77. Kabus, S. *et al.* in, 747–754 (2009) (cit. on p. 92).

78. Kalender, W., Klotz, E. & Kostaridou, L. An algorithm for noise suppression in dual energy CT material density images. *IEEE Transactions on Medical Imaging* **7,** 218–224 (3 1988) (cit. on pp. 40, 105).

79. Kalender, W. A. A phantom for standarization and quality control in spinal bone mineral measurements by QCT and DXA: Design considerations and specifications. *Medical Physics* **19,** 583–586 (3 May 1992) (cit. on p. 94).

80. Kalender, W. A. *et al.* The European Spine Phantom — a tool for standardization and quality control in spinal bone mineral measurements by DXA and QCT. *European Journal of Radiology* **20,** 83–92 (2 July 1995) (cit. on p. 94).

81. Kaup, M. *et al.* Dual-Energy Computed Tomography Virtual Monoenergetic Imaging of Lung Cancer. *Journal of Computer Assisted Tomography* **40,** 80–85 (1 2016) (cit. on p. 82).

82. Kay, S. M. *Fundamentals of Statistical Signal Processing: Est imat ion Theory* () (cit. on pp. 40, 41).

83. Kinoshita, H., Tamaki, T., Hashimoto, T. & Kasagi, F. Factors influencing lumbar spine bone mineral density assessment by dual-energy X-ray absorptiometry: Comparison with lumbar spinal radiogram. *Journal of Orthopaedic Science* **3,** 3–9 (1 Jan. 1998) (cit. on p. 114).

84. Klein, O. & Nishina, Y. Ueber die Streuung von Strahlung durch freie Elektronen nach der neuen relativistischen Quantendynamik von Dirac. *Zeitschrift für Physik* **52,** 853–868 (11-12 Nov. 1929) (cit. on pp. 8, 11).

85. Knuuti, J. *et al.* 2019 ESC guidelines for the diagnosis and management of chronic coronary syndromes. *European Heart Journal* **41,** 407–477 (3 2020) (cit. on p. 46).

86. Ko, B. S. *et al.* Combined CT Coronary Angiography and Stress Myocardial Perfusion Imaging for Hemodynamically Significant Stenoses in Patients With Suspected Coronary Artery Disease. *JACC: Cardiovascular Imaging* **5,** 1097–1111 (11 Nov. 2012) (cit. on p. 46).

87. Koch, V. *et al.* Accuracy and precision of volumetric bone mineral density assessment using dual-source dual-energy versus quantitative CT: a phantom study. *European Radiology Experimental* **5** (1 Dec. 2021) (cit. on pp. 93, 115).

88. Kraitchman, D. L. *et al.* Myocardial perfusion and function in dogs with moderate coronary stenosis. *Magnetic Resonance in Medicine* **35,** 771–780 (5 1996) (cit. on p. 83).

89. Laugerette, A. *et al.* DXA-equivalent quantification of bone mineral density using dual-layer spectral CT scout scans. *European Radiology* **29,** 4624–4634 (9 Sept. 2019) (cit. on pp. 93, 104, 107).

90. Laugerette, A. *et al.* Spectral-detector based x-ray absorptiometry (SDXA): in-vivo bone mineral density measurements in patients with and without osteoporotic fractures. *Biomedical Physics and Engineering Express* (2020) (cit. on pp. 93, 104).

91. Lehmann, L. A. *et al.* Generalized image combinations in dual KVP digital radiography. *Medical Physics* **8,** 659–667 (5 Sept. 1981) (cit. on p. 12).

92. Leng, S. *et al.* Photon-counting detector CT: System design and clinical applications of an emerging technology. *Radiographics* **39,** 729–743 (3 2019) (cit. on p. 37).

93. Levi, J. *et al.* Calibration-free beam hardening correction for myocardial perfusion imaging using CT. *Medical Physics* **46,** 1648–1662 (4 2019) (cit. on p. 47).

94. Li, N. *et al.* Comparison of QCT and DXA: Osteoporosis Detection Rates in Postmenopausal Women. *International Journal of Endocrinology* **2013,** 1–5 (2013) (cit. on pp. 89, 93).

95. Libby, P. & Theroux, P. Pathophysiology of coronary artery disease. *Circulation* **111,** 3481–3488 (25 2005) (cit. on p. 45).

96. Liu, L. Model-based iterative reconstruction: A promising algorithm for today's computed tomography imaging. *Journal of Medical Imaging and Radiation Sciences* **45,** 131–136 (2 2014) (cit. on p. 30).

97. Löffler, M. T. *et al.* X-ray-based quantitative osteoporosis imaging at the spine. *Osteoporosis International* **31,** 233–250 (2 Feb. 2020) (cit. on p. 114).

98. Löffler, M. T. *et al.* Automatic opportunistic osteoporosis screening in routine CT: improved prediction of patients with prevalent vertebral fractures compared to DXA. *European Radiology* **31,** 6069–6077 (8 Aug. 2021) (cit. on p. 114).

99. Löffler, M. T. *et al.* A vertebral segmentation dataset with fracture grading. *Radiology: Artificial Intelligence* **2,** 1–6 (4 2020) (cit. on pp. 104, 107).

100. Löffler, M. T. *et al.* Improved prediction of incident vertebral fractures using opportunistic QCT compared to DXA. *European Radiology* **29,** 4980–4989 (9 Sept. 2019) (cit. on p. 114).

101. Lorensen, W. E. & Cline, H. E. Marching cubes: A high resolution 3D surface construction algorithm. *Computer Graphics* **21** (4 1987) (cit. on p. 124).

102. Lourenco, P. D. M. *et al.* Dual-Energy CT Iodine Mapping and 40-keV Monoenergetic Applications in the Diagnosis of Acute Bowel Ischemia. *American Journal of Roentgenology* **211,** 564–570 (3 Sept. 2018) (cit. on p. 82).

103. Lowekamp, B. C., Chen, D. T., Ibáñez, L. & Blezek, D. The design of simpleITK. *Frontiers in Neuroinformatics* **7** (DEC Dec. 2013) (cit. on p. 107).

104. Madsen, M. T. A simplified formulation of the gamma variate function. *Physics in Medicine and Biology* **37,** 1597–1600 (7 July 1992) (cit. on pp. 49, 53, 81, 83, 91).

105. Maron, D. J. *et al.* Initial Invasive or Conservative Strategy for Stable Coronary Disease. *New England Journal of Medicine* **382,** 1395–1407 (15 2020) (cit. on p. 46).

106. McCloskey, E. *et al.* The osteoporosis treatment gap in patients at risk of fracture in European primary care: a multi-country cross-sectional observational study. *Osteoporosis International* **32,** 251–259 (2 Feb. 2021) (cit. on p. 93).

107. Mechlem, K. *et al.* A post-processing algorithm for spectral CT material selective images using learned dictionaries. *Biomedical Physics and Engineering Express* **3,** 025009 (2 2017) (cit. on pp. 76, 77, 105).

108. Mechlem, K. *et al.* Joint Statistical Iterative Material Image Reconstruction for Spectral Computed Tomography Using a Semi-Empirical Forward Model. *IEEE Transactions on Medical Imaging* **37,** 68–80 (1 Jan. 2018) (cit. on p. 122).

109. Mei, K. *et al.* Bone mineral density measurements in vertebral specimens and phantoms using dual-layer spectral computed tomography. *Scientific Reports* **7,** 1–10 (1 2017) (cit. on p. 93).

110. Miles, K. A. & Griffiths, M. R. Perfusion CT: a worthwhile enhancement? *The British Journal of Radiology* **76,** 220–231 (904 Apr. 2003) (cit. on pp. 81, 85).

111. Miller, P. D. Underdiagnoses and undertreatment of osteoporosis: The battle to be won. *Journal of Clinical Endocrinology and Metabolism* **101,** 852–859 (3 Mar. 2016) (cit. on p. 93).

112. Mischi, M., den Boer, J. A. & Korsten, H. H. M. On the physical and stochastic representation of an indicator dilution curve as a gamma variate. *Physiological Measurement* **29,** 281–294 (3 2008) (cit. on p. 81).

113. Miyabara, Y., Holmes, D., Camp, J., Miller, V. M. & Kearns, A. E. Comparison of calibrated and uncalibrated bone mineral density by CT to DEXA in menopausal women. *Climacteric* **15,** 374–381 (4 2012) (cit. on p. 114).

114. Mozaffarian, D. *et al. Heart disease and stroke statistics-2015 update : A report from the American Heart Association* e29–e39 (2015) (cit. on p. 45).

115. Muenzel, D. *et al.* Spectral Photon-counting CT: Initial Experience with Dual–Contrast Agent K-Edge Colonography. *Radiology* **283,** 723–728 (3 June 2017) (cit. on p. 62).

116. Nabel, E. G. & Braunwald, E. A Tale of Coronary Artery Disease and Myocardial Infarction. *New England Journal of Medicine* **366,** 54–63 (1 Jan. 2012) (cit. on p. 45).

117. Nous, F. M. *et al.* Dynamic Myocardial Perfusion CT for the Detection of Hemodynamically Significant Coronary Artery Disease. *JACC: Cardiovascular Imaging* **15,** 75–87 (1 2022) (cit. on pp. 47, 76, 78).

118. Nuyts, J., Michel, C. & Dupont, P. Maximum-Likelihood Expectation-Maximization Reconstruction of Sinograms with Arbitrary Noise Distribution Using NEC-Transformations. *IEEE TRANSACTIONS ON MEDICAL IMAGING* **20** (5 2001) (cit. on p. 22).

119. Odgaard, A. Three-Dimensional Methods for Quantification of Cancellous Bone Architecture. *Bone* **20,** 315–328 (4 1997) (cit. on p. 126).

120. Of Radiology, A. C. *ACR SPR SSR practice guideline for the performance of quantitative computed tomography (QCT) bone* (2018) (cit. on p. 112).

121. Patel, A. R. *et al.* Society of cardiovascular computed tomography expert consensus document on myocardial computed tomography perfusion imaging. *Journal of Cardiovascular Computed Tomography* **14** (1 2020) (cit. on pp. 47, 48).

122. Pedregosa, F. *et al.* Scikit-learn: Machine Learning in Python. *Journal of Machine Learning Research* **12,** 2825–2830 (2011) (cit. on pp. 64, 109).

123. Pelgrim, G. J. *et al.* Quantitative myocardial perfusion with dynamic contrast-enhanced imaging in MRI and CT: Theoretical models and current implementation. *BioMed Research International* **2016** (2016) (cit. on p. 48).

124. Persson, M. & Groenberg, F. Bias-variance tradeoff in anticorrelated noise reduction for spectral CT. *Medical Physics* **44,** e242–e254 (9 2017) (cit. on p. 76).

125. Phan, C. M. *et al.* Trabecular bone structure of the calcaneus: Comparison of MR imaging at 3.0 and 1.5 T with micro-CT as the standard of reference. *Radiology* **239,** 488–496 (2 May 2006) (cit. on p. 93).

126. Rajendran, K. *et al.* First Clinical Photon-counting Detector CT System: Technical Evaluation. *Radiology* (Dec. 2021) (cit. on pp. 6, 18).

127. Ries, A. *et al.* Improving Image Quality of Sparse-view Lung Cancer CT Images with a Convolutional Neural Network (July 2023) (cit. on p. 30).

128. Roessl, E. & Herrmann, C. Cramér-Rao lower bound of basis image noise in multiple-energy x-ray imaging. *Physics in Medicine and Biology* **54,** 1307–1318 (5 2009) (cit. on pp. 40, 41, 44).

129. Roessl, E., Ziegler, A. & Proksa, R. On the influence of noise correlations in measurement data on basis image noise in dual-energylike x-ray imaging. *Medical Physics* **34,** 959–966 (3 Feb. 2007) (cit. on p. 40).

130. Ronneberger, O., Fischer, P. & Brox, T. U-Net: Convolutional Networks for Biomedical Image Segmentation (May 2015) (cit. on p. 116).

131. Roski, F. *et al.* Bone mineral density measurements derived from dual-layer spectral CT enable opportunistic screening for osteoporosis. *European Radiology* **29,** 6355–6363 (11 Nov. 2019) (cit. on pp. 93, 115).

132. Sánchez-Gracián, C. D. *et al.* Quantitative myocardial perfusion with stress dual-energy CT: iodine concentration differences between normal and ischemic or necrotic myocardium. Initial experience. *European Radiology* **26,** 3199–3207 (9 2016) (cit. on pp. 47, 89).

133. Schardt, P. *et al.* New x-ray tube performance in computed tomography by introducing the rotating envelope tube technology. *Medical Physics* **31,** 2699–2706 (9 2004) (cit. on p. 6).

134. Scherer, K. *et al.* Dynamic Quantitative Iodine Myocardial Perfusion Imaging with Dual-Layer CT using a Porcine Model. *Scientific Reports* **9,** 1–9 (1 2019) (cit. on pp. 45, 47, 79, 82, 84, 86, 88).

135. Schlomka, J. P. *et al.* Experimental feasibility of multi-energy photon-counting K-edge imaging in pre-clinical computed tomography. *Physics in Medicine and Biology* **53,** 4031–4047 (15 Aug. 2008) (cit. on p. 32).

136. Schulz, R. A., Stein, J. A. & Pelc, N. J. How CT happened: the early development of medical computed tomography. *Journal of Medical Imaging* **8** (05 Oct. 2021) (cit. on p. 1).

137. Sellerer, T. *et al.* Dual-energy CT: a phantom comparison of different platforms for abdominal imaging. *European Radiology* **28,** 2745–2755 (7 Feb. 2018) (cit. on pp. 47, 48, 89).

138. Sellerer, T. *et al.* Quantitative dual-energy micro-CT with a photon-counting detector for material science and non-destructive testing. *PLoS ONE* **14,** 1–18 (7 2019) (cit. on p. 122).

139. Shefer, E. *et al.* State of the Art of CT Detectors and Sources: A Literature Review. *Current Radiology Reports* **1,** 76–91 (1 Mar. 2013) (cit. on pp. 25, 26, 32, 43).

140. Shen, L., Pauly, J. & Xing, L. NeRP: Implicit Neural Representation Learning With Prior Embedding for Sparsely Sampled Image Reconstruction. *IEEE Transactions on Neural Networks and Learning Systems* (2022) (cit. on p. 30).

141. Snyder, D. L., Helstrom, C. W., Lanterman, A. D., Faisal, M. & White, R. L. Compensation for readout noise in CCD images. *J. Opt. Soc. Am. A* **12** (2 1995) (cit. on p. 35).

142. So, A. *et al.* Dual-energy CT and its potential use for quantitative myocardial CT perfusion. *Journal of Cardiovascular Computed Tomography* **6,** 308–317 (5 Sept. 2012) (cit. on p. 47).

143. Software, I. M. QCT vs . DXA : What ' s the Score? *Mindways CT Quantifiably Better* (2012) (cit. on p. 112).

144. Sones, R. A. & Barnes, G. T. Noise Correlations In Images Acquired Simultaneously With A Dual-Energy Sandwich Detector. *Medical Physics* **16,** 858–861 (6 1989) (cit. on p. 40).

145. Spiegel, P. K. The first clinical X-ray made in America - 100 years. *American Journal of Roentgenology* **164,** 241–243 (1 Jan. 1995) (cit. on p. 1).

146. Stenner, P., Schmidt, B., Allmendinger, T., Flohr, T. & Kachelries, M. Dynamic Iterative Beam Hardening Correction (DIBHC) in Myocardial Perfusion Imaging Using Contrast-Enhanced Computed Tomography. *Investigative Radiology* **45,** 314–323 (6 June 2010) (cit. on pp. 47, 78).

147. Stewart, B. K. & Huang, H. K. Single-exposure dual-energy computed radiography. *Medical Physics* **17,** 866–875 (5 Sept. 1990) (cit. on p. 2).

148. Swank, R. K. Absorption and noise in x-ray phosphors. *Journal of Applied Physics* **44,** 4199–4203 (9 1973) (cit. on pp. 40, 41).

149. Thompson, H. K., Starmer, C. F., Whalen, R. E. & Mcintosh, H. D. Indicator Transit Time Considered as a Gamma Variate. *Circulation Research* **14,** 502–515 (6 June 1964) (cit. on p. 48).

150. Varga-Szemes, A. *et al.* CT myocardial perfusion imaging. *American Journal of Roentgenology* **204,** 487–497 (3 2015) (cit. on pp. 47, 77).

151. Virtanen, P. *et al.* SciPy 1.0: fundamental algorithms for scientific computing in Python. *Nature Methods* **17,** 261–272 (3 2020) (cit. on pp. 63, 109, 126).

152. Vliegenthart, R. *et al.* Dual-Energy CT of the Heart. *American Journal of Roentgenology* **199,** S54–S63 (Nov. 2012) (cit. on p. 46).

153. Wellenberg, R. H. *et al.* Quantifying metal artefact reduction using virtual monochromatic dual-layer detector spectral CT imaging in unilateral and bilateral total hip prostheses. *European Journal of Radiology* **88,** 61–70 (2017) (cit. on p. 30).

154. White, D. R. An analysis of the Z-dependence of photon and electron interactions. *Physics in Medicine and Biology* **22,** 219–228 (2 Mar. 1977) (cit. on pp. 10, 12).

155. Whiting, B. R. *et al.* Properties of preprocessed sinogram data in x-ray computed tomography. *Medical Physics* **33,** 3290–3303 (9 2006) (cit. on p. 35).

156. Whittier, D. E. *et al.* Guidelines for the assessment of bone density and microarchitecture in vivo using high-resolution peripheral quantitative computed tomography. *Osteoporosis International* **31,** 1607–1627 (9 2020) (cit. on p. 93).

157. Willer, K. *et al.* X-ray dark-field chest imaging for detection and quantification of emphysema in patients with chronic obstructive pulmonary disease : a diagnostic accuracy study. *The Lancet Digital Health* **3,** e733–e744 (11 2021) (cit. on pp. 122, 128).

158. Wischmann, H.-A. *et al.* Correction of Amplifier Non-Linearity, Offset, Gain, Temporal Artifacts, and Defects for Flat Panel Digital Imaging Devices (2002) (cit. on p. 23).

159. Yang, D. H. *et al.* Stress Myocardial Perfusion CT in Patients Suspected of Having Coronary Artery Disease: Visual and Quantitative Analysis - Validation by Using Fractional Flow Reserve. *Radiology* **276,** 715–723 (3 Sept. 2015) (cit. on p. 46).

160. Yaniv, Z., Lowekamp, B. C., Johnson, H. J. & Beare, R. SimpleITK Image-Analysis Notebooks: a Collaborative Environment for Education and Reproducible Research. *Journal of Digital Imaging* **31,** 290–303 (3 June 2018) (cit. on p. 107).

161. Yu, W. *et al. Spinal Bone Mineral Assessment in Postmenopausal Women: A Comparison Between Dual X-ray Absorptiometry and Quantitative Computed Tomography* (1995), 433–439 (cit. on p. 114).

162. Yushkevich, P. A. *et al.* User-Guided 3D Active Contour Segmentation of Anatomical Structures: Significantly Improved Efficiency and Reliability. *Neuroimage* **31** (2006) (cit. on p. 124).

163. Zhu, C., Byrd, R. H., Lu, P. & Nocedal, J. Algorithm 778: L-BFGS-B. *ACM Transactions on Mathematical Software* **23,** 550–560 (4 Dec. 1997) (cit. on p. 63).